UNIVERSITY OF OKLAHOMA

GRADUATE COLLEGE

USING PHYSICOCHEMICAL PROPERTIES WITHIN A DISCRETE ELEMENT MODELING FRAMEWORK AND FRACTAL GEOMETRY THEORY TO UNDERSTAND BEHAVIOR OF UNSATURATED EXPANSIVE CLAYS

A DISSERTATION

SUBMITTED TO THE GRADUATE FACULTY

in partial fulfilment of the requirements for the

Degree of

DOCTOR OF PHILOSOPHY

By

Michelle R. Basham

Norman, Oklahoma

2023

USING PHYSICOCHEMICAL PROPERTIES WITHIN A DISCRETE ELEMENT MODELING FRAMEWORK AND FRACTAL GEOMETRY THEORY TO UNDERSTAND BEHAVIOR OF UNSATURATED EXPANSIVE CLAYS

A DISSERTATION APPROVED FOR THE
SCHOOL OF CIVIL ENGINEERING AND ENVIRONMENTAL SCIENCE

BY THE COMMITTEE CONSISTING OF

Dr. Amy Cerato, Chair

Dr. Andrew Elwood-Madden

Dr. Kanthasamy Muraleetharan

Dr. Kianoosh Hatami

Dr. Gerald Miller

"Clouds are not spheres, mountains are not cones, coastlines are not circles, and bark is not smooth, nor does lightning travel in a straight line."
– Benoit B. Mandelbrot, *Fractals: Form, Chance, and Dimension, 1977.*

Acknowledgements

I would like to thank my advisor, Dr. Amy Cerato for her support, advice, and mentorship throughout my time here at OU. I am thankful for the opportunity to work with you and for the chance to finish my degree. I am also grateful to my committee members, Dr. Kianoosh Hatami, Dr. Andrew Elwood-Madden, Dr. Gerald Miller, and Dr. K.K. Muraleetharan for their valuable feedback and insights that helped me improve the quality of my work. Their knowledge, support, and guidance has been invaluable to me.

I would also like to thank the faculty and staff in the Civil Engineering and Environmental Science department. Laura Swan, Deanna Amidon, and Molly Smith have been invaluable sources of information and support.

Special thanks are due to the Samuel Roberts Noble Microscopy Laboratory for use of the ESEM. I would like to thank Dr. Preston Larson especially for his help collecting the ESEM images.

Table of Contents

List of Tables

List of Figures

Abstract

The volumetric deformations associated with expansive soils pose a risk to infrastructure, costing billions in mitigation annually. Many engineering designs assume the soil is in either the dry state or fully saturated. However, clays used as barrier systems and foundations are in the unsaturated state for the majority of the design life. Therefore, it is necessary to understand the mechanism underlying expansive soil behavior, particularly in response to changes in moisture along cycles of wetting and drying. There is substantial evidence demonstrating that the engineering behavior of these clays is controlled by microscopic, physicochemical forces, i.e., the van der Waals attractive force, double layer force, interlayer force, and mechanical contact forces. The physicochemical forces at the microscale that ultimately govern macroscale behavior, however, are not well understood and there is a need for a conceptual framework to quantify changes in fabric as the soil structure interacts with pore fluid. In order to provide better insight into the evolution of soil fabric under pore fluid changes and the controlling microscale mechanisms that cause swelling, two innovative approaches were utilized with the goal of providing a conceptual framework for quantifying microstructural forces and parameters present that affect macroscale behavior: (1) Discrete Element Modeling (DEM) and (2) Fractal Theory.

Discrete element modeling was employed to provide a method to better predict expansive soil swell pressures. The DEMClay program was adapted to consider physicochemical forces including the van der Waals attractive force, double layer repulsive, and mechanical contact forces in addition to microscale parameters (cation exchange capacity, specific surface area, Hamaker constant) to model microscale forces of expansive clays. The model was calibrated with a single mineral Na-montmorillonite and validated using natural specimens of montmorillonite-bearing soils with widely variable cation exchange capacity (CEC) and specific surface area (S_A) parameters. DEMClay provided accurate predictions of swell pressures and can be employed by practitioners with knowledge of a few key soil parameters.

In addition to implementing a valid model to predict swell pressures of single-mineral and natural soils using physicochemical parameters, concepts from fractal geometry were used to provide the missing quantitative element describing surface features and structure of clay particles. Fractal geometry offers a numerical understanding of the patterns of fabric, structure, and pore networks found on high resolution environmental scanning electron microscopy (ESEM) images of expansive single-mineral clays and natural soils at specific densities and suction. Quantitative assessments of microstructural changes were made using fractal geometry parameters, including fractal dimension and lacunarity, where the fractal dimension describes the complexity of the soil surface and lacunarity describes the texture, or pattern of voids of the fabric. For example, fractal dimension was lower for single-mineral clays than natural clays but lacunarity was higher for the artificial clays than the natural clays. These parameters allow engineers to better understand the evolution of surface complexity of expansive clays with varying mineralogy and physicochemical properties under cycles of hydrologic hysteresis and can be employed as parameters in models focused on predicting expansive soil behavior.

This research advances the understanding of unsaturated expansive soils through analyzing microscale mechanisms including surface complexity, pore fluid hysteresis and physicochemical forces. The outcome of this study provides engineers with a model that can accurately predict macroscale behavior of expansive soils, e.g., swell pressures, based on void ratio, intrinsic physicochemical parameters like S_A and CEC, mineralogical parameters, and suction state and discusses methods in which this model can be further improved. It also details a novel way in which to consider surface complexity of clay minerals through fractal geometry that provides quantitative relationships with many important soil parameters and helps explain the evolution of behavior through suction states.

Chapter 1 Introduction

Expansive soils are prevalent across a quarter of the United States and span over 2,350,000 square kilometers of the Earth's surface. Due to their widespread occurrence, they are an inescapable choice for bearing layers of bridges, roads, and other lightweight structures. The tendency to expand when reacting with pore fluid, along with the low permeability associated with these soils, is beneficial when used as a barrier material for waste containment or the core of earthen dams and levees. However, volumetric strains associated with seasonal wetting and drying cycles can also damage structures: as water evaporates during drying cycles, the resulting increase in suction can cause cracking in compacted clays, which can damage the overlying infrastructure if not constructed with adequate foundation systems. Conversely, as rainfall infiltrates the soil deposit, the water content increases and the soil can swell with enormous swell pressures and large volume changes. The associated mitigation costs exceed that of floods, hurricanes, and earthquakes combined. However, while there are suitable methods to predict macroscale behavior of expansive soils, e.g., swell pressure, heave, and the associated deformations, empirical correlations, e.g., PI, are often used to predict swell potential and swell pressure due to expansive soil movement. Such techniques are inadequate to predict or mitigate damage and a better understanding of the mechanism causing the behavior would better inform design. The wide use of expansive clays in engineering projects necessitates a better understanding of the microscale behavior, particularly over a wide range of pore fluid conditions as the soil experiences cycles of wetting and drying. Models which can capture the microscale forces require a fully developed understanding of the soil fabric at the microscale as moisture conditions vary.

Understanding the microscale mechanisms causing swelling in soils will allow engineers to mitigate, or ideally prevent, the damage caused by expansive soils, which remains a costly and

perplexing Grand Challenge of Geotechnical Engineering. There is considerable evidence demonstrating that physicochemical forces at the microscale, i.e., the double layer repulsive, van der Waals attractive, and interlayer forces, in addition to mechanical contact forces, govern interparticle, interaggregate, and intra-aggregate interactions, influencing soil fabric which ultimately determines macroscopic mechanical behavior of expansive clays. As water content fluctuates within the pore networks of soil, the microlevel forces also change, and suction between particles increases and decreases inversely to the volumetric water content. As suction evolves, fluctuations within the soil fabric occur, which impact the strength, permeability, and other macroscale properties of the soil.

While expansive soils in the unsaturated state have been studied, the mechanisms explaining their behavior remains a challenge to engineers who seek to accurately predict and mitigate volumetric strains under various conditions. Moreover, the many engineering designs assume the soil is in either a dry state (S = 0%) or fully saturated (S = 100%). However, realistically, as-compacted clay used in designs, e.g., barrier systems, cores of dams and levees, and bearing material for foundations and embankments, will be in the unsaturated ($0\% < S < 100\%$) state for the majority of the design life of the project. It is necessary, therefore, to quantify the differences in engineering behavior when selecting appropriate soil for these projects.

Many current methods used to predict soil behavior do not correctly incorporate the true suction state of an expansive soil, and furthermore use empirical parameters relying on Atterberg limits, grain size distribution, and clay fraction. However, Atterberg limits are not fundamental soil properties and two soils with the same plasticity index can vary in behavior if, for example, the mineralogy or geochemistry varies. Plasticity alone has been shown to be inadequate to characterize soil shrinking and swelling at the microscale (e.g., Buhler and Cerato 2007). Similarly,

other empirical parameters utilizing Atterberg limits, i.e., the Skempton activity parameter, are not sufficient to describe the behavior of natural clays. Instead, intrinsic soil parameters, i.e., specific surface area and cation exchange capacity, have been shown to better capture the behavior of clays (e.g., Cerato and Lutenegger 2001; Polidori 2009; Karakan 2022). Other models, utilizing double layer theory, have failed to accurately predict swell pressure for clays of varying mineralogy and structure because double layer theory ignores the chemistry of the clay itself, instead attributing swell pressure solely to the repulsive pressure developed between clay layers (Schanz and Tripathy 2009; Ma et al. 2019). Moreover, the use of empirically-based models is problematic as empirical relations are not based on measured quantities and are not sophisticated enough to capture the complex nature of clay structure. A model based on measured quantities would remove empiricism and therefore uncertainty, better capturing realistic behavior. With advances in technology, it is becoming possible to study these microscale clay particles in more detail and present both qualitative and quantitative methods in which to understand surface phenomena and particle interactions under conditions which explain factors that influence soil behavior. Results of these studies could better inform design and the state of practice.

In order to provide better insight into the evolution of soil fabric under pore fluid changes and the controlling microscale mechanisms that cause swelling, the research approach was twofold with the goal of providing a conceptual framework for quantifying microstructural forces and parameters: (1) Discrete Element Modeling and (2) Fractal Theory. Discrete element modeling was employed to provide a method to better predict expansive swell pressures. The discrete element method (DEM) is a numerical method to analyze problems concerning granular and discontinuous materials such as soils and rock (Rojek et al. 2018). DEM improves upon other continuum models by modeling dynamic motion and mechanical interactions with fewer

parameters, effectively capturing changes in microstructure, deformation, dynamics, and forces (Katti et al. 2009). While most DEM models were created for the analysis of cohesionless materials, there are several available DEM models for clays. However, because the very small particle size of clays has been difficult to model due to computational limitations, many models have considered clays as an aggregate rather than model each individual particle (e.g., Sima et al. 2014; Guo et al. 2017). Other models consider the microscale, interparticle behavior of clays (e.g., Katti et al. 2009; Anandarajah and Amarasinghe 2013; Khabazian et al. 2018), but have yet to reliably predict swell pressure strictly using DEM. This research adapts Anandarajah's (1994) DEMClay program to consider realistic, natural clays and provide swell pressures based on modeled soil fabric, pore fluid parameters, and physicochemical forces. Microscale parameters, i.e., cation exchange capacity, specific surface area, and the Hamaker constant, can be used to model these microscale forces, accurately predicting macroscale engineering behavior, e.g., swell pressure. A sensitivity study was performed to determine the most influential input parameters and the DEMClay model was calibrated using the results of free swell tests of a pure montmorillonite at various void ratios. Once calibrated, the DEMClay model was successfully validated by accurately predicting the swell pressures of several natural expansive clay-bearing soils including montmorillonite and vermiculite mineralogy.

In addition to applying a valid model to predict swell pressures of single-mineral and natural soil using physicochemical parameters, concepts from fractal theory were used to overcome the missing quantitative element. Specifically, fractal geometries describing clay particle surfaces and clay particle structure formed a numerical understanding of the patterns of fabric, structure, and pore networks found on high resolution environmental scanning electron microscopy images of expansive single-mineral clays and natural soils at specific densities and

suction. Mandelbrot (1982) defined a fractal as a geometric figure that scales to some dimension between whole number powers, formalizing a branch of mathematics capable of describing irregular and complex geometries. Fractals have been extensively studied in mathematics and have applications in various fields such as computer graphics (e.g., Devaney et al. 1989; Sala 2021), physics (e.g., Goyet 1996; Zmeskal et al. 2013; Balankin et al. 2016), biology (e.g., Nielsen et al. 2002; Rees 2020), and economics (e.g. Peters 1994; Mosteanu 2019), providing insights into the underlying structures of natural phenomena. Fractal patterns have been observed in nature in the form of tree branching and root systems, mountain ranges, river deltas, lightning branches, and cellular morphologies. Fractal patterns have also been observed in soils and other geomaterials, such as sands and rocks and have been utilized to better understand the microscale mechanisms influencing the macroscale behavior observed in the natural and built environment, such as preferential flow paths, gas diffusion through soil, and hydraulic conductivity models. In this study, quantitative assessments of microstructural changes were made using fractal geometry parameters, including fractal dimension and lacunarity, where the fractal dimension describes the complexity of the soil surface and lacunarity describes the texture, or pattern of voids of the fabric. These parameters allow engineers to better understand the evolution of surface complexity of expansive clays with varying mineralogy and physicochemical properties under cycles of hydrologic hysteresis and can be employed as parameters in models focusing on predicting expansive soil behavior.

1.1 Objectives and Scope of Research

The main goal of this work was to advance the understanding of macroscopic unsaturated expansive soil behavior by analyzing microscale mechanisms that control the behavior of expansive clays. Because the nature of expansive soils is complex, the scope of this investigation

encompasses: (1) developing a model that better predicts macroscale behavior using microscale physicochemical, mineralogical, and/or pore fluid parameters (i.e., model swell pressure) and (2) describing microstructural hierarchical patterns that influence behavior not captured through physicochemical or mineralogical parameters (i.e., analyze surface geometry).

To this end, the following objectives were met: (1) model macroscale behavior, e.g., swell pressure, using microscopic physicochemical and mechanical forces, (2) characterize fabric changes that occur at the microscale in response to changes in pressure, pore fluid, or stabilization reactions using qualitative image analysis, and (3) quantify structural (fabric) parameters that influence macroscale parameters using fractal geometry.

To meet the objectives of this study, the following tasks were completed:

- Performed and analyzed one-dimensional swell pressures for a montmorillonite-bearing clay at varying densities to calibrate the DEMClay model
- Calibrated DEMClay with high-quality experimental 1D swell tests on an expansive, montmorillonite-bearing clay. Validated DEMClay with three naturally occurring swelling-clay-bearing soils from the literature
- Predicted swell pressures of naturally occurring expansive clays with varying physicochemical parameters using DEMClay
- Quantified fabric changes of a stabilized kaolinitic soil using fractal geometry combined with Scanning Electron Microscopy (SEM) and Mercury Intrusion Porosimetry (MIP) results. These fabric changes included structural changes to the soil surface and pore network during stabilization over time and were presented as fractal dimension (surface complexity) and lacunarity (texture, or pattern of voids of the fabric)

- Created Environmental Scanning Electron Microscopy (ESEM) micrographs for specimens of artificial and natural clays along the initial drying and secondary wetting paths of the Soil Water Retention Curve (SWRC) to evaluate the evolution of surface complexity using imaging techniques and fractal geometry. Evaluated effects of magnification scale, silt content, and physicochemical parameters.
- Quantitatively evaluated structural variations occurring with hysteretic moisture changes concerning differences in silt content, initial compaction conditions, equilibration time, and montmorillonite content via fractal geometry.

1.2 Dissertation Outline

Each chapter is adapted from a peer reviewed journal article or is a paper planned as a future publication. The dissertation is organized into the following chapters:

Chapter 2 describes the structural changes over time occurring on the soil surface and within the pore network of a kaolinitic soil stabilized with a calcium-based stabilizer. Structural changes were quantified using imaging techniques and fractal geometry. This chapter developed and validated the fractal analysis techniques that were then extended to expansive soils in Chapter 4.

Chapter 3 details the qualitative evaluation of ESEM micrographs obtained along hysteretic moisture paths of several single-mineral and naturally occurring clays with varying mineralogy, activity, and moisture conditions.

Chapter 4 provides a quantitative evaluation of structure interpreted from the analysis of ESEM micrographs detailed in Chapter 3. Fractal geometry parameters, including fractal dimension and lacunarity, were used to compare changes in microstructure as suction varied.

Chapter 5 discusses the DEMClay program, adapted to predict swell pressures of expansive soils using physicochemical parameters. The calibration, validation, and use of this model with natural soils is detailed.

Chapter 6 summarizes the conclusions of this research and offers recommendations for future work.

Chapter 2 Use of Fractal Geometry Theory to Quantify Pore Structure Evolution and Particle Morphology of Stabilized Kaolinite

2.1 Introduction

Soil improvement is often necessary in the case of problematic soils, such as expansive, compressible, or collapsible soils. Improvement techniques include compaction of loose sand and silt layers (e.g., Rollins and Kim 2010), removal and replacement (e.g., Bharadwaj et al. 2013; Houston et al. 2015), grouting (e.g., Albritton et al. 1984; Karol 2003), and chemical stabilization (e.g., Cerato and Miller 2013; Athanasopoulou 2014). Soil stabilization in clays and organic soils is often achieved through addition of cementitious chemical agents to improve soil performance, e.g., increase shear strength, reduce soil plasticity, reduce compressibility, and reduce shrink or swell potential (Tremblay et al. 2002; Puppala and Cerato 2009; Lin et al. 2013; Lau et al. 2023).

While soil stabilization is common practice, the underlying mechanism of stabilization merits further study, particularly concerning microscale changes which affect macroscale engineering behavior (Lin et al. 2013; Salahudeen et al. 2014; Coudert et al. 2021). Over time, compounds in the calcium-based stabilizer (e.g., Portland cement) react with water to form hydrated compounds. Additionally, the stabilizer causes a pozzolanic reaction: silicon and aluminum within the soil dissolve and react with calcium in the stabilizer to form calcium silicate hydrate (CSH) and calcium aluminate hydrate (CAH). As the hydration and pozzolanic reactions progress, the pore network evolves. Two pore classes emerge: (1) capillary pores and (2) gel pores (Coudert et al. 2021). As hydration reactions occur, CAH and CSH products form, decreasing the volume of the capillary pores. Smaller pores form within the hydrates, often called gel pores (Berodier et al. 2016).

Because stabilization reactions occur at the microscale, there is a need for techniques which properly characterize structure and morphology which inform the performance of the soil (Venkateshaiah et al. 2020), particularly regarding particle size distribution and pore morphology. Currently, the standard of practice for grain and particle size distribution (PSD) is sieve and hydrometer analysis. However, this method is not practical for in-situ analysis (Ventola et al. 2020; Ohm and Hryciw 2014) and methods which can determine particle size and distribution through an image are desired (Ural 2021). Laboratory determination of PSD for clays and silts requires wet sieving and hydrometer analysis which does not provide sufficient discretization of the fabric at the microscale, e.g., particle sizes less than 2 μm, and does not provide a continuous PSD for fine resolutions (Bankole et al. 2019; Yang et al. 2019). Currently, image analysis is the only method which directly measures the grain diameter (Bankole et al. 2019).

Mercury Intrusion Porosimetry (MIP) provides information on pore morphology through a pore size distribution by measuring the size of pores based on the volume of intruded mercury. Because mercury is a nonwetting fluid (i.e., contact angle is greater than 90 degrees), the fluid itself cannot overcome the surface tension to infiltrate pores and therefore an external pressure, applied using a porosimeter, describes the difference in pressure along the mercury meniscus. The method was discovered by Washburn (1921) to determine the pore diameter distribution of porous substances such as charcoal. The change in volume due to an increase in pressure is a response to mercury filling the pores and the pressure has an inverse relation with pore diameter. Therefore, the largest pores are intruded first at lower pressures and smaller pores (or ink-bottle pores) are intruded at higher pressures. Producing a pore size distribution from MIP assumes pores are perfectly cylindrical with circular pore openings. Intruded mercury can only access interconnected, open pores and therefore is a measure of pore entry size distribution rather than true pore size

distribution (Berodier et al. 2016). However, the isolated, enclosed pores contributing to total porosity have been shown to be insignificant in soils (Romero and Simms 2008).

MIP testing on various clays has verified the dual porosity structure that forms under various stresses, i.e., larger inter-aggregate pores and smaller intra-aggregate pores. The inter-aggregate pores control porosity during wetting and drying cycles (Li and Zhang 2009). Under mechanical loading, as the inter-aggregate pores collapse, the intra-aggregate pore volume increases (Koliji et al. 2010). However, Wang and Xu (2007) concluded that dual-porosity theory is not sufficient to describe the pore evolution during primary and secondary consolidation. Instead, the change in cumulative pore volume is due to the collapse of the smaller intra-aggregate pores under pressure.

MIP is often used in conjunction with SEM (or ESEM, Environmental Scanning Electron Microscopy) to characterize the microstructure (e.g., Wang and Xu 2007; Romero and Simms 2008; Li and Zhang 2009). SEM allows for direct characterization of clay fabric at small scales, i.e., particle sizes less than 10 μm. The technique can provide high-resolution images (approximately 1.1 nm) of the specimen surface at high magnifications. SEM images have been used successfully to determine the PSD of the clay fraction of soils (e.g., Hemes et al. 2015; Bankole et al. 2019; Yang et al. 2019). Grain data obtained via SEM (e.g., diameter, perimeter, area, circularity, and aspect ratio) were comparable with grain size classes obtained through the laser diffraction method (LDM) but varied statistically with respect to particle distribution. This variation was attributed to the breakage of particles in treatment for LDM and the limitations of LDM concerning elongated particles such as clays (Bankole et al. 2019). SEM overcomes the limitations associated with LDM, particularly for particle sizes smaller than 2 μm (Yang et al. 2019).

The changes in surface complexity and pore class coincide with changes in strength and transport properties (Lin et al. 2013; Coudert et al. 2021). While MIP is often used to describe the pore size distribution of a soil, MIP alone does not inform particle surface characteristics. Instead, MIP needs to be coupled with surface imaging, e.g., Scanning Electron Microscopy (SEM), to fully describe the pore structure evolution and surface changes. Additionally, most imaging studies only qualitatively describe the pore structure (e.g., Al-Rawas 1999; Al-Rawas and McGown 1999; Lin and Cerato 2014; Zhou et al. 2019; Xu et al. 2020; Han et al. 2022; Ma et al. 2021), specifically structural characteristics such as interparticle flocculation or the presence of hydration products (e.g., Farroukh et al. 2018; Turan et al. 2022). While these observations provide valuable insight into the microstructure, quantitative analysis will assist in developing micro-mechanical models to describe microstructural changes which affect macroscale behavior. Advances in imaging techniques have allowed quantitative analysis of SEM micrographs. Binary images (e.g., black and white thresholded images) obtained from processing SEM micrographs have been used to determine porosity (Zbik et al. 2008) and SEM-based pore size distributions (Zeinali and Abdelaziz 2023). Introducing a quantitative description method to assess soil surface complexity and pore morphology of cement-stabilized soils will provide valuable information regarding their mechanical properties (Jennings et al. 2008). One method to offer quantitative assessment of the physical microscale properties is to utilize fractal geometry.

Fractals are mathematical representations of complex and self-repeating patterns, often found in nature and various abstract systems. The theory of fractal geometry was created to quantify irregularity and variability in complex systems (Mandelbrot 1967; Mandelbrot 1982). Fractals are described through an initiator-generator approach: a recursive algorithm repeatedly applies a set of mathematical rules of transformations (generator) to a simple geometric shape or

equation (initiator). Fractals have been extensively studied in mathematics and have applications in various fields such as computer graphics, physics, biology, and economics, providing insights into the underlying structures and processes of natural phenomena. Fractal theory has been used with soils (e.g., Tyler and Wheatcraft 1989; Levine et al. 2016; Zhou et al. 2018; Barman et al. 2022) and other geomaterials (e.g., Turcotte 2001) and has been utilized to better understand the microscale mechanisms influencing the macroscale behavior observed in the natural and built environment, such as preferential flow paths (e.g., Hatano and Booltink 1992), gas diffusion through soil (e.g., Orbach 1986; Crawford et al. 1993; Anderson et al. 1996), and hydraulic conductivity models (e.g., Tyler and Wheatcraft 1989; Tyler and Wheatcraft 1990; Toledo et al. 1990; Anderson and McBratney 1995; Perfect et al. 1996).

The fractal dimension is a parameter measuring the complexity of a geometric pattern and the fractal dimension of a two dimensional soil image provides information about the soil structure and its connection to pore networks. Because the fractal dimension is an intrinsic characteristic of the surface, an image is appropriate to obtain information of the surface (Yang et al. 2016). The soil-pore interface of an exposed soil section is the surface roughness which can be estimated directly from images (e.g., Hatano et al. 1992; Anderson et al. 1996; Dathe et al. 2001) or indirectly using MIP (e.g., Bartoli et al. 1991; Pachepsky et al. 1995).

Crawford et al. (1993) used images of soils to describe the relations between soil structure and transport processes in soil via the fractal dimension. The fractal dimension measured via a box-counting algorithm of soil images was used to describe preferential flow paths and tortuosity of pore networks. Soils with fractal dimension less than 2 had greater heterogeneity and therefore had reduced diffusion compared to more homogeneous soil-pore networks. Consequently, fractal geometry provides the structural measurement necessary to solve diffusion problems through soils.

Anderson et al. (1996) similarly studied the fractal dimension of soil surfaces by analyzing images of thin film sections. The fractal dimension measured from the pore-soil interface successfully described the diffusion coefficient of a particle moving through a fractal pore network. Hatano et al. (1992) studied patterns of macropores to describe the relationship between fractal dimensions of pore volume and pore surface to explain solute transport through soil. Because transport processes follow irregular, complex patterns through geomaterials, the fractal dimension provided a comprehensive parameter to evaluate these processes. The surface fractal dimension was determined using a box counting procedure on stained two-dimensional images of a soil column and boxes containing stained or partially stained sections were counted. The fractal dimension was found to depend on the type and shape of macropores: greater fractal dimensions were associated with a rougher pore surface and lower fractal dimensions associated with smoother surfaces. Dathe et al. (2001) used images acquired via SEM to develop a relationship between fractal dimension and parameters related to transport processes (e.g., solute transport, hydraulic conductivity, diffusion). SEM images were digitized and segmented into a binary (e.g., greyscale) to differentiate between soil pores and the soil matrix. The fractal dimension obtained from the study provided a quantitative description of soil structure complexity as well as a classification of processes which affect structure with higher fractal dimensions (ranging from 2.88 – 2.91) for lower magnifications and lower fractal dimensions (ranging from 2.56 – 2.60) for higher magnifications. The hierarchical nature of the fractal dimension was an indicator of differing domains of flow patterns within the soil microstructure.

Therefore, to demonstrate how fractals can help develop a better understanding of the evolution of the microstructure with cementation, SEM images and MIP results from Tabet (2015) and Tabet et al. (2018) were used to validate the theory. Tabet (2015) and Tabet et al. (2018) created

a high quality database of SEM and MIP results of a single-mineral clay mixed with a cementitious, calcium-based stabilizer and observed over time for structural changes (SEM) and pore network changes (MIP). These results were used to validate the fractal geometry approach because of the relatively large size of the kaolinite particles and the easily observable CAH and CSH formation. Once it was determined that fractal geometry was a powerful tool to explain surface complexity and showed strong correlations with soil properties (e.g., strength gain over time), additional ESEM images of expansive soils under suction hysteresis were created, the results of which are discussed in Chapters 3 and 4. In this chapter, the fractal dimension obtained via fractal analysis of MIP results was used to determine the evolution of pore classes. The fractal dimension obtained via analysis of surface roughness of SEM micrographs is compared to compressive strength to better quantify changes in fabric that occur with stabilization.

2.2 Background

Geomaterials have been shown to exhibit self-similarity, most easily observed in sands (Zhou et al. 2018; Barman et al. 2022) and rocks (Turcotte 2001). Self-similarity is the mathematical concept that geometric characteristics at one scale will be repeated at another. This can be deterministic (exact) or stochastic (statistical) (Perfect and Kay 1995; Turcotte 2001). While the concept of self-similarity has been apparent for millennia, Mandelbrot (1982) formalized the framework for quantifying irregularity and fragmentation in complex systems through the concept of fractal geometry, visualizing the Mandelbrot set and providing a formal definition of a fractal. The intricate and infinitely complex boundary of the Mandelbrot set exhibits self-similar patterns, with smaller copies of the set appearing at different scales. Mandelbrot defined a fractal as a geometric figure that scales to some dimension between whole number powers, occurring naturally

in many contexts, such as the perimeter of the coastline of Great Britain (Mandelbrot 1967; Mandelbrot 1982).

Self-similarity can be described in soils and other geomaterials with the use of fractal theory, specifically the fractal dimension and lacunarity. Geometric patterns observed at different scales can be related using a power function whose dimension is the fractal dimension:

$$L \propto G^{D_T - D} \quad [1]$$

where L is the summation of characteristic unit, G is the magnitude of the measuring unit, D_T is the topological dimension of the measuring unit (e.g., $D_T = 1$ for a line, 2 for a plane, 3 for volume, etc.), and D is the fractal dimension (after Mandelbrot, 1982). For lengths, D ranges between 0 and 1, for areas D ranges between 1 and 2, and for volumes, D ranges between 2 and 3.

The fractal dimension can be adapted to porous materials such as clays. Turcotte (2001) developed a fractal concept of a porous system using Turcotte's cube. Pore networks of soils follow similar scaling patterns to a three-dimensional Sierpinski carpet as particle size decreases, but the repeating pattern is more complex and would be better described via an algorithm to capture the randomness in the natural pore network.

2.2.1 Fractal Dimension of MIP Data

A fractal dimension can also be interpreted from MIP data (Friesen and Mikula 1987; Romero 1999; Romero and Simms 2008; Fadeev et al. 1996; De la Cuevas 1997; Han et al. 2022). Friesen and Mikula (1987) developed a method to obtain the fractal dimension of the pore surface using a Menger sponge volume filling theory. The fractal dimension can be obtained through equation 2 by regressing the slope on a double-logarithmic plot:

$$log\frac{dV_p}{dr} \propto (D_S - 4)\log p \quad [2]$$

Where dV_p is the pore volume, p is the intrusion pressure, and D_S is the fractal dimension of the surface. The fractal dimension of coal samples studied by Friesen and Mikula (1987) differed between high and low intrusion pressures. For D_S between 1 and 2, the dimension is not consistent with a fractal surface and was interpreted as the fractal dimension of a bulk porous medium. Therefore, they concluded that at this pressure range, mercury was intruded into the interparticle voids rather than surface pores.

Similarly, Romero and Simms (2008) described "intervals of self-similarity" based on linear portions on double-logarithmic plots using equation 2. Fractal dimensions greater than 3 were characteristic of volume-filling pore structure while fractal dimensions between 1 and 2 were considered characteristic of fissure-like structures. De las Cuevas (1997) studied the fractal dimension of the pore space in rock salt. A break in the slope of the double-logarithmic plot was indicative of pore geometry trending between infra-pores (i.e., small, non-intersecting pores less than 100 nm) which were nonfractal and micropores (i.e., small pores between 7.5 μm and 100 nm) which were fractal in structure. Fractal dimensions between 1 and 2 are characteristic of a bulk medium (e.g., intact rock) and dimensions greater than 3 are indicative of compression of the material itself (Fadeev et al. 1996).

Recently, Han et al. (2022) used the MIP fractal dimension (Menger sponge model) to describe pore regions in the structure of concrete specimens. While concrete structure showed self-similar characteristics, the concrete surface was only fractal in certain ranges of pore size such as the macropore region (i.e., pores between 10 μm and 950 μm) and CSH hydrate pore region (i.e., pores less than 10 μm). The fractal dimension from these ranges, both between 2 and 3, showed good correlation with pore specific surface area.

2.2.2 Box Counting Fractal Dimension and Lacunarity

Box counting fractals have also been used to describe soil structure. The benefit of box counting fractals is that they can be derived directly through imaging, and do not require mass or volumetric measurements. The process involves systemically layering a system of grids (or boxes) over an image and counting the number of boxes which contain at least one pixel of the surface. The count is compared to the size of the sampling element using the form:

$$N(\varepsilon) \propto \varepsilon^{-D_b} \quad [3]$$

where $N(\varepsilon)$ is the number of boxes containing at least one pixel of the surface, ε is the box size, and D_b is the box counting fractal dimension (after Dathe et al. 2001).

Lacunarity describes the texture of a fractal set, or the distribution of "holes" along the surface (Mandelbrot 1982). It is often used in addition to fractal dimension to differentiate between fractal sets, as two fractal sets can have the same dimension but vary widely in porosity if the lacunarity differs. This is because the fractal dimension relates variations in structure across different scales of observation but lacunarity measures variability at the same scale (Crawford et al. 1993). Therefore, the box counting fractal dimension describes the roughness and irregularity of the soil surface and the lacunarity describes the pattern of voids along the surface.

2.3 Materials and Methods

2.3.1 Materials

The soil chosen for this study is a kaolinite (SA-1) processed by air flotation, without the addition of dispersive agents, and manufactured by Active Minerals International, LLC in Gordon, GA. SA-1 is a crystalline clay of single mineralogy with relatively large clay particles. The larger particle size allows for better visualization of the interaction between the clay particles and the stabilizer via SEM. The selected stabilizer is a Portland Cement Type I/II, manufactured by Ash

Grove Cement Company in Chanute, KS. The chemical composition of the soil and stabilizer were obtained from their respective manufacturer (Table 2.1).

Table 2.1. Chemical composition of tested materials (values in percentage) (after Tabet 2015)

Chemical Compound	SA-1 Kaolinite	Portland Cement Stabilizer
Al_2O_3	38.40	4.35
CaO	0.06	64.46
CO_2	--	1.58
Fe_2O_3	0.40	3.25
K_2O	0.18	0.42
MgO	0.05	1.93
Na_2O	0.03	0.18
SO_3	--	2.89
SiO_2	45.60	20.78
TiO_2	1.50	--
LOI	13.8	2.20

2.3.2 Methodology

Raw and stabilized kaolinite specimens were prepared by Tabet (2015) and Tabet et al. (2018). In those studies, specimens were compacted to optimal moisture conditions (optimum moisture content and maximum dry density) via Harvard Miniature, stored in 100% humidity conditions, and cured for periods of 1, 7, 14, 28, and 90 days. At each curing time, small cubic specimens were trimmed from the compacted samples for analysis via SEM and separate cubic specimens were trimmed for use with MIP.

2.3.2.1 Scanning Electron Microscopy (SEM)

Raw kaolinite specimens and Portland cement-stabilized kaolinite specimens were prepared by compacting to optimum moisture content (25% and 27% respectively) and maximum dry density (15.0 kN/m^3 and 14.7 kN/m^3 respectively) via Harvard Miniature (71 mm height, 35.6 mm

diameter), as detailed in Tabet (2015). Compacted samples were wrapped in plastic and stored in a humid chamber to cure.

Because SEM operates under high vacuum, the wet specimens were dried using a flash-freezing/freeze-drying technique. Flash-freezing has been considered the most effective and appropriate method for preserving the structural integrity of the sample at the microscale (Delage and Pellerin 1984; Kang et al. 2003; Ferber et al. 2009; Li and Zhang 2009). During rapid freezing at cryogenic temperatures (e.g., -196°C for liquid nitrogen), the water in the soil is set in an amorphous solid state. This transition does not allow expansion of ice which would damage the structure (Penumadu and Dean 2000) and any disturbance due to crystallization is minimal (Lin and Cerato 2014). Cubic samples with dimensions 5 mm x 5 mm x 5 mm were trimmed from compacted, cured specimens and flash frozen at -196°C by immersion in liquid nitrogen.

Frozen samples were then freeze-fractured via chilled blade to expose the internal soil fabric. Freeze-fracturing provides the least sample disturbance because the ice cements the structure in place during fracturing and the fracture plane occurs at weak points in the ice structure rather than the soil skeleton (Delage et al. 1982). Fractured samples were then dried by sublimation for 5 days under 0.25 mBar and -56°C using a Labonco FreeZone 6 freeze-drier. Freeze-drying prevents surface tension effects normally encountered during air-drying (Lin and Cerato 2014). The desiccated specimens were then mounted on an aluminum stub with carbon tape and coated with iridium.

Micrographs were obtained of raw and stabilized kaolinite specimens for curing times of 1, 7, 14, 28, and 90 days via SEM. A Zeiss NEON 40 EsB High Resolution FE-SEM was used to produce micrographs at magnifications of 10,000X in both the horizontal and vertical planes for

each sample. Images were collected with an accelerating voltage between 5 and 10 kV using a secondary electron detector.

2.3.2.2 Particle Size Distribution via SEM Micrographs

The SEM micrographs of stabilized kaolinite were processed in this study to obtain a particle size distribution (PSD) for images of the raw sample and after curing for 1, 7, 14, 28, and 90 days. Image Pro software was used to discretize the SEM micrographs to generate PSD for each image. Image Pro is a proprietary image processing software distributed by Media Cybernetics which allows segmentation, extraction of image features (e.g., soil particles), and measurement of feature geometry (e.g., particle area and diameter). Images of the horizontal cross section were filtered to remove noise, then sharpened to better delineate between the soil particle and void space. Processed images were then segmented into polygonal areas of the flat-lying particles and equivalent spherical diameter was calculated based on the segmented area for each polygon. Particle diameters were collected into a representative particle size distribution curve for each curing time.

2.3.2.3 Box Counting Fractal Analysis and Lacunarity

This study used SEM micrographs generated by Tabet (2015) to determine the surface fractal dimension using a box counting procedure in FIJI/ImageJ (Schindelin et al. 2012; Karperien 2013) after first sharpening then filtering the images to reduce background noise. Next, images were converted to binary using a greyscale threshold, which separated the pore spaces from the soil surface. In this study, the soil surface is designated as black and the pore space is white. Finally, images were cleaned to better distinguish pore space from particle space (Figure 2.1b).

The box counting fractal dimension provides quantitative analysis of the surface complexity of the soil-pore interface. A grid is overlaid on the image and the number of boxes

containing at least one pixel of the image are counted. As the grid size is decreased, the aggregate of boxes containing information from the image increases. The slope of the mesh size against the number of boxes gives the surface fractal dimension on a log-log plot. Figure 2.1c shows one iteration of an overlaid grid.

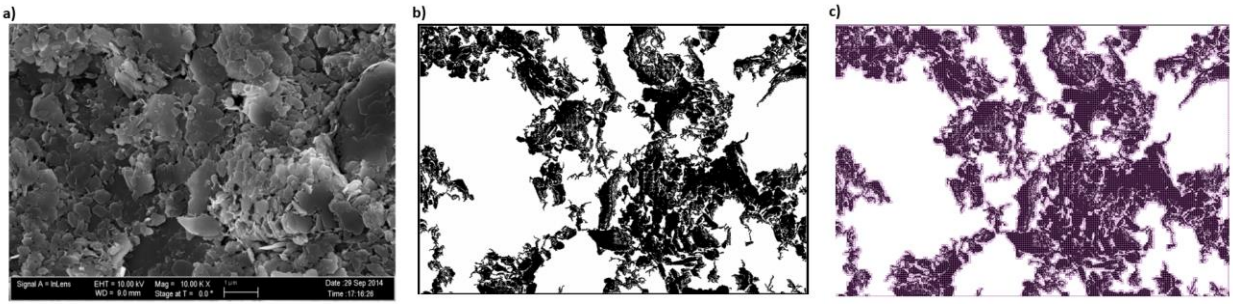

Figure 2.1. Box counting procedure for analysis of SEM micrographs: a) Initial SEM micrograph, b) Binary Image, c) Image overlaid with box counting grid.

The box counting fractal dimension is determined using equation 4, modified from equation 3:

$$N(\varepsilon) \propto \varepsilon^{-FD_{BC}} \quad [4]$$

where N(ε) is the number of boxes containing at least one pixel of soil surface, ε is the grid (box) size, and FD_{BC} is the box counting fractal dimension.

Lacunarity is calculated similarly to the fractal dimension, but instead uses a probability distribution function:

$$Q\ (k,r) = \frac{n_{k\,(r)}}{N(r)} \quad [5]$$

where r is the measure of the side of a box, $n_k(r)$ is the number of boxes counted when the box mass (i.e., count of pixels enclosed in a box) is equivalent to k, where k is an index variable (defining the kth term in the set of n boxes), $Q(k.r)$ is the probability distribution, and $N(r)$ is the total number of boxes (Plotnick et al. 1996; Lee and Lee, 2013). The lacunarity is then calculated according to:

$$\Lambda(r) = \frac{\sum_{k=0}^{r^2} k^2 Q(k,r)}{\left[\sum_{k=0}^{r^2} kQ(k,r)\right]^2} \quad [6]$$

where $\Lambda(r)$ is the lacunarity, the numerator is the second moment of the probability distribution Q (k,r) and the denominator is the square of the first moment of the probability distribution (Lee and Lee, 2013).

2.3.2.4 Mercury Intrusion Porosimetry (MIP)

Tabet (2015) and Tabet et al. (2018) performed MIP on raw and stabilized kaolinite specimens for curing times of 1, 7, 14, 28, and 90 days. MIP sample preparation is similar to that of SEM: cubic samples were trimmed from compacted, cured specimens and freeze-dried. An AutoPore IV 9510 mercury intrusion porosimeter with a maximum mercury pressure of 414 MPa was used. MIP was conducted in two stages: (1) low pressure and (2) high pressure. For the low pressure stage, the sample was subjected to a pressure of 6.7 Pa at 99.993% vacuum. Pressure was incrementally increased until reaching a maximum pressure of 414 MPa.

The pore diameter at each pressure was determined from the modified Washburne equation:

$$P = \frac{-4\,\gamma\,cos\theta}{d} \quad [7]$$

where P is the pressure required to force mercury into a capillary pore of diameter d, γ is the surface tension of mercury, and θ is the contact angle between the soil and fluid (after Washburne 1921). The surface tension of mercury is 485 mN/m and a contact angle of 147° was used (Romero and Simms 2008; ASTM D4404-10).

2.3.2.5 Fractal Analysis of MIP

Fractal dimensions obtained via mercury intrusion data were developed using equation 8, adapted from equation 2, assuming a Menger-sponge volume filling self-similarity:

$$\frac{dV}{dp} \propto p^{FD_{MIP}-4} \quad [8]$$

where V is the intrusion volume, p is the intrusion pressure and FD_{MIP} is the surface fractal dimension obtained from regressing the slope of the straight-line portion on a double-logarithmic plot.

2.4 Results and Analysis

2.4.1 Results of MIP

As discussed in Tabet (2015), pore size distributions for raw and stabilized samples were obtained from the results of MIP testing (Figure 2.2). The pore diameter was determined according to Equation 7 for each intrusion pressure, assuming a contact angle of 147°. While the general shape of the pore size distribution remains unchanged with curing time, the cumulative intruded volume initially increased at 1 day curing then decreased with increasing curing time. Between 1 and 7 days of curing time, the cumulative pore volume decreased then the cumulative volume was similar between the 14 and 90 day samples but was slightly larger for the 28 day sample. The entrance pore diameter (i.e., the pore diameter at 0 mL/g intrusion volume) also decreased with curing time.

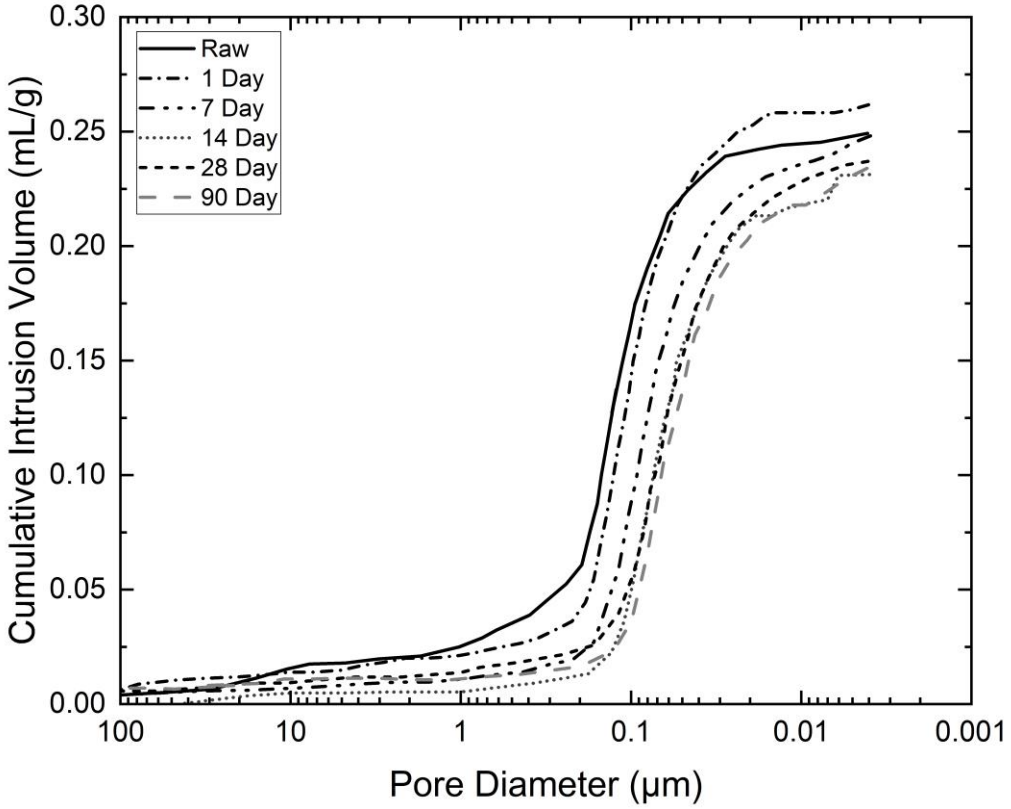

Figure 2.2 Pore size distribution of raw and stabilized specimens subjected to mercury intrusion porosimetry (after Tabet 2015).

The decrease in cumulative pore volume is likely due to the degradation of the larger inter-aggregate pores as hydration products fill the void space. Romero and Simms (2008) noted a decrease in macropore volume with increased compactive effort and with expansion of the microstructure due to changes in suction. Horpibulsuk et al. (2010) also observed an initial increase in total porosity with curing time followed by a decrease after 7 days with which was attributed to the formation of cementitious products. Initially, the volume of small pores (i.e., smaller than 0.1 μm) decreased while the volume of large pore increased because the unhydrated cement stabilizer filled the small pores. However, after 7 days, both the macropore and total pore volume decreased while micropore volume increased as cementation products filled the larger pores.

2.4.2 Results of SEM

Micrographs were collected for raw and stabilized kaolinite specimens for curing times of 1, 7, 14, 28, and 90 days via SEM of the horizontal plane (Figure 2.3) and vertical plane (Figure 2.4) by Tabet (2015). Initially, the kaolinite specimens showed a book-like morphology, most easily observed for the raw specimen in the horizontal plane (Figure 2.3a). In the vertical plane, the kaolinite particles are largely dispersed, showing a high degree of preferential orientation parallel to each other and normal to the direction of compaction (Figure 2.4a).

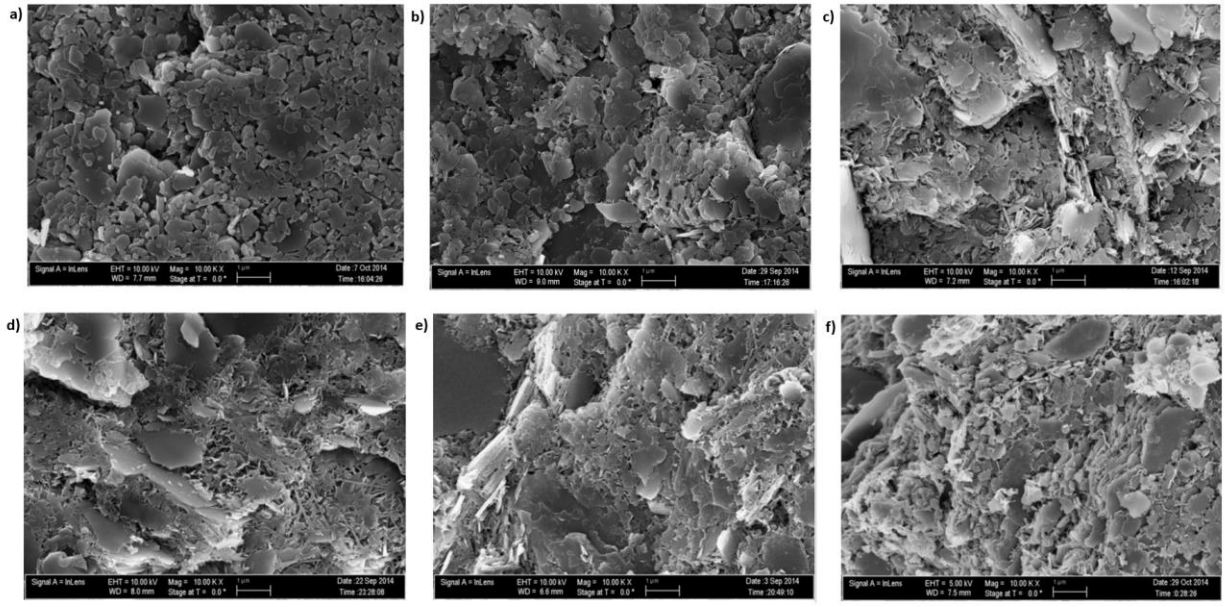

Figure 2.3. SEM micrographs of horizontal cross sections of stabilized kaolinite, 10 kX magnification: a) Raw, b) 1 Day, c) 7 Day, d) 14 Day, e) 28 Day, and f) 90 Day curing time. (from Tabet 2015)

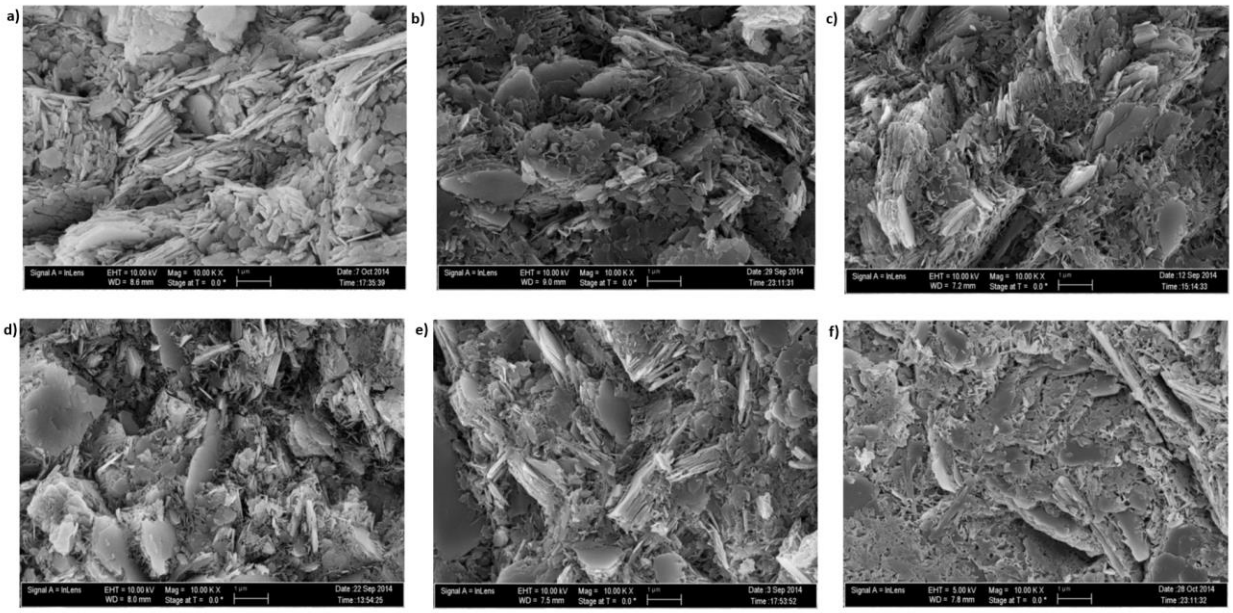

Figure 2.4. SEM micrographs of vertical cross sections of stabilized kaolinite, 10 kX magnification: a) Raw, b) 1 Day, c) 7 Day, d) 14 Day, e) 28 Day, and f) 90 Day curing time (from Tabet 2015)

The formation of hydration products and changing particle orientation is qualitatively visualized through the SEM images. The raw specimen shows a dispersed structure in both the horizontal (Figure 2.3a) and vertical (Figure 2.4a) planes. The 1 day cured specimen shows a lower degree of preferred particle orientation and differences between the horizontal and vertical planes have lessened (Figure 2.3b, Figure 2.4b). After 7 days, the specimen appears more flocculated (Figure 2.5) and CSH fibers are visible, denoted by the circled regions in Figure 2.5.

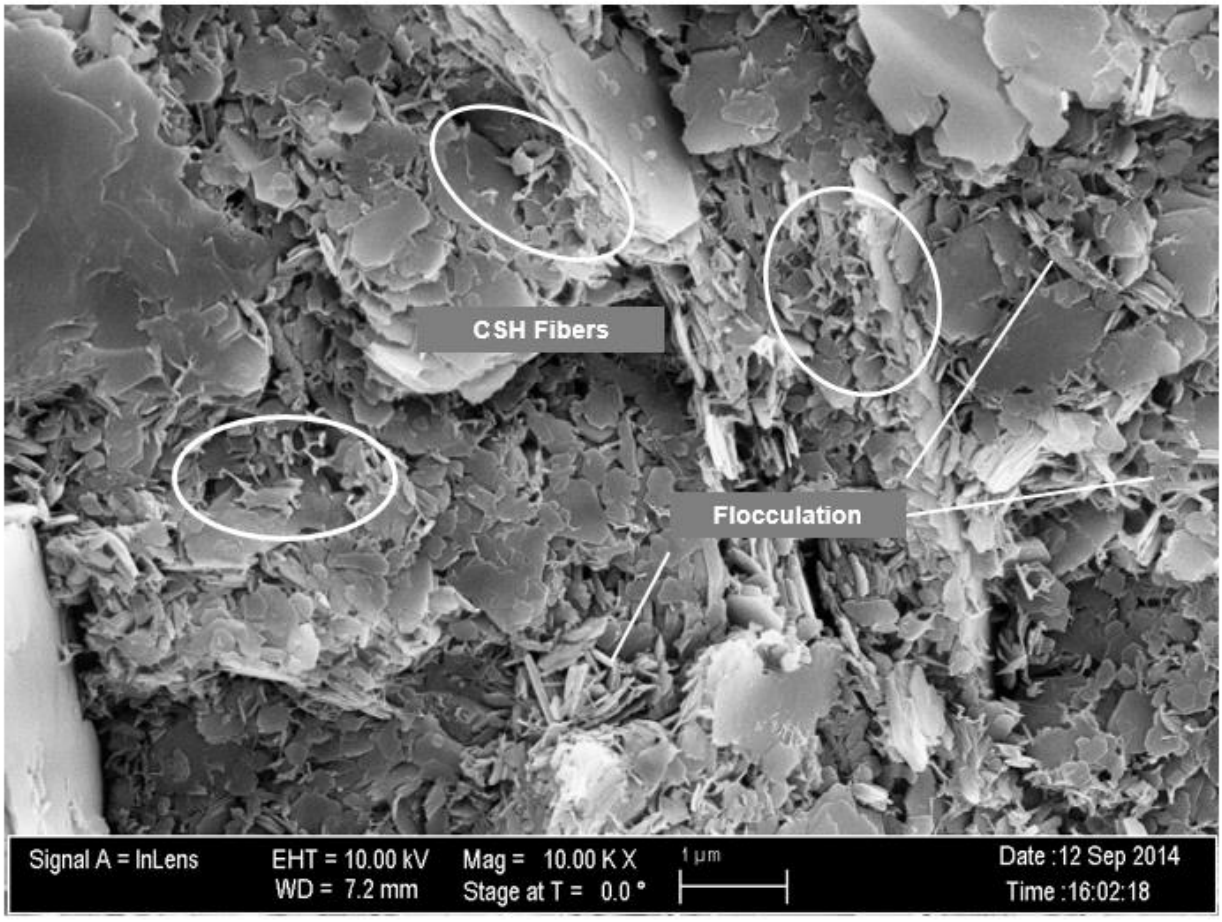

Figure 2.5. Flocculation and fiber formation on the horizontal cross section of the 7 day cured specimen.

After 90 days, the hydration gels have bonded to the soil surface (Figure 2.6), forming a more homogeneous matrix of fused soil-stabilizer particles. The differences between horizontal and vertical planes are (qualitatively) least for the 90 day specimen, with similar flocculation patterns and similar particle sizes and shapes. Moreover, the dissolution of kaolinite particles is visually evident as the predominant shape of particles is no longer hexagonal, but more oblong.

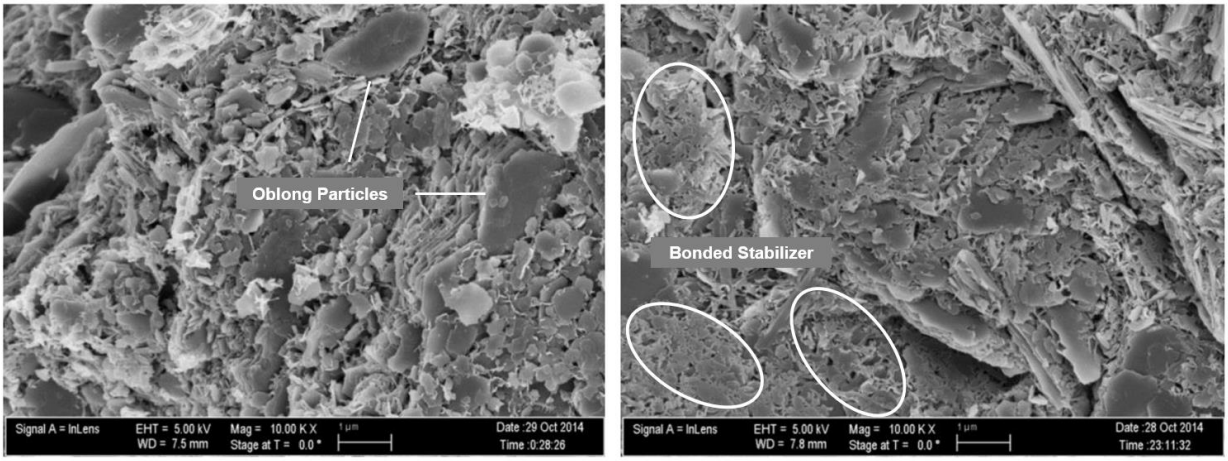

Figure 2.6. Fusion of particle and stabilizer in stabilized 90 day specimen a) horizontal cross section, b) vertical cross section.

2.4.3 Particle Size Distribution (PSD)

SEM micrographs of the horizontal plane were used to generate a particle size distribution of the raw and stabilized soils. An image at 10 kX magnification was segmented via ImagePro for each curing time (Figure 2.7). A polygonal area was calculated for each segment in the image and a particle diameter was calculated based on the area of the polygon assuming an equivalent spherical diameter.

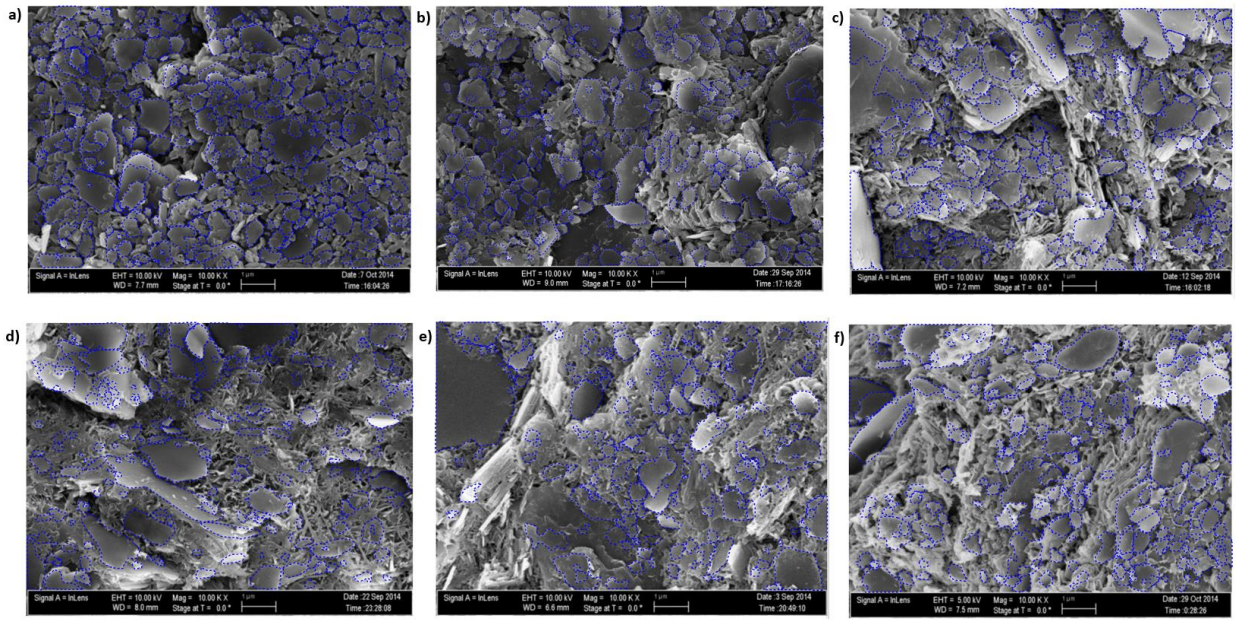

Figure 2.7. Segmented images of horizontal cross sections a) Raw, b) 1 Day, c) 7 Day, d) 14 Day, e) 28 Day, and f) 90 Day curing time.

The PSD was generated for each curing time (Figure 2.8a) based on the segmented polygonal areas. As the curing time increased, overall particle diameters also increased, shown by a shift toward coarser sizes in the PSD. However, when considering the smallest particles (particle diameter between 0.1 and 0.5 μm) comprising finer than 30% of the total area (i.e., finer than 30% of particle size distribution), the pattern does not decrease consecutively with increasing curing time (Figure 2.8b). Instead, particle diameters between 0.1 and 0.4 μm take up a greater portion of the total area than in the raw specimen for curing times between 1 and 14 days. After 28 days, particle diameters between 0.1 and 0.5 μm decreased, taking up a smaller percentage of the total area than in the raw specimen.

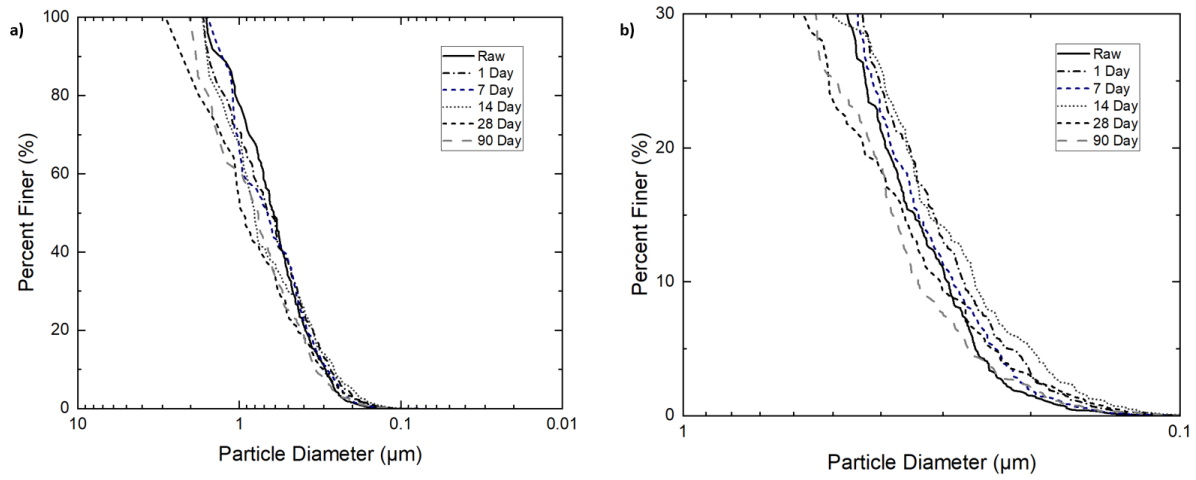

Figure 2.8. Particle size distribution of stabilized specimens a) entire spectrum, b) finer than 30%.

The change in particle size distribution can also be better understood by comparing the change in the particle sizes at 50% finer and 10% finer (d_{50} and d_{10} respectively) (Table 2.2). The d_{50} increased with curing time until reaching 90 days, indicating an increase in the largest particle sizes as the hydration products bonded to the clay surfaces of the largest particles. The d_{10} values decreased as hydration products formed, then increased at 28 days and continued to increase at 90 days as the smaller hydration products merged with the clay particles.

Table 2.2. Change in average and fine particle sizes with curing time.

Curing Time	d_{50} (µm)	d_{10} (µm)
Raw	0.614	0.294
1 Day	0.675	0.273
7 Days	0.681	0.287
14 Days	0.807	0.259
28 Days	0.952	0.306
90 Days	0.774	0.337

This provides a quantitative visualization of the formation of cementation products (CSH, CAH). The smaller particle sizes indicate the presence of the stabilizer and formation of hydration

products. After 28 days of curing, the hydration products have fused to the clay surface, indicated by the larger particle size with the 28 day and 90 day specimens. Similar results were observed by Zhang et al. (2018) for lime-treated soils. After 28 days, the particle size of the treated specimens increased, with a coarser particle size distribution with greater amounts of stabilizer added. This was attributed to pozzolanic products coating the surface of clay particles as well as flocculation causing greater aggregation of individual particles.

2.4.4 Fractal Analysis

2.4.4.1 Fractal analysis of MIP results

Fractal dimensions were obtained from MIP data (FD_{MIP}) according to equation 8 for curing times of 0, 1, 7, 14, 28, and 90 days. For each specimen, the double logarithmic plot of dV/dP versus the intrusion pressure (Figure 2.9) exhibits two separate trends. The slope of each line is used with Equation 8 to determine the fractal dimension of the MIP results. The first slope coincides with intrusion pressures less than 10 MPa (low pressure zone), which is referred to as $FD_{MIP,1}$. The second slope coincides with intrusion pressures greater than 10 MPa (high pressure zone) and is referred to as $FD_{MIP,2}$. The two linear (i.e., linear on a double-logarithmic plot) portions were referred to as "intervals of self-similarity" by Romero and Simms (2008) and indicate a dual-porosity structure. That is, changes in fractal dimensions indicate changes in hierarchical systems. Therefore, because the fractal dimension is constant for each specimen for the interval spanning 0.001 and 10 MPa, and changes to a new constant value for the interval between 10 and 1000 MPa, there are two hierarchical structures in the stabilized soil, or two pore classes.

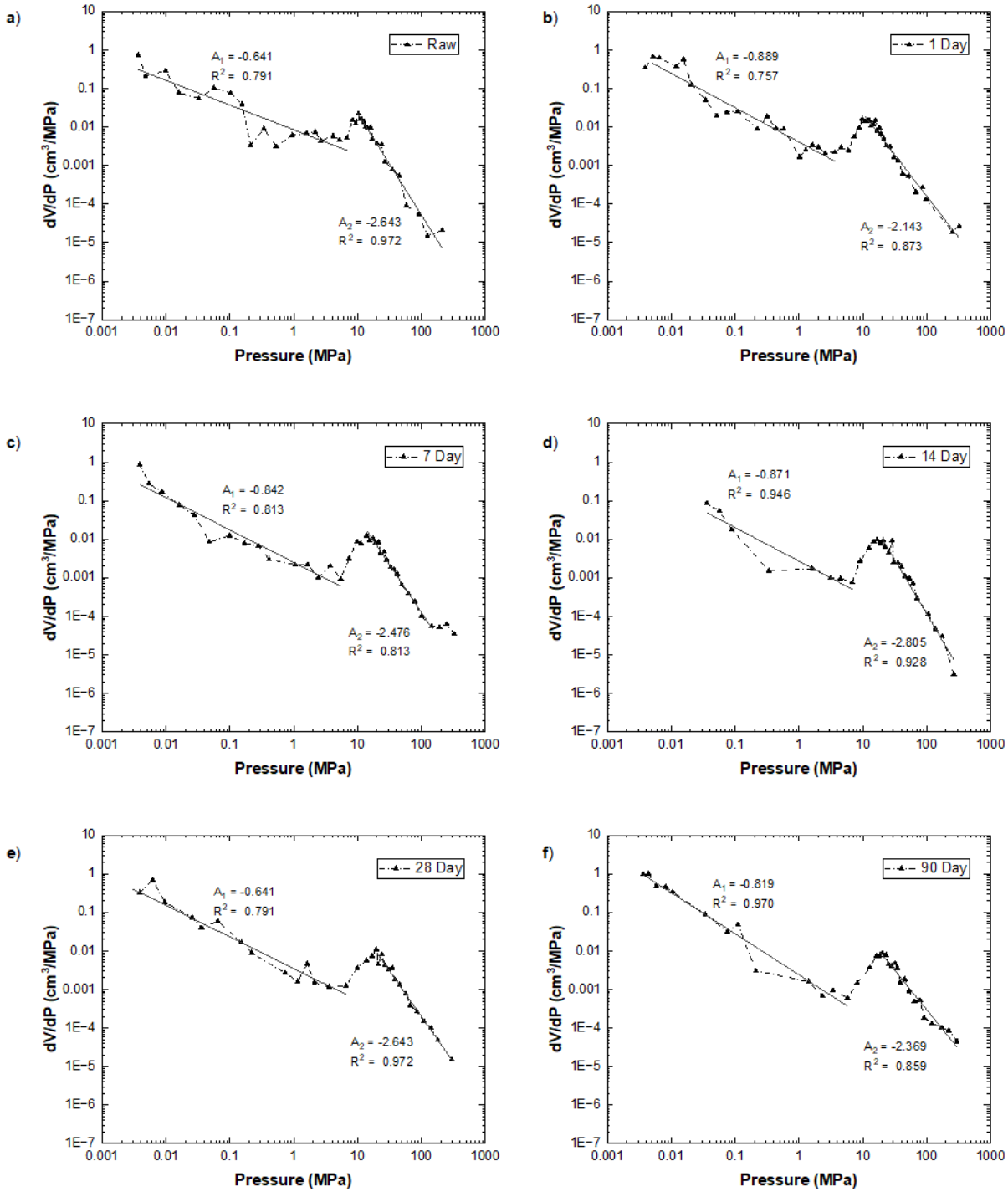

Figure 2.9. Fractal analysis of the pore surface roughness of stabilized kaolinite from MIP data. a) Raw, b) 1 Day, c) 7 Day, d) 14 Day, e) 28 Day, and f) 90 Day curing time.

The fractal dimension of the low-pressure zone ($FD_{MIP,1}$) is greater than 3 at each curing time. Romero and Simms (2008) also encountered fractal dimensions greater than 3 for MIP performed on clays. They considered specimens with surface fractal dimensions greater than 3 to be indicative of a space-filling pore structure. The higher fractal dimensions in the low-pressure zone indicate greater roughness (i.e., complexity), representing a greater variety of void spaces (in terms of diameter and volume) as gel pores develop within the macropores. Similarly, Friesen and Mikula (1987) and De las Cuevas (1996) attributed MIP fractal dimensions greater than 3 to the decrease in bulk volume of the material.

The fractal dimensions within the high-pressure zone are less than 2. Friesen and Mikula (1987) defined fractal dimension between 1 and 2 of coal samples as nonfractal, and instead described a bulk porous medium. That is, at the high pressure range, the small voids behave more as a solid (i.e., fractal dimension is equal to the embedding dimension) than a fractal surface. The increase in pore volume during MIP is due to the intrusion of mercury into the inter-aggregate voids rather than intra-aggregate pores (Fadeev et al. 1996). Likewise, Romero and Simms (2008) described MIP fractal dimensions between 1 and 2 to be characteristic of a fissure-like formation, where a fissure denotes an ideal flat surface rather than a surface with a more complex pattern of voids and accompanying fractal dimension greater than 2 (De las Cuevas 1996).

The pore diameter at which the transition between the two fractal hierarchies occurs also changes with curing time (Table 2.3). As curing time increases, the intrusion pressure at which the transition occurs increases until reaching 28 days, indicating a smaller pore diameter. This is indicative of the changing microstructure as intra-aggregate pores begin to dominate the microstructure and inter-aggregate pores are filled with hydration products. Between 28 days and 90 days, the intrusion pressure slightly decreases, indicating a general stabilization trend in the

microstructure with a slight increase in pore diameter that indicates the fusion of the clay particles with the hydration products.

Table 2.3. Fractal dimensions of pore surface obtained from MIP data

Curing Time (Days)	$FD_{MIP,1}$	$FD_{MIP,2}$	Transition Pore Diameter, µm
Raw	3.359	1.357	0.141
1 Day	3.111	1.857	0.152
7 Day	3.158	1.524	0.118
14 Day	3.129	1.195	0.097
28 Day	3.359	1.357	0.083
90 Day	3.181	1.631	0.089

2.4.4.2 Fractal Analysis of SEM Micrographs

The box counting fractal dimension provides information about the complexity of the surface being imaged. Therefore, the micrographs of the horizontal and vertical cross sections were converted to binary. Black pixels denote the soil surface and white pixels denote the pore area. While the raw specimen in the vertical plane did not show hierarchical information, the binary images of the stabilized specimens showed a clear branching pattern, particularly at 90 days curing time for both the vertical and horizontal cross sections (Figure 2.10, Figure 2.11). Notably, as the kaolinite particles bonded with the stabilizer, preferential planes began to disappear and the differences between horizontal and vertical planes diminished.

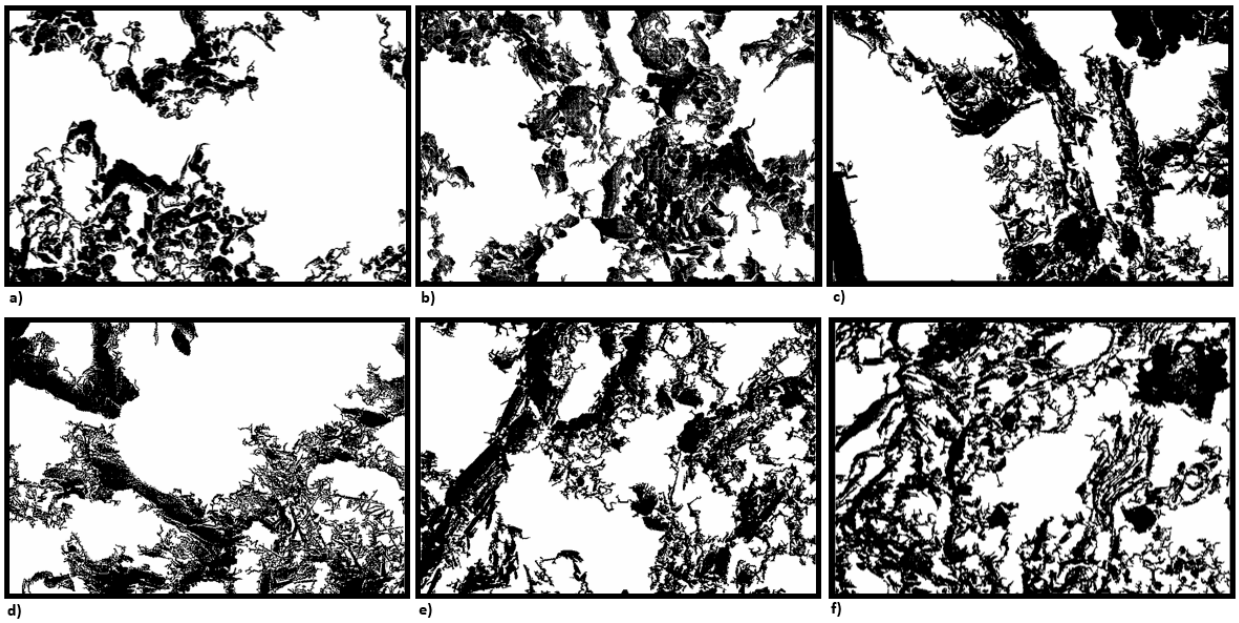

Figure 2.10. Binary images of horizontal cross sections. a) Raw, b) 1 Day, c) 7 Day, d) 14 Day, e) 28 Day, and f) 90 Day curing time.

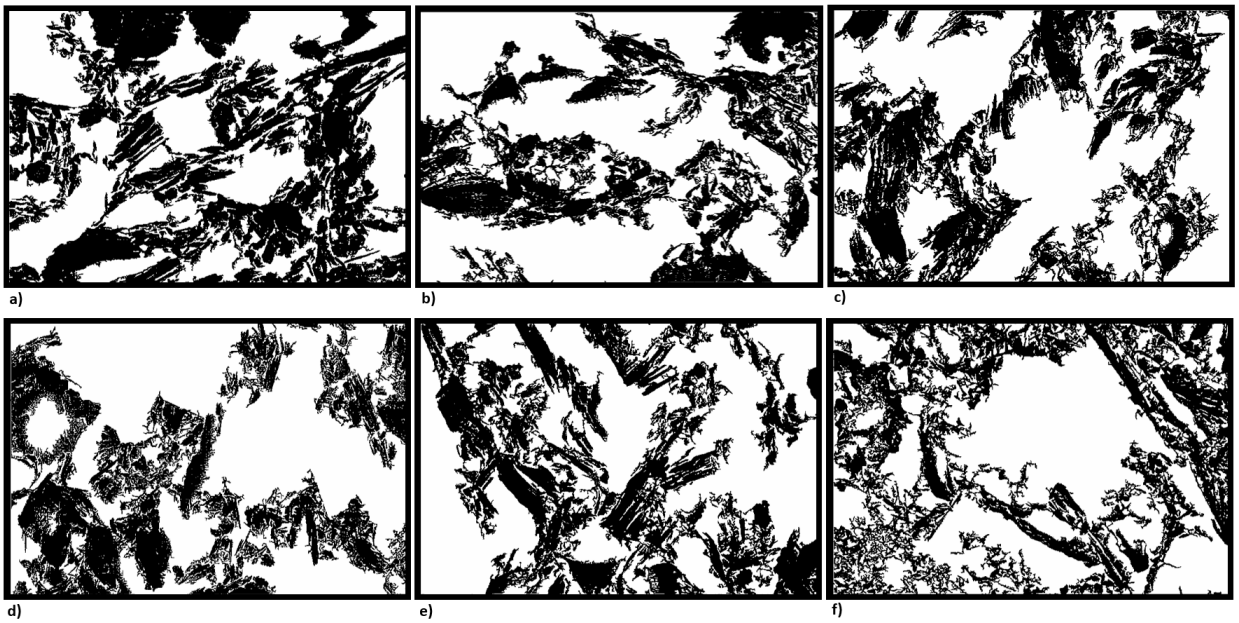

Figure 2.11. Binary images of vertical cross sections. a) Raw, b) 1 Day, c) 7 Day, d) 14 Day, e) 28 Day, and f) 90 Day curing time.

The changing surface morphology is more apparent when comparing the fractal dimension (Figure 2.12a) and lacunarity (Figure 2.12b) between horizontal and vertical cross sections. The initial fractal dimension differs between horizontal and vertical, but shows a decrease then gradual

increase in complexity, overall converging at similar values after 14 days. The surface roughness overall increased as hydration products formed, with the exception of 7 days curing time for the horizontal plane. The trend in fractal dimension quantitatively describes the changing microstructure, particularly along the horizontal plane. Addition of the stabilizer caused an increase in fractal dimension at 1 day, similar to that observed by Zhang et al. (2020) with the addition of nano-stabilizers to soil: when smaller particles are added to the soil, the fractal dimension is larger. The increase in fractal dimension between 14 and 90 days is indicative of the flocculation of particles, creating fractal patterns along the pore surface.

Likewise, the lacunarity between the vertical and horizontal planes in the raw specimen vary widely, showing a large difference in the pattern of voids. However, as curing time increases, the lacunarity values show only small variations and follow the same trend. After only 1 day of curing time, the void pattern shows no significant difference between horizontal and vertical cross sections. Because lacunarity is a statistical measure of the pixel density and distribution, it measures translational and rotational invariance and therefore the degree of dispersion and clustering along a surface (Plotnick et al. 1993; Luo and Lin 2009; Liu and Ostadhassan 2017). Differences in the mass distribution of pixels in an image result in different lacunarity values, with higher lacunarity corresponding to a structure with wider and larger gaps between features and more homogeneous surfaces have lower lacunarity (Liu and Ostadhassan 2017). Therefore, in this study, after 1 day, the horizontal and vertical cross sections show similar patterns of heterogeneity as the particles rearrange in response to the stabilizer.

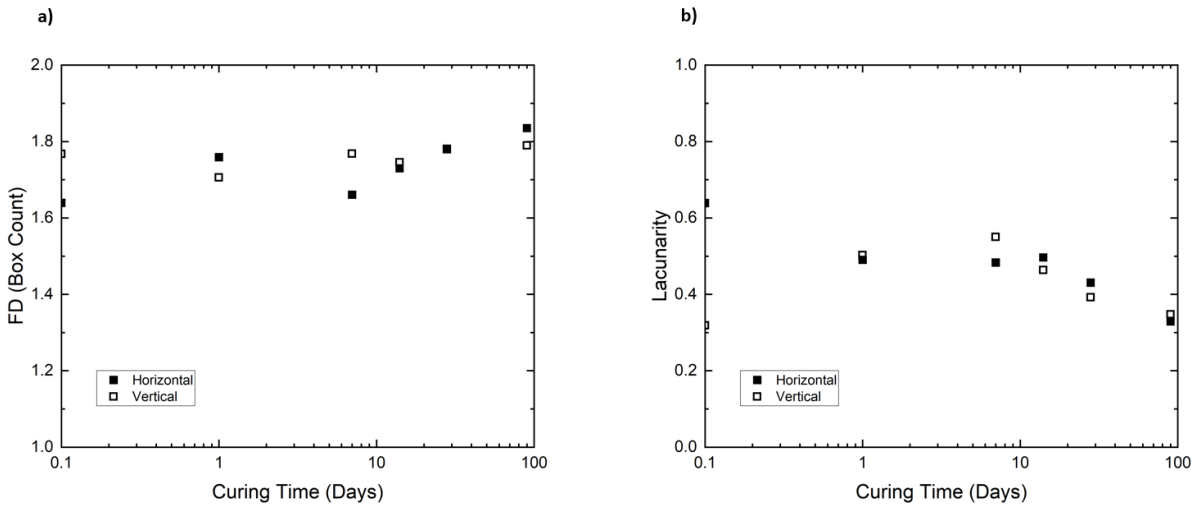

Figure 2.12. Box Counting Analysis: a) Fractal dimensions, b) Lacunarity

The horizontal box counting fractal dimension and lacunarity were compared to unconfined compressive strengths (UCS) determined by Tabet (2015) (Table 2.4). With the exception of the 1 day cured sample, there are strong trends between both fractal dimension and lacunarity with strength. The fractal dimension (Figure 2.13a) and lacunarity (Figure 2.13b) are plotted against UCS for raw specimens and stabilized specimens cured for 7, 14, 28, and 90 days. There is a positive trend between fractal dimension and UCS, with an R^2 of 0.78, showing a positive correlation between surface complexity and strength. That is, as the particles rearrange (flocculate), they create more complex surface patterns, corresponding to increases in compressive strength. There is a stronger negative trend between lacunarity and UCS, with an R^2 of 0.94. As the pore structure becomes more homogeneous (lower lacunarity), the strength increases. Because the lacunarity decreased with curing time, the lower lacunarity denoted smaller, fewer, and more regular gaps between features, corresponding with increased compressive strength.

Table 2.4. Fractal dimension, lacunarity, and unconfined compressive strength for stabilized samples of SA-1 kaolinite

Curing Time (Days)	FD_{BC} (Horizontal)	Lacunarity (Horizontal)	UCS[1] (kPa)
Raw	1.639	0.639	281
1 Day	1.759	0.490	1495
7 Days	1.661	0.483	2450
14 Days	1.730	0.497	2878
28 Days	1.780	0.431	3296
90 Days	1.835	0.329	4087

[1] Tabet (2015)

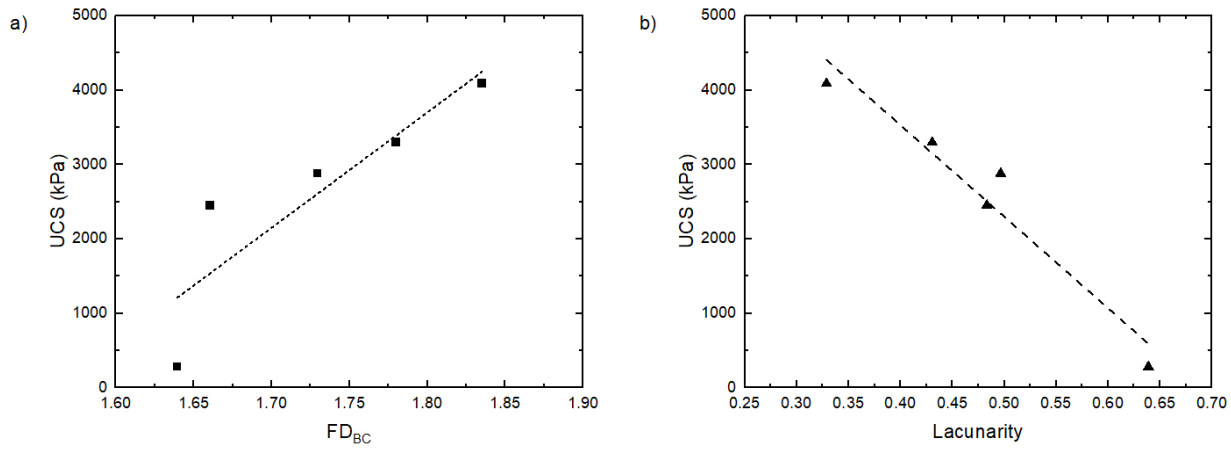

Figure 2.13. Comparison of UCS with a) Box Counting Fractal Dimension (FD_{BC}) and b) Lacunarity (UCS after Tabet 2015).

2.5 Conclusions

This study evaluated the use of fractal geometry to quantitatively describe the evolution of a stabilized kaolin clay with curing time through SEM imaging and MIP porosity data. SEM provided a description of the soil microstructure and MIP provided a description of the pore network. Image analysis of SEM micrographs using FIJI/ImageJ allowed for quantitative characterization of the particle size distribution and fractal geometry (fractal dimension and lacunarity) allowed further quantitative analysis of the soil surface. Similarly, the fractal dimension

of MIP data provided a better understanding of the pore network evolution as stabilization progressed.

The following conclusions were made:

(1) From the grain size distribution, a shift in particle size was observed as curing time progressed. Overall, particle size increased with curing time. However, for the sizes finer than 30% of the overall particle size distribution, the particle diameter first increased until reaching 28 days then decreased. This indicates the formation of cementation products and eventual fusion between clay surface and stabilizer.

(2) The transition pore size between intra-aggregate pore and inter-aggregate pores decreased with stabilization, indicating the filling of large pores with hydration products as intra-aggregate pores began to dominate the microstructure and inter-aggregate pores filled with hydration products.

(3) There are strong trends between both fractal dimension (FD_{BC}) and lacunarity with strength (UCS). As particles flocculate, they rearrange creating more complex surface patterns, corresponding to higher compressive strength. As pore structure becomes more heterogeneous (less homogeneous), the surface exhibits higher lacunarity corresponding to a decrease in strength. Because lacunarity decreased with curing time, lower lacunarity denoted smaller, fewer, and more regular gaps between features coinciding with measured increases in compressive strength.

(4) Particle restructuring can be observed as the particle surface fractal dimensions (FD_{BC}) between vertical and horizontal converge after 14 days. The lacunarity also shows evidence of particle restructuring as the lacunarity values between the vertical and horizontal cross sections converge after only 1 day of curing time.

(5) The soil structure itself was fractal (FD_{BC}), while the pore structure was not (FD_{MIP}). While there was a power law relation between pore diameter and cumulative intruded volume, the surface was not fractal because the fractal dimension was not between the embedding dimension and Euclidean dimension. The soil surface itself had fractal characteristics (FD_{BC} was between 1 and 2) but the pore structure did not (FD_{MIP} was either less than 2 or greater than 3). The fractal dimension and lacunarity obtained from analysis of SEM images provided a better understanding of structural changes with stabilization time.

Chapter 3 Microscale Analysis of Single-Mineral and Naturally Occurring Expansive Soils Along Wetting and Drying Paths Using Environmental Scanning Electron Microscopy (ESEM)

3.1 Introduction

Expansive soils are those soils, most commonly clays, that experience large volumetric strains as the soil skeleton expands and contracts in response to cycles of wetting and drying (Borchardt 1989). Volumetric swelling occurs when the soil adsorbs fluid and volumetric shrinkage is associated with the desorption of pore fluid. This behavior is beneficial when used as barrier material for waste containment or impervious liners (Cui et al. 2002; Miller et al. 2002; Montes-H 2005). However, the shrinking and swelling of the underlying soil can damage infrastructure if not constructed with adequate foundation systems, and associated mitigation costs exceed that of floods, hurricanes, and earthquakes combined (Wray and Meyer 2004; Zamin et al. 2021), in the range of $9-15 billion in the United States alone (Jones and Jefferson 2012; Amakye et al. 2021; Devkota et al. 2022).

As-compacted clay used in infrastructure designs, e.g., barrier systems, cores of dams and levees, and bearing material for foundations and embankments, will be in the unsaturated state ($0\% < S < 100\%$) for most of the design life of the project (e.g., Miller et al. 2002). It is necessary, therefore, to quantify the differences in engineering behavior for a broad range of unsaturated states to better inform design using expansive clays.

There is considerable evidence demonstrating the macroscopic, engineering behavior of these expansive clays is controlled by microscopic, physicochemical forces, i.e., the double layer repulsive, van der Waals attractive, and interlayer forces, in addition to mechanical forces (e.g., Likos and Lu 2004; Mitchell and Soga 2005; Anandarajah and Amarasinghe 2011). As water

content fluctuates within the pore networks of the soil, the microlevel forces also change, and suction between particles increases and decreases inversely to the volumetric water content. This relationship is characterized by the Soil Water Retention Curve (SWRC), which is a constitutive relationship between suction and soil moisture. As suction evolves, fluctuations in the soil fabric occur, which impact the strength, permeability, and other macroscale properties of the soil. While expansive soils in the unsaturated state have been studied extensively, they remain a costly challenge for engineers who seek to accurately predict and mitigate swelling and shrinking movements under various conditions. Understanding the microscale properties and particle interaction at various suction levels is vital in order to better predict how their behavior at the engineering scale. High-quality experimental work studying structural complexity and orientation at the microscale is essential to developing a solution (e.g., Koliji et al. 2010). As technology improves, it is becoming possible to study these microscale clay particles in more detail and present both qualitative and quantitative methods in which to understand surface phenomenon and particle interactions under various conditions that explain factors that influence soil behavior.

Electron microscopy and porosimetry are commonly used to characterize the fabric of clays, providing information on pore networks, particle geometry and orientation, and particle and pore size distributions. However, porosimetry methods such as Mercury Intrusion Porosimetry (MIP) are limited, as MIP can only describe the pore volume accessible by mercury and is bounded by a minimum pore size able to be detected (Sun et al. 2019). Scanning Electron Microscopy (SEM) can image the microscale structure (i.e., < 10 μm) of the soil fabric, providing high-resolution images of the specimen at larger magnifications. However, the SEM chamber operates under a vacuum and requires a completely dried specimen. Due to this critical limitation, SEM is not able to capture the unsaturated state of the soil, particularly at high relative humidity (i.e., low

suction and high degree of saturation) (Koliji et al. 2010; Lin and Cerato 2014). Environmental Scanning Electron Microscopy (ESEM) overcomes this limitation either via a separate dedicated vacuum pump to control chamber vapor pressure or one scroll pump for roughing and backing with a valve allowing water vapor into the chamber (e.g., ThermoFisher Scientific Quattro S used in this study). To prevent charging on the specimen, the ESEM uses gas pressure to allow positively charged ions to be produced by secondary electron scattering. A secondary electron detector (e.g., GSED gaseous secondary electron detector) allows functioning in the environmental mode where a conventional secondary electron detector (ETD) cannot function due to high voltage elements which would cause arcing at higher pressures. Chamber pressure is controlled by a Peltier cooling stage (Lin and Cerato 2014). Moreover, ESEM does not require desiccation or coating which have been shown to affect the microstructure (Romero and Simms 2008; Koliji et al. 2010; Sun et al. 2019).

Historically, ESEM required coupling with SEM because at high chamber humidity (low suction) a film of adsorbed water develops around the specimen which interferes with image quality. Lin and Cerato (2014) noted that for naturally expansive soils, structural information (e.g., particle alignment) was accessible from ESEM micrographs, but broader analysis was not possible due to image quality. Koliji et al. (2010) related microscale and mesoscale structure to macroscale using ESEM by coupling ESEM with MIP and neutron computed tomography (CT) for a Bioley soil. Significant changes in soil fabric were not apparent with ESEM alone through wetting and drying cycles and required additional MIP analysis. Recently, Sun et al. (2019) paired ESEM with MIP on samples of B75 Ca-Mg bentonite. Initial compacted dry density was shown to affect the ability of macropores to retain water even with decreasing suction. Similar results were reported by Villar (2007) and Lloret et al. (2003) where bentonite compacted at lower dry density retained

more water at lower suctions (less than 10 MPa) than samples compacted at higher dry densities. This was attributed to the ability of the macropores to store water at a lower void ratio.

Although microstructural studies of expansive clay minerals have been performed utilizing ESEM, a large majority of these studies focus only on MX80 bentonite (e.g., Montes-H 2005; Montes-H et al. 2005; Seiphoori et al. 2014; Sun et al. 2019; Daniels et al. 2021). While this body of work provides valuable insight into swelling behavior at the aggregate-level (Montes-H 2005), the impact of compaction on surface textures along wetting and drying cycles (Montes-H et al. 2005), and the formation of hydration gels during swelling (Daniels et al. 2021), they are largely single mineral and from a single source. To truly understand the mechanism of expansive clay behavior, a diverse body of high-quality, (i.e., high-resolution) and wide range of natural and single-mineral soil images at the microscale are needed.

This study created ESEM images for soils at varying magnifications (350X, 800X, 3500X), complexity (single mineral clays, natural clays), physicochemical properties (S_A, CEC), initial compaction conditions (optimum moisture content, wet of optimum), and equilibration time (15 minutes, no equilibration). Not only were these images the basis for a quantitative method of microscale analysis, i.e., fractal geometry framework, they were used to facilitate a better understanding of the evolution of soil fabric under suction hysteresis. The images were used to qualitatively compare the variation in structure between the drying cycle and wetting cycle and assess influence of physicochemical parameters as they relate to soil activity. The physicochemical parameters Specific Surface Area (S_A) and Cation Exchange Capacity (CEC) are used together with several alternative definitions of soil activity defined by Cerato and Lutenegger (2005) together with the imaging to better capture soil behavior along the SWRC.

Evaluation of these images together with the physicochemical parameters inherent to each soil provides the basis for a larger framework to better characterize and predict expansive soil movement and swell pressures. The analysis of the imaging performed in this chapter provides the profession an examination of the variation in structure between the drying cycle and wetting cycle and physicochemical properties, while Chapter 4 focuses on the quantitative analysis of these images using fractal geometry. With this broad range of high-resolution image data, qualitative and quantitative analyses using a framework of fractal theory can better describe the structural changes not captured by mineralogy alone.

3.2 Materials and Methods

3.2.1 Materials

Three natural clays of varying morphology and activity were compared to two single-mineral clays to analyze particle structure under suction hysteresis. The natural clays included (1) Carnisaw, a fine, semiactive, thermic Typic Hapludult, weathered from Pennsylvanian shale, (2) Hollywood, a fine, smectitic, thermic Oxyaquic Hapludert, and (3) Heiden, a fine, smectitic, thermic Udic Haplustert, weathered from mudstone. Single-mineral clays were obtained from the Source Clay Mineral Repository, and included KGa-1b, a well-crystallized pure kaolin clay (Kaolinite) and Swy-2 Na-MMT (Na-montmorillonite). The kaolinite and montmorillonite were used to compare large relative particle size and low activity (Kaolinite) and small relative particle size and high activity (Na-montmorillonite). The properties of the natural soils are bounded by those of the single-mineral soils (Table 3.1).

The natural soils were selected so that a range of physicochemical properties, namely specific surface area (S_A) and cation exchange capacity (CEC) were represented. The specific surface area describes the available geometry of the clay surface able to interact with pore fluid,

obtained via the Ethylene glycol monomethyl ether (EGME) method by Lin (2012) and the cation exchange capacity describes the quantity of exchangeable cations required to balance the net negative charge along this surface and was obtained via a 1 N ammonium acetate extraction method by Harris Laboratory, Inc via Lin (2012). Soils with similar specific surface area and cation exchange capacity are expected to behave similarly with respect to internal geometry and porosity, interactions with fluids and solutes, compressibility, and strength (Cerato and Lutenegger 2005).

Table 3.1. Physicochemical properties of tested soils (after Lin 2012 and Cerato 2001)

Soil ID	Total S_a[a] (m^2/g)	External S_a (m^2/g)	Internal S_a (m^2/g)	CEC [b] (meq/100g)	Clay Size minerals (%)
KGa-1b	15.0	12.0	3.0	2.0	K[c] (100)
Carnisaw	107.5	47.5	60.0	27.3	V[d] (12) I[e] (25) K (14)
Hollywood	145.5	40.3	105.2	26.4	M[f] (23) I (21) K (18)
Heiden	229.0	51.5	177.5	50.7	M (37) I (5) K (8)
SWy-Na-MMT	637.0	29.0	608.0	76.4	M (100)

[a] Specific surface area; [b] Cation exchange capacity, [c] Kaolinite; [d] Vermiculite; [e] Illite; [f] Montmorillonite

While the Hollywood soil used in this study was obtained at the same time and location as that used in Lin (2012), the site is highly variable. Clay size fractions of the studied soils were obtained via hydrometer analysis according to ASTM D7928 and are compared to those obtained by Lin (2012) in Table 3.2. Both Heiden and Carnisaw show good agreement between the two studies, but Hollywood differs considerably. Atterberg limits, i.e., plastic limit (w_P), liquid limit (w_L), and plasticity index (PI) determined by Lin (2012) for the natural soils and Cerato (2001) for the single-mineral soils are presented in Table 3.3.

Table 3.2. Clay and silt fraction of tested soils (Clay Fraction %/ Silt Fraction %)

	Heiden	Hollywood	Carnisaw
This Study	55/45	19/81	57/43
Lin (2012)	50/50	62/38	51/49

Table 3.3. Atterberg limits of the studied soils

Soil ID	Plastic Limit (%)	Liquid Limit (%)	Plasticity Index (PI)
KGa-1b[a]	26	42	16
Carnisaw[b]	32	59	27
Hollywood[b]	20	54	34
Heiden[b]	23	67	44
Swy-Na-MMT[a]	35	519	484

[a] after Cerato (2001); [b] after Lin (2012)

3.2.2 Methodology

3.2.2.1 Soil Sample Preparation

Specimens were compacted at target maximum dry density and optimal water content via Harvard miniature mold (71 mm height, 35.6 mm diameter), and additional specimens of Heiden soil were compacted wet of optimum (Table 3.4). Each specimen was first sieved through the No. 200 sieve then mixed with distilled water to the desired water content. Compaction consisted of 5 equal lifts with 10 blows per lift via a 12-inch drop hammer, detailed in Hussey (2010). As-compacted dry density was verified by weighing the compacted sample in the mold, removing a portion from the top and bottom of the sample, and averaging the gravimetric water content.

Table 3.4. Compaction states for ESEM specimens

Soil	Target		Experimental	
	ρ_{dmax} (Mg/m^3)	w_{opt} (%)	ρ_d (Mg/m^3)	w_c (%)
KGa-1b	1.41	28.00	1.44	30.80
Hollywood	1.70	20.60	1.67	20.25
Carnisaw	1.65	26.20	1.52	26.95
Heiden opt	1.58	24.20	1.57	23.38
Heiden w1	1.58	24.20	1.22	41.15
Heiden w2	1.58	24.20	1.25	37.48
Swy-Na-MMT	1.00	59.00	1.02	62.38

Specimens were extruded from the Harvard miniature mold and trimmed to dimensions 1 cm x 1 cm x 5 mm with the thin axis perpendicular to the direction of compaction, similar to the preparation procedure detailed in Lin and Cerato (2014). Trimmed specimens were wrapped in plastic to avoid moisture loss and placed in a humid room until being transported to the ESEM chamber for imaging.

3.2.2.2 Environmental Scanning Electron Microscopy

A ThermoFisher Scientific Quattro S Field-Emission Environmental Scanning Electron Microscope (FE-SEM) was used to obtain micrographs of the studied soils. The device has a voltage range of 0.2 to 30 kV for high vacuum imaging and a low vacuum capability of up to 4,000 Pa. In this particular case, images were collected with the gaseous secondary electron detector (GSED) at 20 kV accelerating voltage in the environmental mode.

Each specimen was trimmed with a small groove along the long axis, perpendicular to the compaction plane. This was to allow better visualization of the internal composition of the soil. Specimens were then mounted to the Peltier cooling stage of the ESEM using carbon tape (Figure 3.1). Once mounted in the chamber, specimens were initially saturated by adjusting relative humidity (RH) to 100% with a 740 Pa chamber pressure at a constant 2 degrees centigrade and allowed to equilibrate for 15 minutes. Equilibration times of 20-30 minutes (e.g., Lin and Cerato 2014), 15 minutes (e.g., Sun et al. 2019), and 10 minutes (e.g., Koliji et al. 2010) have been used, but 15 minutes equilibration was deemed sufficient to obtain moisture equilibrium between pore fluid and chamber humidity by Sun et al. (2019).

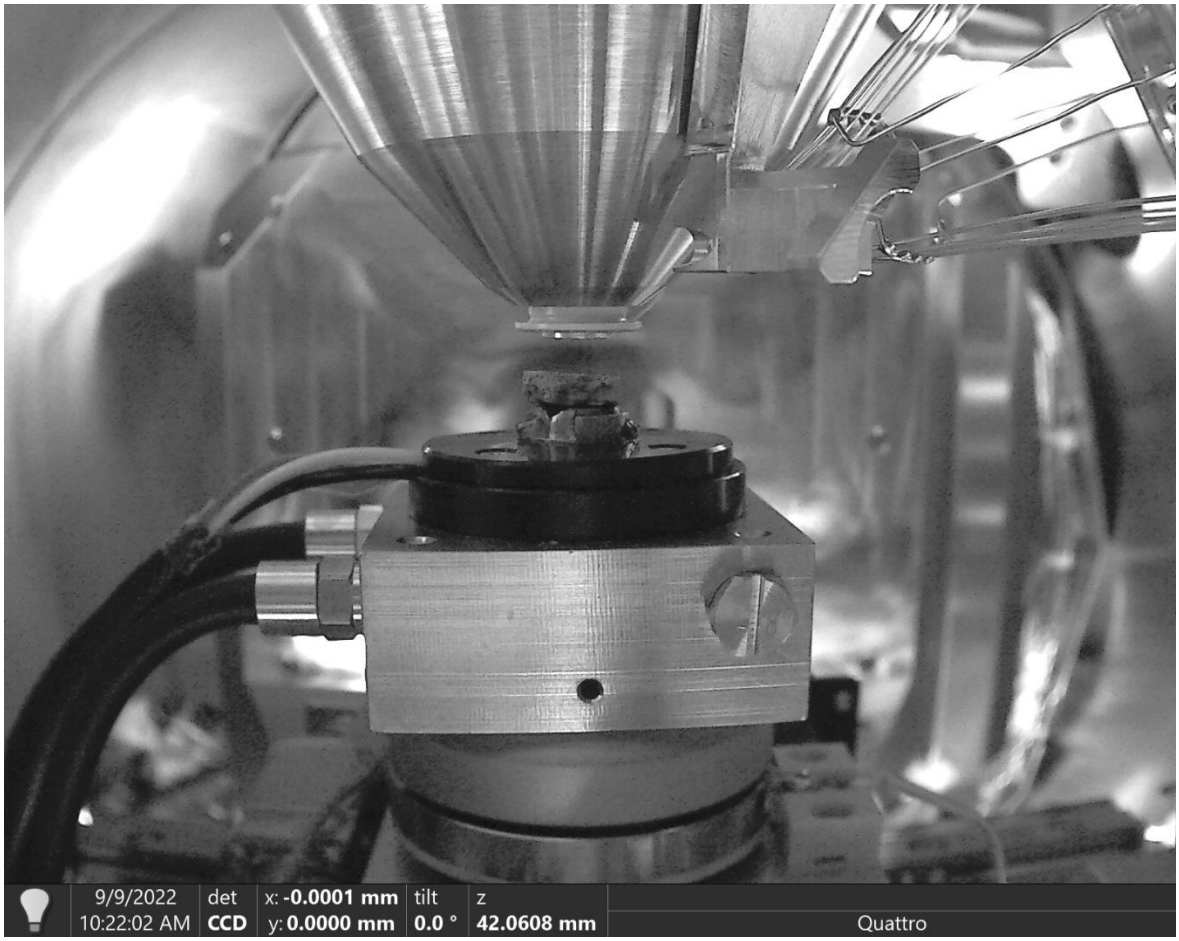

Figure 3.1. Initial seating of specimen in ESEM chamber

SWRCs of Carnisaw, Heiden, and Hollywood (Figure 3.2) were obtained from the experimental data of Lin (2012) using a pressure plate apparatus. Closed-form solutions, such as that of Brooks and Corey (1964), van Genuchten (1980), and Fredlund and Xing (1994) were used to approximate the SWRC from the experimental data. The Brooks and Corey (1964) model is given by:

$$\theta = \theta_r + (\theta_s - \theta_r) \cdot \frac{\psi}{\psi_b}^{\lambda} \quad [1]$$

where θ is the volumetric water content, θs is the saturated volumetric water content, θr is the residual water content, ψ is the suction, ψ_b is the air-entry suction, and λ is a fitting parameter related to the particle size distribution. The van Genuchten model follows the form:

$$\theta(h) = \theta_r + (\theta_s - \theta_r)[1 + (\alpha h)^n]^{-m} \; (n > 2, 0 < m < 1) \qquad [2]$$

where θ is the volumetric water content, θs is the saturated volumetric water content, θr is the residual water content, h is the pressure head, and α, n, and m are fitting parameters (van Genuchten, 1980). Fredlund and Xing (1994) modified van Genuchten's model by assuming a log-linear relationship between volumetric water content and matric potential at lower water contents. The model is given by:

$$\theta(h) = C(h)\frac{\theta_s}{\left[\ln e + \left({}^{h}/_{\alpha}\right)^n\right]^m}$$

and

$$C(h) = 1 - \frac{ln\left(1+{}^{h}/_{h_r}\right)}{ln\left(1+{}^{h_{max}}/_{h_r}\right)} \qquad [3]$$

where the parameters are the same as in Equation 2 and h_{max} is the oven-dry matric potential (Fredlund and Xing 1994). The parameters used in the Brooks and Corey (1964) model are presented in Table 3.5, van Genuchten (1980) in Table 3.6, and Fredlund and Xing (1994) in Table 3.7.

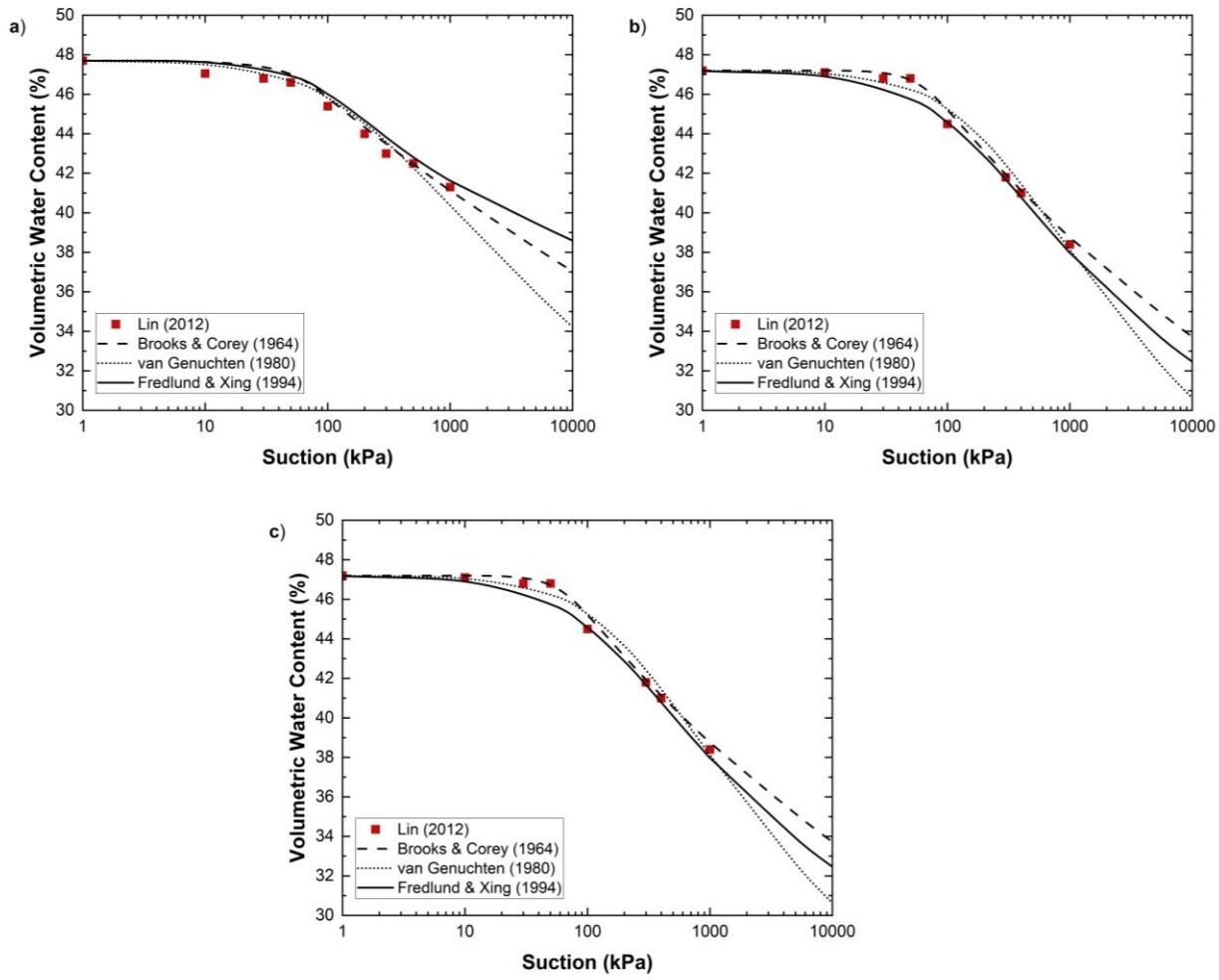

Figure 3.2. Soil water retention curves for a) Carnisaw; b) Heiden; and c) Hollywood (after Lin 2012)

Table 3.5. Fitting parameters for SWRC using Brooks and Corey (1964) method

Parameter	Carnisaw	Heiden	Hollywood
ψ_b (kPa)	43	55	70
θ_r (%)	9.5	16.3	2.3
θ_s (%)	47.7	47.2	43.5
λ	0.06	0.16	0.20

Table 3.6. Fitting parameters for SWRC using van Genuchten (1980) method

Parameter	Carnisaw	Heiden	Hollywood
ψ_b (kPa)	43	55	70
θ_r (%)	9.5	16.3	2.3
θ_s (%)	47.7	47.2	43.5
a	0.0077	0.0056	0.0041
n	1.10	1.19	1.18
m	0.091	0.160	0.153

Table 3.7. Fitting parameters for SWRC using van Fredlund and Xing (1994) method

Parameter	Carnisaw	Heiden	Hollywood
α (kPa)	77	112	121
n	1.48	1.06	1.59
m	0.10	0.23	0.19
θ_s (%)	47.7	47.2	43.5

The range of suction states a soil specimen experiences can be divided into three regimes: (1) the tightly adsorbed regime where pore water is retained via molecular bonding mechanisms, generally occurring between 10 to 1,000 MPa, (2) the adsorbed film regime where water is retained in the form of thin films on the particle surfaces due to solid-liquid interaction mechanisms, generally occurring between 0.1 to 10 MPa, and (3) the capillary regime where the amount of water adsorbed to the soil surface is a function of the particle size distribution and the air-entry pressure, generally occurring between saturation and 0.1 MPa (Lu and Likos 2004). The natural soils in this study were tested to determine the SWRC with suctions ranging from the capillary regime to the adsorbed film regime: 0.01 MPa to 1 MPa (Lin 2012). While the single-mineral soils used in this study did not have a SWRC performed, the kaolinite is expected to experience a relatively comparable range of suctions over a similar range of water contents as the natural soils. The Na-montmorillonite, however, would have experienced a SWRC at much higher suction

values over a similar moisture range, spanning from the adsorbed film regime well into the tightly adsorbed regime, as smectites adsorb more water in the high suction regime than kaolinites and other non-expansive soils (Likos and Lu 2004). For example, a Na-montmorillonite might experience an air-entry value around 35 MPa, whereas the tested natural soils showed an air-entry value around 0.1 MPa, a difference of two orders of magnitude. In this study, all soils were subjected to suctions during imaging starting at zero and progressively increasing to 148 MPa, which is well beyond the range of suctions obtained by Lin (2012) using the pressure plate apparatus. This suction range, however, was chosen to observe fabric changes over all three suction regimes (Table 3.8).

Table 3.8. Suction paths used in ESEM for all specimens

Chamber Pressure (Pa)	RH (%)	Suction (MPa)
740	100	0
665	95	7
532	76	35
350	50	89
220	31	148

Due to the change in pore size and shape between wetting and drying, as well as changes in contact angle and the amount of trapped air, more water is retained by the soil on drying than on wetting for the same range of suction (Tinjum et al. 1997; Lu and Likos 2004). This hysteretic nature was examined in this study by imaging soil samples at the same suctions through the primary drying and secondary wetting portions of the SWRC. The primary wetting portion of the SWRC occurred as the specimen was saturated in the chamber from initial moisture conditions at compaction to a relative humidity of 100%. The primary drying portion of the SWRC occurred as

the specimen was dried from 100% RH to 31% RH and the secondary wetting portion occurred as the specimen was rewetted from 31% RH to 100% RH (Figure 3.3).

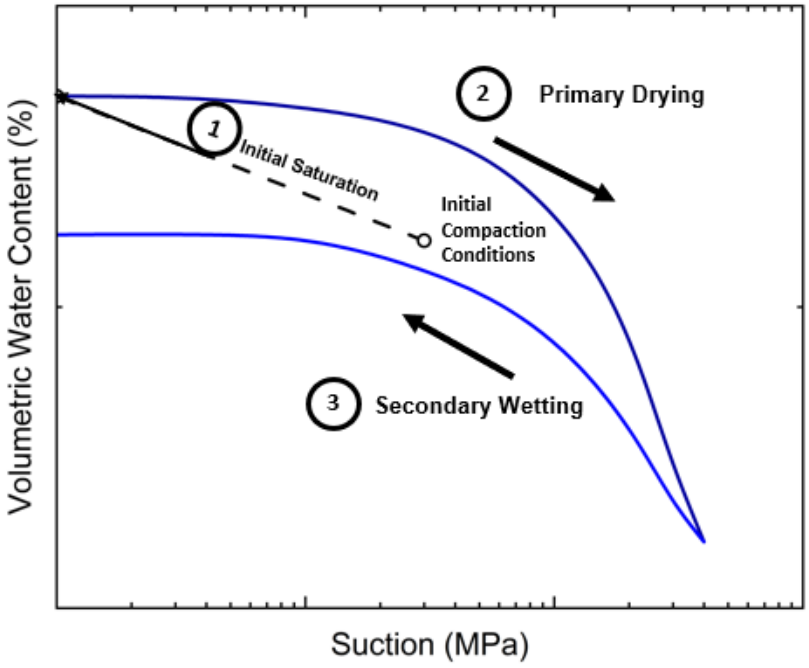

Figure 3.3. Idealized schematic of hysteretic moisture changes

The ESEM device controls chamber humidity by altering chamber pressure and allowing the moisture conditions to equilibrate. Therefore, the sample is subjected to hysteretic moisture cycles at a broad range of suction states without the adverse effects of changes in suction associated with experimental procedures such as the pressure plate and Dewpoint Potentiometer (WP4). For instance, the wetting and rewetting cycles are difficult to obtain with clays due to diffused air blocking moisture from returning to the sample through the pressure plate (e.g., Tinjum et al. 1997; Lin 2012) and other methods, such as the WP4 can only measure suctions up to 80 MPa (e.g., Thakur et al. 2006). Furthermore, due to the issues associated with obtaining the rewetting portion

of the hysteretic SWRC, most studies only perform a single drying-wetting cycle and there is little experimental information for multiple cycles or rewetting cycles (Al-Mahbashi et al. 2023).

To progress along the primary drying curve, several discrete suctions were chosen from the SWRC (Table 3.8). These suctions within the sample were achieved by adjusting the chamber pressure at a constant temperature (2° C) and equilibrated for 15 minutes at each point. A lower limit of 31% RH was encountered, as it was difficult to maintain image quality below this humidity (148 MPa suction) due to constraints regarding image contrast. When the soil became drier than 31% RH, the secondary electron detector could not differentiate the water versus soil phases, returning an image with no contrasting grey scale, i.e., the image was solid black. The soils were imaged along the secondary wetting curve was for the same discrete points and equilibrated for 15 minutes at each pressure until returning to 100% humidity. Suction was calculated from the relative humidity according to:

$$\psi = -\frac{R \cdot T}{\upsilon_{w0} \cdot \omega_v} \ln(RH) \quad [4]$$

where RH is the relative humidity, R is the universal gas constant (8.314 J/mol), T is the temperature (K), υ_{w0} is the specific volume of water (m^3/kg), and ω_v is the molecular mass of water vapor (kg/mol) (Lu and Likos 2004).

While the 0 – 148 MPa range imaged for the ESEM study covered all three suction regimes, there were two major challenges within the adsorbed film regime (e.g., 0.1 – 10 MPa). First, it was difficult to obtain discrete RH values between 90 and 100% (suctions between 10 MPa and 0.1 MPa) because the change in chamber pressure to achieve a small change in RH is small, e.g., at a temperature of 2º C to achieve a 90% RH the chamber pressure should be approximately 625 kPa, whereas at 95% RH the chamber pressure only increased by 40 kPa to 665 kPa. At 100% RH the

chamber pressure would equal 740 kPa. Likos and Lu (2003) reported that it is typical to increase RH in 10% intervals for a humidity-controlled chamber. In this study, RH values were imaged at roughly every 20-25% interval, excluding the first 5% interval.

The second challenge was that even when RH values between 90 and 100% were achieved, adsorbed water often completely obscured the image and discerning differences in structural features was impossible. Fortunately, in this study, an adequate image quality was achieved at 7 MPa (95% RH). Because of these testing difficulties, the majority of the suction values tested in the ESEM are within the tightly adsorbed regime 35 (76% RH), 89 (50% RH), and 148 MPa (31% RH) and the study focuses on the differences in features observed at 100% RH (saturation) within the capillary regime and 7 MPa (95% RH) within the adsorbed film regime with the higher suction values representing the tightly adsorbed regime.

Micrographs were collected at magnifications of 350X, 800X, and 3500X corresponding to horizontal field widths of 592 μm, 259 μm, and 59.2 μm, respectively along both the drying and wetting paths (e.g., Figure 3.4). The 350X magnification provided a broad view at the aggregate level, while the 3500X magnification allowed a better visualization of the interparticle level. The 800X magnification provided an intermediate view between the aggregate and particle separation.

To compare differences in compaction states, Heiden was compacted at optimum moisture content (Heiden opt) and wet of optimum (Heiden w1). Additionally, to compare differences in equilibration times, specimens of Heiden clay compacted wet of optimum were equilibrated at different intervals during imaging. Heiden w1 was equilibrated for 15 minutes at each suction while Heiden w2 was not equilibrated, instead micrographs were continuously collected along the drying and wetting paths.

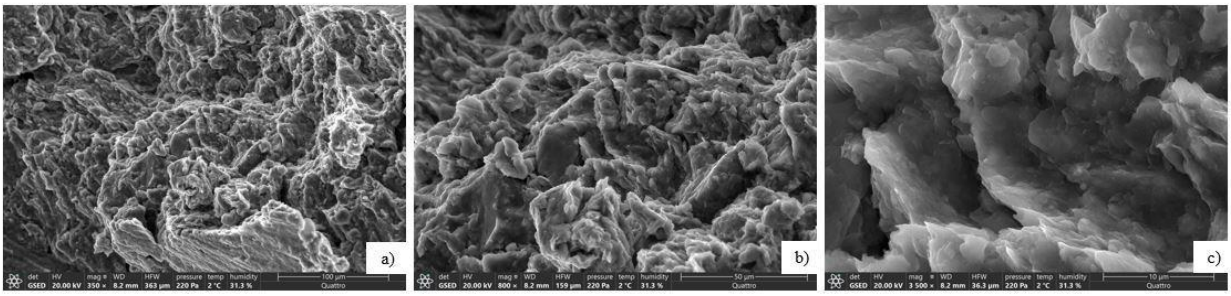

Figure 3.4. Magnification variation of Carnisaw specimen, 158 MPa, 1.52 Mg/m^3: a) 350X; b) 800X; c) 3500X

3.3 Results

3.3.1 Comparison of Fabric Between Drying and Wetting States

Micrographs of the tested soils at 35 MPa along the primary drying and secondary wetting paths are presented in Figures 3.5-3.7. Variation in structure between the drying cycle and wetting cycle is qualitatively described herein.

Images of Kaolinite, Hollywood, Carnisaw, Heiden opt, and Heiden w1 at 350X magnification are presented in Figure 3.5. Figures 3.5 a-e show the soil state at 35 MPa along the primary drying path and Figures 3.5 f-g show the soil state at 35 MPa along the secondary wetting path. The 35 MPa suction is within the tightly adsorbed regime and past the adsorbed film regime and the influence of bound water on the visibility of textural soil features is more noticeable between soil types. At this magnification, a film of adsorbed water is visible particularly for the Hollywood and Heiden w1 specimens. However, changes in fabric are only obvious for the Heiden w1 specimen, while little change is apparent for the other soils. Clear aggregate formation is visible for the Hollywood and Kaolinite, but not for the Carnisaw and Heiden soils.

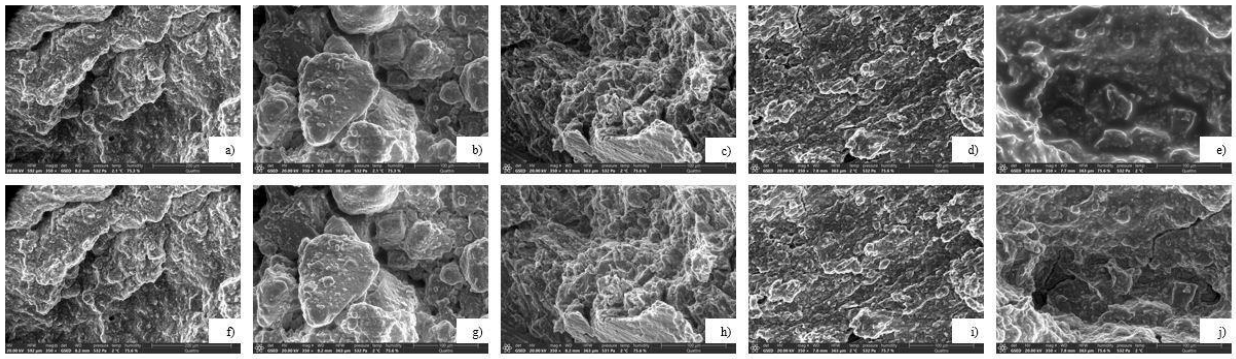

Figure 3.5. Primary drying of tested soils, 350X magnification, 35 MPa suction: a) Kaolinite; b) Hollywood, c) Carnisaw, d) Heiden opt, e) Heiden w1. Secondary wetting of tested soils, 350X magnification, 35 MPa suction: f) Kaolinite, g) Hollywood, h) Carnisaw, i) Heiden opt, j) Heiden w1

Figure 3.6 shows micrographs of Kaolinite, Hollywood, Carnisaw, Heiden opt, Heiden w1, and Na-montmorillonite at 800X magnification. Figures 3.6 a-f show micrographs collected along the primary drying cycle at 35 MPa and Figures 3.6 g-l show micrographs collected along the secondary wetting cycle at 35 MPa. There were no obvious differences between the Kaolinite, Carnisaw, or Heiden opt specimens between the drying and wetting cycles. However, more features are visible for the Hollywood and Heiden w1 specimens during rewetting than during drying. While a thick film of adsorbed water is visible during drying, the same film does not appear at the same pressure during secondary wetting. Moreover, there is evidence of desiccation cracking in the Heiden w1 and Na-montmorillonite specimens.

At 3500X magnification, more structural features are visible, shown in Figure 3.7. Micrographs collected at 35 MPa along the primary drying cycle (Figures 3.7a-f) are compared to micrographs collected at 35 MPa along the secondary wetting cycle (Figures 3.7g-l). At this magnification, it is clear that the size distribution of particles is more uniform for the Kaolinite and Na-montmorillonite specimens and more varied for the Carnisaw, Hollywood, and Heiden specimens. Moreover, the Carnisaw particles are flocculated, while the Hollywood and Heiden

specimens are more dispersed with more face-to-face particle orientations observed on the Heiden opt specimen. There are no observable changes in the Kaolinite, Carnisaw, and Heiden opt specimens between drying and wetting. While differences adsorbed water layer are apparent for the Hollywood specimen, structural changes are not readily apparent. Volumetric changes are visible for the Heiden w1 and Na-montmorillonite specimens. There are no noticeable differences in the water layer surrounding the Na-montmorillonite, but the specimen appears flocculated along the drying cycle and more dispersed along the wetting cycle. The Heiden w1 specimen shows clear evidence of hysteretic fluid loss as the adsorbed water film is thinner around the clay surface on rewetting than on drying.

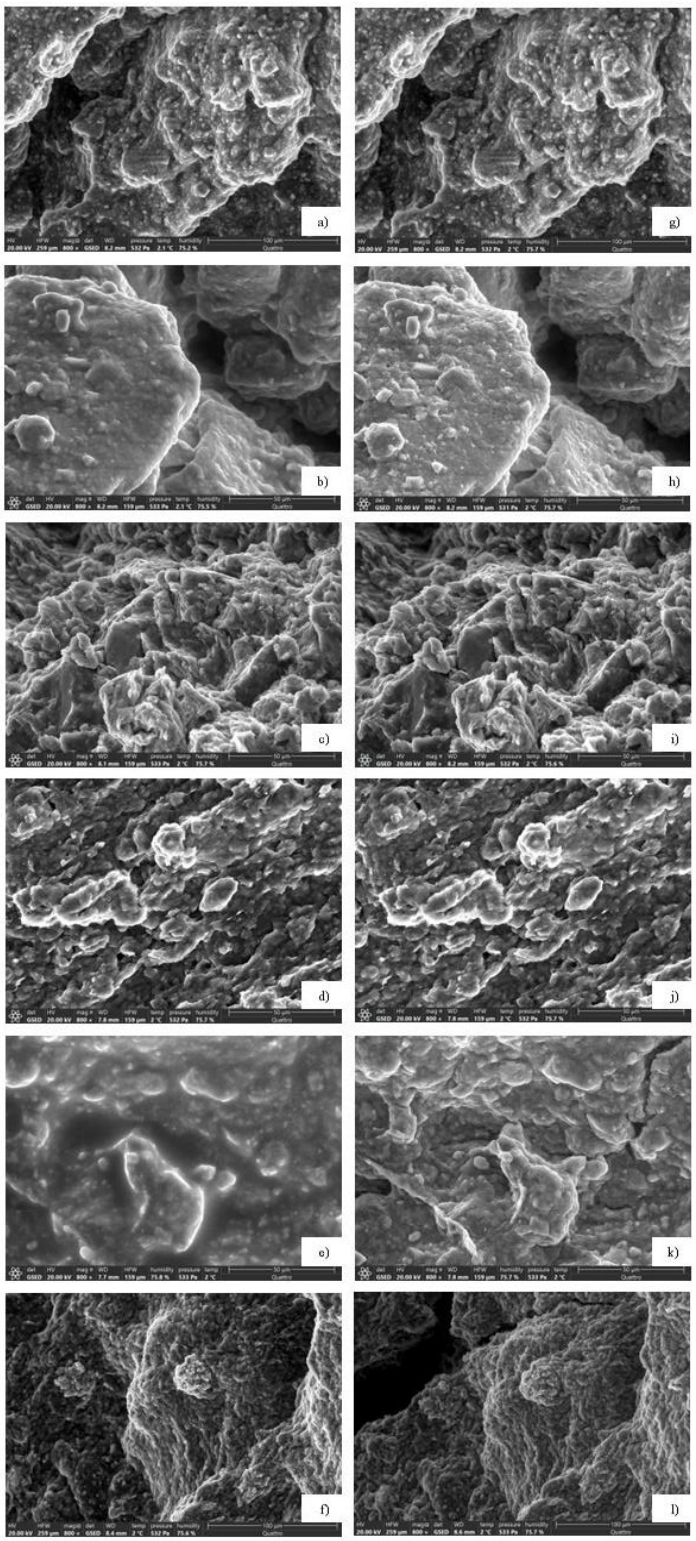

Figure 3.6. All tested soils, 800X magnification, 35 MPa suction. Primary drying: a) Kaolinite, b) Hollywood, c) Carnisaw, d) Heiden opt, e) Heiden w1, f) Na-montmorillonite. Secondary wetting: g) Kaolinite, h) Hollywood, i) Carnisaw, j) Heiden opt, k) Heiden w1, l) Na-montmorillonite

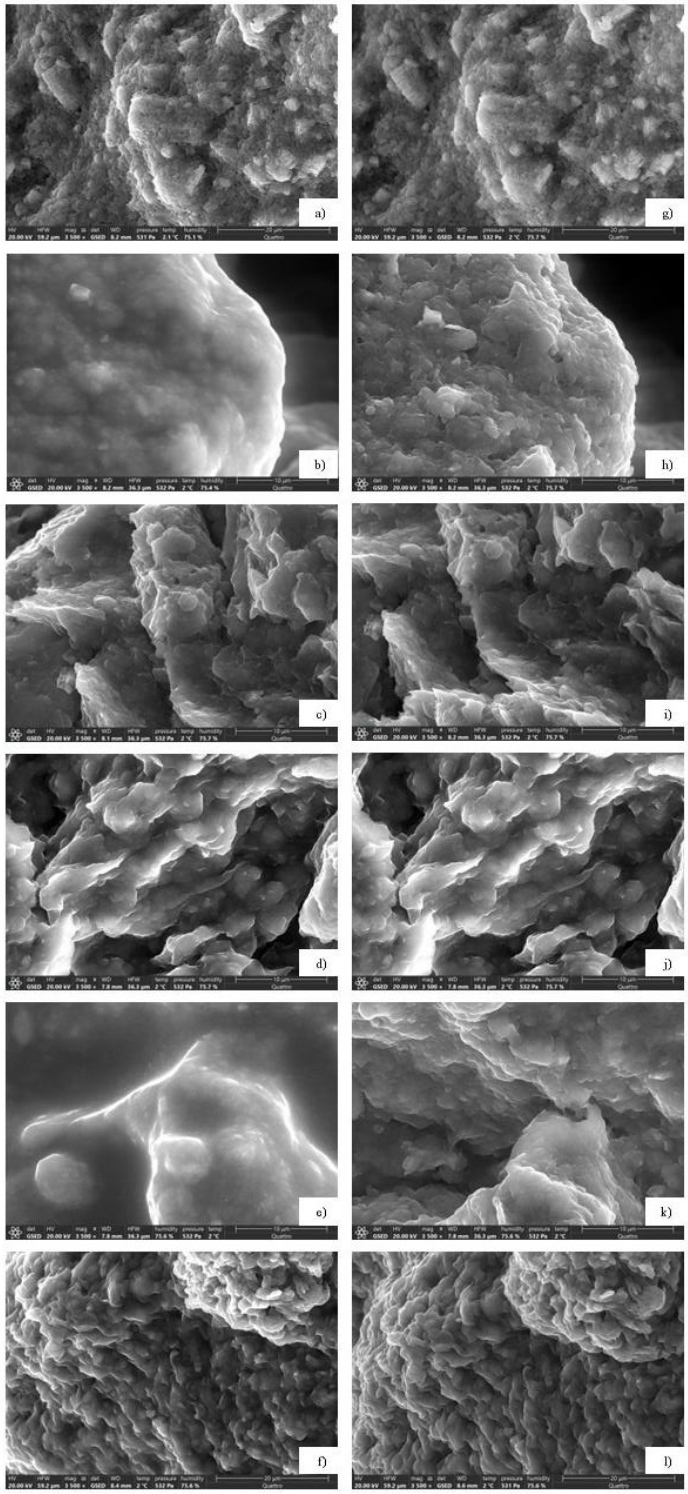

Figure 3.7. All tested soils, 3500X magnification, 35 MPa suction. Primary drying: a) Kaolinite, b) Hollywood, c) Carnisaw, d) Heiden opt, e) Heiden w1, f) Na-montmorillonite. Secondary wetting: g) Kaolinite, h) Hollywood, i) Carnisaw, j) Heiden opt, k) Heiden w1, l) Na-montmorillonite

3.3.2 Fabric Dependence on Initial Compaction State and Equilibration Time

Heiden specimens were compacted wet of optimum moisture conditions to compare the effects of initial conditions on fabric. Micrographs of Heiden w1 at 350X magnification were collected along the primary drying cycle (Figure 3.8a-e) and the secondary wetting cycle (Figure 3.8f). Notably, an adsorbed water layer formed at 0 MPa (100% RH) but did not completely obscure the image. At 7 MPa suction (94.4% RH), however, the adsorbed water layer thickened, completely obscuring the image. Once the suction increased to 35 MPa (75.6% RH), the bound water layer thickness decreased but still remained around the surface of the pores. This layer decreased once suction increased to 89 MPa (49.7% RH), but desiccation cracking occurred as the fluid layer receded. Moreover, volumetric shrinking is evident between 89 MPa and 148 MPa (Figure 3.8d, Figure 3.8e). No volumetric changes were evident along the rewetting cycle, regarding either volumetric swelling or the reemergence of the adsorbed water layer.

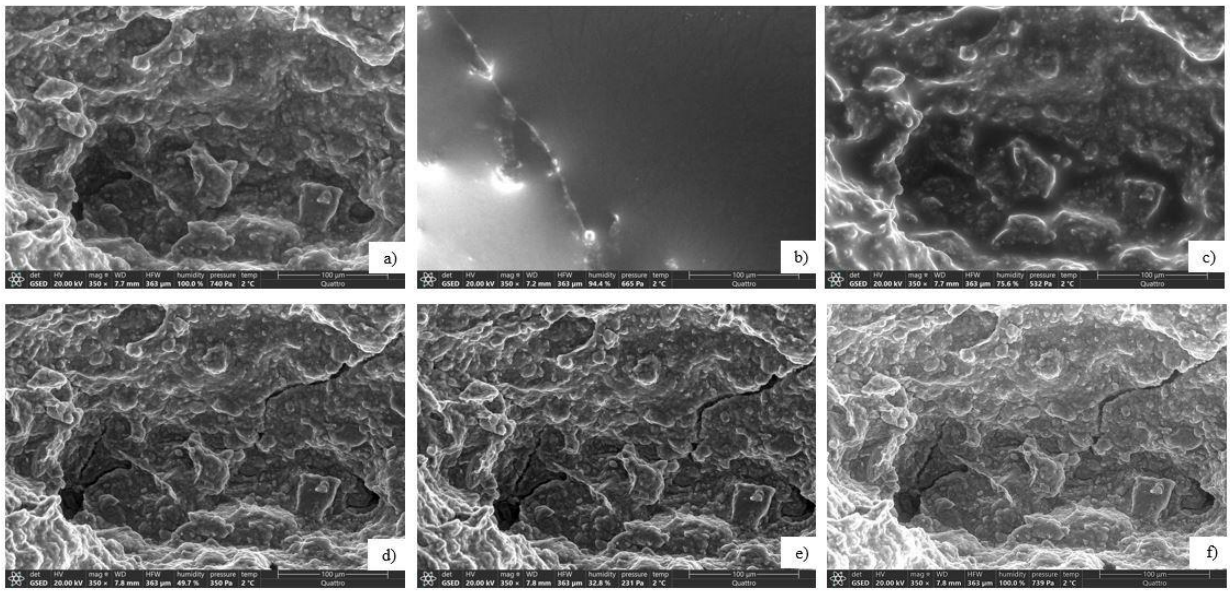

Figure 3.8. Primary drying and secondary wetting of Heiden w1, 350X Magnification, 1.22 Mg/m^3: a) 0 MPa, b) 7 MPa, c) 35 MPa, d) 89 MPa, e) 148 MPa, f) 0 MPa

An additional specimen of Heiden was compacted wet of optimum (Heiden w2) to compare effects of equilibration time on fabric. While Heiden w1 was equilibrated for 15 minutes at each discrete suction along the SWRC, Heiden w2 was imaged continuously with no equilibration time between points. Micrographs of Heiden w2 along the primary drying curve at 350X magnification are presented in Figure 3.9. While similar structural behavior was observed for Heiden w2 as Heiden w1, several notable differences occurred. A film of adsorbed water formed along the clay surface at 0 MPa and increased in thickness as suction increased. However, this bound water layer thickness receded with suctions greater than 35 MPa and was consistently thinner for the Heiden w2 than Heiden w1 specimen. Moreover, although the Heiden w2 specimen did show evidence of structural realignment (Figure 3.9 b-c), no desiccation cracking was observed.

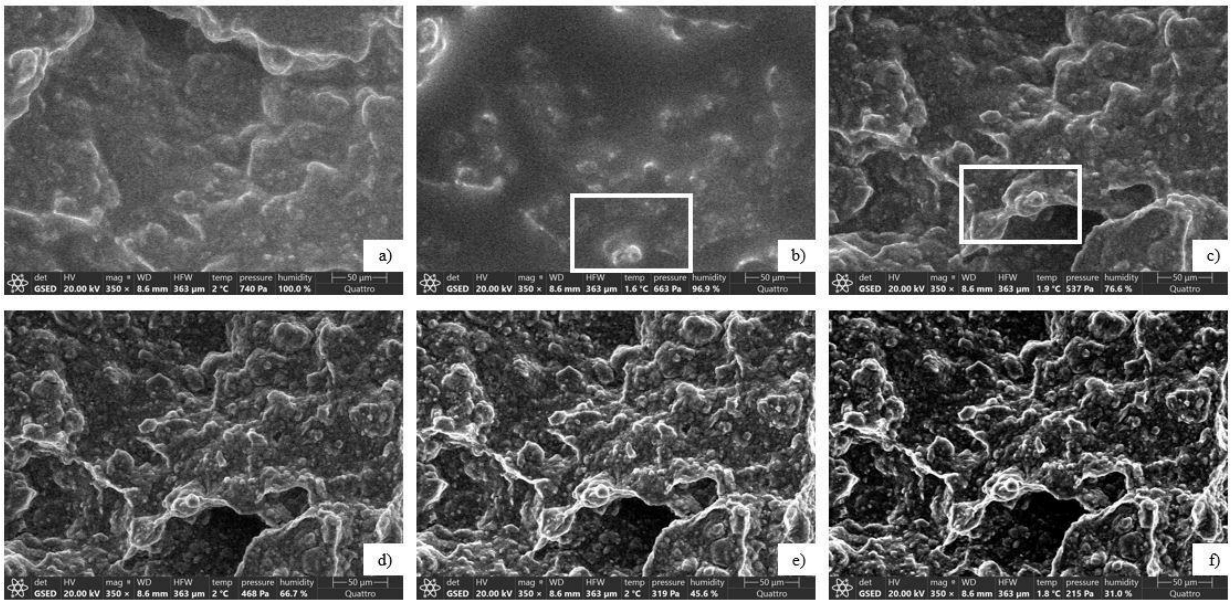

Figure 3.9. Primary drying of Heiden w2, 350X Magnification, 1.25 Mg/m^3: a) 0 MPa, b) 4 MPa, c) 35 MPa, d) 51 MPa, e) 100 MPa, f) 148 MPa

3.3.3 Influence of Silt Content on Structure

Micrographs of the Hollywood specimen at 800X magnification are presented in Figure 3.10. At 0 MPa suction (100% RH), a thick film of adsorbed water completely covered the specimen. As

the drying cycle progressed, at 8 MPa (93.7% RH), the water film thinned, showing features still obscured by fluid (Figure 3.10a). More clay features appeared at 35 MPa and little evidence of volumetric strains is apparent between 35 MPa and 148 MPa. As the specimen progressed back along the secondary wetting cycle, no changes were apparent at 35 MPa, but adsorbed water reappeared at 0 MPa (100% RH). However, while the layer of adsorbed water did reappear, the thickness of the layer diminished between the drying and wetting cycles.

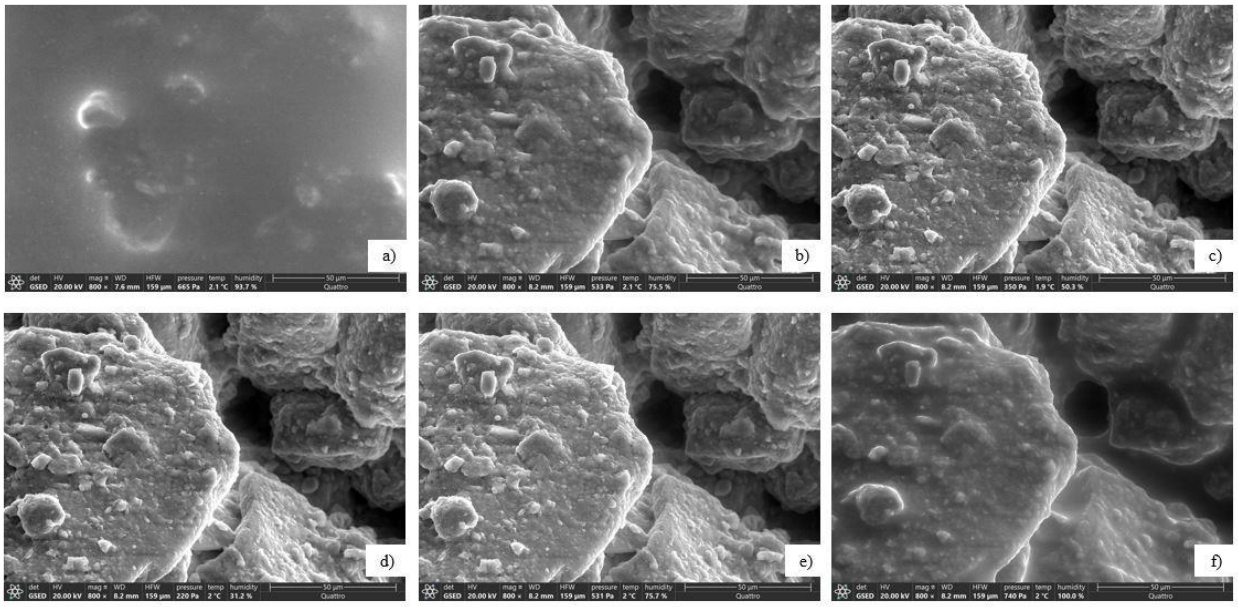

Figure 3.10. Primary drying and secondary wetting of Hollywood specimen, 800X magnification, 1.67 Mg/m^3: a) 8 MPa, b) 35 MPa, c) 87 MPa, d) 148 MPa, e) 35 MPa, f) 0 MPa

3.4 Discussion

3.4.1 Correlation with Physicochemical Properties

Activity has been used to explain the tendency of soil to chemically interact with the environment, specifically regarding the soil's inclination to retain water. The greater the activity, the more likely the soil is to chemically interact with pore fluid. Soil activity was first defined by Skempton (1953) to describe the influence of mineralogical and physical characteristics on soil plasticity. That is, the range of water contents at which water can be adsorbed to the clay surface is dependent on the

type of clay minerals contained in the soil as well as the fraction of the deposit containing those minerals. Skempton activity is given in Equation 5:

$$A = \frac{PI}{CF} \quad [5]$$

where A is the Skempton activity, PI is the plasticity index ($w_L - w_P$), and CF is the fraction of the soil finer than 2 μm (Skempton 1953).

However, soils with the same plasticity index can vary in behavior if the mineralogy varies (Cerato and Lutenegger 2005) and plasticity alone has been shown to be inadequate to characterize soil shrinking and swelling on the macroscale (e.g., Buhler and Cerato 2007). Instead, physicochemical parameters intrinsic to each soil better describe how soil will interact with the pore fluid. The relative activity (A_R) uses the specific surface area of the clay fraction to normalize the PI, better defining the impact of the clay fraction on plasticity (Quigley et al. 1985):

$$A_R = \frac{PI}{S_A} \quad [6]$$

The S_A activity (A_S) utilizes the influence of the clay specific surface area on the plasticity, replacing PI with S_A to calculate activity (Locat et al. 2003).

$$A_S = \frac{S_A}{CF} \quad [7]$$

The clay fraction is useful to describe activity because of the net negative charge along the clay surface, which is not present in nonplastic soils. A more direct measurement of the activity due to the clay fraction, then, is to account for the net negative charge along the surface, quantified by the CEC. The CEC activity (A_{CEC}) is given by Equation 4 (Cerato and Lutenegger 2005):

$$A_{CEC} = \frac{CEC}{CF} \quad [8]$$

The calculated activity values of the tested soils are presented in Table 3.9.

Table 3.9. Activity values of the studied soils

Soil ID	Skempton Activity (PI/CF)	Relative Activity (PI/S_a)	S_A Activity (S_A/CF)	CEC Activity (CEC/CF)
KGa-1b	0.44	1.07	0.41	0.06
Carnisaw	0.47	0.25	1.89	1.05
Hollywood	1.79	0.23	7.66	5.54
Heiden	0.80	0.19	4.16	3.23
SWy-Na-MMT	8.01	0.76	10.55	10.07

Skempton (1953) described kaolinitic clays as nearly inactive and Na-montmorillonite clays as the most highly active (i.e., activity greater than 2.0). Therefore, the Kaolinite is not expected to shrink and swell with changing suction while the Na-montmorillonite is expected to exhibit the greatest amount of shrinking and swelling, while the natural soils would fall somewhere in between. However, the Skempton activity is not sufficient to describe the behavior of the studied soils. Based on the calculated Skempton activity values, the Kaolinite and Carnisaw specimens are expected to exhibit similar behavior, contrary to the behavior observed through ESEM. The Carnisaw specimen showed visual evidence of volumetric strain during the drying cycle while the Kaolinite did not. The relative activity (A_R) is also insufficient to describe the clay behavior. Using this calculation, the Kaolinite has higher relative activity than the Na-montmorillonite, which was not observed.

The S_A activity and CEC activity better describe microstructural phenomena. The Kaolinite, which did not exhibit shrink/swell behavior and did not form a layer of adsorbed water has the lowest activity using either metric. Carnisaw has the next lowest activity (1.89, 1.05) and experienced the least amount of qualitatively observed deformation of the natural soils. Additionally, Carnisaw did not develop a layer of bound water along the clay surface. When considering the Heiden and Hollywood specimens at optimum conditions, the calculated activity is reasonable to explain the lack of adsorbed water experienced by the Heiden opt specimen, but

further explanation is necessary for the Heiden specimens compacted wet of optimum. The Heiden soil has the greatest montmorillonite content and lowest kaolinite content (Table 3.1) of the natural soils and a similar clay fraction to the Carnisaw (Table 3.2). Therefore, of the natural soils, Heiden would be expected to exhibit greater activity than the Carnisaw for the same range of suctions.

3.4.2 Effect of Initial Compaction Conditions

The Heiden soils compacted wet of optimum developed a thick layer of adsorbed water once equilibrated to 100% RH while the Heiden soil compacted at optimum moisture conditions and maximum dry density did not. The adsorbed water layer is the tightly bound water film around negatively charged clay particles and changes thickness depending on the suction state, surface area of the clay particles, the type and valency of adsorbed exchangeable cations, the surface charge density of the soil mineral, and chemistry of the pore fluid, i.e., becomes smaller as the cation valence and electrolyte concentration increases and pH decreases (Lu and Likos 2004).

Changes in the thickness of the adsorbed water layer can be studied in the ESEM images along the suction path through observation of bound water blurring the image at wet of optimum because the sample is more dispersed. The image becomes clearer for soils at optimum moisture content when the layer is smaller, indicated by more distinct features visible on the clay surface at all magnifications. This difference in the formation of this film of water between optimum and wet-of-optimum is due to differences in moisture and subsequent void space initially contained in the wet of optimum soils. Heiden opt was compacted at a higher dry density (lower void ratio) than Heiden w1 and Heiden w2 and a lower initial water content. Therefore, there was less available free water to form a layer of bound water along the surface.

Inter-aggregate pore volume is a driving factor in structural changes of expansive clays and is influenced by dry density (Dieudonne et al. 2017). At greater dry densities, the contribution of

the macropores to total void volume is reduced. Therefore, greater suction values are required to empty pores of fluid (i.e., higher air-entry values are formed). At the same suction range, the capillary pore fluid in the Heiden opt specimen remained within the macropores, while the suction values required to release fluid from the Heiden w1 and w2 macropores was met, resulting in pore fluid bound to the clay surface.

The observed hysteretic behavior of the bound water, i.e., thinner adsorbed water layers along the rewetting curve, is due mainly to capillary forces within the specimen, occurring within the inter-aggregate pore space. For more densely compacted soils, this inter-aggregate pore space is negligible compared to the intra-aggregate region (Dieudonne et al. 2017). Cui et al. (2002) also noted an "irreversibility" of cyclic response for unsaturated soils at lower suctions, due to the increase in the volume of macropores, i.e, intra-aggregate space.

Similar behavior has been observed at the macroscale for soils of varying clay fractions and activities (Cerato et al. 2008). Initial specimen preparation affects the collapse potential of compacted clay specimens: denser, more dispersed specimens exhibit a lower collapse potential than loose specimens. The implication is significant because expansive soils are commonly compacted wet of optimum to encourage volumetric swelling with increases in pore fluid. However, desiccation cracking was observed for the specimen prepared wet of optimum (Heiden w1) and was not observed for the specimen compacted at optimum conditions (Heiden opt).

3.4.3 Effect of Equilibration Time

There was a noticeable difference in structure based on the equilibration time allowed between the Heiden w1 and Heiden w2 specimens. The formation of the thicker diffuse water layer in the Heiden w1 specimen is likely due to the difference in time the specimen was subjected to each suction interval. When equilibration time is allowed, unbound water in the sample dissipates to the

chamber atmosphere and stabilizes at an equilibrium point (Lin and Cerato 2014). When this time is not allowed, the unbound water continues extending/receding and never stabilizes. While the fluid front did progress in the case of Heiden w2, water molecules bonded with the soil surface but continued to flow, resulting in a thinner bound water layer. Desiccation cracking was not observed in Heiden w2 likely because the forces associated with bonded fluid evaporating were not given time to develop.

Montes-H et al. (2004) employed equilibration times of 20 minutes for specimen drying and 30 minutes for the wetting stage. Similar desiccation cracking to that of the Heiden w1 was observed because of water evaporation from the soil surface. Lin and Cerato (2014) also employed 30 minutes of equilibration time for each suction interval, and comparable structural changes were observed during sample drying. An interval of 15 minutes for equilibration was deemed comparable by Sun et al. (2019).

3.4.4 Influence of Silt Content

The Hollywood soil studied has a high silt content compared to clay content (81% silt, 19% clay). The clay fraction has a low CEC and relatively low S_A, therefore interactions with pore fluid at the clay surface level are unlikely and the formation of a thick diffuse layer of water is not expected for this soil. Instead, the pore fluid observed in the Hollywood micrographs is likely due to dilation because of the high silt content in response to the induced suction rather than physicochemical forces along the surface. As the specimen was saturated to 100% RH, pore water rushed to the surface, lending a sheen of water unable to be penetrated by the microscope. Instead of adsorbing to the soil surface, the water formed an unbonded layer above the soil.

3.5 Conclusions

Structural deformations that occur at the microscale influence parameters, which affect macroscale behavior. As particles realign in reaction to changes in pore fluid, pore networks expand and contract, affecting the fluid storage, permeability, and strength at the macroscale. A better understanding of these microlevel structural changes will result in a better conception of the engineering behavior of expansive soils, ultimately leading to better construction practices when these soils are present.

This work compared three natural soils and two single-mineral clays along the primary drying and secondary wetting cycles. Variations in physicochemical properties (S_A, CEC), initial moisture content (optimal moisture, wet of optimum), and equilibration time (15 minutes, no equilibration) were considered. Qualitative analysis of the microstructure concerning the formation of adsorbed water and evidence of volumetric shrink/swell was performed.

The following conclusions can be inferred:

- Conventional methods to describe activity, particularly those which rely on plasticity index, are not sufficient to explain changes in the microstructure. Specifically, the Skempton activity parameter failed to differentiate between specimens with significant differences in montmorillonite content. Carnisaw (A = 0.47) and Kaolinite (A = 0.44) would be expected to have similar volumetric strains as pore water varied, but the fabric of the Carnisaw specimen evolved through hysteresis and the Kaolinite specimen remained essentially inert. Similarly, the relative activity (A_R), also using PI in its calculation, fails to assess realistic soil behavior. Using A_R, Kaolinite is most probable to react to pore fluid and Heiden is the least probable. Instead, activity parameters using physicochemical parameters (S_A, CEC) better predict the likelihood of clays to react with changing pore fluid.

- Effects of initial compaction conditions observed at the macroscale are also observed at the microscale. Soils compacted wet of optimal moisture conditions are more prone to developing a dispersed clay structure and develop a thicker layer of adsorbed water. As bound water evaporates during drying the soil matrix experiences desiccation cracking as the fluid layer recedes.
- Equilibration time affects the ability of unbound water to form electrical bonds with the negatively charged soil surface. While a layer of adsorbed water does form even in the case of no equilibration time, the thickness of this layer is minimized and forces which would lead to desiccation cracking on pore fluid evaporation are not allowed to fully develop.
- Silt content causes a layer of unbonded water to form due to the dilatancy of the silt content in the specimen. This layer of water differs from the electrostatic double layer as it is unbonded to the soil surface in the case of silty soil.

Chapter 4 Fractal Approach to Analysis of Expansive Soil Microstructure Along Hysteretic Moisture Cycles

4.1 Introduction

Expansive soils are prevalent across a quarter of the United States and span over 2,350,000 square kilometers of the Earth's surface, as depicted in Figure 4.1. Their widespread occurrence makes them an unavoidable choice for supporting structures such as bridges, roads, and lightweight construction, as noted by Borchardt in 1989. However, volumetric strains (i.e., shrinking and swelling) associated with seasonal wetting and drying cycles damages these structures, requiring billions in mitigation costs annually (e.g., Amakye et al. 2021; Devkota et al. 2022). Because of their low permeability and tendency to expand with the introduction of pore fluid, expansive soils are often used as barrier materials in waste containment facilities and as the core of earthen dams and levees (Montes-H 2005). As water evaporates during drying cycles, however, the resulting increase in suction can cause cracking in compacted clays (Miller et al. 2002). The wide use of expansive clays in engineering projects necessitates a better understanding of the microscale behavior, particularly over a range of pore fluid conditions as the soil experiences cycles of wetting and drying. Models which can capture the microscale forces require a fully developed understanding of soil fabric at the microscale with variation in saturation and ideally, a quantitative analysis of the clay structure.

Physicochemical forces at the microscale govern inter-particle, inter-aggregate, and intra-aggregate interactions, influencing soil fabric which ultimately determines the macroscopic mechanical behavior (e.g., strength, swell potential, and permeability) of expansive clays. Electron microscopy is a tool commonly used to characterize the geometric structure of expansive soils at the micro- and nanoscale. Scanning Electron Microscopy (SEM) allows direct imaging of the soil

structure at the particle/aggregate range (i.e., < 10 μm) where physicochemical forces dominate (Romero and Simms 2008). However, this technique requires fully desiccated specimens and is not appropriate for studies concerning fabric changes with soil moisture. Instead, ESEM (Environmental Scanning Electron Microscopy) images soil specimens across a wide range of chamber humidities and pressures, particularly at high relative humidity (RH) where saturation is high and suction is low.

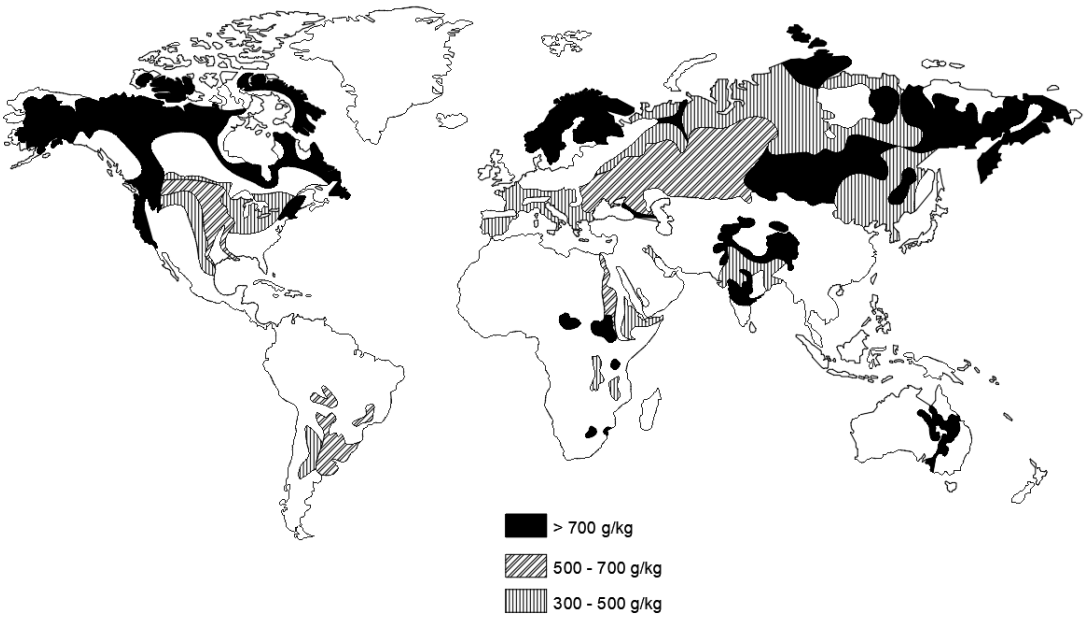

Figure 4.1. Map of expansive soils in the world (after Borchardt 1989).

The majority of ESEM studies have provided qualitative, rather than quantitative, analysis (e.g., Montes-H 2005; Koliji et al. 2010; Lin and Cerato 2014; Chapter 3 herein). Lin and Cerato (2014) studied evolutions in microstructure for Carnisaw (low swelling capacity) and Eagle Ford (high swelling capacity) soils. ESEM was able to characterize the fabric, but only qualitative characteristics were obtained, e.g., grain orientation, anisotropy of particles, and visualization of cracking. Similar qualitative analysis was performed by Koliji et al. (2010) for mechanical loading

of natural and reconstituted soil specimens. Sun et al. (2019) paired ESEM with Mercury Intrusion Porosimetry (MIP) and water retention curve measurements to evaluate the evolution of bentonite microstructure through wetting and drying hysteresis, with focus on pore structure. Through image analysis of ESEM micrographs, volumetric strains, changes in aggregate volume, and pore families (micro- and macropores) were determined. Most recently, a qualitative study of natural and single-mineral soils along the wetting and drying paths of the soil water retention curve (SWRC) using ESEM was performed and is presented in Chapter 3 herein. The variation in structural changes was analyzed considering differences in physicochemical parameters, i.e., cation exchange capacity (CEC) and specific surface area (S_A) and the associated activity. Equilibration time, silt content, and initial moisture content affected the formation of the adsorbed water layer along the soil surface.

Concepts from fractal geometry can provide this missing quantitative assessment of the clay structure, presenting a numerical understanding of the patterns of fabric, structure, and pore networks. The theory of fractal geometry was formalized by Mandelbrot (1982) to quantify irregularity and fragmentation in complex systems. Mandelbrot defined a fractal as a geometric figure that scales to some dimension between whole number powers. Fractal patterns have been observed in nature in the form of tree branching and root systems (Oppelt et al. 2000), mountain ranges (Liucci and Melelli 2017; Rak et al. 2020), river deltas (Balkhanov and Bashkuev 2004), lightning branches (Mandelbrot 1982; Tsonis 1987), and cellular morphologies (Smith et al. 1996). Fractal patterns have also been observed in soils and other geomaterials, such as sands (Levine et al. 2016; Zhou et al. 2018; Barman et al. 2022;) and rocks (Turcotte 2001).

This study compares the surface complexity of three natural soils to two single-mineral soils through cycles of suction hysteresis. ESEM micrographs were collected at discrete points

along the primary drying and secondary wetting paths for each soil. Fractal geometry, namely the box-counting fractal dimension and associated lacunarity, were used to quantitatively describe changes in particle morphology and complexity with changing physicochemical forces and suction state. Changes in complexity with respect to clay fraction, equilibration time, and compaction conditions were assessed. Understanding the change in complexity with suction may provide insight into the range of movement an expansive soil unit experiences through seasonal wetting/drying cycles. While the mineralogy of expansive soils is known, mineralogy alone is not sufficient to predict macroscale behavior and therefore, pairing it with fabric complexity may provide a deeper understanding of the contribution of the microscale geometry to macroscale engineering behavior.

4.2 Background

Many natural systems are complex, and as such require complex mathematics to describe the geometry and heterogeneity of their features. Fractal geometry is a theoretical framework to quantitatively measure patterns too complex for traditional Euclidean mathematics. Fractals follow the concept of self-similarity, or scale invariance, in which similar features are repeated at smaller scales (Smith et al. 1996). Self-similarity can be deterministic (exact) or stochastic (statistical) (Perfect and Kay 1995; Turcotte 2001).

The fractal dimension measures the change in complexity, or detail, with changes in scale. Complexity (e.g., irregularity and fragmentation) of a surface is quantified by relating a characteristic scale to the aggregation of a measured feature through a power function:

$$L \propto G^{-D} \quad [1]$$

where L is the summation of the characteristic unit (e.g., summation of boxes covering a surface), G is the magnitude of the measuring unit (e.g., length of the side of a box), and D is the fractal dimension (after Mandelbrot 1982).

The concept of the fractal dimension is best explained using the trivial case with non-fractal geometries. Consider the 1-dimensional case: a line segmented in half results in two new line segments, each one-half of the original length. Using Equation 1: $2 = (1/2)^{-1}$, therefore the fractal dimension of a line is 1.0. For the 2-dimensional case, the length and width of a square are segmented in half, resulting in 4 new squares, each linear dimension ½ of the original linear dimension of each side of the original square. Using Equation 1: $4 = (1/2)^{-2}$, and the fractal dimension is 2.0 (after Mandelbrot 1967). This can be continued without loss of generality for increasing Euclidean dimensions. For fractal geometries, which exhibit self-similarity, the fractal dimension is not a whole number, but lies between integer values. This can be expanded to natural features, such as the length of the coastline of Great Britain (Mandelbrot 1967).

Geomaterials, while rarely deterministic fractals, can be modeled as stochastic fractal systems. The Menger Sponge and Turcotte's cube are three-dimensional adaptations of the Sierpinski fractal, all deterministic fractal representations of porous systems (Turcotte 2001). Pore networks of soils follow similar scaling patterns as particle size decreases, but the repeating pattern is not deterministic, and instead requires more complex analysis to quantify the randomness in the pore system with changing scale (i.e., stochastic self-similarity). Fractals have been used to describe pore-size distribution, pore surface area, and particle- and aggregate-size distribution, and can be correlated with fragmentation, adsorption, and permeability (Perfect and Kay 1995). Most recently (Chapter 2), the fractal dimension and lacunarity were used to quantify the evolution of compressive strength for stabilized kaolinitic soils over time.

Mass and volume fractal dimensions (ranging between 2 and 3) have been used to analyze soil texture, water retention capacity, and pore networks (Tyler and Wheatcraft 1990; Perfect et al. 1996; Gimenez et al. 1997) from the particle size distribution and analysis of thin-film sections. Coarser soils were characterized by lower fractal dimension, e.g., closer to 2, and finer soils (with more complex pore networks) had higher fractal dimension, e.g., closer to 3 (Fazeli et al. 2010). Guber et al. (2005) performed similar studies on mass fractals of the particle size distribution for disturbed samples with diameters ranging from 0.001 to 0.25 mm and found that aggregates are no longer fractal at complete saturation, e.g., mass fractal dimension reaches a whole number value.

Because particle size distribution is known to affect the water retention capacity of soils, effort has been placed into relating the fractal dimension of the particle size distribution to the Soil Water Retention Curve (SWRC) (Toledo et al. 1990; Tyler and Wheatcraft 1992; Crawford 1994; Fazeli et al. 2010). Many of these studies used image analysis of thin-film sections, a precursor to image analysis of ESEM micrographs, to obtain the particle size distribution on non-expansive soils. A relationship between the fractal dimension and SWRC for expansive soils is valuable because the geometrically based fractal dimension removes the empirical factors from the calculation of the retention curve (Tyler and Wheatcraft 1990). While these studies developed the initial framework for relating fractal geometries to soil behavior, they consider sandy soils (e.g., Toledo et al. 1990), explicitly ignore expansive soils (e.g., Tyler and Wheatcraft 1992), or use methodologies that require a mass fractal or particle size distribution at a scale much larger than the micro- and nanoscale (e.g., Tyler and Wheatcraft 1992; Fazeli et al. 2010). Fractal dimensions of expansive soils obtained through an image, discretized to the aggregate or particle level, would

provide a quantitative assessment of the microscale behavior of expansive clays in the unsaturated state.

The box counting fractal dimension is useful to describe the complexity of soil structure and has been recognized as the simplest yet most accurate method for characterizing surface structure (Liu et al. 2005). Box counting fractals are beneficial as they can be derived directly through an image and do not require sieving or gravimetric analyses. In the box counting technique, a system of grids (i.e., pixels or boxes) is systematically layered over an image and the number of grids (boxes) containing at least one pixel of the structure of interest (e.g., soil surface) are counted. The count is compared to the size of the sampling element (grid size) and the slope on a double- logarithmic plot is the box counting fractal dimension, according to:

$$N(\varepsilon) \propto \varepsilon^{-D_{BC}} \quad [2]$$

Where $N(\varepsilon)$ is the number of boxes containing at least one pixel of pore space, ε is the grid size, and D_{BC} is the box counting fractal dimension (after Dathe et al. 2001).

Liu et al. (2005) used a box counting fractal analysis (window analysis method) of SEM images to evaluate pore structure in expansive soils. They noted a magnification effect on fractal dimension, for magnifications between 200X and 3,000X there was a threshold ratio of 0.1 between the original image and magnified image. That is, fractal dimensions were not constant with changes in the size proportion (i.e., ratio of magnified image size to the original image size) of the image. The fractal dimension was relatively constant (ranging between 2.1472 and 2.1527) for size proportions ranging between 1 and 0.1 but sharply increased for size proportions less than 0.1. Sun et al. (2020) determined a decrease in box counting fractal dimension as magnification increased for expansive soils imaged via ESEM. This was ascribed to the greater number of aggregate features captured under lower magnification than higher magnifications. However, the

percent difference between fractal dimension calculated at 800X and 50,000X magnifications by Sun et al. (2020) was less than 3 percent. Fractal dimension does not change as drastically between magnifications as lacunarity because there is a limiting texture when reaching magnifications that only provide information of a single individual particle. This is the representative elementary area (REA) or representative elementary volume (REV) of the image (Luo and Lin 2009; Liu and Ostadhassan 2017) beyond which variation does not change. It is necessary to obtain a balance between viewing surface texture while achieving magnifications of the microstructural fabric of aggregated particles where fractal dimensions are valid.

Lacunarity is useful to describe the texture of a fractal set, or the mass distribution of pores along the surface (Mandelbrot 1982; Allain and Cloitre 1991). Because two fractal sets may have the same complexity, lacunarity is used to differentiate the pattern of complexity. Consider the Cantor dot sets in Figure 4.2: while each set has the same box counting fractal dimension, the generator of each set differs, resulting in differing patterns of holes, and therefore different lacunarity. Structures with wider and larger gaps between features have higher lacunarity (Liu and Ostadhassan 2017) and more coarse textures have higher lacunarity while finer surfaces have lower lacunarity (Ling et al. 2016).

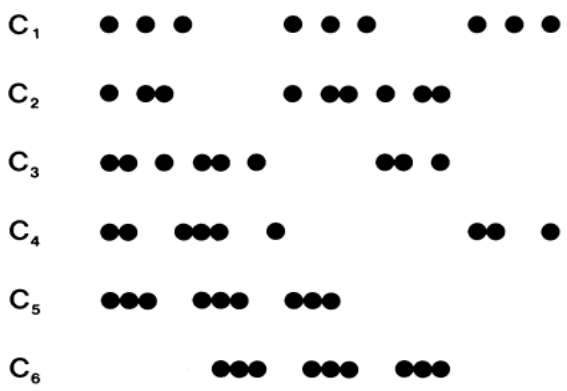

Figure 4.2. Cantor dot sets with differing lacunarity (from Allain and Cloitre 1991)

Lacunarity describes the translational and rotational invariance as well as the degree of dispersion and clustering, and the existence of hierarchical structure (Plotnick et al. 1993; Luo and Lin 2009; Liu and Ostadhassan 2017). Pores along the soil surface cause heterogeneity in the image, while a truly invariant image has equally sized and distributed pores (Roy et al. 2010). As the image is rotated or translated, the image changes, detailed in the change in mass distribution of foreground pixels (Karperien 2013). While two images may have the same box-counting fractal dimension, lacunarity differentiates between the patterns detailed on the surface, assessing the pixel distribution of the image. Lacunarity is given by:

$$\Lambda(r) = \frac{\sum_{k=0}^{r^2} k^2 Q(k,r)}{\left[\sum_{k=0}^{r^2} kQ(k,r)\right]^2} \quad [3]$$

where $\Lambda(r)$ is the lacunarity, the numerator is the second moment of the probability distribution Q *(k,r)* and the denominator is the square of the first moment of the probability distribution (Lee and Lee, 2013). *Q (k,r)* is a probability distribution function given by

$$Q\ (k,r) = \frac{n_{k\,(r)}}{N(r)} \quad [4]$$

where r is the measure of the side of a box, $n_{k(r)}$ is the number of boxes counted when the box mass is equivalent to k, $Q(k.r)$ is the probability distribution, and $N(r)$ is the total number of boxes (Lee and Lee, 2013). The greater the degree of gap clustering, i.e., heterogeneity of pores, the greater the lacunarity (Roy et al. 2010).

Baer et al. (2009) paired box-counting fractal analysis with lacunarity to describe desiccation cracking patterns of silts. Soils with more space between desiccation cracking areas had higher lacunarity while soils with a denser pattern of cracking had low lacunarity. Luo and Lin (2009) used lacunarity calculations paired with fractal dimension of X-Ray Tomography (CT) results to assess solute distribution and transport with macropore structure. A dependence on box-size was observed for lacunarity of the CT images: for the same image, lacunarity decreased as grid size increased. As the mesh (grid) became coarser, i.e., larger box size, the variance between grids decreased resulting in lower lacunarity. Additionally, higher lacunarity was associated with greater degrees of clustering. Because lacunarity is sensitive to structural differences it can be used to describe microstructural patterns and moreover, can be used to describe soil structures which are not fractal. Scale dependence on magnification has also been observed for lacunarity of soils and rocks (e.g., Pendelton et al. 2005; Liu and Ostadhassan 2017) and metallic surfaces (e.g., Ling et al. 2016). Hierarchical information available at one scale is not evident at all scales and therefore the same material must be imaged at varying magnifications to understand the variance of features with scale (Pendelton et al. 2005; Ling et al. 2016).

The majority of studies relating fractal dimension to soils and other geomaterials focus on mass and volume fractals and therefore require physical tests such as a grain size distribution or MIP. MIP is destructive, requires mercury to perform, and provides information about the pore structure rather than the soil fabric, i.e., arrangement and roughness of particles. To understand the

fabric changes at the microscale, grain size distributions utilizing a mass fractal are impossible and imaging techniques using ESEM are desired. The box counting technique uses images at any scale to provide information about the complexity of the surface (fractal dimension) and heterogeneity of the surface (lacunarity). Of the studies performed using fractal dimension with expansive clay (Sun et al. 2020), only one soil was analyzed and the magnifications exceeded the threshold value where fractal dimension effectively changes. Extrapolation from that size range to a larger particle or aggregate scale is difficult. Furthermore, even less information is available regarding the lacunarity of expansive soils (Luo and Lin 2009; Liu and Ostadhassan 2017). Therefore, in this work, magnification effects on fractal dimension and lacunarity were assessed using a single-mineral soil at five magnifications and one relative humidity where the clearest image was present. Initial moisture conditions, equilibration time and compaction state of one of the natural soils were also considered to gain a better understanding of how seasonal wetting and drying cycles effect the range of movement of expansive soils.

In addition, the relationship between surface complexity and physicochemical parameters, fractal dimension and lacunarity of two single mineral and three natural expansive soils were analyzed at discrete points along the primary drying and secondary wetting paths of the soil water retention curve. In this way, the effect of suction on the soil microstructure could be quantitatively assessed via fractal dimension and lacunarity on both the single mineral and natural expansive soils.

4.3 Materials and Methods

4.3.1 Materials

Three naturally occurring, expansive soils were selected based on their broad range of mineralogy, morphology, and activity. The soils were analyzed for changes in fabric under varying suctions

and compared to that of laboratory-derived, single-mineral clays. The physicochemical properties of the natural soils are bounded by those of the artificial soils (Table 4.1).

Table 4.1. Physicochemical properties of tested soils (after Lin 2012 and Cerato 2001)

Soil ID	Total S_a[a] (m^2/g)	CEC [b] (meq/100g)	Clay Fraction (%)	PI (%)	Clay Size Minerals (%)
Kaolinite	15.0	2.0	36.2	16	K[c] (100)
Carnisaw	107.5	27.3	56.6	27	V[d] (12) I[e] (25) K (14)
Hollywood	145.5	26.4	18.8	34	M[f] (23) I (21) K (18)
Heiden	229.0	50.7	54.8	44	M (37) I (5) K (8)
Na-Montmorillonite	637.0	76.4	60.4	484	M (100)

[a] Specific surface area; [b] Cation exchange capacity, [c] Kaolinite; [d] Vermiculite; [e] Illite; [f] Montmorillonite

The artificial clays were obtained from the Source Clay Mineral Repository, and included KGa-1b, a well-crystallized pure kaolin clay (Kaolinite) and Swy-2 Na-MMT (Na-montmorillonite). The natural soils included (1) Carnisaw, a fine, semiactive, thermic Typic Hapludult, weathered from Pennsylvanian shale, (2) Hollywood, a fine, smectitic, thermic Oxyaquic Hapludert, and (3) Heiden, a fine, smectitic, thermic Udic Haplustert, weathered from mudstone. Heiden specimens were compacted at optimum moisture conditions (Heiden opt), wet of optimum with equilibration time of 15 minutes (Heiden w1), and wet of optimum with no equilibration time (Heiden w2).

4.3.2 Methodology

4.3.2.1 Environmental Scanning Electron Microscopy (ESEM)

A theoretical framework for understanding the microscale soil structure requires a high-quality, carefully curated dataset of soil specimens under a wide range of suction conditions. To this end, specimens of the studied soils were imaged using Environmental Scanning Electron Microscopy (ESEM) along the primary drying path (suctions ranging from 0 MPa to 148 MPa) and back along the secondary wetting path (suctions ranging from 148 MPa to 0 MPa). The ESEM procedure, and

resulting dataset are detailed in Chapter 3. Specimens were compacted at the maximum dry density and optimum moisture content and trimmed to dimensions 1 cm x 1 cm x 5 mm with the thin axis perpendicular to the direction of compaction. A V-shaped groove was carefully trimmed in the center of the specimen after seating in the chamber so that the internal structure could be viewed with the microscope (Lin and Cerato 2014). While it is not feasible to ensure perfect repeatability of sampled fabric, the compaction procedure has been standardized (e.g., Hussey 2010) to ensure reasonable repeatability between samples. Disturbance due to trimming ESEM specimens was minimal (Lin 2012).

The ESEM equipment used in this study was a ThermoFisher Scientific Quattro S Field-Emission Environmental Scanning Electron Microscope (FE-SEM) with a voltage range of 0.2 to 30 Kv for high vacuum imaging and low-vacuum capability of up to 4000 Pa. Specimens were initially saturated by adjusting relative humidity to 100% at a constant temperature of 2 degrees centigrade and equilibrated for 15 minutes (primary wetting). Samples were dried at discrete points along the primary drying curve (0 MPa, 7 MPa, 35 MPa, 89 MPa, 148 MPa) between 0 MPa (100% RH) and 148 MPa (31% RH) and equilibrated for 15 minutes at each suction. Images were collected along the secondary wetting curve at the same suction values until again reaching 0 MPa.

Micrographs were collected at magnifications of 350X, 800X, and 3500X at each suction value and with the gaseous secondary electron detector (GSED) at 20 kV accelerating voltage in the environmental mode. The 350X magnification provided a broad view of the inter-aggregate space, while the 800X magnification provided a view of the intra-aggregate space. The 3500X magnification provided an analysis of the interparticle level.

4.3.2.2 Fractal Analysis of ESEM Micrographs

Morphological analysis of ESEM micrographs was performed using ImageJ/FIJI, with focus on the box counting fractal dimension and lacunarity. ImageJ is an open-source image analysis software developed by the National Institute of Health (NIH). FIJI (Schindelin et al. 2012) is a release of ImageJ which contains several relevant image processing plugins, specifically fraclac, which contains a suite of fractal analysis, lacunarity, and particle morphology applications (Karperien 2013).

Images were processed first by sharpening the image, then filtering to reduce background noise. To differentiate between solid phase and pore phase, images were converted to binary with black indicating soil surface and white to indicate pore space. Because the contrast within the ESEM device is not constant as chamber humidity changes, a single greyscale threshold was not appropriate for all images and instead was adjusted until soil features were clearly visible in the binary image. For this analysis, bound water was considered as part of the solid phase, while free water was considered as part of the pore phase. Binary images were then cleaned to better distinguish between pore space and particle space (Figure 4.3), revealing a clear fractal branching pattern (e.g., Figure 4.3c).

Surface complexity was analyzed using the box-counting fractal via the fraclac plugin of FIJI. The box counting fractal dimension, $FD_{BC,}$ was calculated for each image according to equation 2. A standard box count was employed, where a grid was overlaid over the binary image and grids containing at least one pixel (ε) of the foreground image (soil phase) were summed ($N(\varepsilon)$). This process was repeated for successively smaller grid sizes to obtain the box counting fractal dimension for each image. Figure 4.4c shows one iterative of this procedure for a Hollywood specimen, with the grids overlaying the soil surface features.

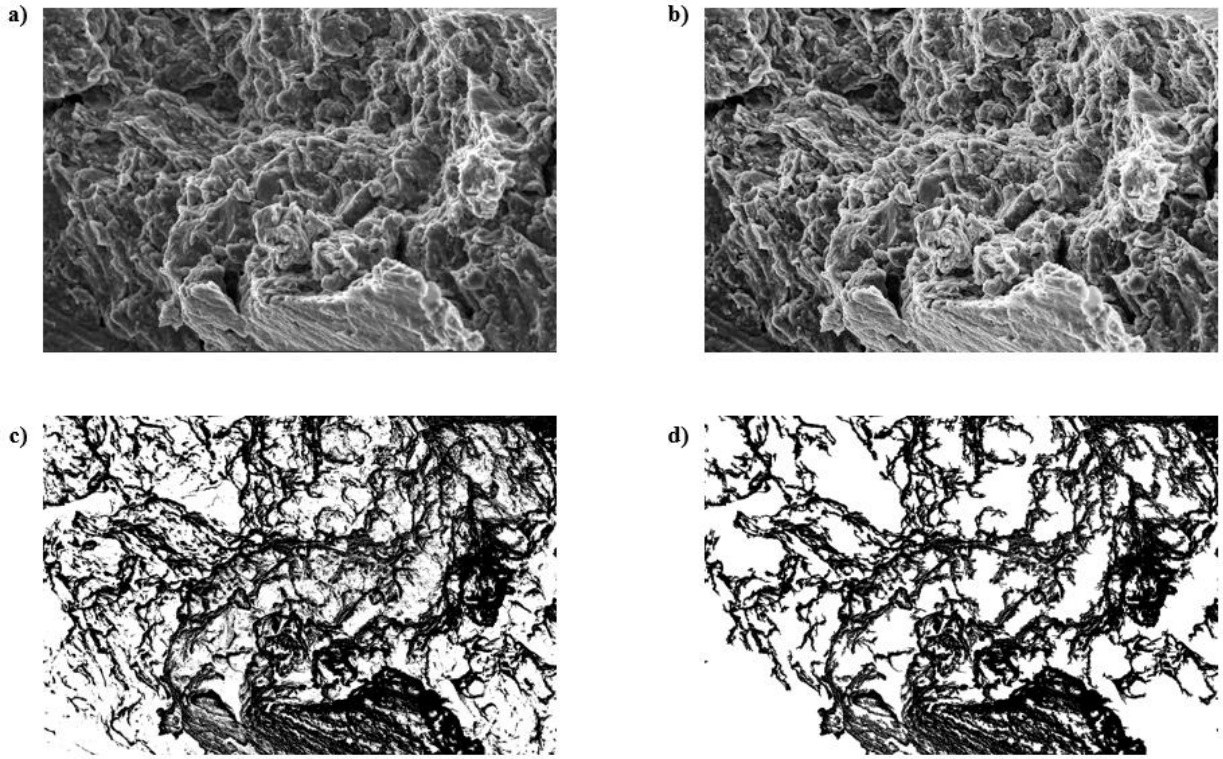

Figure 4.3. Image processing procedure for fractal dimension, lacunarity using FIJI of Carnisaw specimen. a) ESEM micrograph; b) Sharpened, processed image; c) Binary image; and d) Final image.

Lacunarity was assessed similarly to fractal dimension. The same binary images used to determine fractal dimensions were used for lacunarity analyses. The lacunarity was calculated according to pixel density. That is, the distribution of pixels in each ε-sized grid summed in the box-counting procedure was binned, evaluated for mean pixels per grid and standard deviation of pixels per grid, and a lacunarity value was calculated according to equation 3.

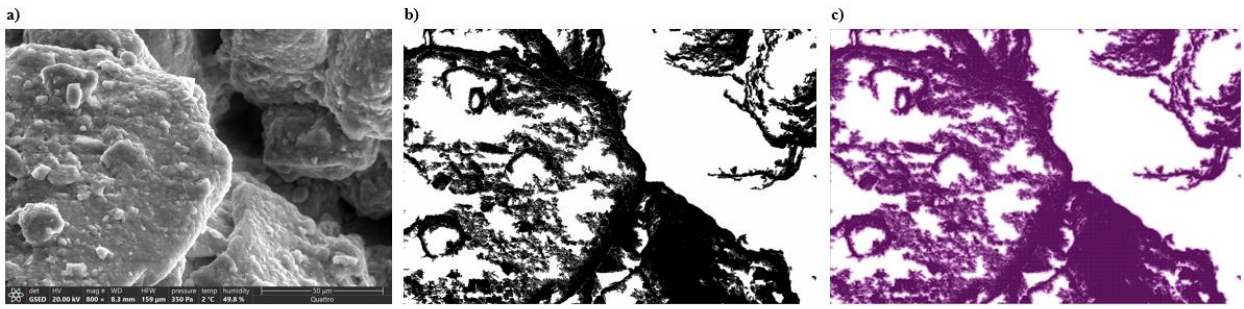

Figure 4.4. Box counting procedure for analysis of ESEM micrographs, Hollywood specimen at 800X magnification, 89 MPa suction: a) Initial ESEM micrograph; b) Binary Image; c) Image overlaid with box counting grid.

4.4 Results and Discussion

4.4.1 Effect of Magnification on Fractal Dimension and Lacunarity

While fractal dimension and lacunarity are scale-invariant properties, in natural stochastically self-similar systems, e.g., soil surfaces, the fractal nature is impacted by the scale of observation. Crawford (1994) described a cutoff length below which fractal scaling is no longer relevant. This is because fractal dimension, particularly the box counting fractal dimension, is a measure of the complexity of a surface. At a certain scale, the complexity of the surface reaches a limiting value and is no longer fractal.

To assess the impact of this trend and determine the scale appropriate for fractal analysis, Na-montmorillonite was imaged at magnifications of 350X, 800X, 3,500X, 7,500X, and 10,000X (Figure 4.5a). The effect of magnification is best detailed using Na-montmorillonite because it does not contain particles of varying mineralogy and it has the smallest average particle size, therefore will cover the greatest range of particle sizes with changes in magnification. At 148 MPa (31% RH), the image was the clearest, with the least impact from bound water on the soil surface.

Fractal dimension showed a piecewise linear trend with magnification, with 3,000X as a transition point. 350X and 800X had similar dimensions, while 3,500X, 7,500X, and 10,000X

images had similar fractal dimensions. With greater magnification, more textural features of the surface are visible in the image, resulting in a higher fractal dimension. At 350X and 800X, more interaggregate pores are visible, and the contribution of the soil surface to the image complexity is diminished (i.e., lower fractal dimensions). This is overall consistent with the results of Sun et al. (2020) for the range of magnifications greater than 1,000X. They noted a decrease in fractal dimension with increasing magnification for Czech bentonite with a constant linear trend, with a total decrease in fractal dimension less than 0.1 between one order of magnitude of magnification, e.g., 10^3X and 10^4X.

Lacunarity decreased linearly as magnification increased (Figure 4.5b). This is because the mass distribution of pore phase decreased with magnification. At 350X, more interaggregate pores were visible, but at 10,000X, soil particles comprised a greater proportion of the image. This resulted in a more homogeneous image, with lacunarity of 0.47 compared to the more heterogeneous image at 350X with a lacunarity of 0.67. This is consistent with Luo and Lin (2009) where lacunarity decreased with finer scale. Conversely, Roy et al (2010) observed an increase in fracture clustering of sandstone sediments as the scale of observation decreased, i.e., lacunarity of fracture patterns increased as the magnification increased. However, the scale of the Roy et al. (2010) study was much coarser than the microfabric observed for the Na-montmorillonite micrographs.

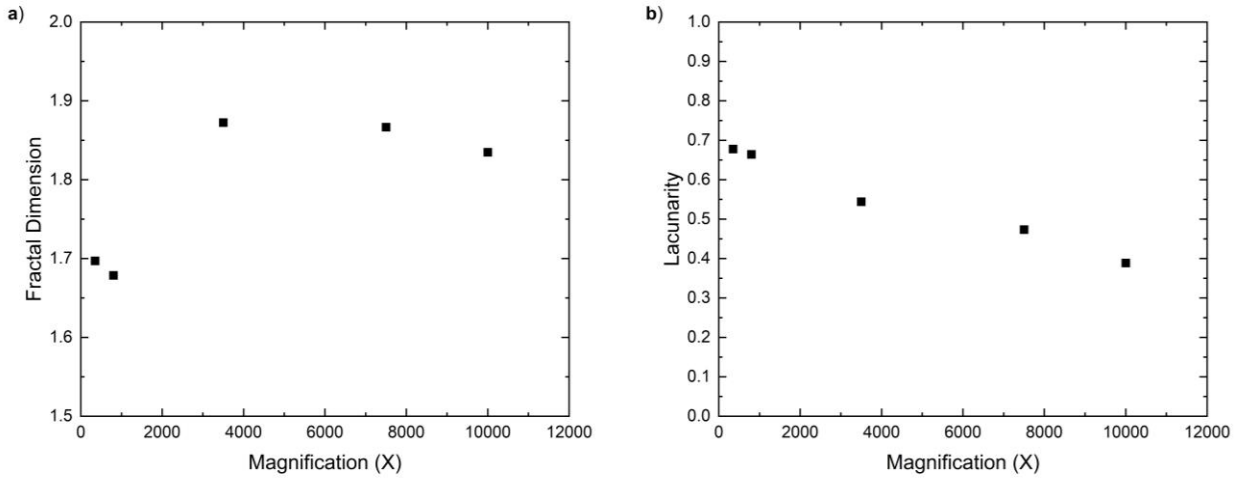

Figure 4.5. Scaling properties of Na-montmorillonite specimen with a) Fractal dimension; b) Lacunarity.

4.4.2 Effect of Suction on Fractal Dimension and Lacunarity

4.4.2.1 Fractal Dimension

The fractal dimensions along the primary drying and secondary wetting suction curves are presented in Figure 4.6 and Table 4.2 for magnifications of 350X, 800X, and 3,500X of each of the studied soils. The fractal dimension showed very little variation in the case of the Kaolinite, Carnisaw, and Heiden opt specimens, through either the drying or the wetting cycles. The fractal dimension of the Kaolinite specimen was the lowest, i.e., below 1.7, indicating low surface complexity. While the fractal dimension of the Carnisaw specimen showed little variation with respect to suction and magnification, there was a slight increase for all specimens between 7 MPa and 35 MPa. As bound water evaporated to equilibrium with the chamber atmosphere, greater surface features were visible.

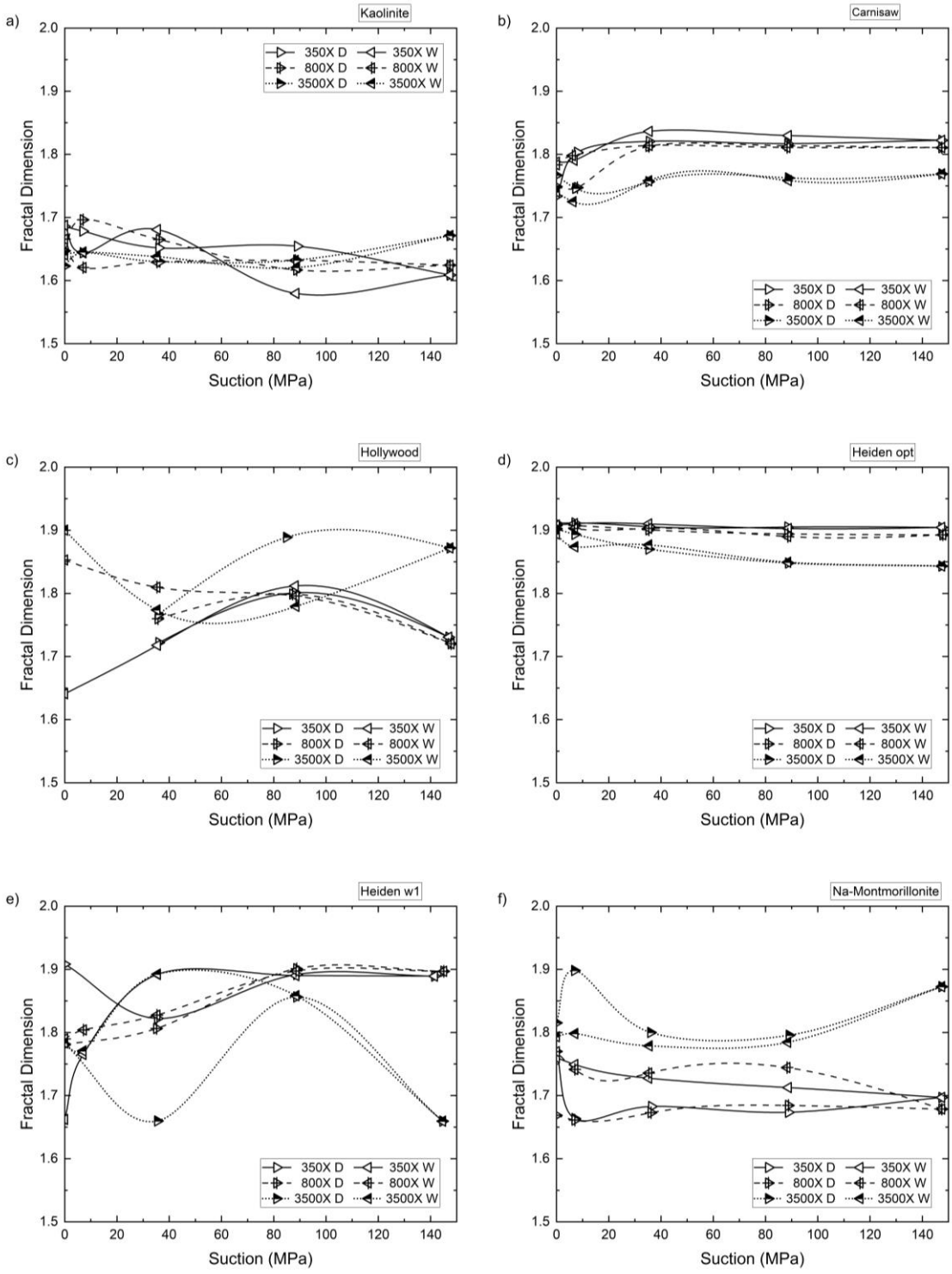

Figure 4.6. Fractal dimension of tested soils along primary drying (D) and secondary wetting (W) suction paths for magnifications of 350X, 800X, and 3500X: a) Kaolinite; b) Carnisaw; c) Hollywood; d) Heiden opt; e) Heiden w1; and f) Na-montmorillonite. (Note: symbols are pointing in the direction of progression along the SWRC)

In the Hollywood soil, the increasing suction caused the void spaces between the particles to increase with increasing pressure, resulting in volumetric changes. However, structural changes were recovered, as evidenced by the lack of hysteretic changes in the fractal dimension. At magnifications of 350X and 800X, the fractal dimension changes, but returns to the same value along the same path, likely as a result of the high silt content in the specimen. Due to the low clay fraction, bound water is unlikely to form along the surface of the Hollywood specimen, and the interpreted fractal dimension changes as a result of free water which rose to the surface under low suction (high humidity), evaporated at high suction (low humidity), and returned on rewetting.

The fractal dimension of the Heiden opt specimen did not change with suction but did show scale dependence between 800X and 3,500X. Similarly, there was little difference between fractal dimensions between the 800X and 350X for Heiden w1, but fractal dimension did change with suction. As suction increased, fractal dimension also increased, indicating an increase in the complexity of the soil surface as features emerged with drying. Hysteretic changes were observed at all scales, most dramatically at 3,500X. While fractal dimensions overall increased along the drying path and decreased along the rewetting path, the fractal dimension was higher on rewetting for suctions between 80 MPa and 0 MPa. Greater structural features emerged as the soil dried, and bound water did not return to obscure these features during the wetting cycle.

Similar hysteretic behavior was observed in the Na-montmorillonite specimen, particularly for images collected at 350X and 800X. However, at 3,500X, the fractal dimension decreased during the rewetting cycle. Moreover, there was no significant difference between the fractal dimensions observed between 350X and 800X at the same suction values, but there was a difference at 3,500X.

Table 4.2. Fractal dimensions of the studied soils

Soil	Magnification (X)	Suction (MPa)								
		Drying					Wetting			
		0	7	35	89	148	89	35	7	0
Kaolinite	350	1.686	1.678	1.652	1.654	1.609	1.580	1.681	1.644	1.688
	800	1.647	1.696	1.665	1.617	1.624	1.632	1.629	1.621	1.666
	3500	1.623	1.644	1.630	1.632	1.671	1.621	1.638	1.645	1.641
Hollywood	350	--ˆ	--	1.722	1.801	1.731	1.812	1.718	--	1.641
	800	--	--	1.760	1.799	1.720	1.796	1.808	--	1.853
	3500	--	--	1.767	1.889	1.872	1.779	1.774	--	1.900
Carnisaw	350	1.734	1.803	1.821	1.817	1.822	1.830	1.836	1.790	1.788
	800	1.749	1.747	1.813	1.814	1.811	1.811	1.814	1.798	1.783
	3500	1.767	1.746	1.757	1.763	1.769	1.758	1.758	1.725	1.740
Heiden opt	350	1.911	1.912	1.906	1.905	1.905	1.903	1.910	1.910	1.908
	800	1.909	1.908	1.901	1.894	1.893	1.890	1.903	1.903	1.908
	3500	1.903	1.893	1.870	1.848	1.843	1.849	1.877	1.874	1.894
Heiden w1	350	1.908	--	1.822	1.892	1.889	1.890	1.892	1.765	1.662
	800	1.781	--	1.806	1.901	1.897	1.897	1.827	1.804	1.790
	3500	--	--	1.660	1.856	1.659	1.858	1.892	1.771	--
Na-montmorillonite	350	1.770	1.664	1.683	1.674	1.697	1.713	1.728	1.749	1.760
	800	1.669	1.661	1.673	1.684	1.679	1.744	1.736	1.741	1.770
	3500	1.815	1.898	1.800	1.796	1.873	1.784	1.779	1.798	1.793

ˆ Not available due to water obscuring image.

4.4.2.2 Lacunarity

The lacunarity results are presented in Figure 4.7 and Table 4.3. The Kaolinite specimen showed little variation in lacunarity throughout both the drying and wetting cycles. Specifically, there was no significant change in lacunarity with suction for images obtained at 800X and 3,500X, but the lacunarity did vary for the 350X micrograph series. While the pore system did appear to expand then contract, the change occurred at the inter-aggregate pore structure.

A small dependence of lacunarity on scale was observed for the Carnisaw specimen. While lacunarity decreased with increasing suction for images obtained at 350X and 800X, lacunarity values were overall the same between the two magnifications. At 3,500X, lacunarity values were higher than those obtained at 350X and 800X and first increased along the drying path and increased along the wetting path.

No hysteretic features were observed for the Hollywood specimen in terms of lacunarity. This is likely due to the high silt content of the soil. At low suctions, free water rose to the surface,

increasing the complexity of the pattern of voids. As suction increased, this free water equilibrated with the chamber atmosphere and the heterogeneity of the surface decreased. As the free water front moved, the original pattern of surface complexity was recovered.

The lacunarity of Heiden opt did not change with suction but did show scale dependence with magnification. As magnification increased, the lacunarity also increased. Interestingly, the lacunarity of Heiden w1 showed evidence of hysteresis with suction, particularly at 350X magnification. As suction increased during the primary drying cycle, the sample surface became more heterogeneous (increasing lacunarity) but during the first rewetting cycle, lacunarity continued to increase. This is evidence of the soil particles aggregating, resulting in volumetric strains at the aggregate-level (i.e., an increase in macropores volume) not recovered with the return of chamber humidity. Na-montmorillonite specimens showed similar hysteretic behavior. At 350X, 800X, and 3,500X magnifications, the lacunarity tended to decrease with increasing suction and decrease on rewetting. However, for each suction increment, the lacunarity on rewetting was lower than the lacunarity on primary drying.

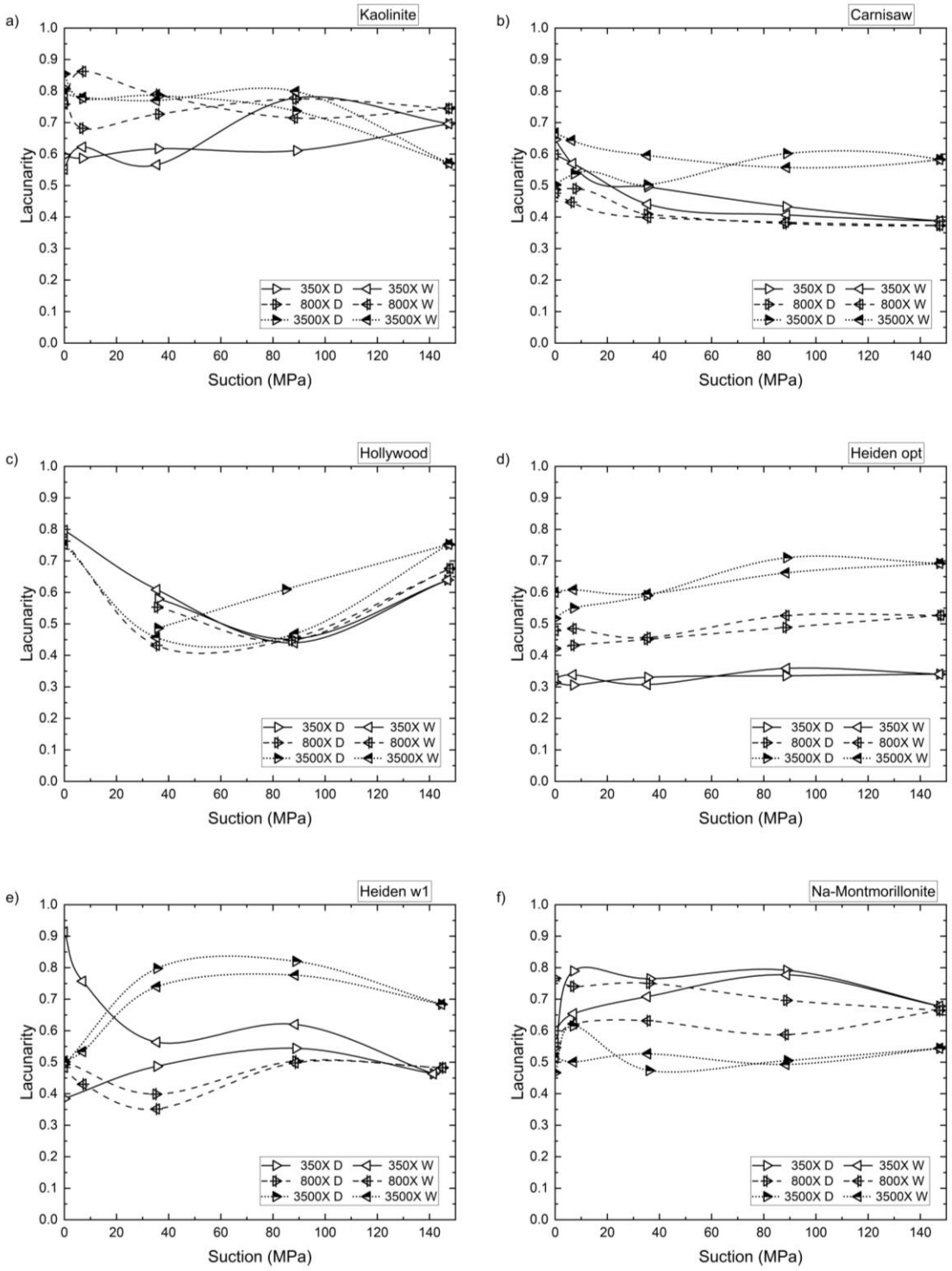

Figure 4.7. Lacunarity of tested soils along primary drying (D) and secondary wetting (W) suction paths at magnifications of 350X, 800X, and 3500X: a) Kaolinite; b) Carnisaw; c) Hollywood; d) Heiden opt; e) Heiden w1; and f) Na-montmorillonite. (Note: Symbols are pointing in the direction of progression along the SWRC)

Table 4.3. Lacunarity of the studied soils

Soil	Magnification (X)	Suction (MPa)								
		Drying					Wetting			
		0	**7**	**35**	**89**	**148**	**89**	**35**	**7**	**0**
Kaolinite	350	0.595	0.587	0.617	0.611	0.696	0.778	0.566	0.622	0.552
	800	0.808	0.682	0.727	0.775	0.745	0.715	0.789	0.862	0.758
	3500	0.855	0.776	0.785	0.736	0.571	0.799	0.770	0.780	0.792
Hollywood	350	-- ˆ	--	0.579	0.452	0.640	0.440	0.609	--	0.797
	800	--	--	0.553	0.448	0.676	0.457	0.432	--	0.763
	3500	--	--	0.487	0.610	0.753	0.469	0.457	--	0.752
Carnisaw	350	0.647	0.554	0.496	0.433	0.388	0.407	0.441	0.570	0.598
	800	0.487	0.490	0.409	0.380	0.373	0.383	0.398	0.447	0.475
	3500	0.503	0.537	0.502	0.602	0.583	0.557	0.596	0.644	0.667
Heiden opt	350	0.315	0.306	0.330	0.335	0.341	0.359	0.307	0.338	0.328
	800	0.422	0.432	0.451	0.489	0.527	0.489	0.451	0.432	0.422
	3500	0.518	0.550	0.590	0.710	0.692	0.662	0.595	0.608	0.600
Heiden w1	350	0.385	--	0.487	0.544	0.463	0.620	0.564	0.757	0.914
	800	0.502	--	0.399	0.504	0.483	0.498	0.352	0.431	0.483
	3500	0.493	--	0.798	0.820	0.684	0.776	0.740	0.534	0.504
Na-montmorillonite	350	0.546	0.790	0.765	0.792	0.678	0.777	0.708	0.654	0.600
	800	0.766	0.741	0.750	0.696	0.664	0.587	0.632	0.622	0.562
	3500	0.467	0.615	0.474	0.505	0.544	0.493	0.527	0.501	0.516

ˆ Not available due to water obscuring image.

4.4.3 Impact of Soil Type and Equilibration Time on Fractal Geometries

Figure 4.8 compares all tested soils at 800X magnification along the primary drying cycle. Notably, while the Na-montmorillonite has the smallest particle size and greatest influence of physicochemical properties, i.e., highest CEC and S_A, the fractal dimension over the entire primary drying suction range is similar to that of the Kaolinite specimen and does not show much variation over the range of suction tested. Therefore, the fractal dimension appears independent of mineralogy and particle size. The natural soils all have a higher fractal dimension, which follows from the greater complexity in the texture of the natural soils than the pure clays, and with the exception of Heiden opt, show a much greater variability with suction than the single-mineral clays.

Based on the differences between the Heiden specimens, equilibration time within the chamber is clearly significant to understanding the structure. The fractal dimension of Heiden opt

effectively did not change during drying, while Heiden w1 and Heiden w2 varied in dimension while drying. For lower suctions (0-7 MPa), the fractal dimension of the three soils was comparable. For suction greater than 89 MPa, Heiden opt and Heiden w1 had similar fractal dimension, while Heiden w2 had lower values, similar to that of the artificial clays. As the Heiden opt and Heiden w1 specimens dried, their features dispersed and similar void patterns emerged. However, for the Heiden w2 specimen, the particles aggregated on drying, resulting in greater void spaces and less pixel density of surface features.

Compared to the single-mineral soils, the natural soils had an overall lower lacunarity (Figure 4.8b) and did not show variation in lacunarity while drying. Because lacunarity is a measure of the heterogeneity of the surface, it is interesting that the single-mineral clays have a less homogeneous pattern of voids than the natural soils. This is likely a feature of the gradation of the soils and associated pattern of void space. Moreover, the single-mineral clays showed greater variation in lacunarity on drying than Hollywood and Carnisaw, particularly for suctions greater than 40MPa. For the single-mineral soils, the pattern of voids became more homogeneous between 0 and 40 MPa, then stabilized to an asymptotic value of pixel density.

Lacunarity is also impacted by equilibration time. The Heiden w2 specimen, which was not allowed to equilibrate between discrete suction points, shows a divergence in lacunarity value from the Heiden opt and Heiden w1 specimens. While Heiden opt and Heiden w1 both gradually increase in lacunarity while drying, Heiden w2 first increases between 7 and 20 MPa, then the specimen gradually decreases in lacunarity until reaching 148 MPa (31% RH). This behavior coincides with the formation of bound water to the soil surface: a film of adsorbed water formed around the Heiden w2 specimen between 0 and 20 MPa and receded for suctions greater than 35

MPa. The bound water caused greater heterogeneity in the image, i.e., wider and increasing pore area between surface features, resulting in higher lacunarity.

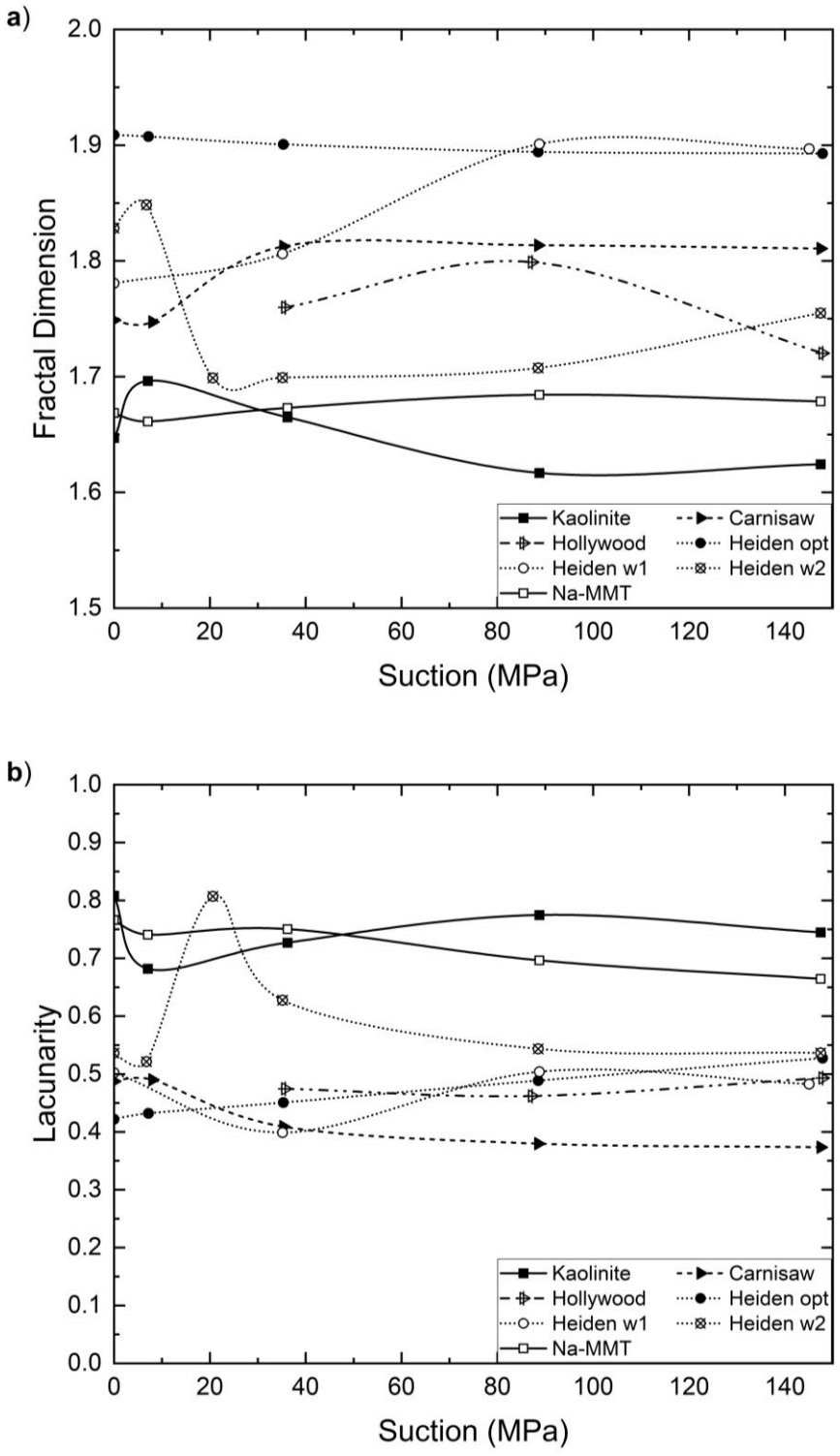

Figure 4.8. Comparison of tested soils at 800X magnification along primary drying cycle: a) Fractal dimension; b) Lacunarity.

4.4.4 Impact of Physicochemical Parameters on Fractal Dimension and Lacunarity

Physicochemical parameters (CEC, S_A) were compared to fractal dimension and lacunarity for a magnification of 800X and suction of 148 MPa (Figure 4.9). There does appear to be a positive correlation ($R^2 = 0.83$) between fractal dimension and cation exchange capacity (Figure 4.9a) with the exception of the Na-montmorillonite and the Carnisaw, to a lesser extent. Similarly, there is a strong positive correlation ($R^2 = 0.94$) between fractal dimension and S_A with the exception of the Na-montmorillonite specimen (Figure 4.9b). The Kaolinite and Na-montmorillonite specimens had similar fractal dimensions (1.6713 and 1.6786 respectively) but varied in CEC and S_A. However, for the natural soils, as both CEC and S_A increased, the fractal dimension also increased. There was a less obvious trend between lacunarity and physicochemical parameters. Again, the Kaolinite and Na-montmorillonite specimens had similar lacunarity but varied widely in CEC and S_A. For the natural soils, the general trend was a decrease in lacunarity with both CEC (Figure 4.9c) and S_A (Figure 4.9d). However, Hollywood and Carnisaw have similar CEC but vary in lacunarity upon drying. It is likely that the silt content of the Hollywood specimen resulted in a more homogeneous specimen when imaged. A similar result is apparent for the Hollywood and Carnisaw specimens when considering the relationship between S_A and lacunarity. This is likely because the single-mineral soils are overall poorly graded and therefore allow more area for voids between particles (higher lacunarity). The natural soils are more well graded, with smaller particles occupying the sub voids between larger particles and therefore less area for voids between particles (lower lacunarity). This is significant because it implies that mineralogy and physicochemical parameters alone cannot characterize microstructural behavior. Instead, these properties work in tandem with geometry to influence fabric changes of expansive soils.

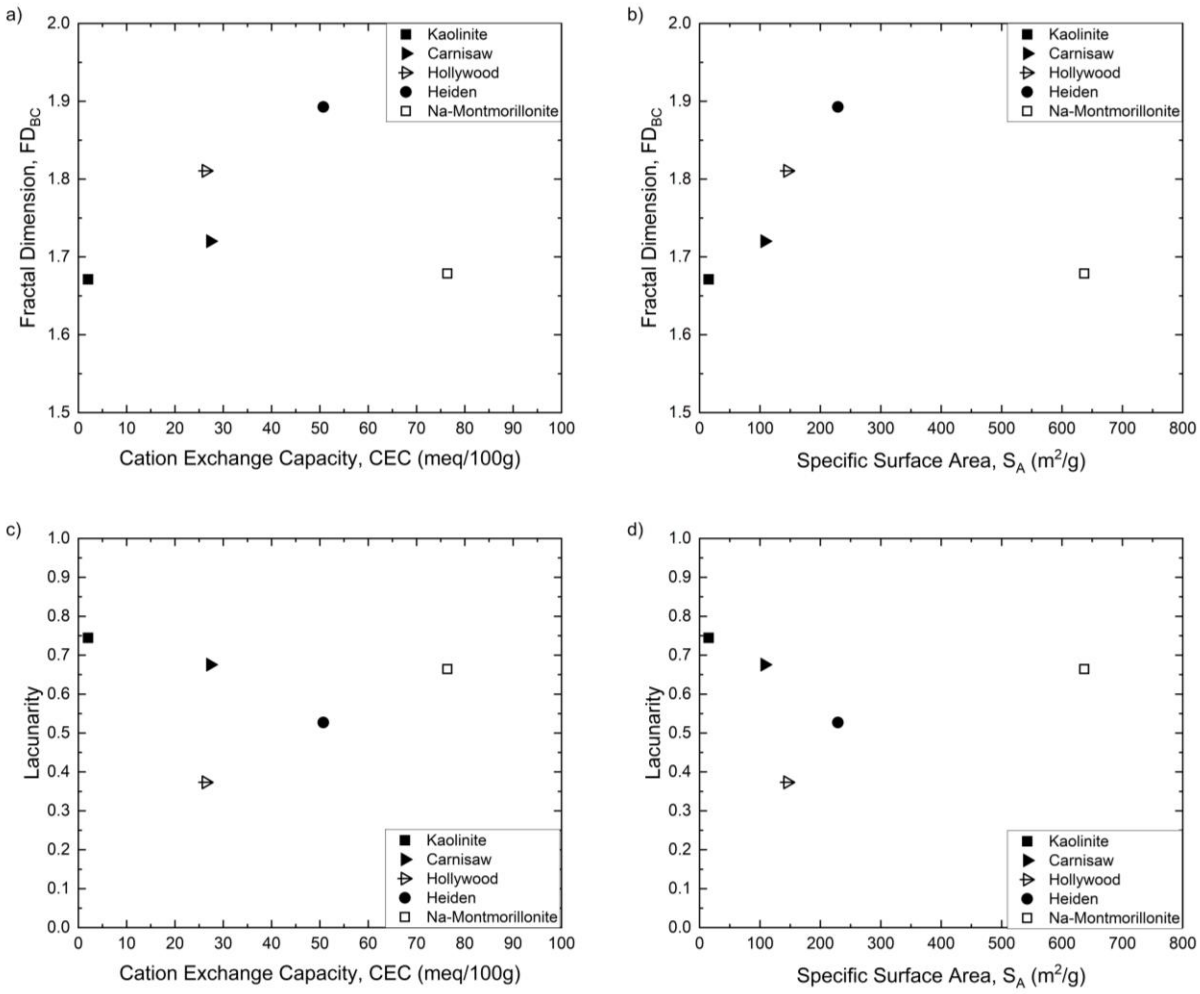

Figure 4.9. Relationship between physicochemical parameters and fractal geometries at 148 MPa and 800X magnification: a) CEC and fractal dimension; b) CEC and lacunarity; c) S_A and fractal dimension; and d) S_A and lacunarity.

4.5 Conclusions

This study compared the evolution of surface complexity of expansive clays with varying mineralogy and physicochemical properties under cycles of hydrologic hysteresis (primary drying and secondary wetting cycles). Variations in physicochemical properties (S_A, CEC), initial moisture conditions (optimal moisture, wet of optimum), and equilibration times (15 minutes, no equilibration) were considered.

The following conclusions were made:

- The interpreted box counting fractal dimension was affected by the scale at which the image was obtained, particularly between 3,500X and 800X magnification. There was a transition point, around 3,000X magnification, for the fractal dimension of Na-montmorillonite. At higher magnifications, more textural features are visible but at lower magnifications more interaggregate pores were visible and the contribution of surface texture diminished. Fractal dimensions obtained at 3,500X tended to be lower for all soils except Hollywood and Na-montmorillonite. Overall, fractal dimensions at 350X and 800X were similar for all soils. There was no statistical difference in fractal dimension obtained for Kaolinite.
- Lacunarity was also affected by the scale. Lacunarity interpreted from micrographs of Na-montmorillonite decreased linearly with increasing magnification. For the natural soils, lacunarity increased with magnification, with the smallest difference between images obtained at 350X and 800X. The trend was the opposite for the single-mineral soils.
- Soils compacted wet of optimum show hysteretic behavior throughout one drying/wetting cycle with respect to surface complexity while soils compacted at optimum conditions do not.
- Single-mineral clays (Kaolinite, Na-montmorillonite) have lower surface complexity (i.e., fractal dimension) than natural clays (Carnisaw, Heiden, Hollywood) but higher lacunarity. Fractal dimension and lacunarity of single-mineral clays seem to be independent of particle size, S_A, and CEC.
- Physicochemical properties and mineralogy alone cannot characterize microstructural changes of expansive soils, as evidenced by the lack of trend between fractal dimension

and physicochemical parameters of the single-mineral clays and natural clay. Instead, geometry of the surface in tandem with these properties characterizes fabric changes with changes in suction.

The fractal dimensions and lacunarity obtained can be used to improve models which attempt to describe aspects of expansive clay behavior in the unsaturated state, particularly relating to changes in pore fluid. Because fractal dimension and lacunarity are obtained from geometric measurements, models which incorporate the fractal dimension remove the unknown component associated with empirically based models.

Chapter 5 Evaluation of Swell Pressures via Modeling Microscale Parameters of Expansive Clays

5.1 Introduction

When expansive soils interact with fluid, the resulting volumetric deformations result in shrinking and swelling of the soil skeleton. Swelling of expansive clays is characterized by an expansion of the interlayer pore area and the interparticle pore area as the clay structure hydrates (Yuan et al. 2016; Pusch 2019). The pressure required to maintain a constant void ratio, i.e., suppress volumetric expansion, as the soil absorbs water is the swell pressure (Drnevich et al. 1986; Arifin et al. 2021; Du et al. 2021). If the surrounding material exerts a pressure less than this swell pressure, the result is volumetric swelling. Factors influencing the swelling ability of soils include the dry density (Cimen et al. 2012; Zou et al. 2018; Keskin et al. 2023), montmorillonite content (Qi and Vanapalli 2015; Mehta and Sachan 2017; Zou et al. 2018; Reddy et al. 2020), and chemical parameters such as cation exchange capacity and surface area (Cimen et al. 2012; Mehta and Sachan 2017; Reddy et al. 2020) in addition to the chemistry of the pore fluid (Karnland et al. 2006; Zou et al. 2018).

This swelling can be beneficial, as the deformation and low hydraulic conductivity associated with expansive clays acts as a barrier for transport of hazardous wastes, e.g., radioactive waste repositories, landfill liners, etc. (Karnland et al. 2006; Sun et al. 2015; Zeng et al. 2019; Watanabe and Tanaka 2023). Notably, smectite soils, e.g., montmorillonite, possess a self-sealing property as the expansion of the soil skeleton fills voids between the clay layer and backfill material (Karnland et al. 2006; Amarasinghe and Anandarajah 2013; Sun et al. 2015). Moreover, the swelling of montmorillonites involves absorption of permeant fluids and a rearrangement of

soil particles, limiting and effectively inhibiting the transport of contaminants in the soil (Sun et al. 2015).

However, volumetric deformation of montmorillonite-bearing soils can also damage lightweight structures if used as a foundation material (Erzin and Gunes 2013). Vertical swell pressures (VSP) cause heave and lateral swell pressures (LSP) can damage retaining walls, basement walls, tunnels, and piles (Liu and Vanapalli 2019; Abdollahi and Vahedifard 2020; Zhang et al. 2020a), even resulting in substantial uplift pressure on pile foundations (Liu and Vanapalli 2019). Mitigation of structural damage due to expansive soils costs billions of dollars annually (e.g., Cimen et al. 2012; Qi and Vanapalli 2015; Goodarzi et al. 2016; Keskin et al. 2023). Therefore, it is necessary to obtain a reliable model to predict swell pressures exerted by these soils (Das et al. 2010; Ezrin and Gunes 2013). Furthermore, the current laboratory techniques, e.g., free swell and swell index tests, to determine swell pressure are time consuming and complex (e.g., Sun et al. 2015; Keskin et al. 2023) and a model which could realistically capture expansive clay behavior is needed (Zou et al. 2018; Khabazian et al. 2018). The current modeling techniques do not account for forces at scales smaller than the macroscale and do not accurately capture realistic swell pressures (Sun et al. 2015; Katti et al. 2015).

The discrete element method (DEM) is a numerical method to analyze problems concerning granular and discontinuous materials such as soils and rock (Rojek et al. 2018). DEM improves upon other continuum methods by modeling dynamic motion and mechanical interactions with fewer parameters, effectively capturing changes in microstructure, deformation, dynamics, and forces (Katti et al. 2009). While most DEM models were created for the analysis of cohesionless materials, there are several available DEM models for clays. Because the very small particle size of clays has been difficult to model due to computational limitations, many models

have considered clays as an aggregate rather than model each individual particle (e.g., Sima et al. 2014; Guo et al. 2017). Other models consider the microscale, interparticle behavior of clays (e.g., Katti et al. 2009; Anandarajah and Amarasinghe 2013; Khabazian et al. 2018), but have yet to reliably predict swell pressure strictly using DEM.

The Bolt (1956) model was the first to incorporate interparticle forces, and others later developed more complex models incorporating clay shape, contact forces, and stiffness (e.g., Jiang et al. 2006; Luding 2008). Jiang et al. (2006) adapted a two-dimensional DEM contact theory of bond rolling resistance into a DEM code to determine the yielding behavior of bonded granulate materials, such as cementitious sands. The model assumes that bonded particles are in contact over a continuously distributed contact width, differing from earlier assumptions that particles are bonded at discrete points. Luding (2008) developed a simplified DEM contact model to simulate the flow behavior of cohesive fine powders by quantifying macroscopic properties, e.g., cohesion, friction, tensile strength, dilatancy, and stiffness, and microscopic properties, e.g., contact adhesion and friction. Inputs include a relative velocity parameter, stiffness parameters, friction coefficient parameters, and viscosity parameters to obtain force as a function of the accumulated particle contact deformations. The results of the model were compared to experimental results obtained from uniaxial, strain-controlled tension testing on loose (relative density less than 45 percent) powder (maximum grain size less than 2 microns) samples. The model simulates a cohesive, fine powder, and can be adapted to clays using more realistic particle-contact parameters, particularly the polar, double-diffuse layer surrounding clay particles.

DEM has been used to analyze shrinkage and desiccation cracking of soils using mesoscale parameters and aggregate-level discretization (e.g., Sima et al. 2014; Guo et al. 2017). Sima et al. (2014) utilized a three-dimensional DEM model, simulating clay particles as a collection of

aggregates connected through cohesive physicochemical and mechanical bonds. To simplify computation, aggregate geometry was modeled as a series of spherical grains rather than stacks of platy composites. Shrinkage was modeled using relationships between grain size, water content, and drying time. Soil suction was modeled using contact stiffness and tensile strength parameters. Guo et al. (2017) used DEM to study the effect of water content and particle size on shrinkage and desiccation cracking of expansive clays. The model focuses on mesoscale parameters, i.e., shear and tensile strength, compression modulus, temperature, and Poisson's ratio, circumventing the need for microscale parameters such as mineralogy, suction, and interparticle forces. To simplify computations, soil is regarded as a medium consisting of aggregates separated by interaggregate pore spaces, simulated using discrete polygonal-shaped blocks. Contact parameters including particle stiffness, bond strength, and the frictional coefficient were determined through empirical correlations with unconfined compression testing (UCT) of bentonite specimens at varying water contents. The model was able to replicate the generation and pattern of cracking for both major and minor desiccation cracks.

Katti et al. (2009) used DEM to study the mechanism of swelling for Na-montmorillonite specimens. The model uses microscale parameters, i.e., the double-layer force, van der Waals force, surface charge density, and cation exchange capacity, along with macroscale parameters, i.e., gravity and mechanical forces, to characterize the macroscale behavior of expansive clays. Swell pressures established through the DEM model were verified using a controlled uniaxial swelling device (CUS) on saturated samples of Na-montmorillonite under constant volume conditions and SEM analysis of the structure was performed at each stage of swelling. The model was able to simulate up to 1200 cuboid particles. Using DEM simulations, they found that interlayer forces between water molecules and clay sheets cause the deformations that are

responsible for structural deformations which characterize swelling. Additionally, they found a threshold particle spacing which contributes to swelling. Beyond this threshold spacing, particle subdivisions (i.e., division of larger agglomerates into smaller sub-particles when water enters the clay interlayer space) occur, increasing interparticle interactions which increase the magnitude of swelling.

Khabazian et al. (2018) used DEM to investigate volumetric changes in soils containing mixtures of montmorillonite and kaolinite. The model considers physiochemical forces between particles during consolidation testing for both flexible and nonflexible elements to analyze the interparticle forces, deformations, and bending deflection of individual elements. The elemental composition and fabric structure were determined using Scanning Electron Microscopy (SEM) and X-Ray Diffraction (XRD). Particle deflection was verified using SEM imaging taken during consolidation testing. The model results of consolidation pressures with different proportions of kaolinite and montmorillonite were verified against laboratory compression tests on the specimens of varying mineral compositions. Simulations with flexible particles more closely correlated to laboratory compression results than simulations using rigid particles, particularly at high consolidation pressures.

Bayesteh and Hoseini (2021) established a two-dimensional DEM model to study the reorientation of montmorillonite, kaolinite, and illite particles during swelling. The code improves on the work of Beyesteh and Mirghasemi (2013), which uses the double-layer repulsive force and mechanical contact parameters to simulate consolidation behavior of montmorillonites. The 2021 model incorporates the van der Waals attractive force, mineral composition, and pore fluid chemistry to simulate swelling and sedimentation. Model results were verified against laboratory oedometer and sedimentation tests. Overall, there was good agreement between DEM simulations

and the results of laboratory experimentation. DEM results revealed that the double-layer repulsive force, along with number of double-layer contacts and particle weight controlled particle reorientation. Additionally, montmorillonite particles reoriented in a dispersed structure under high swelling pressures and a flocculated structure under low swell pressures.

Anandarajah (1994) developed a two-dimensional DEM program (DEMClay) to simulate the molecular physics of clay particles, particularly interparticle forces and changes in soil fabric. Clays are modeled as cuboidal rods with the ability to bend, achieved by dividing particles into sequences of discrete elements. Interparticle contacts are defined as interaction between discrete elements at a number of points and intraparticle contact is defined as the interaction between discrete elements at a single connection point. Rotations are allowed at element connection points. Loading consists of boundary loading at interparticle contacts, gravity loading, and van der Waals and double and interlayer forces. Inter- and intraparticle mechanical forces are simulated at particle contacts or when distance between particles is within a specified tolerance, i.e., particle and double layer spacing. The model assumes interparticle contacts are not capable of carrying moment or tensile force. Physicochemical forces are simulated as electrostatic forces between particles, the summation of the double layer, van der Waals, and interlayer forces. The model was improved by Anandarajah and Amarasinghe (2013) to study the swelling of Na-montmorillonite. The model was adapted to incorporate layer spacing in addition to particle spacing through the results of molecular dynamics studies relating interlayer pressure to particle separation distance (Amarasinghe and Anandarajah 2013). Particles are modeled as thin rectangular blocks placed at random orientation and location within a sample assembly and compressed with mechanical and interparticle forces. Constant-volume swelling is simulated by initiating all interparticle forces and moving the horizontal walls inward.

Attention has also been directed toward molecular dynamics (MD) models to predict swell pressures of expansive clays. MD models improve on studies performed using Monte-Carlo simulations by modeling the time-dependent processes of interlayer hydration unable to be captured using solely Monte-Carlo techniques (Amarasinghe and Anandarajah 2013; Shankar 2019). Amarasinghe and Anandarajah (2013) used a MD model to assess the force-displacement relationship associated with particle separation distances in swelling montmorillonites. They discovered that at small particle separation distances, cation concentration diverges from that predicted by double layer theory but for moderate to large particle separations, the double layer theory holds. Katti et al. (2015) used MD simulations to evaluate the mechanism of crystalline swelling in sodium montmorillonite. van der Waals forces and d-spacing, as well as cation attraction, controlled the attraction of water molecules into the interlayer space, thereby controlling crystalline swelling. Du et al. (2021) combined double layer theory into an MD model to determine the effect of potential energy and the van der Waals force on swell pressure of sodium montmorillonite. Montmorillonite content in the model was represented by differing values of CEC. Yang et al. (2021) used MD simulations to predict the swelling pressure of bentonite at a range of temperatures and fluid pressure. The force from hydration and the double layer force were found to control the swell pressure in distilled water for d-spacings between 1.6 and 2.6 nm. While MD simulations provide valuable insight into the atomic structure and phenomena of clay expansion, there is a large computational cost associated with the use of molecular dynamics models and simulation sizes are confined to the atomic level (Amarasinghe and Anandarajah 2013). Therefore, results of MD can be utilized to better develop larger scale models such as DEM.

Models utilizing artificial intelligence (AI) have also been utilized to predict the swell pressure and swell potential of expansive soils. Das et al. (2010) created a model to predict swell

pressure using an artificial neural network (ANN) using natural moisture content, dry density, liquid limit, plasticity index, and clay fraction. However, the model does not account for the physicochemical parameters such as CEC and S_A. Jalal et al. (2023) used a genetic algorithm (GA) to produce gene expression programming (GEP) and multigene expression programming (MEP) models for the prediction of swell pressure. Inputs included plasticity, clay fraction, water content, dry density, and specific gravity, but did not include microscale parameters.

This research adapts Anandarajah's (1994) DEMClay program to consider realistic, natural clays and provide swell pressure based on modeled soil fabric, pore fluid parameters, and physicochemical forces. Microscale parameters, i.e., CEC, S_A, and Hamaker constant, can be used to model these microscale forces, accurately predicting macroscale engineering behavior, e.g., swell pressure. A sensitivity study was performed to determine the most influential input parameters and then the DEMClay model was calibrated with pure montmorillonite experimental swell pressure results at various void ratios. After the calibration, the DEMClay model was successfully validated by accurately predicting the swell pressures of several natural montmorillonite-bearing soils.

5.2 Microscale Forces Associated with Expansive Clays

Macrolevel behavior, e.g., shrink and swell phenomena, of fine-grained soils is controlled by physicochemical forces at the microscopic, i.e., interparticle and interlayer level. While interparticle forces between coarse-grained materials, i.e., silts, sands, and gravels, are governed only by mechanical interactions, i.e., normal, shear, and bending forces, interparticle interactions between clays involve both the mechanical forces in addition to physicochemical forces, i.e., van der Waals attractive and double-layer and interlayer repulsive forces (Anandarajah and

Amarasinghe 2011). Together, these forces alter the soil fabric (Likos and Lu 2004), resulting in changes to the volume, permeability, and strength of the soil.

Generally, physicochemical forces include the double layer repulsive force and the van der Waals attractive force. When pore fluid is absent, e.g., an assembly of dry powders, the double layer force is absent (Anandarajah and Amarasinghe 2012). Attraction between assemblies is governed by the van der Waals force and repulsion is governed by the double layer and interlayer (mechanical) forces (Anandarajah and Amarasinghe 2012). The van der Waals force is a weak electrostatic force which develops between particles arising from shifts in the electron shell causing polarity in the atom or molecule, resulting in further polarization in adjacent particles (Keil and Mayer 2014). The van der Waals force diminishes with sufficient distance between particles, described by the Hamaker constant (Hamaker 1937; Anandarajah 2000; Faure et al. 2011). The double layer force develops in response to changes in electrical charge along the particle surface, quantified by the surface electrical potential or surface charge density. When the soil interacts with pore fluid, ions are redistributed and a gradient in electrical potential develops, forming a thin, diffuse, layer of adsorbed cations surrounded by a layer of electroneutral ions, or the diffuse double layer. Electrostatic forces between double layers allows the development of repulsive forces between particles (Hensen and Smit 2002; Yao and Anandarajah 2003; Mojid 2011).

While the double layer force describes repulsion between particles, the interlayer force describes repulsion between layers with occur at small particle separations. As the distance between layers decreases, the mechanism of swelling is dominated by the interlayer repulsive force rather than the double layer repulsive force (Anandarajah and Amarasinghe 2013). The interlayer is the gap between assemblages of octahedral and tetrahedral units, i.e., layers. When water is transported into the interlayer space, increasing numbers of hydrating layers are intercalated in the

space between the 2:1 sheets and the basal spacing increases, resulting in swelling (Karnland et al. 2006; Laird 2006; Cygan et al. 2009). The magnitude of the interlayer force is much larger than the double layer force, up to 100 times larger at similar separation distances (Van Olphen 1977; Anandarajah and Amarasinghe 2013) but decreases to zero at sufficient layer separations.

Volumetric deformations associated with shrinking and swelling of expansive soils are controlled by microscale parameters, specifically montmorillonite content, cation exchange capacity, and specific surface area (Mehta and Sachan 2017; Reddy et al. 2020). The mechanism of swelling is controlled by the dominant microlevel force: interlayer forces produce crystalline swelling and double layer forces result in osmotic swelling (Anandarajah and Amarasinghe 2013). When fluid enters the pores of an initially dry soil, a double layer develops between particles, creating a repulsive force between them. Consequently, fabric changes cause positive volumetric change, or osmotic swelling. When water molecules enter the interlayer space, they produce additional repulsive forces, resulting in crystalline swelling. The controlling factor for the dominant swelling mechanism is the particle separation: for large separations, the electrostatic forces govern behavior (osmotic swelling), while for small separations, crystalline swelling dominates (Anandarajah and Amarasinghe 2013).

5.3 DEMClay

The DEMClay program used in this study utilizes code adapted from Anandarajah (1994). The program was implemented using Intel one API Fortran compiler and the graphical interface was built using Microsoft Visual Studio. Particle assemblies created via DEM were used to simulate one-dimensional swell tests.

The code uses physicochemical and geometric parameters to generate a particle assembly of two-dimensional plate-like particles modeled from a number of discrete elements. Particle interactions are simulated through mechanical contact forces, van der Waals attractive forces, and double layer and interlayer repulsive forces. An overview of the code architecture is detailed in schematic form in Figure 5.1.

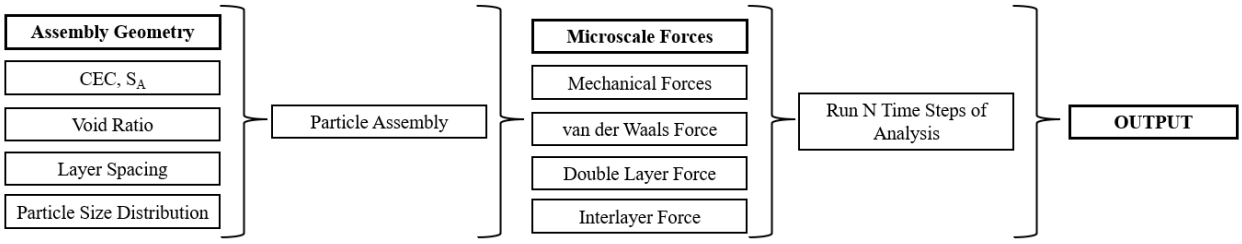

Figure 5.1 Architecture of DEMClay

5.3.1 Parameters Defining the Assembly

5.3.1.1 Defining dimensions of assembly area

The particle assembly is defined by the walls bounding the specimen and the size of the wall assembly defines the maximum dimensions of the specimen. Walls are rigid boundaries that can be subjected to rigid body displacements but not rotations. Wall coordinates are defined in a counterclockwise manner beginning with the south-west corner. Since walls are expected to move, both with consolidation and swelling, an outer buffer is maintained at least 10% larger than the inner box dimensions. For example, a 1.5 μm x 1.5 μm sample requires a sample box 1.8 μm x 1.8 μm (Figure 5.2)

The size of the wall assembly, along with the number of discrete elements chosen, will mainly affect the void ratio. For the same number of discrete elements, a large assembly area will result in a higher void ratio (less dense specimen) and a smaller assembly area results in a lower

void ratio (more dense specimen). Differences in horizontal swell pressures were analyzed for differing assembly geometries.

Three different assembly dimensions were considered in this analysis: (1) a typical oedometer assembly with 1:3 height to width ratio (Figure 5.2), (2) a square assembly with 1:1 height to width ratio (Figure 5.3), and (3) a typical triaxial assembly with 3:1 height to width ratio (Figure 5.4).

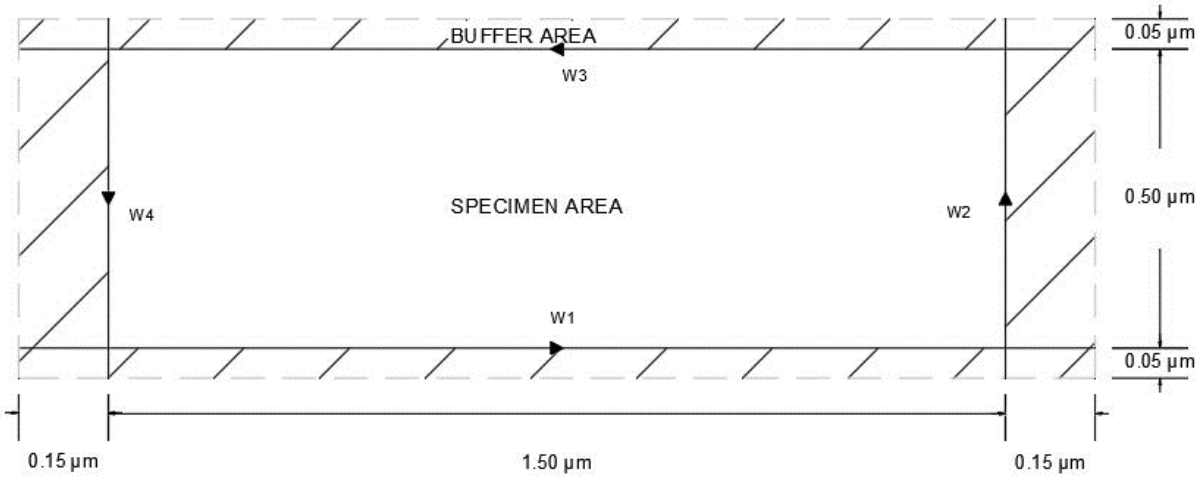

Figure 5.2. Schematic of DEM Assembly with a 1:3 height to width ratio

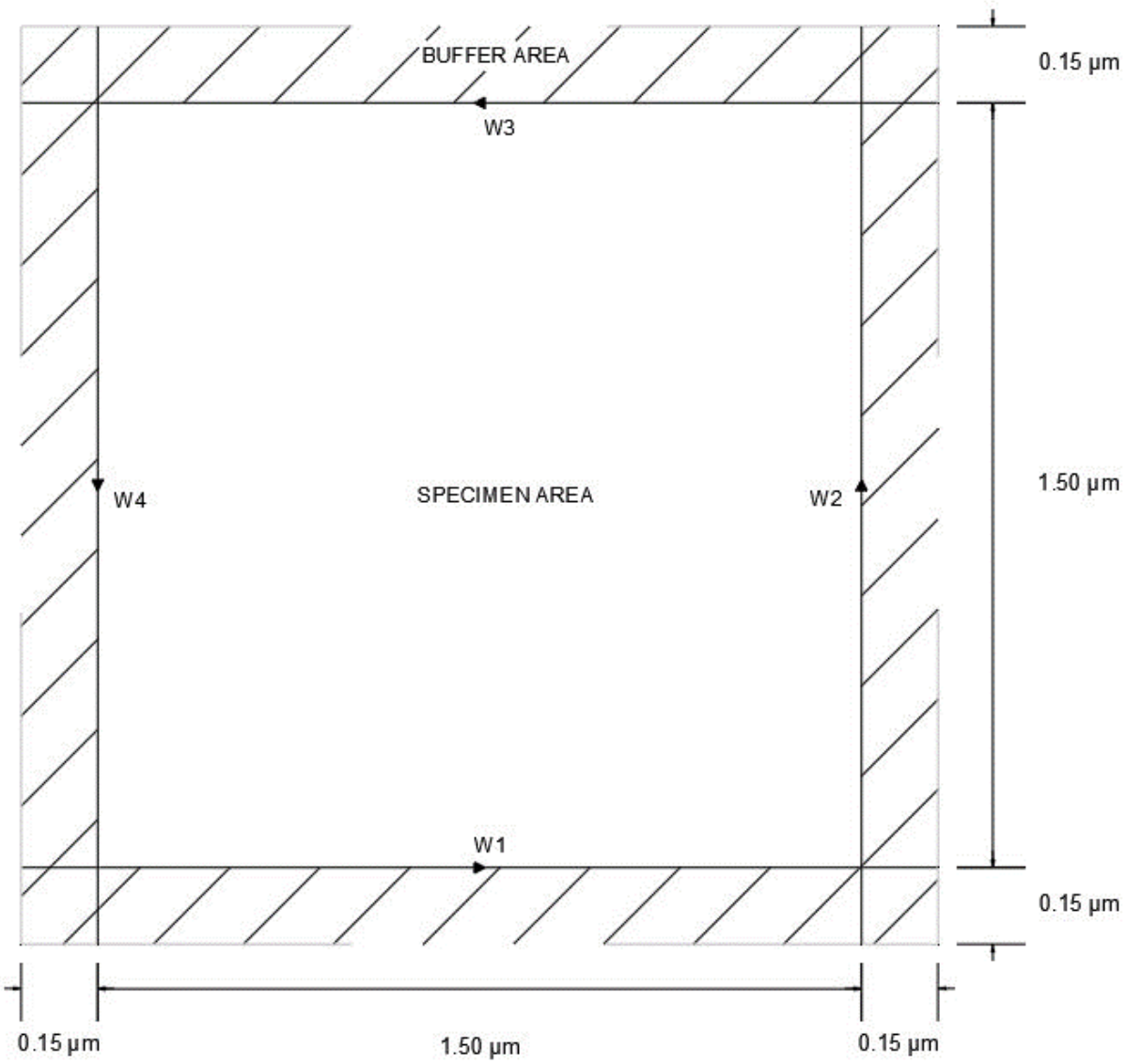

Figure 5.3. Schematic of DEM Assembly with a 1:1 height to width ratio

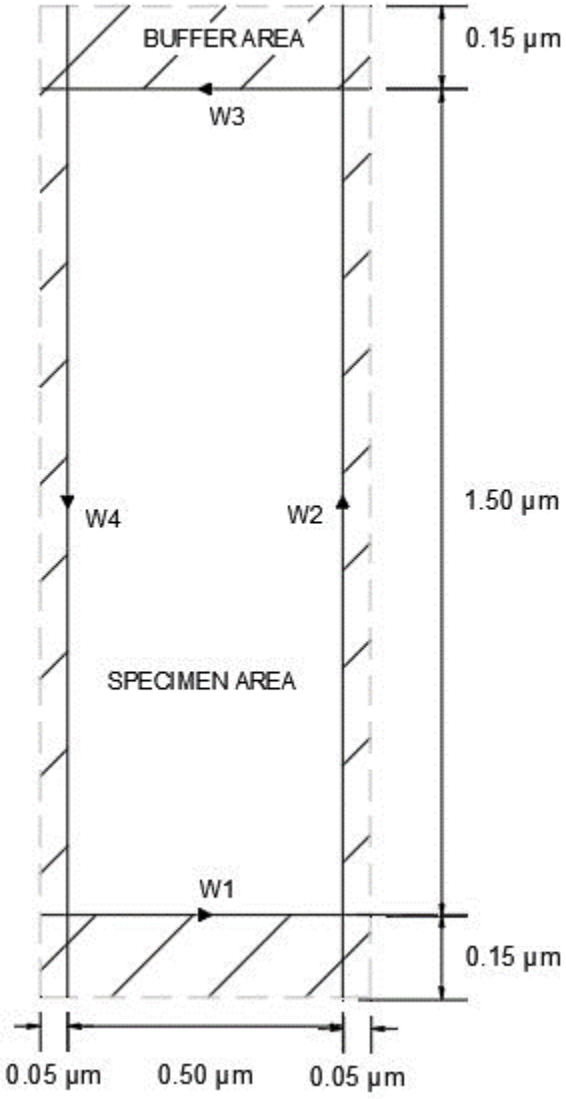

Figure 5.4. Schematic of DEM Assembly with a 3:1 height to width ratio

5.3.1.2 Defining number and size of particles:

The particle assembly is defined by the number of discrete elements, size of discrete elements, and particle and layer spacing. The number and size of discrete elements affects the void ratio of the assembly. Particles are created from discrete elements: the minimum number of discrete elements making up one particle is one, i.e., particle size cannot be smaller than the size of a discrete

element. Consequently, the size of a discrete element is equivalent to the minimum particle size and the maximum particle size is a multiple of the discrete element length (L_{DEM}).

In order to create a realistic soil sample, a grain size distribution histogram is needed. For example, for the montmorillonite sample used to calibrate the model, particles were modeled with a minimum length of 25 nm and a maximum length of 100 nm. The Na-montmorillonite particle size distribution included histogram bins of 10% between 75 and 100 nm, 50% between 50 and 75 nm, and 40% between 25 and 50 nm.

Assemblies are defined first at the particle-scale to analyze the effects of interparticle forces and later discretized into layer-scale to assess the effects of interlayer forces. In the particle assembly, a particle is formed from multiple layers and their associated interlayer spacings, detailed in schematic form in Figure 5.5. The thickness of a single layer of a montmorillonite mineral, including two tetrahedral units and one octahedral unit, is 0.656 nm (Anandarajah and Amarasinghe 2013), while the basal spacing, i.e., the thickness of a single layer and the interlayer separation distance, is generally 1 nm in the dry, or collapsed, state (Van Olphen 1977; Karnland et al. 2006; Katti et al. 2009; Anandarajah and Amarasinghe 2013; Pusch 2019), also commonly referred to as the d-spacing ($d_{(001)}$) because it is calculated from the (001) harmonics of XRD (Katti et al. 2009). The layer spacing (d) is determined according to:

$$d = \frac{2000}{G_S \cdot S_A} \quad [1]$$

where G_S is the specific gravity of the clay particle and S_A is the specific surface area (Anandarajah 2000). The layer spacings of the studied soils are presented in Table 5.1. The specific gravity of each soil was assumed to be the same regardless of particle size, and therefore the G_S obtained via pycnometer testing was used for this study. The actual, measured layer spacing can differ from

idealized, theoretical values due to differences in packing arrangements of interlayer water molecules or interstratification of layers of hydrates (Laird 2006).

Table 5.1. Layer spacing of the studied soils

Soil	G_S	S_A (m^2/g)	Layer spacing (nm)
Na-montmorillonite	2.70	637.0	1.16
Heiden	2.77	229.0	3.15
Hollywood	2.78	145.5	4.94
Carnisaw	2.77	107.5	6.72

While the layer spacing of the Na-montmorillonite is relatively close to that reported in the literature, the layer spacing of the Carnisaw soil is nearly one order of magnitude higher than the rest of the studied soils. This follows from the significantly lower specific surface area of the Carnisaw compared to the other expansive soils. Moreover, it follows that the natural soils would have larger spacing between layers due to their larger relative sizes.

The interlayer thickness (δ) is then determined from the layer spacing (d) by assuming 0.656 nm for the layer (2:1) thickness and simply subtracting the sheet thickness from the total spacing (Table 5.2). Particle thickness is determined assuming 5 layers per particle (Figure 5.5), but allowing a maximum of 7 layers, according to the following relation:

$$H_{DEM} = (N \cdot d) \cdot \big((N-1) \cdot \delta\big) \quad [2]$$

where H_{DEM} is the particle thickness as well as the thickness of a discrete element, N is the number of layers per clay particle, d is the layer spacing, and δ is the interlayer separation thickness.

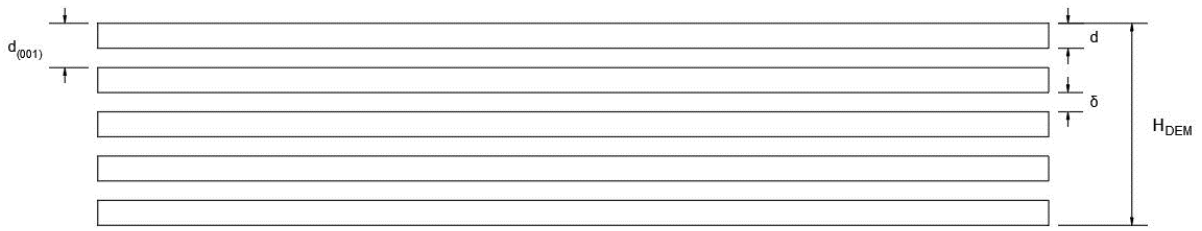

Figure 5.5. Schematic of Na-montmorillonite particle

Table 5.2. Discrete element thickness (H_{DEM}) for the studied soils

Soil	d (nm)	δ (nm)	H_{DEM} (nm)
Na-montmorillonite	1.16	0.51	5.31
Heiden	3.15	2.50	13.27
Hollywood	4.94	4.29	20.43
Carnisaw	6.72	14.54	28.37

5.3.2 Parameters Defining Forces

While the cation exchange capacity (CEC) and specific surface area (S_A) are not direct inputs into the code, they are the primary physicochemical parameters which impact the outputs of the analysis. Specifically, CEC and S_A affect the surface potential and interparticle and interlayer spacing. Therefore, as these physicochemical parameters are intrinsic soil properties, they are used to differentiate between different soils used in DEMClay.

The following relation has been adopted for the surface potential:

$$\psi_0 = 0.08614 \cdot \left(\frac{T \cdot 2sinh^{-1}\left(\frac{290000\frac{CEC}{S_A}}{230\sqrt{n \cdot \varepsilon \cdot T}}\right)}{v} \right) \quad [3]$$

where ψ_0 is the surface potential (mV) T is the temperature (Kelvin), CEC is the cation exchange capacity (meq/100g), S_A is the specific surface area (m^2/g), n is the electrolyte concentration of the

pore fluid (mol/L), ε is the dielectric constant of the pore fluid, and v is the cation valence. The pore fluid parameters are presented in Table 5.3. The surface potential for each of the studied soils is presented in Table 5.4.

Table 5.3. Pore fluid parameters

Pore Fluid	T (K)	n (mol/L)	ε	v
Distilled Water	293	0.04	80.0	1.0

Table 5.4. Surface potential of the studied soils

Soil	S_A (m^2/g)	CEC (meq/100g)	Ψ_0 (mv)
Na-montmorillonite	637.0	76.4	116
Heiden	229.0	50.7	219
Hollywood	145.5	26.4	210
Carnisaw	107.5	27.3	226

5.3.2.1 Mechanical Forces

Mechanical forces on clay particles include intraparticle bending, and interparticle shear and normal forces. Mechanical forces occur when two particles cross within a pre-defined separation distance.

Clay particles are modeled as thin, one-dimensional rods comprised of a number of discrete elements. While cohesionless soils tend to be bulky, clays are platelike, with length several orders of magnitude larger than the width (Anandarajah 1994). Each discrete element is a rigid body and bending deformation occurs at the junction of two discrete elements, modeled as element rotation. That is, elements are rigid, but particles are deformable. Particle breakage is not considered in this study.

Interparticle normal and shear forces comprise the mechanical forces between particles. Particles are assigned a normal and shear stiffness as well as contact cohesion and friction parameters. The normal force is given by:

$$F_n = \frac{A \cdot E}{L_{DEM}} \cdot u_n \quad [4]$$

where F_n is the normal force, A is the cross-sectional area of the discrete element, E is Young's modulus, I is the second moment of inertia of the discrete element, L_{DEM} is the length of a discrete element, and u_n is the displacement in the normal direction (after Anandarajah 2000).

Normal forces are modeled as nonlinear elastic, with compressive forces positive and the normal stiffness coefficient (k_n) given by:

$$k_n = 100 \cdot E \cdot \frac{H_{DEM}}{L_{DEM}} \quad [59]$$

where E is Young's modulus, H_{DEM} is the thickness of a discrete element, and L_{DEM} is the length of a discrete element. A value of 0.003 N/μm used for Young's Modulus in this study. The normal force is related to the stiffness coefficient by

$$F_n = k_n \cdot u_n \quad [6]$$

Shear forces are modeled as elastic, perfectly plastic with a shear stiffness coefficient (k_s) given by:

$$k_s = 0.5 \cdot k_n \quad [7]$$

The shear force is related to the shear stiffness by:

$$F_s = k_s \cdot u_s \quad [8]$$

Normal and shear forces are related by Mohr-Coulomb condition:

$$F_S = F_n \tan\phi \quad [9]$$

where F_S is the shear force, F_n is the normal force, and ϕ is the interparticle friction angle. Interparticle cohesion is assumed to be zero for the mechanical force contribution. This study adopts an interparticle friction angle of 20 degrees (Anandarajah and Amarasinghe 2013).

5.3.2.2 Interparticle Forces

Interparticle interactions are dominated by mechanical forces, the van der Waals force, and the interparticle repulsive force. The solution for the double layer repulsive force with increasing separation distance between two particles was solved using finite difference method by Anandarajah and Chen (1994) for the effect of particle orientation and in general by Chen and Anandarajah (1993). Surface potential, physicochemical parameters, and interparticle geometry, e.g., rotation and separation distance, showed the greatest impact on the interparticle repulsive force.

The interparticle repulsive force then is governed by double layer repulsions arising from pore fluid chemistry and interparticle geometry. The double layer thickness is calculated assuming all soils have similar pore fluid at the same temperature. The thickness of the double layer (Debye length) is given by

$$\left(\frac{1}{K}\right) = \sqrt{\frac{\varepsilon kT}{8\pi n v^2 e^2}} \qquad [10]$$

where *(1/K)* is the thickness of the double layer, ε is the dielectric constant of the fluid, k is the Boltzmann constant (1.380649 x 10^{-23}), T is the temperature (Kelvin), n is the ion concentration of the pore fluid (mol/L), v is the cation valence, and e is the electron charge.

5.3.2.3 Interlayer Forces

This model has the capability of simulating interlayer force in addition to interparticle force. The interlayer attractive force is dominated by the van der Waals attractive force. The van der Waals

force is a function of the Hamaker constant (A) and the geometry between layers, specifically the overlapping length of a pair of layers (parallel or perpendicular), minimum separation distance between layers, the angle between layers, and the layer thickness (Anandarajah and Chen 1997). The Hamaker constant adopted in this study is 0.87 x 10^{-20} J (Chen and Anandarajah 1996; Anandarajah and Amarasinghe 2013).

The interlayer forces are simulated by discretizing the particle assembly into layers. For the Swy Na-montmorillonite used in this study, the maximum number of layers used was 7 and across the particle assembly, the average number of layers per particle was 5. While discretizing each particle into layers provides a more accurate account of all microscale forces, the computational time is exponentially larger than running the model at the interparticle force level. Therefore, the calibration and validation of the model is presented at the interparticle force level.

The interlayer repulsive force is a function of the physicochemical parameters of the soil, the surface potential (ψ_0), chemistry of the pore fluid, the thickness of the double layer, and the geometry and orientation of particles (Anandarajah and Chen 1994). Simulations using molecular dynamics determined the cutoff distance for which the van der Waals force was constant, and the interlayer repulsive force controlled the net force (Amarasinghe and Anandarajah 2013).

5.3.2.4 Damping Forces

Because the DEM analysis is dynamic, both global and local (contact) damping are employed. Global damping is visco-elastic, where the damping force is proportional to the relative particle velocity.

Local damping occurs at the particle contacts and the damping coefficient is proportional to the element stiffness. The local damping force for two particles in any direction *d* is calculated as:

$$F_d = \frac{2 \cdot \beta}{\sqrt{\frac{k_d}{m}}} \cdot k_d \cdot \dot{v}_d \quad [11]$$

where F_d is the local damping force in direction *d*, β is the fraction of critical damping, k_d is the stiffness of an element in direction *d*, *m* is the mass of a discrete element, and is the relative velocity between two discrete elements at the interelement contact in direction *d* (after Anandarajah 2000).

5.3.3 Generating Model Output

Once the particle assembly and force parameters have been defined, the assembly is consolidated by moving the horizontal walls until reaching a desired void ratio. Loading, e.g., swelling, is simulated by activating the appropriate forces using a desired time step. Forces and particle orientations are stored for each time step of analysis.

Stresses on walls are generated from summation of the forces at the contacts between the particles and assembly walls. Swell pressures are calculated from these forces as the average of the contact forces over the length of the assembly wall. Vertical swell pressure is the average of this calculation over the horizontal walls and lateral swell pressure is the average over the vertical walls.

The time step was determined through trial and error. It has been noted that the time step used in DEM simulations can affect the accuracy of the results if it is too large. The time step was chosen to be small enough that elements did not cross but large enough to limit the computational requirements of the simulation. However, the time step used has no physical basis and relies instead on computational limitations (Anandarajah 2000; Katti et al. 2009).

5.4 Results and Discussion

5.4.1 Calibration of DEMClay Model

A version of DEMClay (DEMClay$_{2013}$) was used by Anandarajah and Amarasinghe (2013) to evaluate swell pressures of a general specimen of Na-montmorillonite. The input parameters used to generate the DEMClay$_{2013}$ results are presented in Table 5.5, along with the input parameters used in this study for Swy Na-montmorillonite, the montmorillonite used in the ESEM study. The origin and properties of Swy Na-montmorillonite are detailed in *Chapter 3*. Notable parameters that influence the output are the number of discrete elements (N_{ELEM}), length of the discrete element (L_{DEM}), thickness (height) of a discrete element (H_{DEM}), maximum particle velocity (V_{MAX}), magnitude of wall velocity (V_{WALL}), and surface potential (ψ_0). While CEC and S_A are not direct inputs, they are included because they influence the particle spacing and surface potential inputs.

Table 5.5. DEMClay base parameters for Na-montmorillonite used in Anandarajah and Amarasinghe (2013)[1] and this study[2].

N_{ELEM}	L_{DEM} (nm)	H_{DEM} (nm)	V_{MAX} (nm/s)	V_{WALL} (nm/s)	ψ_0 (mv)	CEC (meq/100g)	S_A (m^2/g)
10,000[1]	25	4.656	6 x 10^6	5 x 10^6	96.0	100.0	800.0
10,000[2]	25	5.307	6 x 10^6	5 x 10^6	116.0	76.4	637.0

The DEMClay$_{2013}$ montmorillonite and Swy Na-montmorillonite have similar basal spacing (0.93 and 1.15 nm respectively). The resulting particle thickness calculated from this basal spacing for both soils rounds to 5 nm (4.656 and 5.307 nm respectively). Therefore, the length of a discrete element of Swy Na-montmorillonite was kept at 25 nm for this study. Because the physicochemical parameters (CEC, S_A) are measured values for each soil, they were not changed while calibrating the model. Similarly, the surface potential is calculated based on these measured parameters and was also kept constant during calibration. Instead, focus was placed on changing

parameters which are inherent to the model rather than the soil itself (e.g., number of discrete elements in the assembly, particle spacing between elements, particle velocity, and wall velocity).

DEMClay$_{2013}$ was compiled using Absoft Pro Fortran; however, as of 2022, Absoft ceased operations and was rendered obsolete. Therefore, Intel oneAPI was used to compile changes made to the DEMClay program. The most important difference between the two compilers lies in the implementation of the random number generator. When using Absoft to compile DEMClay, the random number generation is locked. However, through Intel oneAPI, the RAND() function is called, resulting in DEMClay output changes with changes in the number of discrete elements and grain size distribution of the assembly. Notably, DEMClay$_{2013}$ would not run assemblies with N_{ELEM} other than 10,000 discrete elements. Therefore, comparison of results with differing assemblies generated with the Absoft Compiler to the Intel oneAPI compiler is impossible.

The complete results of the sensitivity analysis are available in Appendix B. Selected results that impacted the analysis are discussed herein. When using the Absoft compiler, there was no difference in swell pressure or void ratio observed when changing L_{DEM}. This is likely due to the locking of the random number generator. Because the program is not able to randomly place discrete elements into an assembly, changes to the geometry of the assembly (i.e., number of discrete elements, size of discrete elements) will not affect the result. Therefore, all calibration of the swell pressure model was performed using the DEMClay program compiled using the Intel oneAPI compiler.

5.4.1.1 Effect of Number of Discrete Elements (N_{ELEM})

The number of discrete elements included in the assembly affects the computing time required to run the model. For a greater number of discrete elements, computing times are longer and for smaller numbers of discrete elements, computing times are shorter. An assembly of Swy Na-

montmorillonite was run with the same parameters detailed in Table 5.5, with maximum particle velocity V_{MAX} of 6.0 x 10^6 nm/s and wall loading rate V_{WALL} of 5.0 x 10^6 nm/s for both vertical and horizontal walls (i.e., K_0 = 1.0). The number of discrete elements in the assembly was varied between 1,000 and 10,000 (Table 5.6) for a target void ratio of 1.0.

Table 5.6. Effect of number of discrete elements on void ratio and swell pressure.

N_{ELEM}	L_{DEM} (nm)	H_{DEM} (nm)	V_{MAX} (nm/s)	V_{WALL} (nm/s)	Void Ratio, e	σ_S (kPa)	σ_H (kPa)
10,000	25	5.307	6 x 10^6	5 x 10^6	0.98	1,034	3,025
9,500	25	5.307	6 x 10^6	5 x 10^6	0.98	1,025	2,440
9,000	25	5.307	6 x 10^6	5 x 10^6	0.98	1,045	2,430
8,000	25	5.307	6 x 10^6	5 x 10^6	0.99	910	2,605
7,000	25	5.307	6 x 10^6	5 x 10^6	0.98	588	1,875
6,000	25	5.307	6 x 10^6	5 x 10^6	1.01	555	1,905
5,000	25	5.307	6 x 10^6	5 x 10^6	1.02	556	1,900
4,000	25	5.307	6 x 10^6	5 x 10^6	1.01	948	2,590
3,000	25	5.307	6 x 10^6	5 x 10^6	1.02	1,395	2,495
2,000	25	5.307	6 x 10^6	5 x 10^6	1.50	495	1,899
1,000	25	5.307	6 x 10^6	5 x 10^6	3.77	-	1,165

For the Na-montmorillonite specimen, the number of elements in the assembly largely does not affect the void ratio until reaching a limiting value at 3,000 discrete elements (Figure 5.6a). At smaller particle assemblies, it is more difficult to obtain the target void ratio (1.0) because there are not enough particles in the assembly to cover the box dimension with the given particle size distribution and particle spacing. However, between 3,000 and 10,000 discrete elements, the void ratio rounds to 1.0 (Table 5.6).

The number of discrete elements has somewhat of an effect on the swell pressure (Figure 5.6b). The vertical swell pressure is similar for assemblies of 8,000 to 10,000 and 4,000 discrete elements but is much lower for other assemblies. Similar effects are observed for the lateral (horizontal) swell pressure. The smallest number of discrete elements in an assembly that

maintains the same void ratio and similar swell pressures is 4,000. Therefore, because the differences in swell pressure and void ratio were small between 10,000 and 4,000 discrete elements, assemblies were created using 4,000 elements to minimize computational time.

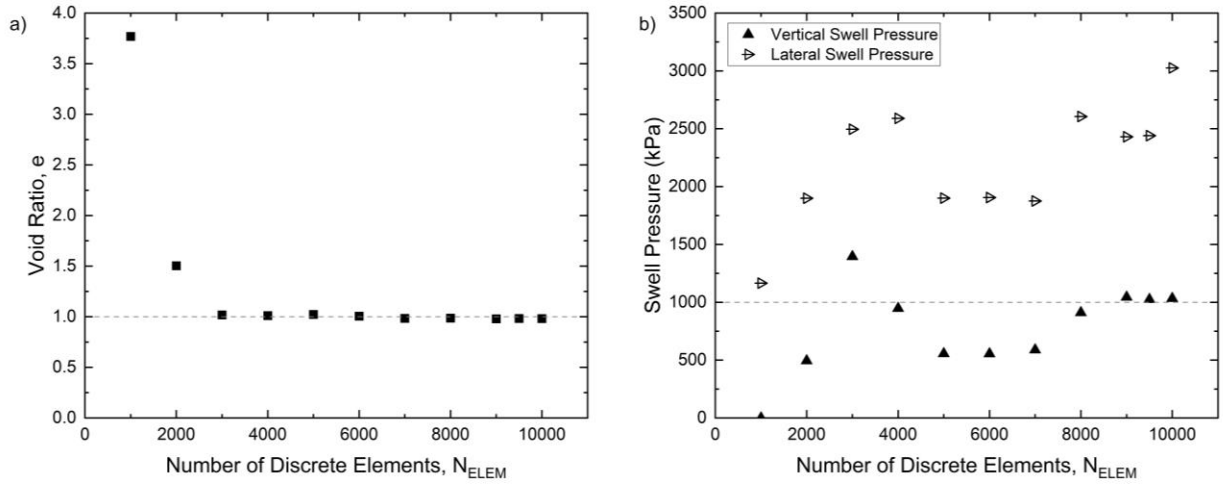

Figure 5.6. Effect of number of discrete elements on a) void ratio; and b) swell pressure.

5.4.1.2 Effect of Particle Spacing (D)

A range of void ratios were achieved through variation of the parameters influencing the maximum distance allowed between two adjacent particles, either edge-to-edge or edge-to-face particle alignment for assemblies of Na-montmorillonite. Particle spacing is calculated according to:

$$D = \left(H_{DEM} \cdot d_{cutoff}\right) \cdot S \qquad [12]$$

where D is the minimum distance between two adjacent particles, H_{DEM} is the thickness of a discrete element, d_{cutoff} is the maximum distance between particles at which interparticle mechanical contact forces begin, determined by Amarasinghe and Anandarajah (2013) to be 0.8 nm using MD studies, and S is the particle separation modifier.

The mechanical separation distance (d_{cutoff}) was chosen to describe the mechanical contact force, which acts even when the distance between particles is nonzero (Anandarajah and Lavoie 2002). Moreover, because the van der Waals attractive force is infinite at small separation distances (Anandarajah and Chen 1977) and the interparticle repulsive force is large at the same separation distances, the model assumes constant values for both forces when separation between particles is less than d_{cutoff}. The total force between particles is the resultant net force between the van der Waals attractive force, interparticle repulsive force, and mechanical contact force (Figure 5.7).

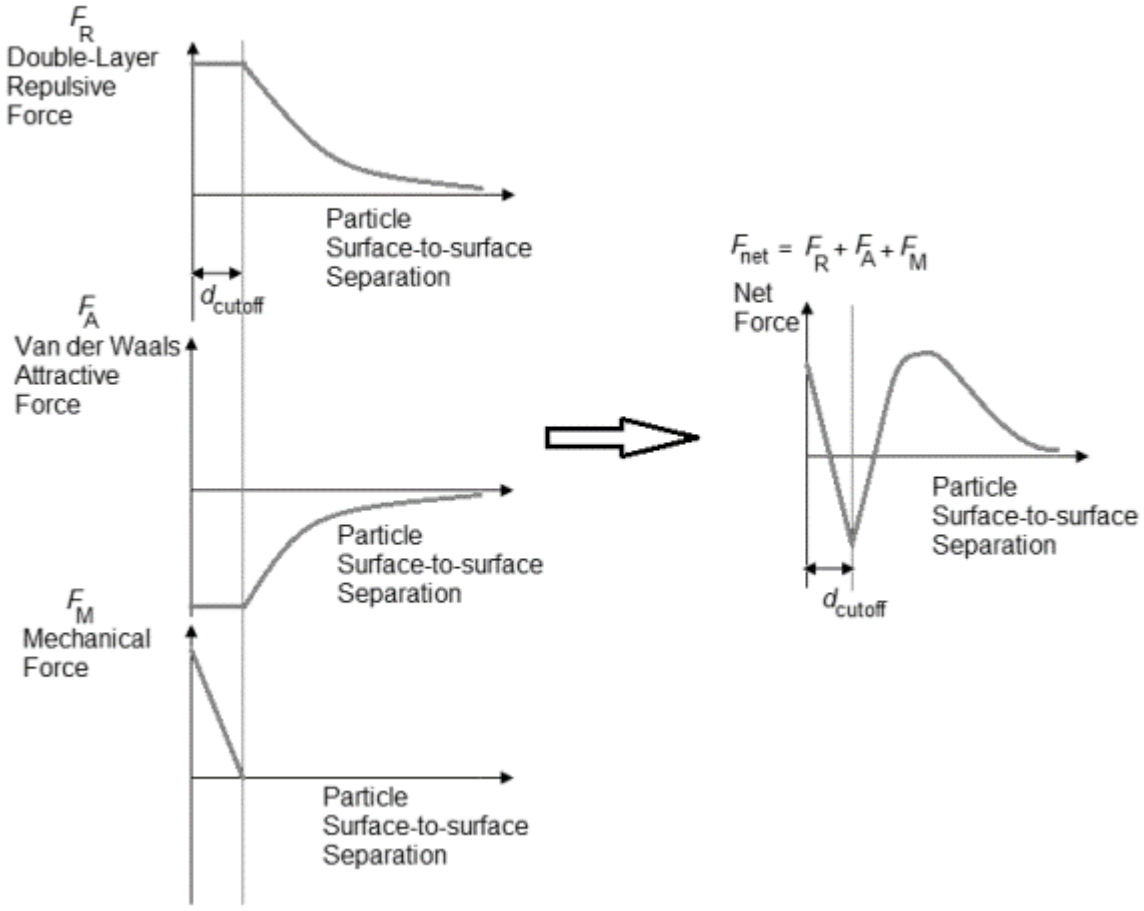

Figure 5.7. Force-separation relations for determining d_{cutoff} distance (Anandarajah 2014)

Modifying the S parameter allows changes to the void ratio of the assembly. Decreasing the S parameter decreases the minimum spacing required between two particles and therefore

results in a lower void ratio (denser specimen) and larger particle spacing results in looser specimens (higher void ratio). The effect of spacing on void ratio is shown in Figure 5.8a for particle assemblies of 10,000 discrete elements per assembly and Figure 5.8b for particle assemblies of 4,000 discrete elements per assembly for an oedometer, triaxial, and square assembly geometry. Note the differing y-scale void ratio range between 10,000 and 4,000 discrete elements.

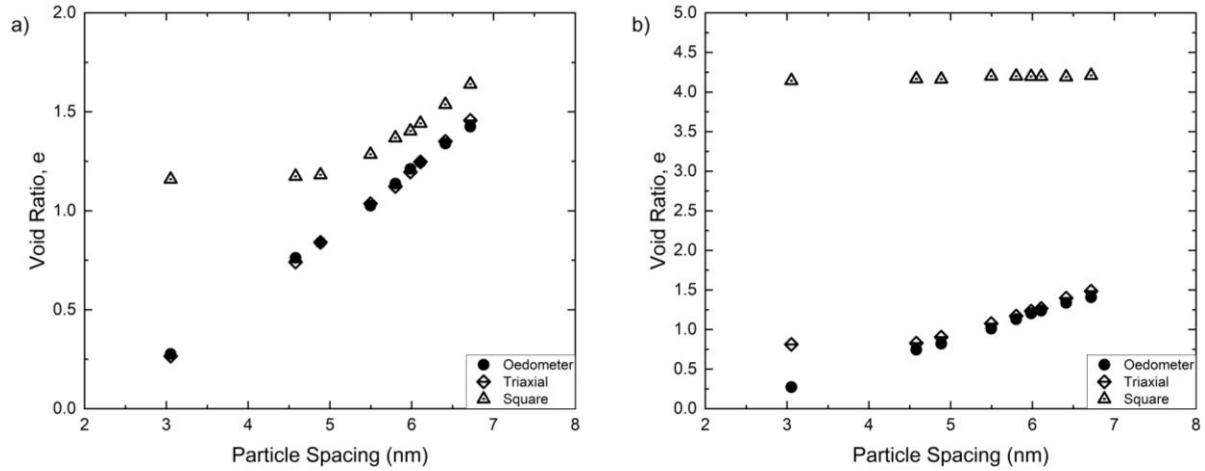

Figure 5.8. Effect of minimum particle spacing on void ratio of particle assemblies of Na-montmorillonite: a) 10,000 discrete elements; b) 4,000 discrete elements

Overall, for assemblies with 10,000 maximum discrete elements, there appears to be a linear relationship between minimum particle spacing and void ratio for the oedometer and triaxial box assemblies. However, for the square assembly, there is a piecewise linear relationship. For minimum particle separations greater than 5.5 nm, there is a linear relationship with void ratio, but for minimum particle separations less than 5.0 nm, the void ratio reaches a limiting value. For assemblies created using maximum 4,000 discrete elements, there is a greater dependence on assembly geometry. For the same particle size distribution and discrete element dimensions, assemblies created in a square assembly are much less dense than those created in an assembly patterned after a triaxial or oedometer cell. Because the square assemblies are created at such a

low density, particle spacing does not affect void ratio. For the triaxial assemblies using 4,000 discrete elements, there is a limiting value at 5.0 nm particle spacing below which minimum particle spacing does not affect the void ratio of the specimen. The oedometer cell assembly had a linear relationship between particle spacing and void ratio, similar to the relationship for assemblies of 10,000 discrete elements (Table 5.7). Therefore, using 4,000 discrete elements is a valid alternative to 10,000 elements when considering effects on void ratio with respect to particle spacing.

Table 5.7. Void ratio of particle assemblies based on particle spacing and number of discrete elements

Particle Spacing (nm)	Oedometer		Triaxial		Square	
	$e_{4,000}$	$e_{10,000}$	$e_{4,000}$	$e_{10,000}$	$e_{4,000}$	$e_{10,000}$
6.72	1.41	1.43	1.48	1.46	4.21	1.64
6.41	1.34	1.34	1.40	1.35	4.19	1.54
6.11	1.24	1.25	1.27	1.25	4.20	1.44
5.98	1.21	1.21	1.23	1.20	4.20	1.40
5.80	1.13	1.14	1.17	1.12	4.20	1.37
5.50	1.01	1.03	1.08	1.04	4.20	1.29
4.89	0.82	0.84	0.90	0.84	4.16	1.18
4.58	0.75	0.76	0.83	0.74	4.17	1.17
3.05	0.27	0.28	0.81	0.27	4.14	1.16

The geometry of the assembly also affected swell pressure: swell pressures were higher for the oedometer assembly than the triaxial and square assemblies (Table 5.8) for every particle spacing (D) tested. While the swell pressures differed between triaxial and oedometer assemblies, the general trend was similar for particle spacing less than 5.0 nm (lower void ratios) but the magnitude of swell for oedometer tests continued to be much higher than that of triaxial assemblies. With oedometer assemblies, as the particle spacing decreases, the void ratio continues to decrease whereas with the triaxial assemblies, even though the particle spacing is decreasing,

the void ratio stops changing much, seemingly encountering a limiting void ratio for that particular geometry. The effect of particle spacing on swell pressure is most notable for the square assembly with a 1:1 ratio between height and width (Figure 5.9). For a 1:1 particle assembly, then, particle spacing must be adjusted to obtain a similar void ratio and therefore similar swell pressure to the other assembly geometries. For all DEM assembly geometries, as the particle spacing decreases, i.e., the specimen becomes denser, the swell pressure increases. This is because the soil particles are closer, providing greater change for the interparticle repulsive force to activate (Cimen et al. 2012). Sun et al. (2015) also noted a strong positive correlation between dry density and swell pressure of bentonite clays. However, it is notable that there is not an exact linear (or exponential) relationship between swell pressure and void ratio obtained from the model.

Table 5.8. Effect of particle spacing (D) on void ratio and vertical swell pressure, N_{ELEM} = 4,000, L_{DEM} = 25 nm, H_{DEM} = 5.307 nm, VMAX = 6 x 10^6 nm/s, VWALL = 5 x 10^6 nm/s

D (nm)	Oedometer		Triaxial		Square	
	Void Ratio, e	σ_S (kPa)	Void Ratio, e	σ_S (kPa)	Void Ratio, e	σ_S (kPa)
6.11	1.238	129	1.265	-	4.194	-
5.98	1.204	130	1.233	-	4.194	-
5.80	1.130	387	1.171	171	4.199	-
5.50	1.011	948	1.074	-	4.199	-
5.19	.9380	4,000	0.994	573	4.180	139
4.58	0.745	5,390	0.828	4,070	4.165	725
4.27	0.629	8,285	0.823	5,515	4.178	730
3.66	0.432	27,350	0.810	18,900	4.170	1,740
3.36	0.337	33,050	0.806	29,450	4.158	2,655
3.05	0.273	45,700	0.811	33,800	4.143	3,005
2.44	0.266	67,300	0.794	41,700	4.135	4,470

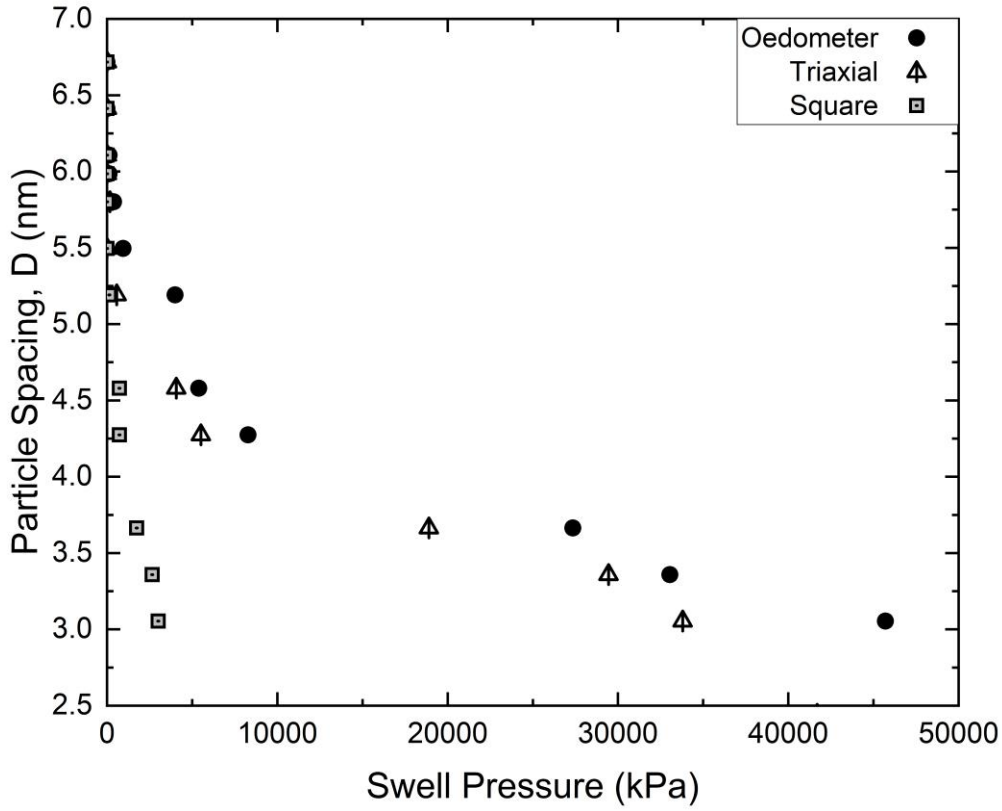

Figure 5.9 Effect of minimum particle spacing on vertical swell pressure of Na-montmorillonite

5.4.1.3 Effect of Discrete Element Thickness (H_{DEM})

To understand the effect of varying particle thickness, H_{DEM} was varied between 5 and 30 nm. Two different target void ratios were chosen: a loose assembly (e = 1.23) and a dense assembly (e = 0.75). While H_{DEM} is a calculated parameter, it is affected by the specific surface area, specific gravity, and number of layers per particle. Different soils will have different particle thicknesses and therefore different discrete element thicknesses. Therefore, it is important to assess the relationship between particle thickness (H_{DEM}) and swell pressure.

Changing the particle thickness affected the void ratio as well as swell pressure. For both dense (Table 5.9) and dense (Table 5.10) assemblies, in general, increasing H_{DEM} also increased the void ratio. This is reasonable because the number of elements and minimum spacing are held constant, but a larger specimen is being placed into the same dimensions. Overall, swell pressure tends to increase with particle thickness. However, no trend between H_{DEM} and swell pressure can be interpreted directly because of the change in void ratio.

Table 5.9. Effect of discrete element thickness (H_{DEM}) on swell pressure, constant S = 0.75

N_{ELEM}	L_{DEM} (nm)	H_{DEM} (nm)	V_{MAX} (nm/s)	V_{WALL} (nm/s)	S	Void Ratio, e	σ_S (kPa)	σ_H (kPa)
4,000	25	5.000	6×10^6	5×10^6	0.75	0.744	5,625	8,295
4,000	**25**	**5.307**	**6×10^6**	**5×10^6**	**0.75**	**0.745**	**5,390**	**4,885**
4,000	25	10.000	6×10^6	5×10^6	0.75	0.650	14,050	7,475
4,000	25	15.000	6×10^6	5×10^6	0.75	0.642	29,850	30,300
4,000	25	20.000	6×10^6	5×10^6	0.75	0.699	37,900	39,450
4,000	25	25.000	6×10^6	5×10^6	0.75	0.736	62,300	34,200
4,000	25	30.000	6×10^6	5×10^6	0.75	0.809	52,650	91,150

Table 5.10. Effect of discrete element thickness (H_{DEM}) on swell pressure, constant S = 1.0

N_{ELEM}	L_{DEM} (nm)	H_{DEM} (nm)	V_{MAX} (nm/s)	V_{WALL} (nm/s)	S	Void Ratio, e	σ_S (kPa)	σ_H (kPa)
4,000	25	5.000	6×10^6	5×10^6	1.0	1.236	217	447
4,000	**25**	**5.307**	**6×10^6**	**5×10^6**	**1.0**	**1.238**	**129**	**140**
4,000	25	10.000	6×10^6	5×10^6	1.0	1.173	451	525
4,000	25	15.000	6×10^6	5×10^6	1.0	1.272	-	1,435
4,000	25	20.000	6×10^6	5×10^6	1.0	1.364	-	-
4,000	25	25.000	6×10^6	5×10^6	1.0	1.449	730	1,055
4,000	25	30.000	6×10^6	5×10^6	1.0	1.544	940	-

To better compare the effects of particle thickness on swell pressure, then, the particle spacing parameter (S) was adjusted to maintain a constant void ratio with changes in H_{DEM}. There was no large difference in vertical swell pressure between discrete element thickness of 5 nm and 5.307 nm for either loose or dense specimens. Once particle spacing was adjusted to maintain a constant void ratio of e = 0.75 for dense specimens (Table 5.11) and e = 1.23 for loose specimens

(Table 5.12), a clearer trend appeared. As H_{DEM} increases, vertical swell pressure also increases (Figure 5.10). With larger particle thickness, there is greater opportunity for edge-to-face and edge-to-edge preferential alignment of particles, increasing the probability of particle contacts and therefore swelling. When the particles are aligned in a face-to-face assembly, particle-particle contacts are less likely to occur and therefore the swell pressure is lower for these assemblies.

Table 5.11. Effect of discrete element thickness (H_{DEM}) on swell pressure, varying S to maintain e = 0.75

N_{ELEM}	L_{DEM} (nm)	H_{DEM} (nm)	V_{MAX} (nm/s)	V_{WALL} (nm/s)	S	Void Ratio, e	σ_S (kPa)	σ_H (kPa)
4,000	25	5.000	6×10^6	5×10^6	0.750	0.744	5,625	8,295
4,000	**25**	**5.307**	**6×10^6**	**5×10^6**	**0.750**	**0.745**	**5,390**	**4,885**
4,000	25	10.000	6×10^6	5×10^6	0.800	0.745	6,500	5,345
4,000	25	15.000	6×10^6	5×10^6	0.795	0.748	10,750	6,855
4,000	25	20.000	6×10^6	5×10^6	0.770	0.759	40,700	15,675
4,000	25	25.000	6×10^6	5×10^6	0.755	0.736	63,950	26,400
4,000	25	30.000	6×10^6	5×10^6	0.730	0.754	77,150	112,000

Table 5.12. Effect of discrete element thickness (H_{DEM}) on swell pressure, varying S to maintain e = 1.23

N_{ELEM}	L_{DEM} (nm)	H_{DEM} (nm)	V_{MAX} (nm/s)	V_{WALL} (nm/s)	S	Void Ratio, e	σ_S (kPa)	σ_H (kPa)
4,000	25	5.000	6×10^6	5×10^6	1.000	1.236	217	447
4,000	**25**	**5.307**	**6×10^6**	**5×10^6**	**1.000**	**1.238**	**129**	**140**
4,000	25	10.000	6×10^6	5×10^6	1.035	1.232	27	-
4,000	25	15.000	6×10^6	5×10^6	0.985	1.231	980	1,435
4,000	25	20.000	6×10^6	5×10^6	0.960	1.231	447	-
4,000	25	25.000	6×10^6	5×10^6	0.920	1.226	2,370	5,325
4,000	25	30.000	6×10^6	5×10^6	0.890	1.228	6,880	4,135

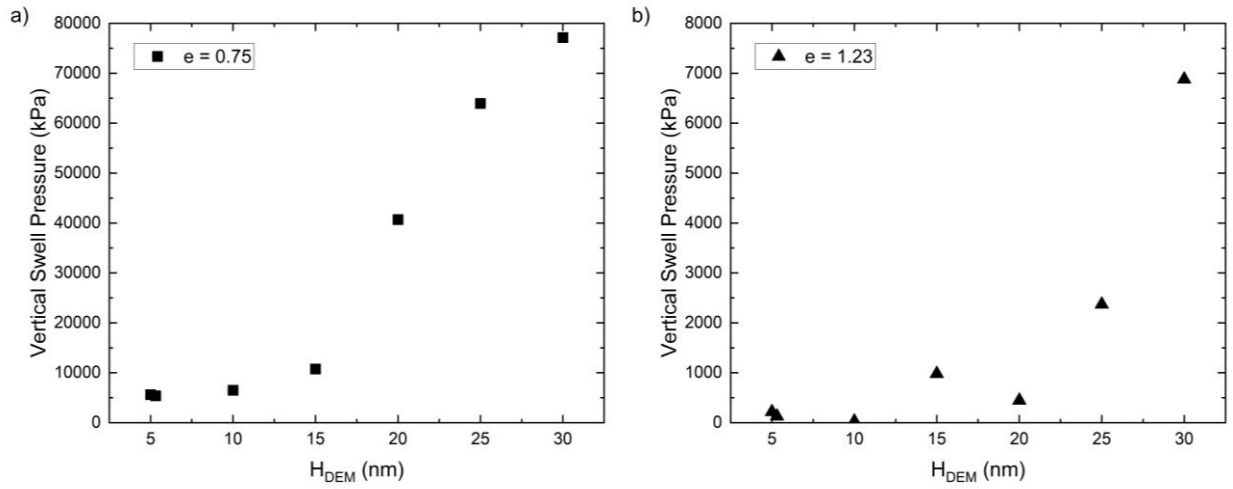

Figure 5.10. Effect of changing discrete element thickness on swell pressure a) e = 0.75 (dense); and b) e = 1.23 (Loose) (Note: dense sample scale is 10x the loose sample scale).

5.4.1.4 Effect of Discrete Element Length (L_{DEM})

The length of a discrete element (L_{DEM}) is not a function of input values in the same manner as H_{DEM}. Instead, L_{DEM} is chosen so that the smallest particle length is equal to L_{DEM} and the maximum particle length is a multiple of L_{DEM}. The discrete element length was varied between 25 and 55 nm while maintaining the assembly at N_{ELEM} = 4,000 discrete elements, H_{DEM} = 5.307 nm, the particle velocity at a constant $V_{MAX} = 6 \times 10^6$ nm/s and horizontal and vertical loading rates at $V_{WALL} = 5 \times 10^6$ nm/s. Void ratios of 0.75 (dense) and 1.23 (loose) were chosen to assess the effect of density on swell pressure with changing discrete element length.

There was no trend between discrete element length and swell pressure for either dense (Table 5.13) or loose (Table 5.14) assemblies. This is because as L_{DEM} increased, the void ratio also increased. Assemblies with higher void ratios resulted in lower swell pressures.

Table 5.13. Effect of discrete element length on swell pressure, constant S = 0.75

N_{ELEM}	L_{DEM} (nm)	H_{DEM} (nm)	V_{MAX} (nm/s)	V_{WALL} (nm/s)	S	Void Ratio, e	σ_S (kPa)	σ_H (kPa)
4,000	**25**	**5.307**	**6 x 10^6**	**5 x 10^6**	**0.75**	**0.745**	**5,390**	**4,885**
4,000	30	5.307	6 x 10^6	5 x 10^6	0.75	0.839	6,045	11,375
4,000	35	5.307	6 x 10^6	5 x 10^6	0.75	0.882	4,095	8,105
4,000	40	5.307	6 x 10^6	5 x 10^6	0.75	0.953	7,030	6,120
4,000	45	5.307	6 x 10^6	5 x 10^6	0.75	0.973	2,459	6,665
4,000	50	5.307	6 x 10^6	5 x 10^6	0.75	1.024	3,580	9,290
4,000	55	5.307	6 x 10^6	5 x 10^6	0.75	1.141	5,725	5,695

Table 5.14. Effect of discrete element length on swell pressure, constant S = 1.0

N_{ELEM}	L_{DEM} (nm)	H_{DEM} (nm)	V_{MAX} (nm/s)	V_{WALL} (nm/s)	S	Void Ratio, e	σ_S (kPa)	σ_H (kPa)
4,000	**25**	**5.307**	**6 x 10^6**	**5 x 10^6**	**1.000**	**1.238**	**129**	**140**
4,000	30	5.307	6 x 10^6	5 x 10^6	1.000	1.377	41	910
4,000	35	5.307	6 x 10^6	5 x 10^6	1.000	1.369	-	226
4,000	40	5.307	6 x 10^6	5 x 10^6	1.000	1.469	90	610
4,000	45	5.307	6 x 10^6	5 x 10^6	1.000	1.559	70	-
4,000	50	5.307	6 x 10^6	5 x 10^6	1.000	1.552	-	-
4,000	55	5.307	6 x 10^6	5 x 10^6	1.000	1.665	310	-

Therefore, in order to better compare the effects of changing L_{DEM}, the spacing parameter (S) was adjusted to maintain a constant void ratio of 0.75 for dense specimens (Table 5.15) and 1.23 for loose specimens (Table 5.16). At the same void ratio and same particle thickness, swell pressure increased with discrete element length for both loose and dense specimens. Because H_{DEM} is held constant, interlayer spacing is not changing and therefore the effect is not due to interlayer forces but instead interparticle interactions.

Table 5.15. Effect of discrete element length on swell pressure, varying S to maintain e = 0.75

N_{ELEM}	L_{DEM} (nm)	H_{DEM} (nm)	V_{MAX} (nm/s)	V_{WALL} (nm/s)	S	Void Ratio, e	σ_S (kPa)	σ_H (kPa)
4,000	**25**	**5.307**	**6×10^6**	**5×10^6**	**0.750**	**0.745**	**5,390**	**4,885**
4,000	30	5.307	6×10^6	5×10^6	0.700	0.730	10,600	19,800
4,000	35	5.307	6×10^6	5×10^6	0.685	0.743	11,000	16,800
4,000	40	5.307	6×10^6	5×10^6	0.640	0.733	14,600	13,550
4,000	45	5.307	6×10^6	5×10^6	0.640	0.737	16,000	11,010
4,000	50	5.307	6×10^6	5×10^6	0.625	0.726	12,300	10,695
4,000	55	5.307	6×10^6	5×10^6	0.565	0.738	21,500	15,100

Table 5.16. Effect of discrete element length on swell pressure, varying S to maintain e = 1.23

N_{ELEM}	L_{DEM} (nm)	H_{DEM} (nm)	V_{MAX} (nm/s)	V_{WALL} (nm/s)	S	Void Ratio, e	σ_S (kPa)	σ_H (kPa)
4,000	**25**	**5.307**	**6×10^6**	**5×10^6**	**1.000**	**1.238**	**129**	**140**
4,000	30	5.307	6×10^6	5×10^6	0.935	1.227	449	1,460
4,000	35	5.307	6×10^6	5×10^6	0.915	1.222	512	454
4,000	40	5.307	6×10^6	5×10^6	0.890	1.224	2,950	975
4,000	45	5.307	6×10^6	5×10^6	0.865	1.235	1,915	1,855
4,000	50	5.307	6×10^6	5×10^6	0.845	1.227	3,610	4,275
4,000	55	5.307	6×10^6	5×10^6	0.790	1.230	6,290	4,260

There was a nonlinear trend between L_{DEM} and swell pressure (Figure 5.11). In general, swell pressure tends to increase with discrete element length: for dense specimens (e = 0.75), the trend is linear with the exception of L_{DEM} = 50 nm and for loose specimens (e = 1.23), the trend is exponential with the exception of L_{DEM} = 40 nm. Similar to the effect of H_{DEM}, as discrete elements increase in length, preferential orientations emerge within the assembly to achieve the target void ratio. Longer discrete elements result in stiffer particles which allow less space for face-to-face preferential orientation, resulting in more particle-particle contacts and therefore higher swell pressure.

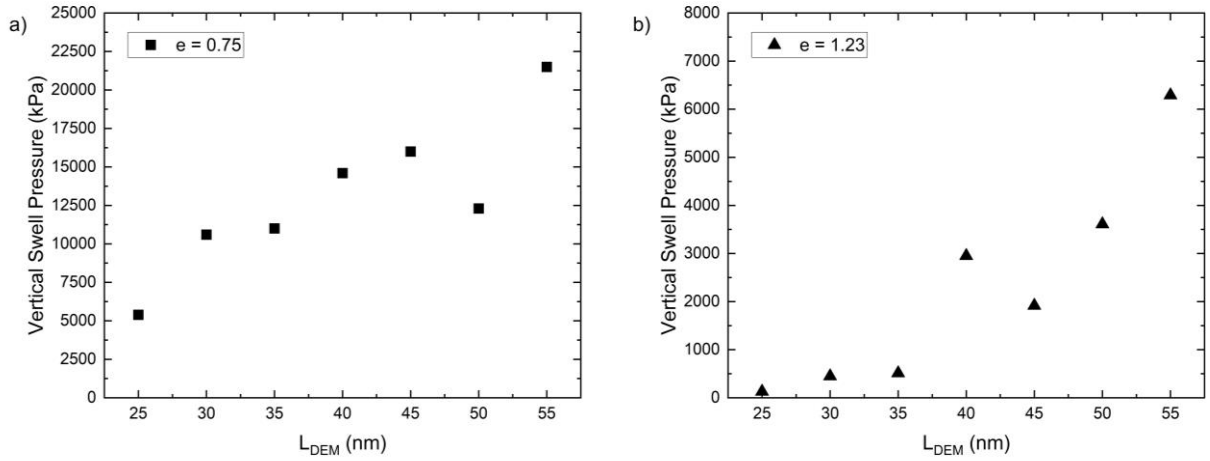

Figure 5.11. Effect of discrete element length on swell pressure: a) e = 0.75 (dense); b) e = 1.23 (loose)

5.4.1.5 Effect of Wall Velocity (V_{WALL})

The loading on the specimen is controlled by the wall velocity (V_{WALL}) and the time step used in the analysis. Because the assembly walls are modeled with the same density as the discrete elements comprising soil particles, vertical wall movement simulates overburden pressure and horizontal wall movement represents horizontal earth pressure. Greater vertical wall velocity corresponds to greater overburden pressure while lower wall velocity corresponds to lower overburden, i.e., near-surface conditions.

In this study, V_{WALL} was varied between 4 x 10^3 and 4 x 10^7 nm/s for void ratios e = 0.75 (Table 5.17), 1.0 (Table 5.18), and 1.25 (Table 5.19). The same V_{WALL} loading was maintained for vertical and horizontal wall for each run to maintain K_0 = 1.0 conditions. The effect of geometry under K_0 loading conditions is discussed in detail in Section *5.4.1.6*. Particle velocity was maintained at a constant 6 x 10^6 nm/s for assemblies with 4,000 discrete elements with H_{DEM} = 5.307 nm and L_{DEM} = 25 nm.

Table 5.17. Effect of wall velocity on swell pressure, e = 0.75

N_{ELEM}	L_{DEM} (nm)	H_{DEM} (nm)	V_{MAX} (nm/s)	V_{WALL} (nm/s)	Void Ratio, e	σ_S (kPa)	σ_H (kPa)
4,000	25	5.307	6×10^6	4×10^3	0.746	4,610	4,255
4,000	25	5.307	6×10^6	4×10^6	0.745	5,225	4,755
4,000	25	5.307	6×10^6	5×10^6	0.745	5,390	4,885
4,000	25	5.307	6×10^6	6×10^6	0.745	5,555	5,015
4,000	25	5.307	6×10^6	8×10^6	0.745	5,915	5,275
4,000	25	5.307	6×10^6	2×10^7	0.743	8,175	6,825
4,000	25	5.307	6×10^6	4×10^7	0.743	8,175	6,825

Table 5.18. Effect of wall velocity on swell pressure, e = 1.0

N_{ELEM}	L_{DEM} (nm)	H_{DEM} (nm)	V_{MAX} (nm/s)	V_{WALL} (nm/s)	Void Ratio, e	σ_S (kPa)	σ_H (kPa)
4,000	25	5.307	6×10^6	4×10^3	1.086	105	350
4,000	25	5.307	6×10^6	4×10^6	1.082	424	1,025
4,000	25	5.307	6×10^6	5×10^6	1.081	524	1,350
4,000	25	5.307	6×10^6	6×10^6	1.080	705	1,756
4,000	25	5.307	6×10^6	8×10^6	1.078	1,230	2,837
4,000	25	5.307	6×10^6	2×10^7	1.072	4,025	6,575
4,000	25	5.307	6×10^6	4×10^7	1.070	5,490	8,105

Table 5.19. Effect of wall velocity on swell pressure, e = 1.25

N_{ELEM}	L_{DEM} (nm)	H_{DEM} (nm)	V_{MAX} (nm/s)	V_{WALL} (nm/s)	Void Ratio, e	σ_S (kPa)	σ_H (kPa)
4,000	25	5.307	6×10^6	4×10^3	1.255	-	-
4,000	25	5.307	6×10^6	4×10^6	1.251	96	32
4,000	25	5.307	6×10^6	5×10^6	1.250	129	140
4,000	25	5.307	6×10^6	6×10^6	1.249	162	248
4,000	25	5.307	6×10^6	8×10^6	1.247	297	680
4,000	25	5.307	6×10^6	2×10^7	1.236	2,475	4,902
4,000	25	5.307	6×10^6	4×10^7	1.234	3,345	6,760

There is a small change in void ratio with changes in wall velocity (Table 5.17, 5.18, 5.19). However, overall, the percent difference between the maximum and minimum void ratio is less than 2%. There is a positive correlation between V_{WALL} and swell pressure (Figure 5.12). As overburden pressure increases, the vertical swell pressure increases, until leveling off around $V_{WALL} = 2 \times 10^7$ nm/s. This limiting pressure is more exaggerated for the denser specimen (e =

0.75), but the rate of increase in swell pressure decreases for the intermediate (e = 1.0) and loose (e = 1.25) specimens as well. Swelling has been shown to increase with depth (Sikh 1993; She et al. 2019) and swell pressure has been shown to increase with depth until reaching a limiting depth (She et al. 2019) where the overburden pressure is sufficiently large to prevent deformation.

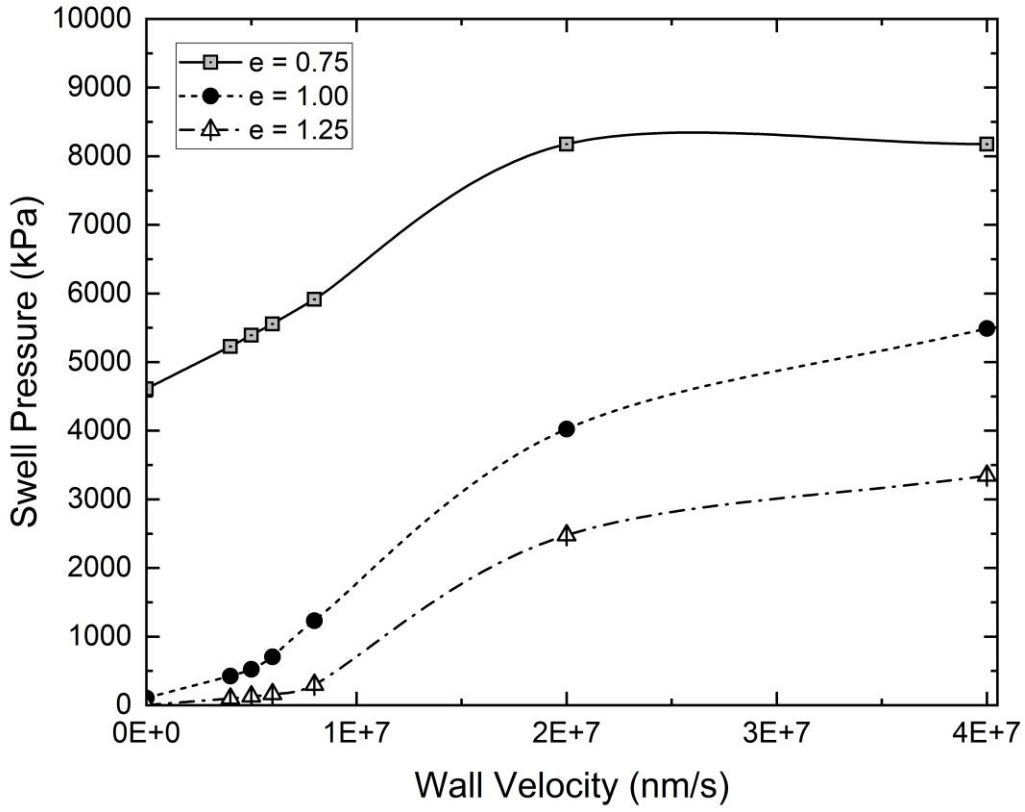

Figure 5.12. Effect of wall velocity (V_{WALL}) on vertical swell pressure.

5.4.1.6 Effect of K_0 Conditions

Different K_0 conditions were achieved by adjusting the ratio of horizontal to vertical wall velocity. The time step and density were kept constant between iterations, therefore K_0 conditions were calculated directly through a ratio of horizontal wall velocity to vertical wall velocity. In this study,

K_0 values of 2, 1, 0.5 and 0.33 were used to assess the influence of loading conditions and assembly geometry on vertical and horizontal swell pressures. While the walls were moved inward to simulate loading, this should not be confused with active pressure. The loading associated with the DEM simulation is not related to horizontal or vertical strain and the walls were rigid with no rotation allowed, therefore K_0 conditions prevailed.

Vertical and horizontal swell pressures (VSP and LSP, respectively) using an oedometer assembly (Figure 5.13) were obtained using 4,000 discrete elements of Na-montmorillonite. For void ratios greater than 1.0, there was little difference in VSP, while VSP varied slightly for void ratios less than 1.0. Generally, for iterations with void ratio less than 1.0, VSP decreased with decreasing K_0. The opposite effect was observed for horizontal swell pressure. Overall, iterations with K_0 values of 2 had higher LSP than specimens with higher magnitude of loading in the vertical than horizontal (i.e., $K_0 < 1$). There was only a small difference in LSP between $K_0 = 1.0$ and 0.33 for both vertical and horizontal cases and LSP was generally lower for $K_0 = 0.5$.

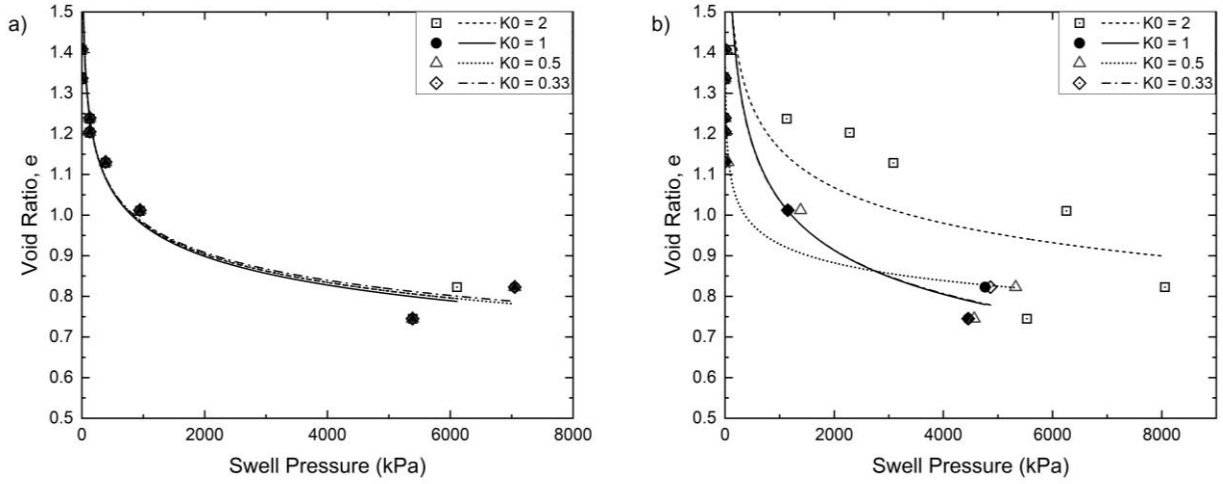

Figure 5.13. DEM swell pressures for Na-montmorillonite assemblies of varying K_0 conditions (K_0 = 2, 1, 0.5, 0.33) in oedometer assembly (1:3) using 1:3, 3:1, 1:1 height to width ratio: a) Vertical swell pressure; b) Horizontal swell pressure (LSP).

Vertical and horizontal swell pressures using a triaxial assembly (Figure 5.14) of 4,000 discrete elements of Na-montmorillonite. There was a noticeable difference in the magnitude of swell pressure between vertical and horizontal for every value of K_0. For all values of K_0, LSP was smaller for void ratios less than 1 and higher for void ratios greater than 1.0. There was no noticeable difference between vertical swell pressures for all values of K_0. Conversely, LSP was greatest for the $K_0 = 1$ case and overall the same for cases where K_0 is 2, 0.5, and 0.33.

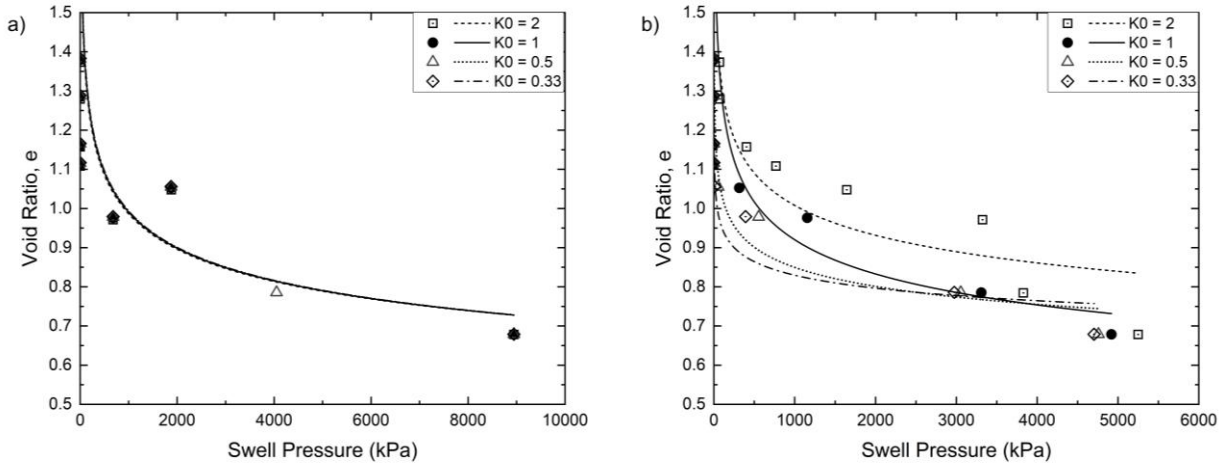

Figure 5.14. DEM swell pressures for Na-montmorillonite assemblies of varying K_0 conditions (K_0 = 2, 1, 0.5, 0.33) in triaxial assembly (3:1) using 1:3, 3:1, 1:1 height to width ratio: a) Vertical swell pressure (VSP); b) Horizontal swell pressure (LSP).

To better illustrate changes in swell pressure with K_0, the swell pressures were plotted against K_0 conditions for the oedometer setup (Figure 5.15) and the triaxial setup (Figure 5.16). For the oedometer assembly, both LSP and VSP overall increased as void ratio decreased. There was more variation in LSP with K_0 than VSP. VSP was largely independent of K_0 with the exception of $K_0 = 2$, where horizontal load was greater than the vertical load and the additional force was transferred to the total swell pressure in the vertical direction. LSP tended to decrease as K_0 decreased. The restricted vertical heave was translated into a vertical load applying pressure to walls 1 and 3 (Liu and Vanapalli 2019; Zhang et al. 2020a).

LSP was higher than VSP for K_0 greater than 1 at corresponding void ratios, particularly for denser specimens. Similar results have been observed for montmorillonite specimens by Ofer (1981). This is likely because due to the geometry of the assembly, horizontal particle movement is more restrained than vertical movement within the assembly. Greater strains have been shown to reduce swell pressure (Liu and Vanapalli 2019), therefore since the particles are less free to move in the horizontal direction, the pressures against the rigid walls are greater. LSP was lowest for $K_0 = 1.0$, and greatest for $K_0 = 2$. This is likely due to the orientation of particles as particle orientation contributes to swelling anisotropy and swelling is greatest when the soil particles are oriented in parallel (Liu and Vanapalli 2019; Zhang et al. 2020a).

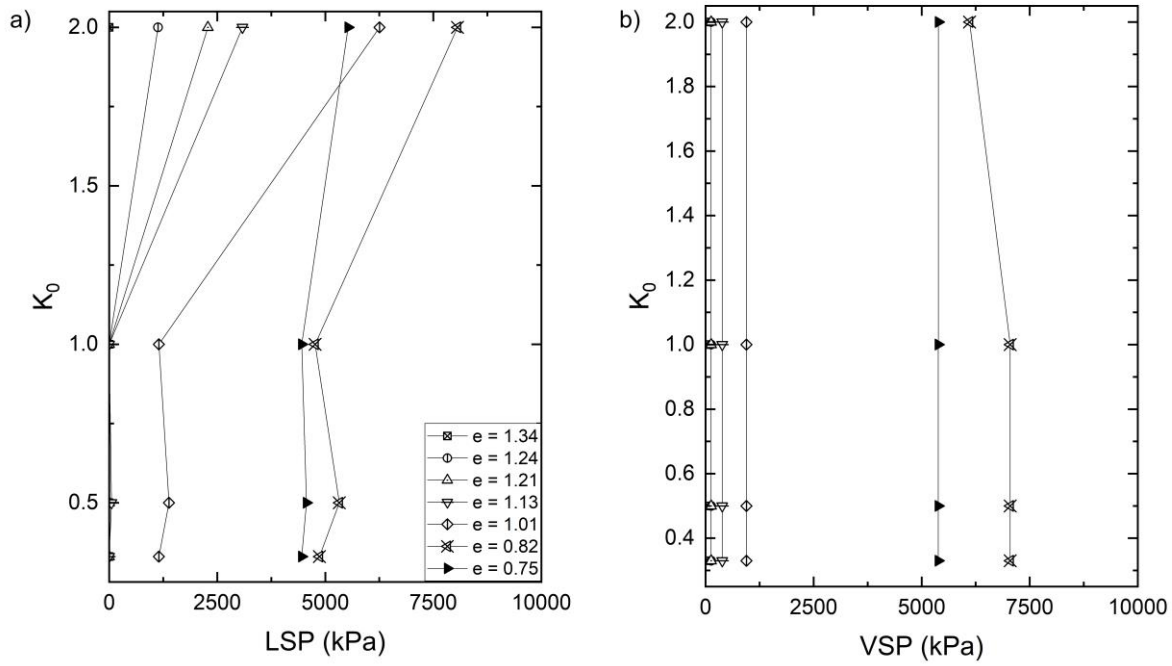

Figure 5.15. DEM swell pressures for varying K_0 conditions using oedometer assembly: a) Lateral swell pressure (LSP); b) Vertical swell pressure (VSP)

Swell pressure results using the triaxial assembly differed from results using the oedometer assembly. Notably, VSP was overall higher than LSP for void ratios less than 1 and decreased once reaching $K_0 = 0.33$. This anisotropy was observed for expansive clays by Zhang et al. (2020),

where the ratio of lateral to vertical swell pressure was as low as 0.27 to 0.31. This is largely due to the arrangement of the montmorillonite particles: in the triaxial assembly particles are largely oriented parallel with the horizontal walls. Additionally, LSP decreased as K_0 decreased for all void ratios until increasing for $K_0 = 0.33$. This is because the horizontal pressure decreased as K_0 decreased and swell pressure is affected by the magnitude of the load (Abdollahi and Vahedifard 2020; Zhang et al. 2020a). For the $K_0 = 0.33$ loading condition, the horizontal confining pressure is so much lower than vertical pressure that a greater number of contacts occurred between the horizontal walls and particles, increasing the horizontal swell pressure.

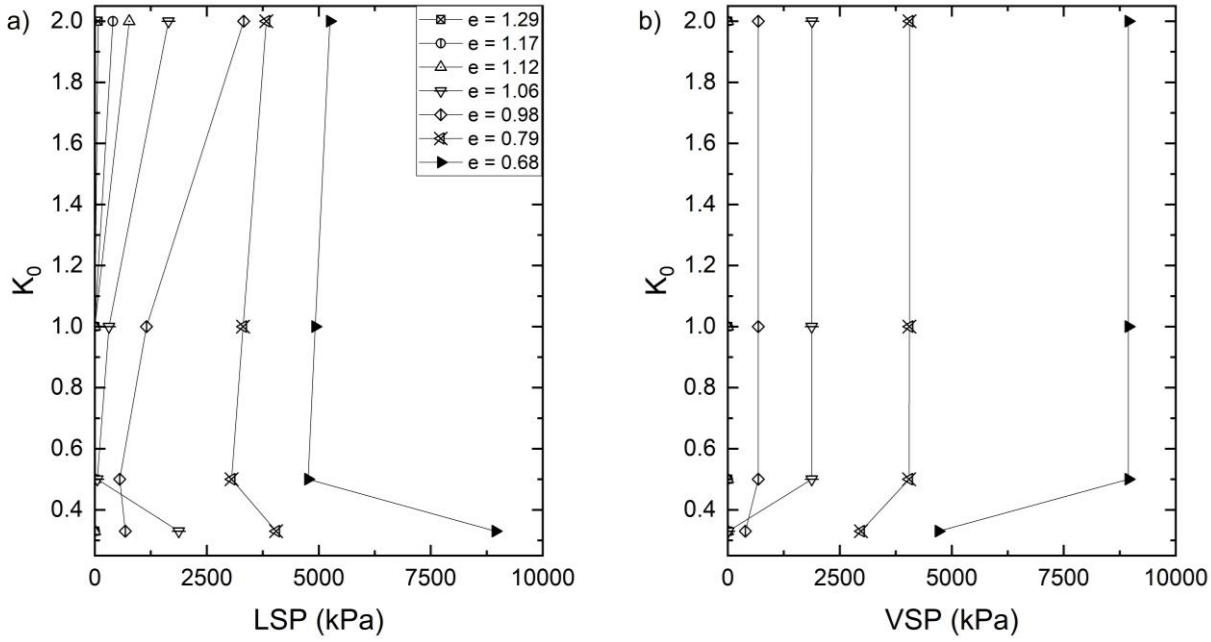

Figure 5.16. DEM swell pressures for varying K_0 conditions using triaxial assembly: a) Lateral swell pressure (LSP); b) Vertical swell pressure (VSP)

5.4.1.7 Effect of Particle Velocity (V_{MAX})

The particle velocity controls the speed at which the discrete elements move as they come to equilibrium. This particle velocity used in the model is not based on a measured quantity and is

only used to control the particle damping. The greater the velocity allowed, the greater the damping. The relationship between particle velocity and swell pressure is complicated and depends on multiple factors describing the assembly geometry. Therefore, a wide range of particle velocities (V_{MAX}) between 0 and 1 x 10^7 nm/s were used to assess the impact of particle geometry on swell pressure for varying discrete elements lengths (L_{DEM} = 25, 35, 45, and 55 nm), varying discrete element thickness (H_{DEM} = 5, 10, 15, 20, and 30 nm), and varying void ratios (e = 0.7, 1.0, and 1.25). Particle velocity does not affect the void ratio, however, the velocity did affect both the vertical and horizontal swell pressures.

5.4.1.7.1 Relationship between V_{MAX} and L_{DEM}

The correlation between particle velocity and discrete element length was studied for both vertical and horizontal swell pressures for L_{DEM} = 25, 36, 45, and 55 nm. Particle thickness (H_{DEM}) was kept at 5.307 nm and wall velocity (V_{WALL}) was maintained throughout each iteration at 5 x 10^6 nm/s with K_0 = 1.0 conditions. The effect of this relationship on specimen density was studied using e = 0.7 (Table 5.20), e = 1.0 (Table 5.21), and e = 1.25 (Table 5.22).

Table 5.20. Effect of particle velocity and discrete element length on swell pressure, e = 0.7; H_{DEM} = 5.307 nm; V_{WALL} = 5 x 10^6 nm/s

V_{MAX} (nm/s)	L_{DEM} = 25 nm		L_{DEM} = 35 nm		L_{DEM} = 45 nm		L_{DEM} = 55 nm	
	σ_S (kPa)	σ_H (kPa)	σ_S (kPa)	σ_H (kPa)	σ_S (kPa)	σ_H (kPa)	σ_S (kPa)	σ_H (kPa)
0	17,500	13,250	11,900	12,015	9,340	3,015	1,756	5,515
1.0 x 10^6	14,700	12,450	9,525	10,630	8,555	2,925	1,919	4,871
2.0 x 10^6	12,300	11,550	7,485	9,745	6,930	2,815	1,591	3,680
3.0 x 10^6	10,265	10,550	5,760	8,935	5,700	2,725	1,363	2,710
4.0 x 10^6	8,490	9,680	4,225	8,130	4,930	2,640	1,230	2,395
5.0 x 10^6	7,275	9,260	3,460	7,470	4,255	2,565	1,177	2,120
6.0 x 10^6	5,935	8,810	2,645	6,635	3,570	2,460	1,144	1,985
7.0 x 10^6	5,320	8,415	2,110	6,290	3,065	2,375	1,111	1,925
8.0 x 10^6	4,885	8,005	1,735	6,115	2,565	2,280	1,078	1,865
9.0 x 10^6	4,495	7,690	1,543	5,970	2,120	2,240	1,045	1,805
1.0 x 10^7	4,150	7,540	1,499	5,945	1,725	2,185	1,017	1,745

For the dense specimen (e = 0.7), swell pressure decreases with increasing particle velocity (Figure 5.17). While the trend is not linear, there is a correlation between swell pressure and V_{MAX}. Additionally, the trend is the same for L_{DEM} = 25, 35, and 45nm. While swell pressures were higher for L_{DEM} = 25 nm, there was little variation between L_{DEM} = 35 and 45 nm as particle velocity increased. However, swell pressure remains mostly constant for L_{DEM} = 55 nm.

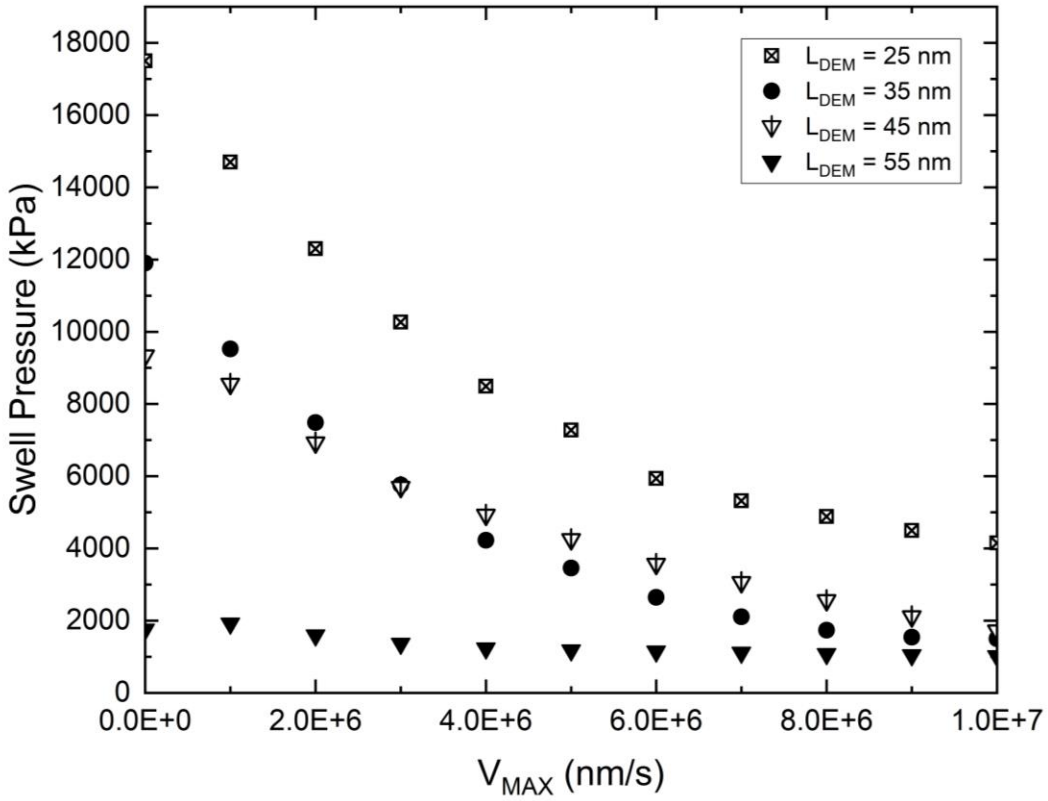

Figure 5.17. Effect of particle velocity on swell pressure and varying L_{DEM}, e = 0.7. H_{DEM} = 5.307 nm, V_{WALL} = 5.0 x 10^6 nm/s.

For the moderately dense specimen (e = 1.0), swell pressures also decreased with increasing particle velocity (Figure 5.18). There is a nonlinear correlation between swell pressure and V_{MAX}. Additionally, the trend is the same for L_{DEM} = 25, 35, and 45nm. Swell pressures remained mostly constant for the L_{DEM} = 55 nm specimen.

Table 5.21. Effect of particle velocity and discrete element length on swell pressure, e = 1.0; H_{DEM} = 5.307 nm; V_{WALL} = 5 x 10^6 nm/s

V_{MAX} (nm/s)	L_{DEM} = 25 nm		L_{DEM} = 35 nm		L_{DEM} = 45 nm		L_{DEM} = 55 nm	
	σ_S (kPa)	σ_H (kPa)	σ_S (kPa)	σ_H (kPa)	σ_S (kPa)	σ_H (kPa)	σ_S (kPa)	σ_H (kPa)
0	6,510	3,035	4,350	4,005	2,000	428	386	0
1.0 x 10^6	4,885	2,200	3,360	3,255	1,095	343	66	0
2.0 x 10^6	3,415	1,685	2,660	2,800	501	335	0	0
3.0 x 10^6	2,545	1,345	2,130	2,680	278	322	0	0
4.0 x 10^6	1,970	1,265	1,815	2,575	178	315	0	0
5.0 x 10^6	1,670	1,175	1,735	2,590	179	304	0	0
6.0 x 10^6	1,393	1,125	1,714	2,600	207	299	0	0
7.0 x 10^6	1,281	1,075	1,753	2,730	237	294	0	0
8.0 x 10^6	1,197	1,015	1,822	2,755	266	288	0	0
9.0 x 10^6	1,136	954	1,892	2,910	975	755	0	0
1.0 x 10^7	1,152	939	1,965	2,865	1,330	1,290	0	0

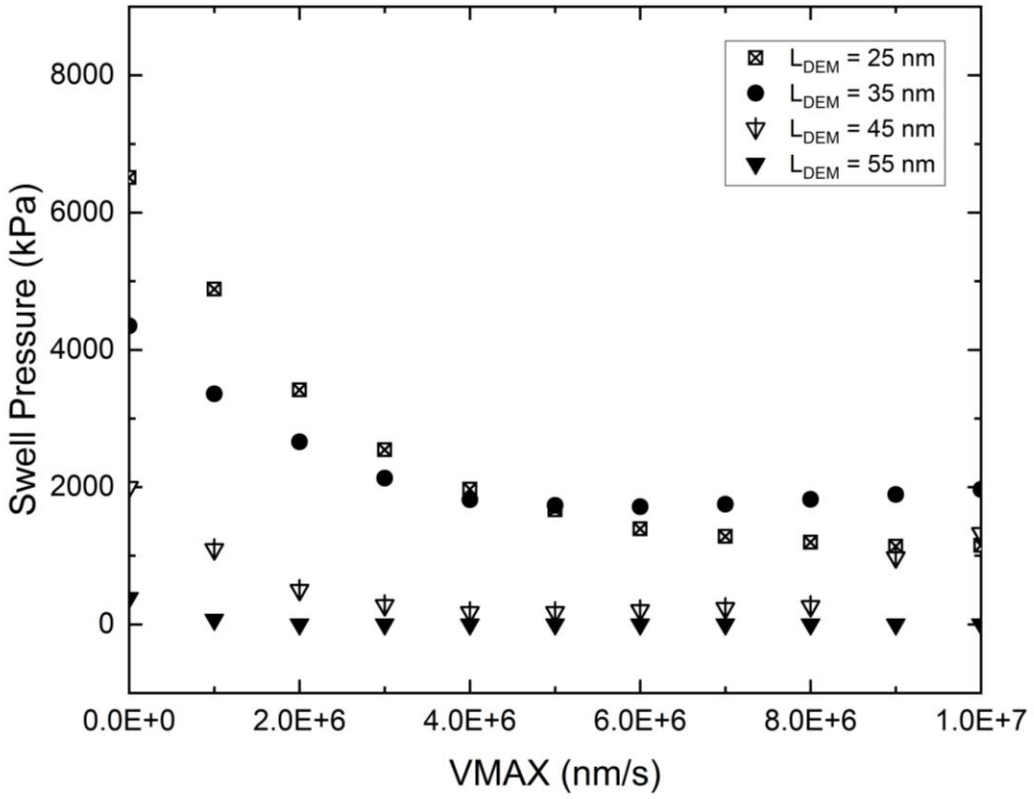

Figure 5.18. Effect of particle velocity on swell pressure and varying $L_{DEM,}$ e = 1.0. H_{DEM} = 5.307 nm, V_{WALL} = 5.0 x 10^6 nm/s.

For the loose specimen (e = 1.25), swell pressures were mostly zero for all discrete element lengths tested (Figure 5.19). No trend was discernable between swell pressure and particle velocity for this loose particle assembly between V_{MAX} = 0 and 1 x 10^7 nm/s. There was a slight decrease between particle velocities of 0 and 4 x 10^6 nm/s; however, there are not enough nonzero values to develop any mathematical relation. The randomness of the relation in this range is likely due to the high void ratio: because the particles are not closely packed in the assembly, particles are less likely to encounter interparticle mechanical interactions as the denser specimens and therefore particle velocity is less influential.

Table 5.22. Effect of particle velocity and discrete element length on swell pressure, e = 1.25; H_{DEM} = 5.307 nm; V_{WALL} = 5 x 10^6 nm/s

V_{MAX} (nm/s)	L_{DEM} = 25 nm		L_{DEM} = 35 nm		L_{DEM} = 45 nm		L_{DEM} = 55 nm	
	σ_S (kPa)	σ_H (kPa)	σ_S (kPa)	σ_H (kPa)	σ_S (kPa)	σ_H (kPa)	σ_S (kPa)	σ_H (kPa)
0	756	117	118	-	-	-	-	-
1.0 x 10^6	343	18	17	-	-	-	-	-
2.0 x 10^6	135	-	-	-	-	-	-	-
3.0 x 10^6	70	-	-	-	-	-	-	-
4.0 x 10^6	15	-	-	-	-	-	-	-
5.0 x 10^6	46	-	-	-	-	-	-	-
6.0 x 10^6	129	-	-	-	-	-	-	-
7.0 x 10^6	211	-	-	-	-	-	-	-
8.0 x 10^6	292	-	-	-	-	-	-	-
9.0 x 10^6	374	-	-	-	-	-	-	-
1.0 x 10^7	455	28	-	-	52	-	-	-

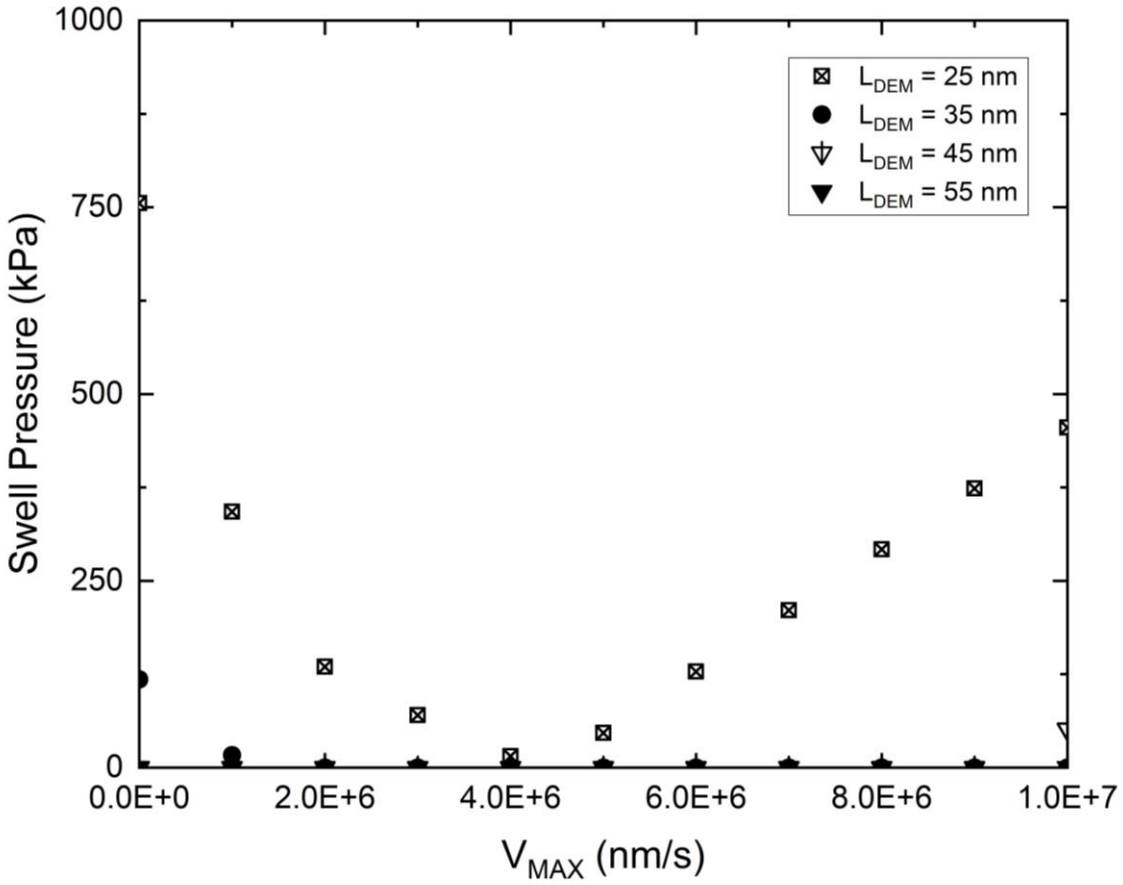

Figure 5.19. Effect of particle velocity on swell pressure and varying $L_{DEM,}$ e = 1.25. H_{DEM} = 5.307 nm, V_{WALL} = 5.0 x 10^6 nm/s, V_{MAX} between 0 and 1 x 10^7 nm/s

There is clearly a complex, nonlinear relationship between V_{MAX}, swell pressure, and void ratio. A transition occurs between dense and loose specimens at e = 1.0 where swell pressure decreases with decreasing particle velocity between V_{MAX} = 0 and 1 x 10^7 nm/s. For loose specimens, however, swell pressures increase with increasing particle velocity (Figure 5.20). While swell pressures remain zero for loose specimens with large discrete element length (i.e., e = 1.25, L_{DEM} = 55 nm), there is a nonlinear increase in swell pressure with increasing particle velocity for the range of V_{MAX} between 6 x 10^6 and 5 x 10^7 nm/s (Table 5.23). Moreover, swell pressure decreases as L_{DEM} decreases.

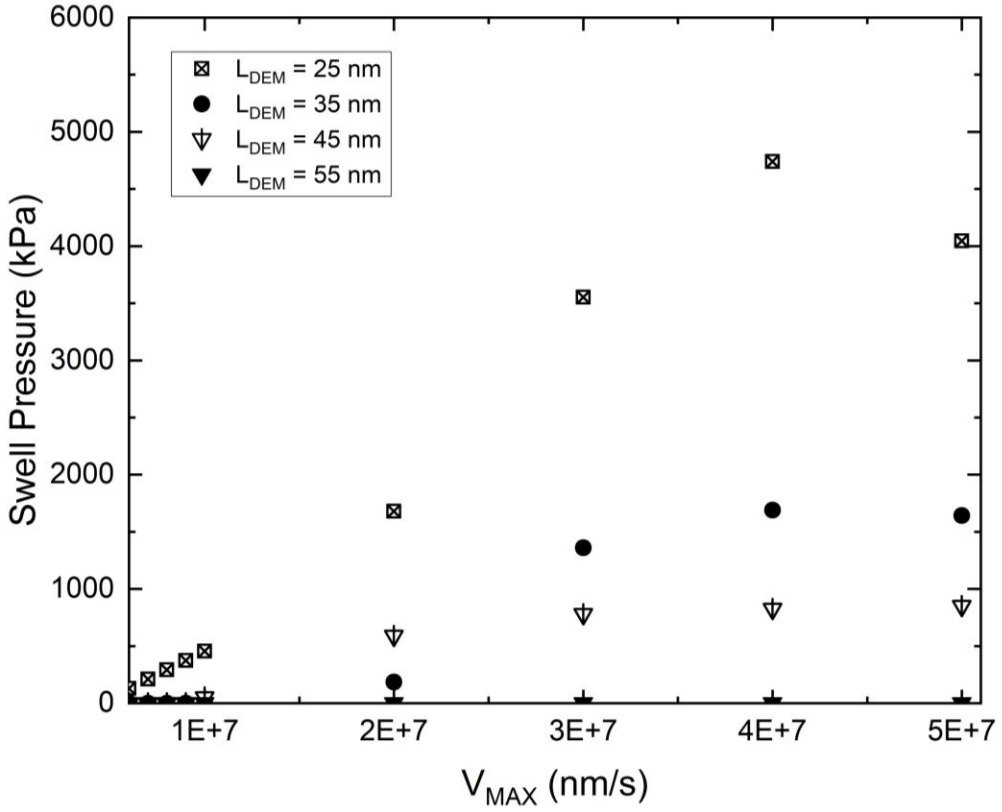

Figure 5.20. Effect of particle velocity on swell pressure and varying $L_{DEM,}$ e = 1.25. H_{DEM} = 5.307 nm, V_{WALL} = 5.0 x 10^6 nm/s, V_{MAX} between 6 x 10^6 and 5 x 10^7 nm/s

Table 5.23. Effect of particle velocity on swell pressure and varying L_{DEM}, e = 1.25. H_{DEM} = 5.307 nm, V_{WALL} = 5.0 x 106 nm/s, V_{MAX} between 6 x 10^6 and 5 x 10^7 nm/s

V_{MAX} (nm/s)	L_{DEM} = 25 nm		L_{DEM} = 35 nm		L_{DEM} = 45 nm		L_{DEM} = 55 nm	
	σ_S (kPa)	σ_H (kPa)	σ_S (kPa)	σ_H (kPa)	σ_S (kPa)	σ_H (kPa)	σ_S (kPa)	σ_H (kPa)
6.0 x 10^6	129	-	-	-	-	-	-	-
7.0 x 10^6	211	-	-	-	-	-	-	-
8.0 x 10^6	292	-	-	-	-	-	-	-
9.0 x 10^6	374	-	-	-	-	-	-	-
1.0 x 10^7	455	28	-	-	52	-	-	-
2.0 x 10^7	1,680	680	185	195	590	-	-	-
3.0 x 10^7	3,554	1,020	1,360	1,175	780	660	-	-
4.0 x 10^7	4,740	1,010	1,690	2,100	825	655	-	-
5.0 x 10^7	4,045	975	1,642	2,350	850	655	-	-

5.4.1.7.2 Relationship between V_{MAX} and H_{DEM}

The effect of particle velocity on swell pressure for varying discrete element thicknesses was studied for void ratios e = 0.7 (Table 5.24) and e = 1.0 (Table 5.25). Particle length (L_{DEM}) was kept at 25 nm and wall velocity (V_{WALL}) was maintained throughout each iteration at 5 x 10^6 nm/s with K_0 = 1.0 conditions. Discrete element thickness (H_{DEM}) was varied using H_{DEM} = 5, 10, 15, 20, and 30 nm.

Table 5.24. Effect of particle velocity and discrete element thickness on vertical swell pressure, e = 0.7, L_{DEM} = 25 nm; V_{WALL} = 5 x 10^6 nm/s

V_{MAX} (nm/s)	H_{DEM} = 5	H_{DEM} = 10	H_{DEM} = 15	H_{DEM} = 20	H_{DEM} = 30
0	16,100	22,950	38,700	68,400	-
1.0 x 10^6	13,800	19,400	35,150	62,900	-
2.0 x 10^6	11,750	16,450	31,700	57,600	-
3.0 x 10^6	10,065	14,000	28,250	52,400	-
4.0 x 10^6	9,220	11,965	24,900	47,350	-
5.0 x 10^6	8,110	10,115	21,950	42,600	-
6.0 x 10^6	7,165	8,355	19,450	37,900	-
7.0 x 10^6	6,395	7,415	17,600	33,750	-
8.0 x 10^6	5,740	6,335	15,850	29,850	-
9.0 x 10^6	5,480	5,615	14,300	26,650	-
1.0 x 10^7	5,145	4,845	13,200	23,950	-

For the loose specimen (e = 0.7), swell pressure decreased as particle velocity increased (Figure 5.21). Unlike the relationship between L_{DEM} and V_{MAX}, the slope of the trend is not the same for differing values of H_{DEM}. While all swell pressures decreased with increasing V_{MAX}, as H_{DEM} increases, the slope of the trendline flattens, and reduces to zero for H_{DEM} = 30 nm.

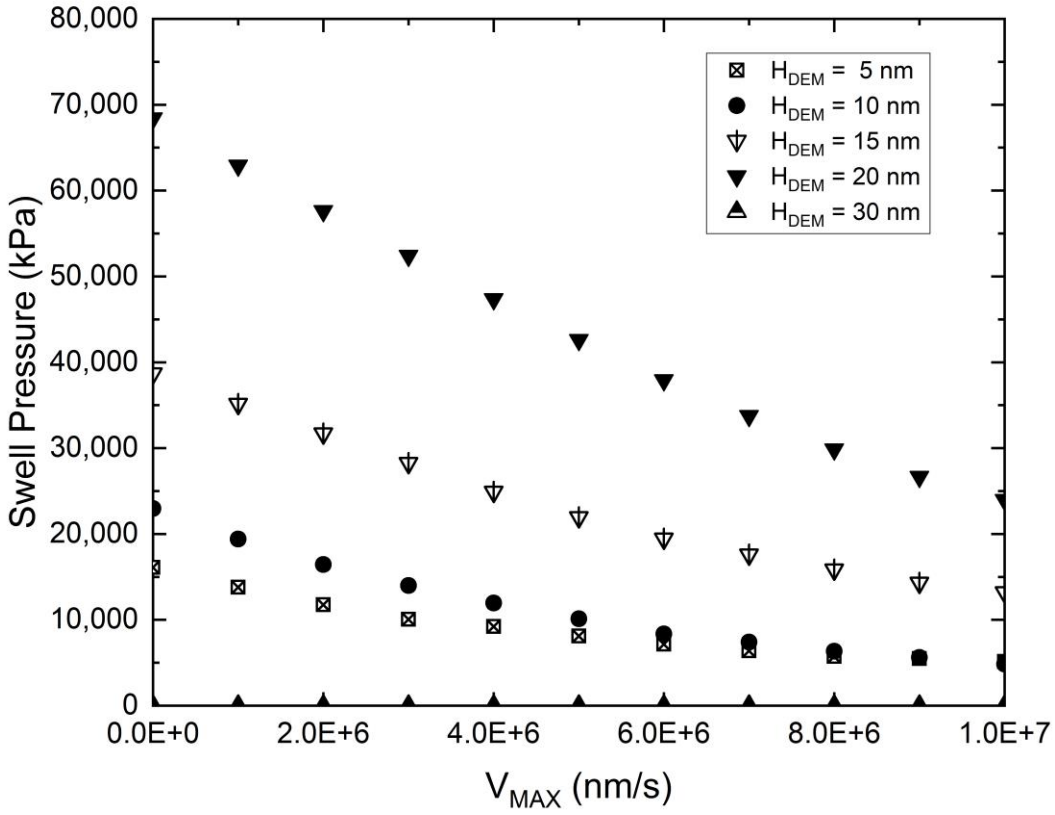

Figure 5.21. Effect of particle velocity on swell pressure and varying $H_{DEM,}$ e = 0.7. L_{DEM} = 25 nm, V_{WALL} = 5.0 x 10^6 nm/s.

For the denser specimen (e = 1.0), swell pressure decreased as particle velocity increased (Figure 5.22). The swell pressure decreased with increasing V_{MAX} for all values of H_{DEM}. Moreover, as H_{DEM} increased, the slope of the trendline flattened, and reduces to zero for H_{DEM} = 30 nm, similar to the behavior of the dense specimen.

Table 5.25. Effect of particle velocity and discrete element thickness on vertical swell pressure, e = 1.0, L_{DEM} = 25 nm; V_{WALL} = 5 x 10^6 nm/s

V_{MAX} (nm/s)	H_{DEM} = 5	H_{DEM} = 15	H_{DEM} = 20	H_{DEM} = 30
0	6,050	6,940	12,350	-
1.0 x 10^6	4,865	5,815	10,235	-
2.0 x 10^6	3,990	5,275	8,585	-
3.0 x 10^6	3,505	4,775	7,240	-
4.0 x 10^6	3,255	4,110	6,115	-
5.0 x 10^6	3,130	3,655	5,220	-
6.0 x 10^6	3,075	3,255	4,595	-
7.0 x 10^6	3,025	2,715	4,265	-
8.0 x 10^6	3,005	2,375	4,050	-
9.0 x 10^6	3,020	2,200	3,935	-
1.0 x 10^7	3,095	1,735	3,875	-

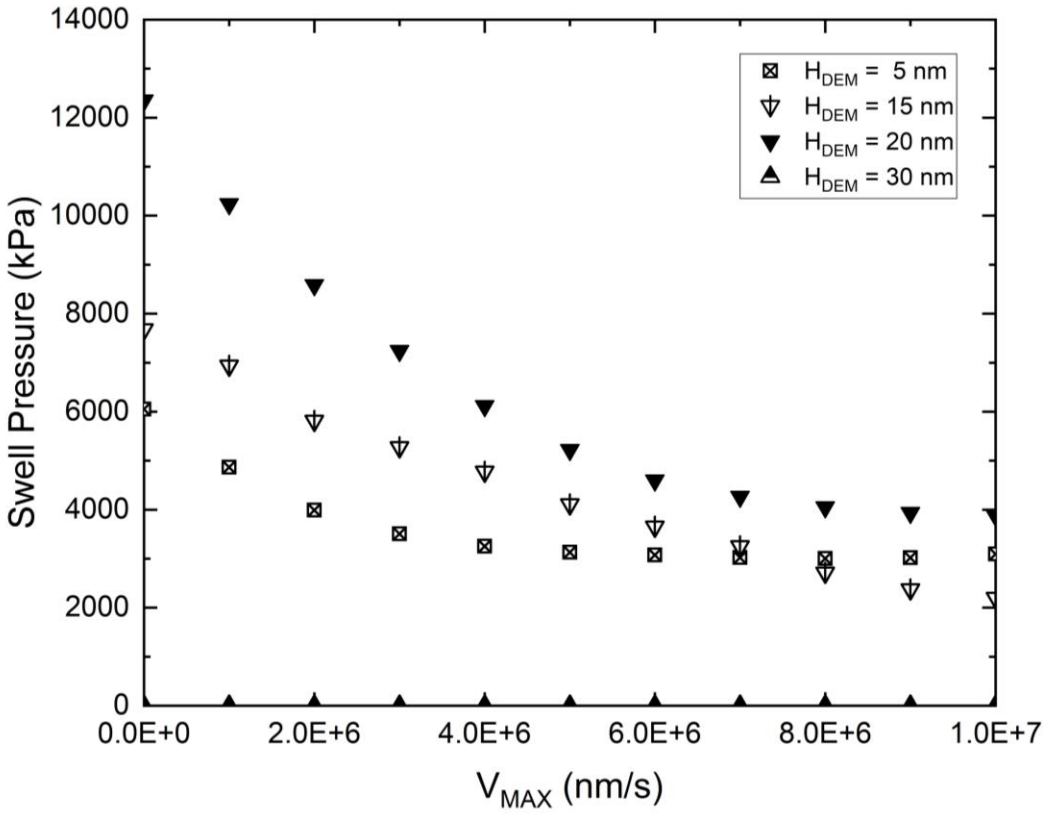

Figure 5.22. Effect of particle velocity on swell pressure and varying $H_{DEM,}$ e = 1.0. L_{DEM} = 25 nm, V_{WALL} = 5.0 x 10^6 nm/s.

5.4.1.7.3 Relationship between V_{MAX} and e

To further investigate the relationship between V_{MAX} and e in loose specimens (i.e., void ratio greater than 1.0), a series of simulations were performed for void ratios 1.1, 1,2, 1.3, 1,4, 1.5, and 3.0 with a particle thickness H_{DEM} = 5.307 nm and discrete element length L_{DEM} = 30 nm (Table 5.26). K_0 conditions were maintained for each simulation with horizontal and vertical wall velocity maintained at $V_{WALL} = 5 \times 10^6$ nm/s.

Table 5.26. Effect of particle velocity (V_{MAX}) on swell pressure by varying void ratio. $V_{WALL} = 5 \times 10^6$ nm/s, L_{DEM} = 30 nm, H_{DEM} = 5.307 nm.

V_{MAX} (nm/s)	e = 1.1	e = 1.2	e = 1.3	e = 1.4	e = 1.50	e = 3.0
5.0×10^6	3,480	2,340	82	-	184	-
6.0×10^6	3,070	2,110	49	-	-	-
7.0×10^6	2,845	1,895	36	22	18	-
8.0×10^6	2,665	1,715	103	103	67	-
9.0×10^6	2,505	1,570	191	188	121	-
1.0×10^7	2,350	1,430	287	282	184	-
2.0×10^7	2,332	1,165	287	97	745	-
3.0×10^7	1,984	1,255	1,345	1,490	985	-
4.0×10^7	1,960	1,270	1,715	2,025	1,165	-
5.0×10^7	1,938	1,390	1,645	1,890	1,335	290

For loose specimens (i.e., e greater than 1.0), there is a transition point between e = 1.1 and e = 1.3 regarding the effect of V_{MAX} on swell pressure (Figure 5.23). For assemblies with e = 1.1 and e = 1.2, swell pressure decreases as particle velocity decreases, leveling off around $V_{MAX} = 2 \times 10^7$ nm/s. For looser assemblies with e = 1.4 and e = 1.5, swell pressure increases with increasing particle velocity, leveling off around $V_{MAX} = 2 \times 10^7$ nm/s. It seems that swell pressures converge to similar swell pressures for e = 1.1 to e = 1.5 at $V_{MAX} = 5 \times 10^7$ nm/s. However, for the very loose specimens (i.e., e = 3.0), swell pressure is zero until reaching particle velocities greater than $V_{MAX} = 4.5 \times 10^7$ nm/s.

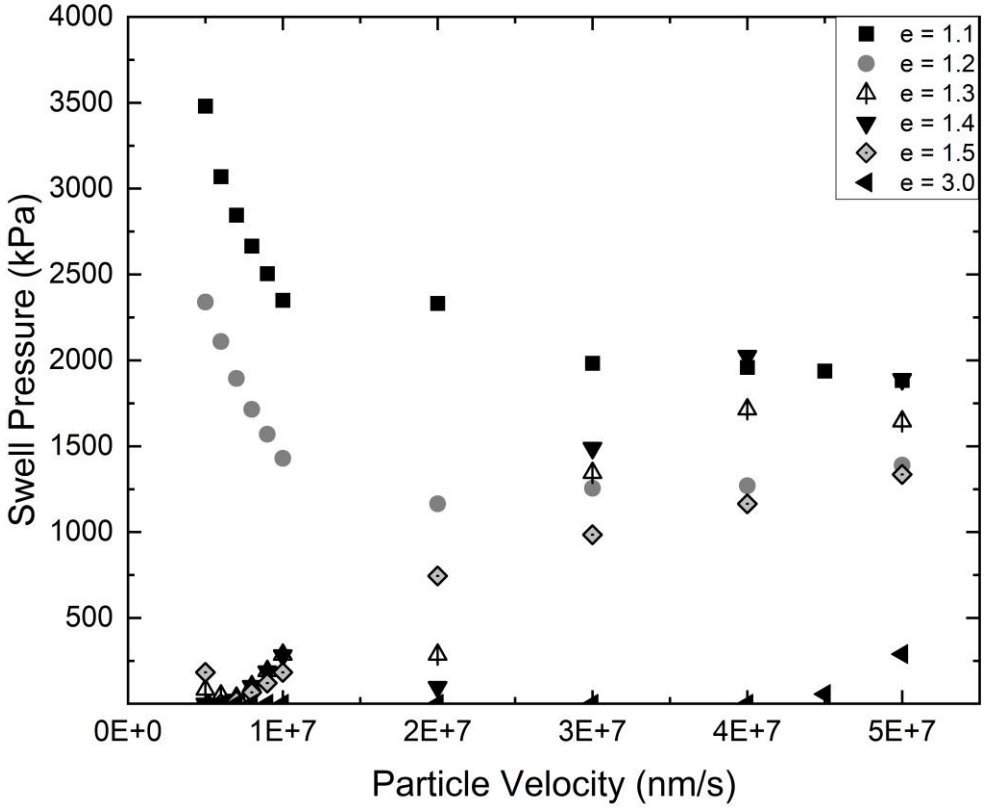

Figure 5.23. Effect of particle velocity (V_{MAX}) and void ratio on swell pressure. L_{DEM} = 30 nm, H_{DEM} = 5.307 nm, V_{WALL} = 5 x 10^6 nm/s.

5.4.1.8 Free Swell Testing of Na-montmorillonite

After the relationship between the input parameters and swell pressures were developed through the sensitivity study, DEMClay was calibrated to predict swell pressures of a single-mineral clay (Swy Na-montmorillonite) at varying void ratios. Experimental data was necessary to develop a swell pressure-void ratio relationship for the soil with known CEC, S_A parameters. One-dimensional swell tests were performed on specimens of Swy Na-montmorillonite to calibrate the swell pressures obtained using DEMClay. Swell tests were performed according to ASTM D4546-

14, method A and ASTM D2435-04 with a seating load of 1.5 kPa. The results of these swell tests are presented in Figure 5.24.

Specimens were compacted inside an oedometer ring (7.1 cm diameter, 1.9 cm height) at void ratios ranging from 1.1 to 3.0, seated in the oedometer cell, and inundated with distilled water until reaching equilibrium. Once the specimens swelled to their maximum potential (i.e., equilibrium state), incremental loading according to ASTM D2435-04 was performed until returning to the original specimen height.

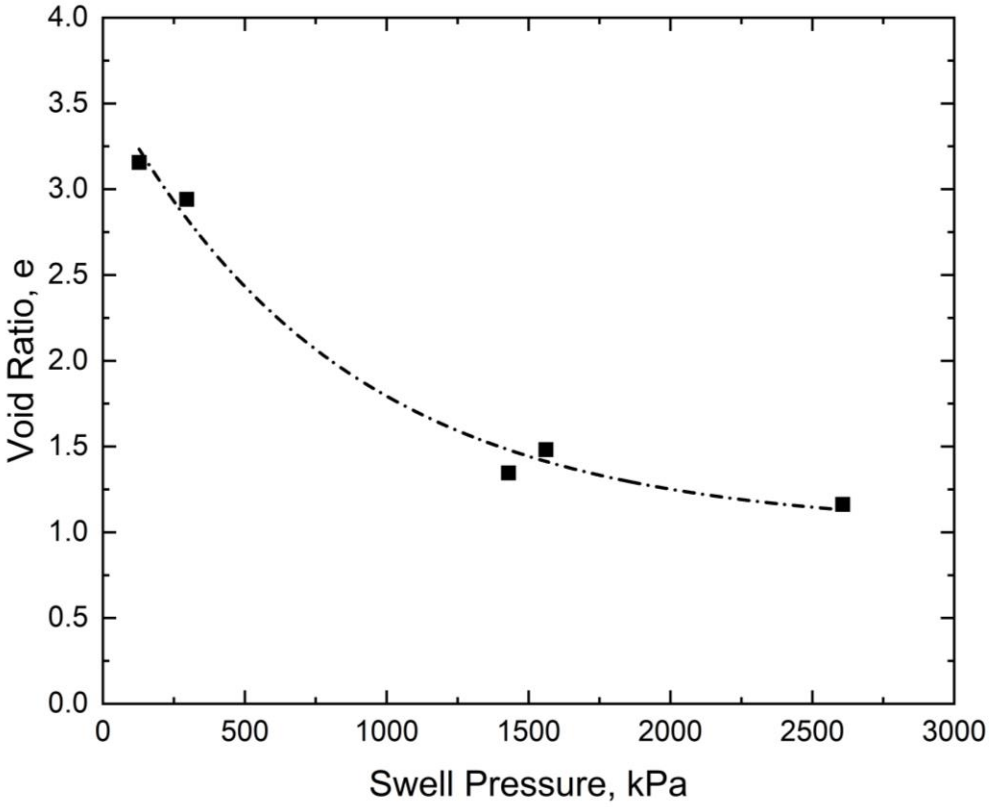

Figure 5.24. Swell pressures of Swy Na-montmorillonite from one-dimensional free swell tests.

The results of this study are compared to that reported in the literature for natural montmorillonite-bearing soils with varying dry density, montmorillonite content, and sampling locations (Table 5.27). Because void ratio and specific gravity were not reported for every study,

results are compared using dry density rather than void ratio (Figure 5.25). The results of this study show good agreement with that of Karnland et al. (2006) for the Milos Na-montmorillonite and Wyoming Na-montmorillonite, better detailed in Figure 5.26, which compares the soils between swell pressures of 0 and 5,000 kPa.

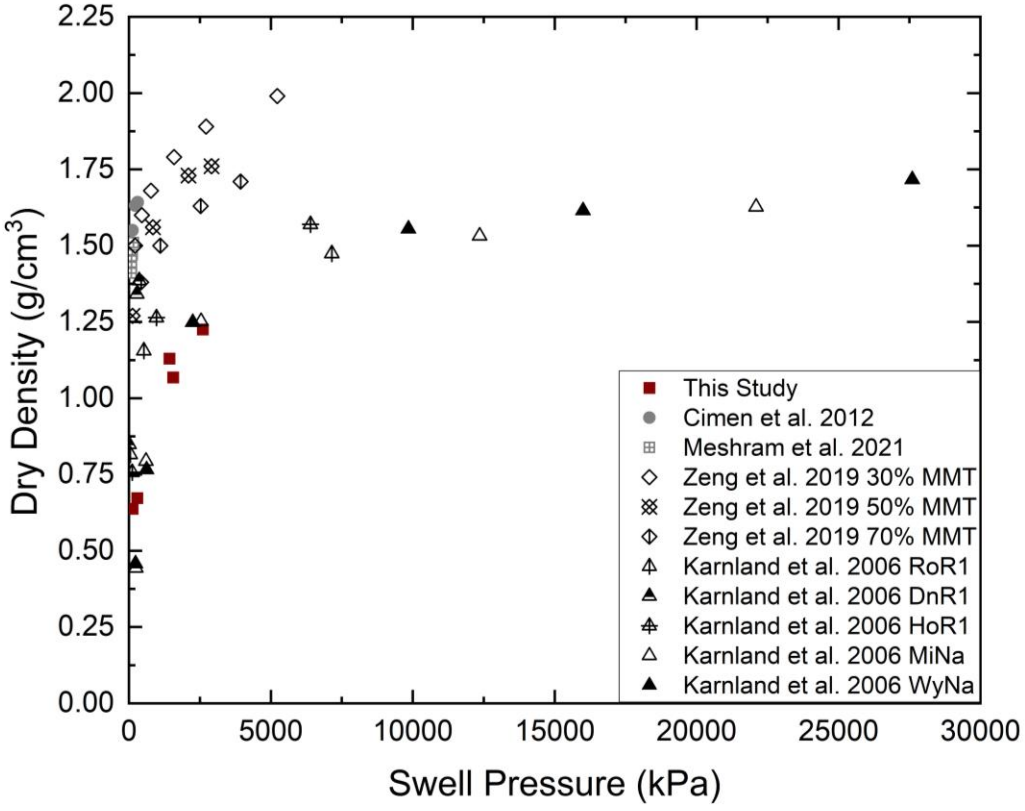

Figure 5.25. Swell pressures of montmorillonite-bearing soils

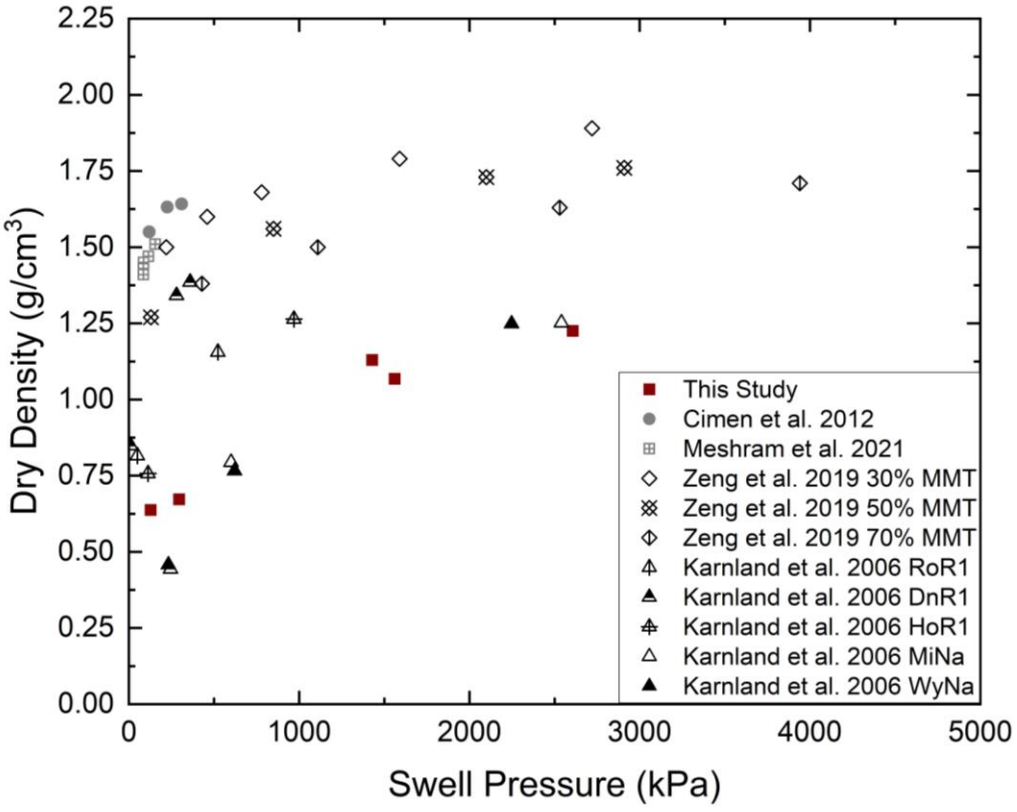

Figure 5.26. Swell pressures of Na-montmorillonite bearing soils (0 to 5,000 kPa)

The free swell testing in this study and in Cimen et al. (2012) was performed using a strain-controlled method, i.e., allowing the specimen to swell, incrementally loading the specimen to the original height, then interpreting the swell pressure from the load required to return to 0% strain. This method simulates the loading conditions of a lightweight structure near-surface such as highways and railways (Kayabali and Demir 2011). Stress-controlled swell testing utilizes a load cell and force transducer, which does not allow deformation, but instead interprets the swell pressure as the load necessary to maintain a constant volume (IAEA 2013; Zeng et al. 2019), which simulates the loading of a soil under a grade-beam, for example. The results of interpreted swell pressures between the methods are comparable (IAEA 2013). This can be viewed in this study (Figure 5.26) where the strain-controlled swell pressures of the Na-montmorillonite of this study

are comparable to the stress-controlled swell pressures of Karnland et al. (2006), Zeng et al. (2019), and Meshram et al. (2021). However, Kayabali and Demir (2011) found that the strain-controlled free swell method and stress-controlled method showed high correlation but the strain-controlled procedure overpredicted swell pressures of Ankara clays due to the higher pressure needed to expel pore water absorbed by the soil during inundation and saturation.

While the data resulting from laboratory testing of Na-montmorillonite shows good agreement with that reported in the literature, there are several important limitations associated with using this method. Most importantly, Na-montmorillonite has a high swelling capacity and at high dry densities (low void ratios), can reach swell pressures in the 1-10 MPa range (e.g., Karnland et al. 2006; Zeng et al. 2019). With the oedometer setup used with ASTM D4546, the lever arm is no longer balanced once reaching greater loading conditions and the setup could tip or possibly break the lever arm. Based on experimental trials conducted in this study, loading at pressures greater than 2 MPa is the reasonable maximum for this setup and greater pressures are not recommended. Therefore, loading beyond these pressures for very dense specimens is not possible using this procedure and a constant-volume cell with an attached load cell should be used instead.

Table 5.27. Swell pressures reported for montmorillonite-bearing soils.

Reference	Soil	Dry Density (g/cm^3)	Montmorillonite Content (%)	Swell Pressure (kPa)
Karnland et al. 2006	Wyoming - WyNa	0.458	81.4	232
		0.766	81.4	621
		1.249	81.4	2248
		1.555	81.4	9850
		1.615	81.4	16000
		1.717	81.4	27600
Karnland et al. 2006	Milos – MiNa	0.444	80.6	245
		0.794	80.6	600
		1.252	80.6	2540
		1.532	80.6	12360
		1.627	80.6	22100
Karnland et al. 2006	Czech - RoR1	0.816	69.4	50
		1.156	69.4	523
		1.474	69.4	7150
Karnland et al. 2006	Danish - HoR1	0.757	59	113
		1.264	59	970
		1.57	59	6400
Karnland et al. 2006	Czech - DnR1	0.849	21	10
		1.386	21	360
		1.342	21	280
Cimen et al. 2012	Bentonite	1.642	55	310
		1.632	52	225
		1.550	50	120
Zeng et al. 2019	MX80/COx	1.50	30	220
		1.60	30	460
		1.68	30	780
		1.79	30	1590
		1.89	30	2720
		1.99	30	5230
Zeng et al. 2019	MX80/COx	1.27	50	130
		1.56	50	850
		1.73	50	2100
		1.76	50	2910
Zeng et al. 2019	MX80/COx	1.38	70	430
		1.50	70	1110
		1.63	70	2530
		1.71	70	3940
Keskin et al. 2023	Bentonite	1.173	75	275
		1.214	77	275
Meshram et al. 2021	BC-Bentonite	1.51	10	155
		1.47	20	115
		1.45	30	87
		1.43	40	86
		1.41	50	85

5.4.1.9 Calibration of Model Using Swy Na-montmorillonite

Results of one-dimensional free swell tests were used to calibrate the results of assemblies of Swy Na-montmorillonite obtained using the DEMClay swell pressure model. Vertical swell pressures ($\sigma_{s,V}$) were obtained by averaging the swell pressures along the horizontal walls (W1 and W3) and horizontal (lateral) swell pressures ($\sigma_{s,H}$) were obtained by averaging the swell pressures along the vertical walls (W2 and W4). Inputs specific to Na-montmorillonite, which were not changed, include the height of the discrete element (H_{DEM}), specific surface area (S_A), cation exchange capacity (CEC), and surface potential (ψ_0). Particle spacing and surface potential are functions of the S_A and CEC as well as the chemistry of the pore fluid. For this study, pore fluid parameters reflect that of distilled water. The interlayer and interparticle attractive force was modeled through the Hamaker constant, here 0.87×10^{-20} J, discussed in *5.3.2.3*. These constant inputs are presented in Table 5.28.

Table 5.28. Constant parameters specific to Swy Na-montmorillonite

H_{DEM} (nm)	A (J)	S_A (m^2/g)	CEC (meq/100g)	ψ_0 (mv)
5.307	0.87×10^{-20}	637.0	76.4	116.0

Other parameters not inherent to Swy Na-montmorillonite were changed to calibrate the results to more closely match the experimental results. Particle velocity, wall velocity, number of discrete elements, and discrete element length were initially the same as those used by Anandarajah and Amarasinghe (2013), as a reference point. Assemblies were initially modeled with 10,000 discrete elements per assembly. As discussed in Section *5.4.1.1*, the smallest number of discrete elements to use without negatively affecting the void ratio and swell pressure was 4,000, therefore assemblies of 4,000 discrete elements were used in the calibration of the model. The initial discrete element length was 25 nm, which gives a 5:1 ratio between length and height of the smallest

particle size. The initial maximum particle velocity (V_{MAX}) was 6.0 x 10^6 nm/s and the initial wall velocity (V_{WALL}) was 5.0 x 10^6 nm/s on both the vertical and horizontal walls. Only K_0 = 1 conditions were considered when calibrating the model. However, differing K_0 conditions are discussed in section *5.4.1.6*.

The model was initially run with the same model parameters used in DEMClay$_{2013}$ (Table 5.29), with N_{ELEM} updated to 4,000 discrete elements and H_{DEM} = 5.307 nm (Initial) to reflect Swy Na-montmorillonite. Different void ratios were obtained by changing the minimum spacing allowed between particles via the *S* parameter as discussed in Section *5.4.1.2*. The initial input parameters did not capture the relationship between density and swell pressure (Figure 5.27). Therefore, discrete element length was changed to L_{DEM} = 30 nm (Iteration A) to better reflect the greater particle thickness of Swy Na-montmorillonite to the Na-montmorillonite used with DEMClay$_{2013}$. While swell pressures were still zero for loose specimens (Table 5.30), there were nonzero values for e = 1.3. Next, V_{MAX} was changed to 1 x 10^6 nm/s (Iteration B). While there were nonzero values for e < 1.5, the swell pressures values were too high for e < 1.3 and too low for e > 1.34 (Table 5.30). Therefore, based on the results of the sensitivity study for L_{DEM} = 30 nm and loose assemblies (e.g., Figure 5.23), a value of 5 x 10^7 nm/s was used for V_{MAX} to better match swell pressures for void ratios greater than 1.5 (Iteration C).

Table 5.29. Initial and final model parameters

Iteration	V_{MAX} (nm/s)	V_{WALL} (nm/s)	L_{DEM} (nm)	N_{ELEM}
Initial	6 x 10^6	5 x 10^6	25	4,000
A	6 x 10^6	5 x 10^6	30	4,000
B	1 x 10^6	5 x 10^6	30	4,000
C	5 x 10^7	5 x 10^6	30	4,000
Final	Varies	5 x 10^6	30	4,000

Swell pressures began to converge toward experimental results, particularly for large void ratios, but for void ratios between 1.0 and 1.5, the swell pressure was less than experimental. After several iterations, using $V_{MAX} = 5 \times 10^7$ nm/s provided the closest values to experimental. Selected iterations are shown in Figure 5.27. It is important to note that the appropriate choice of V_{MAX} to allow the model to predict swell pressure most accurately is quantified by an exponential decay and a power relationship between V_{MAX} and void ratio depending on whether the void ratio is below 1.1 or above 1.3, respectively. There is a transition zone between void ratios of 1.1 and 1.3.

Using the five different samples of Swy Na-montmorillonite, all at different void ratios, and the subsequent iterations of V_{MAX} that most closely approximated the experimental swell pressure values for each void ratio, an exponential decay relationship was determined (Figure 5.28) between V_{MAX} and void ratio greater than 1.1 (looser soils). Using the particle velocity determined through the exponential decay relationship for each void ratio, DEMClay swell pressures were determined (Final) which converged toward the experimental values. This relationship allows the user to choose an appropriate V_{MAX} for any soil with sample void ratios between 1.1 and 3.0.

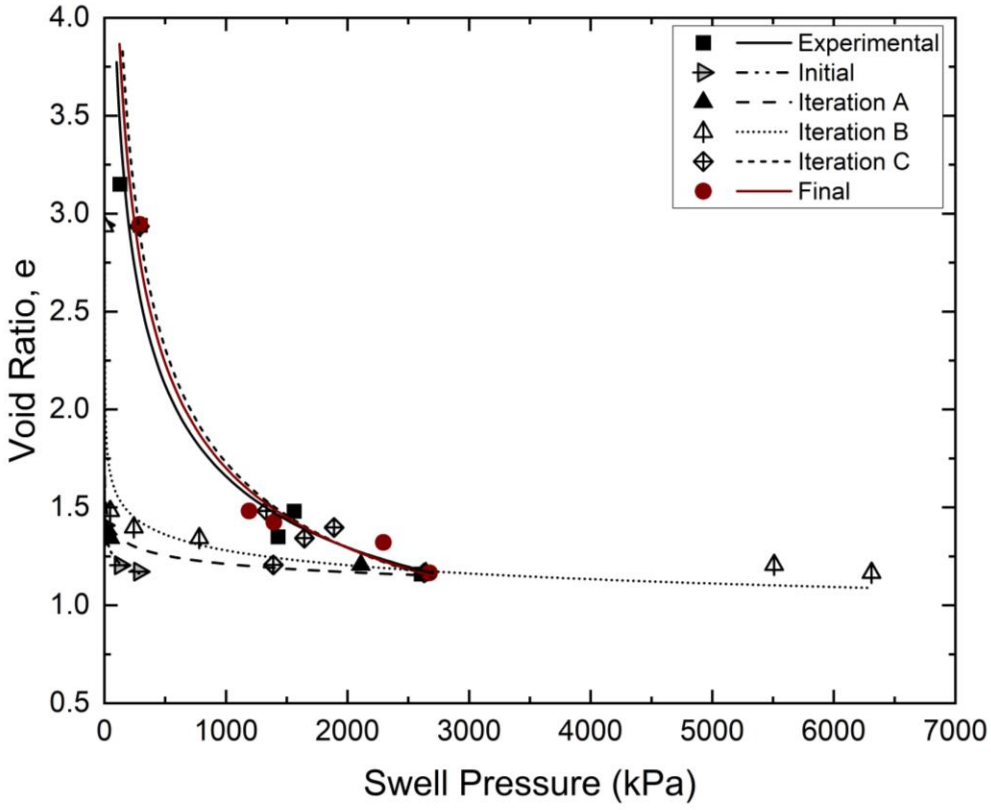

Figure 5.27. Calibration of DEMClay to Swy Na-montmorillonite

It is notable that while the Final values are closer to the experimental values, the swell pressures obtained in Iteration C using V_{MAX} = 5 x 10^7 nm/s also converge on the experimental swell pressures (Figure 5.27). This is likely due to the convergence of all the samples at varying void ratios around a V_{MAX} = 5 x 10^7 nm/s within the swell pressure range 1000 – 2500 kPa noted in Figure 5.23.

Table 5.30. Swell pressures for selected iterations of DEMClay.

Initial		Iteration A		Iteration B		Iteration C		Final	
e	σ_s (kPa)	e	σ_s (kPa)	e	σ_s (kPa)	e	σ_s (kPa)	e	σ_s (kPa)
3.0	-	3.0	-	3.0	-	3.0	290	3.0	291
1.5	-	1.5	-	1.5	49	1.5	1,335	1.5	1,190
1.4	-	1.4	-	1.4	242	1.4	1,890	1.4	1,395
1.3	-	1.3	49	1.3	781	1.3	1,645	1.3	2,295
1.2	287	1.2	2,645	1.2	6,310	1.2	2,632	1.2	2,675

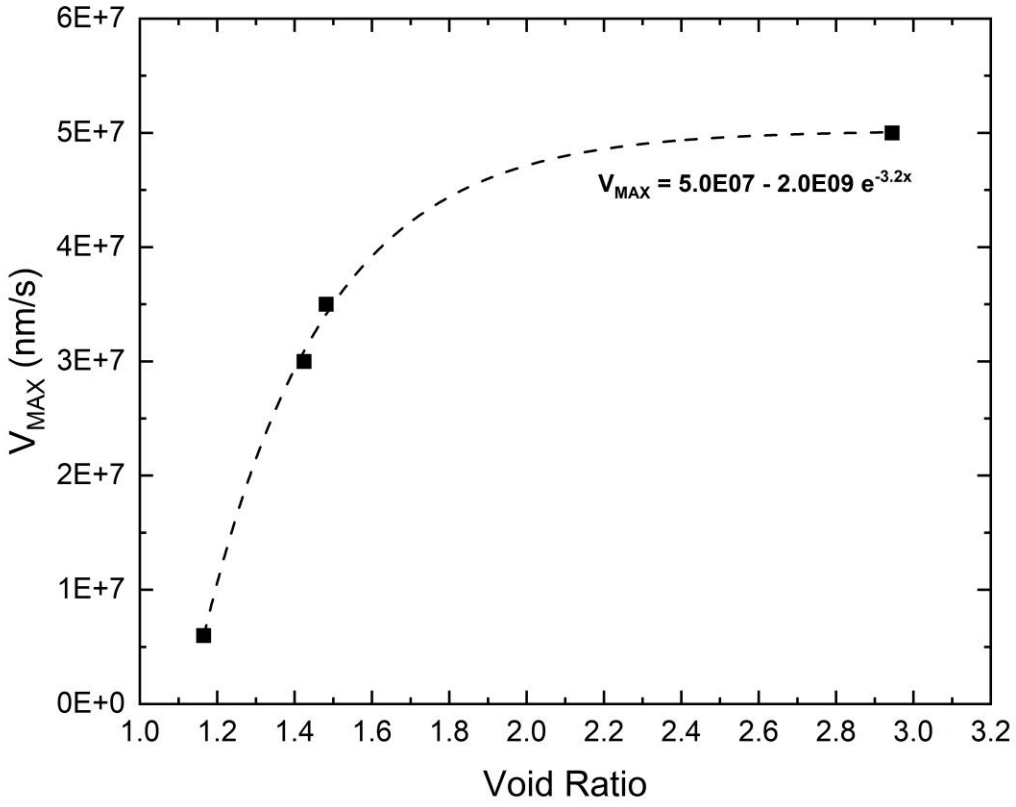

Figure 5.28. Relationship between void ratio and particle velocity for loose specimens with void ratios greater than 1.1.

Due to the high swelling nature of the Swy Na-montmorillonite, the samples could not be compacted to void ratios denser than 1.1 without exceeding the testing capabilities of the rear-

loading Wykeham Farrance frames. Therefore, values from the literature were pulled in an attempt to create a calibration between V_{MAX} and void ratio for void ratios less than 1.1. The soils found in the literature had experimental swell pressures determined from samples with void ratios detailed in Table 5.31. The input parameters used in the DEMClay model for these three soils are shown in Table 5.32.

Table 5.31. Results of DEMClay simulations of montmorillonite soils

WyR1				WyNa				FrNa			
Experimental		DEMClay		Experimental		DEMClay		Experimental		DEMClay	
e	σ_S	e	σ_S	e	σ_S	e	σ_S	e	σ_S	e	σ_S
2.65	156	2.65	0	2.63	621	2.65	0	2.59	80	2.58	0
1.31	1,020	1.34	1,017	1.23	2,248	1.24	1,990	1.35	500	1.32	460
0.90	4,190	0.91	4,470	0.79	9,850	0.79	8,435	0.95	1,640	0.93	3,645
0.81	7,590	0.83	7,345	0.72	16,000	0.72	13,950	0.69	4,100	0.68	16,050
0.69	12,470	0.70	12,500	0.62	27,600	0.62	24,750	0.57	8,960	0.58	25,900

Note: All swell pressure values in kPa

Table 5.32. Input parameters for Na-montmorillonite soils in literature

Soil	N_{ELEM}	L_{DEM} (nm)	H_{DEM} (nm)	V_{MAX} (nm/s)	V_{WALL} (nm/s)	ψ_0 (mv)	CEC (meq/100g)	S_A (m^2/g)
WyR1[1]	4,000	25	4.493	Varies	5 x 10^6	196.0	86.0	750.0
WyNa[1]	4,000	25	4.493	Varies	5 x 10^6	193.0	80.0	750.0
FrNa[1]	4,000	25	4.479	Varies	5 x 10^6	149.5	34.0	750.0

[1] Karnland et al. (2006)

The Wyoming (WyR1) soil was run using a constant V_{MAX} = 5 x 10^7 nm, the same particle velocity used with the Swy Na-montmorillonitic soil in this study. The swell pressures were smaller than the literature values when the specimen was at its densest state (void ratio (e) = 0.69). Additionally, it was difficult to obtain a swell pressure value for any inputs at L_{DEM} = 25 nm for soil with void ratio greater than e = 2.0. This was because the assembly was so loose that particles were not interacting in a way that would induce a pressure on the assembly walls. For each void ratio greater than 1.1, particle velocity was adjusted according to the relationship found previously

between void ratio and particle velocity in Figure 5.28 and as can be seen from the results, accurately predicted the experimental swell pressures. For the samples with void ratios below 1.1, however, the relationship between V_{MAX} and void ratio was found to be different. This relationship was determined for void ratios less than 1 using the same sensitivity study methodology as detailed in section *5.4.1.7.3*. The relationship between V_{MAX} and void ratio in dense soils (void ratio less than 1.3) is shown in Figure 5.29 with a power relation.

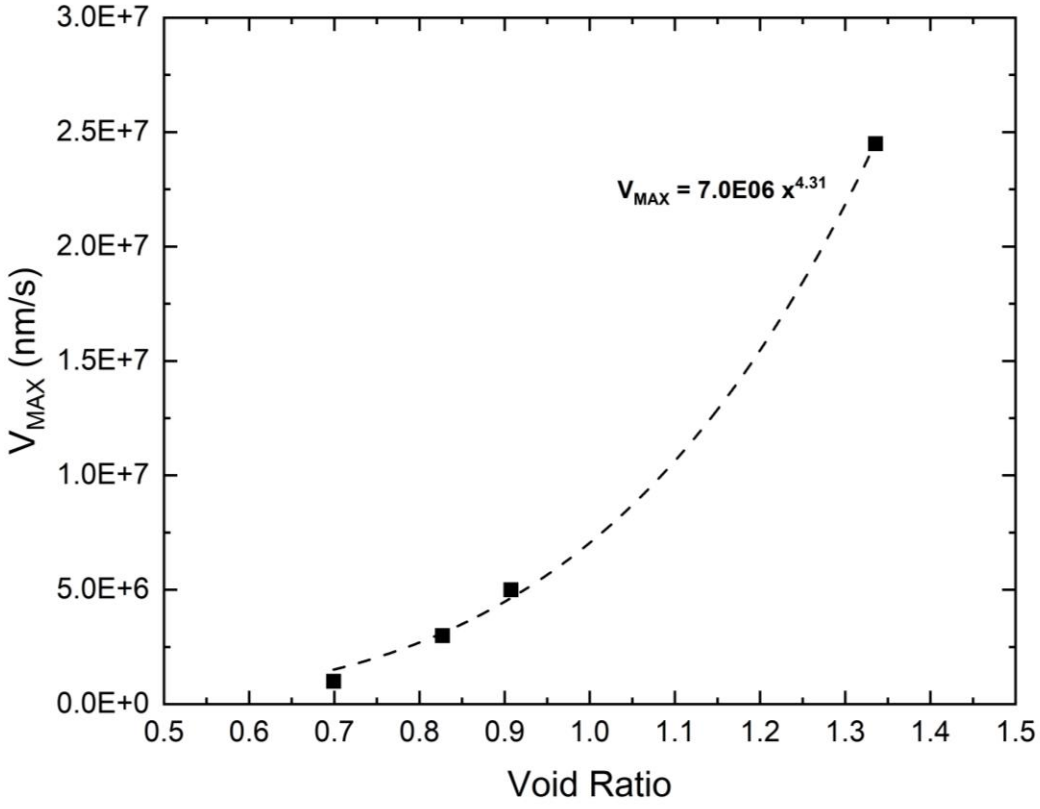

Figure 5.29. Relation between void ratio and particle velocity for loose specimens with void ratios less than 1.1

It should be noted that while the void ratio at 1.3 was included in creating the relationship for the dense specimens, the range of void ratios between 1.1 and 1.3 can be considered a transition zone. That is, either the relationship of V_{MAX} and void ratio of loose (exponential decay) or the

relationship of V_{MAX} and void ratio of dense samples (power function) can be used when determining an appropriate V_{MAX} for samples with void ratios within this density range. For example, the relationship between V_{MAX} and void ratio developed in Figure 5.28 for loose specimens with void ratios greater than 1.1 was used for the WyR1 specimens with void ratios greater than 1.3 with great success. However, similar results would occur had the relationship between V_{MAX} and void ratio for dense specimens been used. The results of the DEMClay validation using montmorillonite-bearing soils are presented in Table 5.32 and Figures 5.30 and 5.31.

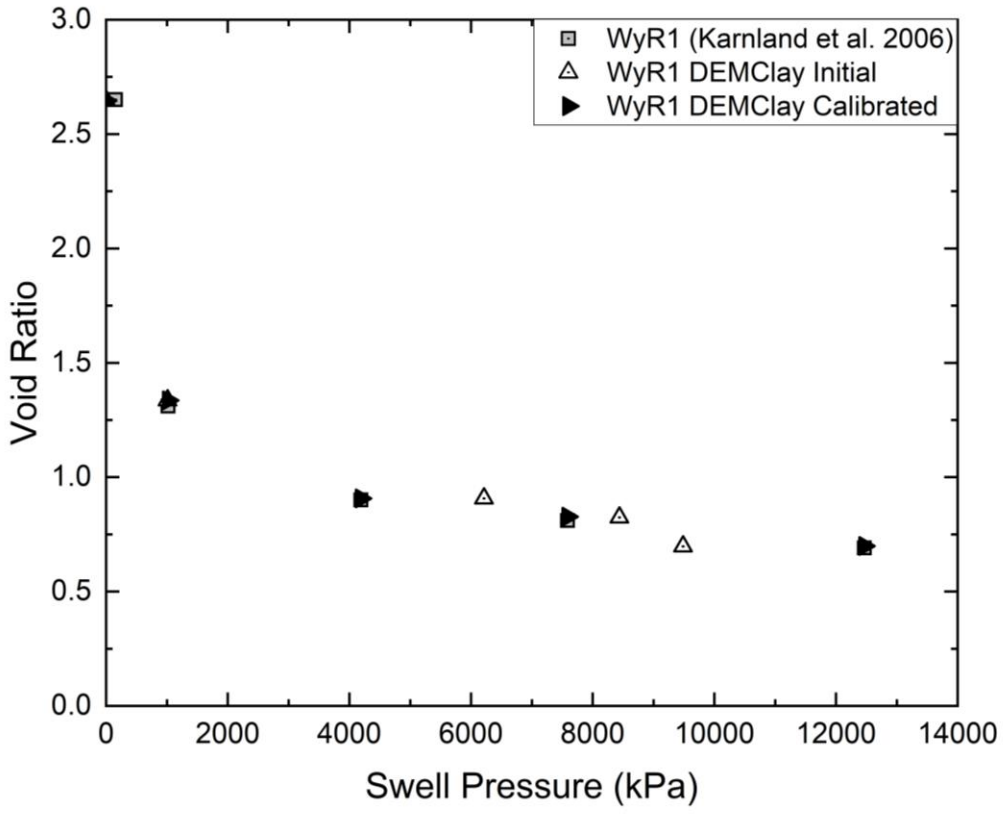

Figure 5.30. Validation of DEMClay using WyR1 montmorillonite

Using the calibration developed with the WyR1 montmorillonite, the swell pressures obtained via DEMClay for the WyNa montmorillonite and FrNa montmorillonite are fairly close to the reported values (Figure 5.31). However, the model is again not able to produce a swell pressure for void ratios greater than 2.0. While the DEMClay values are not exact, they show good agreement with the reported values and the model shows promise for predicting swell pressures of montmorillonite-bearing soils. The WyNa soil showed good agreement using the e-V_{MAX} relationship developed in Figure 5.28 for loose soils (e greater than 1.23) and Figure 5.29 for dense soils (e = 0.62 – 1.23). The FrNa, however, was less accurate. This is attributed to the difference in montmorillonite content between the soils. The model was calibrated using a pure, artificial montmorillonite (Swy Na-montmorillonite). Higher swell pressures are associated with greater amounts of montmorillonite and therefore the lower swell pressures for dense specimens are difficult for the model to match. The WyNa, WyR1, and Swy Na-montmorillonite all had montmorillonite fraction greater than 80% while the FrNa soil had less than 30% montmorillonite fraction (Karnland et al. 2006).

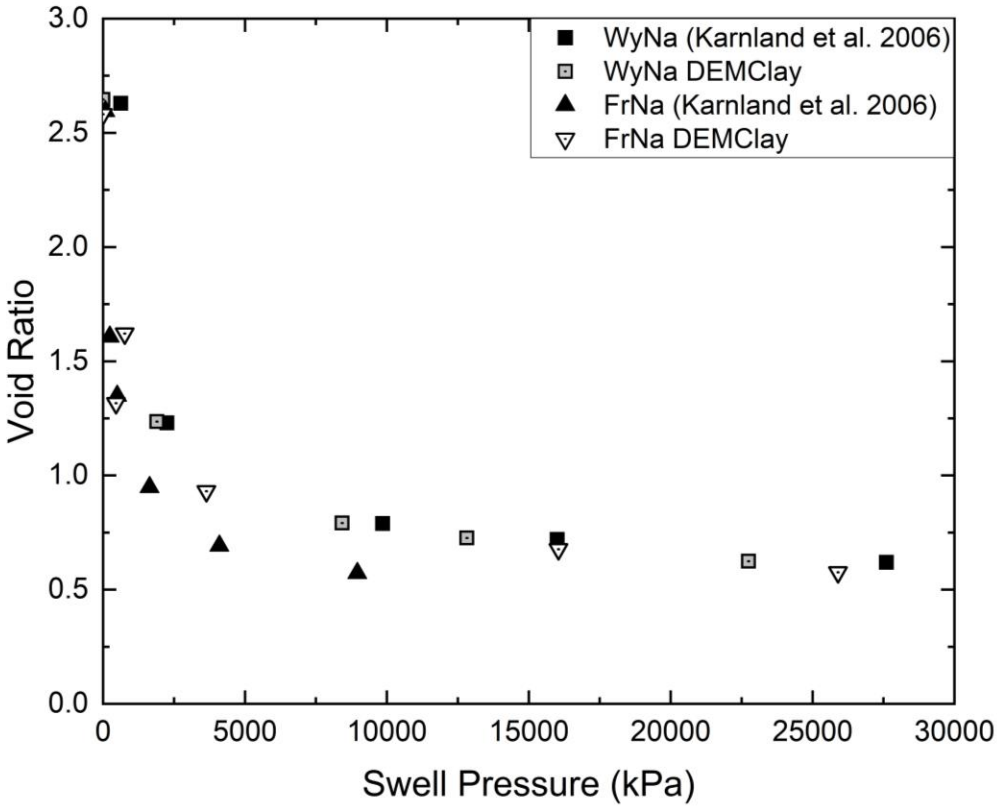

Figure 5.31. Validation of DEMClay using Wyoming and Friedland Na-montmorillonites.

5.5.3 Validation of DEMClay Using Natural Soils

Once the model was calibrated using Swy Na-montmorillonite and model parameters were chosen to best fit the model to the experimental results, natural soils were used to validate the DEMClay swell pressures. Input parameters specific to each soil were changed (e.g., ψ_0, H_{DEM}), while parameters calibrated from the simulation using Na-montmorillonite were kept constant (e.g., V_{MAX}, V_{WALL}, N_{ELEM}). Other parameters differed due to differences in particle spacing and size (e.g., D, L_{DEM}). Because the particles of natural soils are larger than the single-mineral montmorillonite, a larger discrete element length (L_{DEM}) was used, i.e., 35 nm rather than 30 nm, but kept small enough to maintain a similar length to width ratio. The length of the discrete element affects the minimum particle size as the minimum size allowable is the length of one discrete

element. Additionally, L_{DEM} affects the bending and stiffness of the specimen, detailed in *5.3.2.1*. The input parameters of the soils used in the DEMClay validation are presented in Table 5.33.

Table 5.33. Input parameters for natural soils in the literature

Soil	N_{ELEM}	L_{DEM} (nm)	H_{DEM} (nm)	V_{MAX} (nm/s)	V_{WALL} (nm/s)	ψ_0 (mv)	CEC (meq/100g)	S_A (m^2/g)
Hollywood[1]	4,000	30	20.433	Varies	5×10^6	209.5	26.4	145.5
Heiden[1]	4,000	30	13.268	Varies	5×10^6	219.0	50.7	229.0
Carnisaw[1]	4,000	40	28.366	Varies	5×10^6	225.6	27.3	107.5

[1] Lin (2012)

CEC and S_A are inherent soil parameters, therefore, naturally-occurring soils of varying mineralogy and montmorillonite content can be modeled based on these physicochemical parameters. To this end, assemblies of Heiden, Hollywood, and Carnisaw soils were simulated for swell pressure. Because swell pressures were obtained experimentally via an oedometer, the DEMClay oedometer assembly (1:3 height to width ratio) was chosen to model swell pressures of the natural soils. While CEC and S_A are not direct inputs into the model, they are the driving physicochemical parameters which affect interparticle spacing, interlayer spacing, and surface potential.

The expansive mineral in Carnisaw is vermiculite, while in Hollywood and Heiden the expansive mineral is montmorillonite. The thickness of a vermiculite layer and interlayer is in the range of 1 to 1.4 nm in the dry state (Suk et al. 2013; Zhang et al. 2020b), slightly larger than that of montmorillonite, which is reflected in the larger particle thickness of Carnisaw than the Hollywood, Heiden, and Na-montmorillonite (Table 5.1). Carnisaw has similar CEC to Hollywood (27.3 and 26.4 meq/100g respectively) and has a lower but comparable S_A (107.5 and 145.5 m^2/g respectively) (Table 5.4).

The swell pressures of natural soils (Heiden, Hollywood, and Carnisaw) used in the model validation are presented in Table 5.34. Heiden, Hollywood, and Carnisaw were tested at optimum moisture conditions by Lin (2012). All free swell tests were performed according to ASTM D4546-14 with a seating load of 1 kPa.

Table 5.34. Swell pressures of the natural soils (after Lin 2012)

Soil ID	Dry Density (g/cm^3)	Moisture Content (%)	Swell Pressure (kPa)
Heiden	1.58	24.2	230
Hollywood	1.70	20.6	141
Carnisaw	1.65	26.2	75

The results of free swell simulations on natural soils via DEM are presented in Table 5.35 along with the experimental results of Lin (2012) for Heiden, Hollywood, and Carnisaw compacted at optimum moisture and maximum dry density. The results obtained via DEM show good agreement with the experimental results for Hollywood and Heiden clays. However, while the model approximates the swell pressure of Carnisaw, it overpredicts the determined experimental values, but not outside the typical range of acceptable experimental error. This is mostly due to the low swell pressure of the Carnisaw soil at a relatively high density (e = 0.68) and the fact that the swelling mineral in Carnisaw is vermiculite, not montmorillonite. The model was calibrated for montmorillonite soils with high swell pressures and increasing swell pressure with increasing density. Therefore, it is possible that a soil property other than geometry, physicochemical parameters, and density could cause the low experimental swell pressure. The relationship between void ratio and swell pressure in some natural clays may be better captured through a mineralogical parameter in addition to or in place of geometry and physicochemical forces.

Table 5.35. Swell pressures of natural soils: DEM vs experimental results

Soil	Experimental		DEM		%
	e	σ_s (kPa)	e	σ_s (kPa)	Difference
Heiden	0.75	230.0	0.70	212.5	-7.6
Hollywood	0.64	141.0	0.63	146.5	+3.9
Carnisaw	0.68	75.0	0.69	114.5	+52.7

The DEMClay model differentiated between soils using the physicochemical parameters CEC and S_A. While this allows for different soils to be modeled in terms of layer spacing and surface potential, there are other factors beyond physicochemical and mechanical forces which control clay behavior. Specifically, the mineralogy of the clay particle and surface complexity must be considered in addition to mechanical, interparticle, and interlayer forces when describing swelling. A model which considers the mineralogy of the soil, as well as the type of interlayer cation (e.g., K, Mg, Al, Fe) in addition to CEC, S_A could even more accurately capture the potential swell pressures of expansive clays.

5.5 Conclusions

The DEMClay program was evaluated using assemblies of Na-montmorillonite for its viability as a model to predict swell pressures of expansive clays. DEMClay-derived swell pressures were calibrated against free swell pressures from laboratory testing (ASTM D4546). Assembly geometry (oedometer, triaxial, and square assembly type), loading conditions (W_{VALL} = 4 x 10^3 – 4 x 10^7 nm/s) (K_0 = 2, 1, 0.5, 0.33), particle spacing (3-7 nm), number of discrete elements (1,000 - 10,000), and particle velocity (V_{MAX} = 0 – 1 x 10^7 nm/s) were evaluated for their effect on horizontal and vertical swell pressure.

Once the model was calibrated using Na-montmorillonite, it was validated using montmorillonites reported in the literature with differing montmorillonite content and physicochemical parameters (CEC, S_A). The model was then used to predict swell pressures of

natural soils (Heiden, Hollywood, Carnisaw) of varying mineralogy, physicochemical parameters, and silt content.

The following conclusions can be drawn:

- Free swell tests performed on specimens of Na-montmorillonite showed exponentially increasing swell pressure with decreasing void ratio (increasing specimen density). The results of the one-dimensional oedometer testing showed good agreement with the swell pressures of Na-montmorillonite soils with similar physicochemical parameters and montmorillonite content.

- Swell pressures of Na-montmorillonite obtained via DEMClay swell model showed good agreement with experimental results. Models considering interlayer forces in addition to interparticle physicochemical and mechanical forces better approximate swell pressures of loose specimens. Assemblies that do not consider the interlayer force better approximates swell pressures of dense specimens.
- For all assembly dimensions (1:3, 3:1, and 1:1 horizontal to vertical), void ratio increased with increasing spacing between particles. For the same number of discrete elements in the assembly, decreased space between particles results in a denser specimen. There was no observable difference between the 1:3 (oedometer) and 3:1 (triaxial) assembly regarding void ratio. Instead, particles oriented parallel to the longer dimension.

- Based on the sensitivity study performed on assemblies of Na-montmorillonite, the particle velocity parameter had the greatest effect on swell pressure outside of measured parameters (e.g., CEC, S_A, void ratio, particle thickness). However, the relationship between particle velocity and swell pressure also relies on the geometry of the particle assembly, specifically

the void ratio, discrete element length, and particle thickness. For dense specimens, swell pressure decreases as particle velocity increases. Conversely, for loose specimens swell pressure decreases as particle velocity increases. An exponential decay relationship was determined between void ratio and particle velocity for soils with void ratios greater than 1.1 that was used to accurately predict swell pressure of various natural clay results. For soils with void ratios less than 1.1, there was a power relation between void ratio and particle velocity.

- Because the focus of DEMClay is to model swell pressures for highly expansive soils, the model is less accurate for low swell pressures at greater densities (void ratio less than 0.6). This is particularly true in cases where soils have the same physicochemical parameters, swelling minerals, and geometry but differing mineral composition, which results in differing laboratory-derived swell pressures at the same void ratios.
- Vertical swell pressures (VSP) were largely independent of K_0 while lateral swell pressures (LSP) tended to decrease with decreasing K_0. Particle orientation was observed to have an effect on the ratio of LSP to VSP. LSP trended higher than VSP for the oedometer assembly while VSP trended higher than LSP for the triaxial assembly.
- The physicochemical parameters cation exchange capacity (CEC) and specific surface area (S_A) were effectively used to model swell pressure. The surface potential, interlayer spacing, and interparticle spacing are largely determined by these inherent soil parameters. Simulated swell pressures from the calibrated DEMClay model overall showed good agreement with the results of laboratory free swell tests on the same soils but tended to overpredict swell pressures for the Carnisaw soil which differed in mineralogy from the other soils. It is possible that adding a mineralogical factor as well as a factor that captured

the type of interlayer cation (e.g., K, Mg, Al, Fe) or layer charge could even more accurately capture the potential swell pressures of expansive clays.

Chapter 6 Conclusions and Recommendations for Future Work

The main goal of this work was to advance the understanding of macroscopic unsaturated expansive soil behavior by analyzing microscale mechanisms that control the behavior of expansive clays. Because the nature of expansive soils is complex, the scope of the investigation encompassed: (1) developing a model that better predicted macroscale behavior using microscale physicochemical, mineralogical and/or pore fluid parameters (i.e., model swell pressure) and (2) describing microstructural hierarchical patterns that influence behavior not captured through physicochemical or mineralogical parameters (i.e., analyze surface geometry).

To this end, the following objectives were met: (1) model macroscale behavior, e.g., swell pressure, using microscopic physicochemical and mechanical forces, (2) Characterize fabric changes that occur at the microscale in response to changes in pressure, pore fluid, or stabilization reactions using qualitative image analysis and fractal geometry, and (3) quantify structural (fabric) parameters that influence macroscale parameters using fractal geometry.

The following tasks were completed for this study:

- Performed and analyzed one-dimensional swell pressures for a montmorillonite-bearing clay at varying densities to calibrate the DEMClay model.
- Calibrated DEMClay with high-quality experimental 1D Swell tests on an expansive, montmorillonite-bearing clay. Validated DEMClay with single mineral and naturally occurring swelling-clay-bearing soils from the literature.
- Predicted swell pressures of naturally occurring expansive clays with varying physicochemical parameters using DEMClay.

- Quantified fabric changes of a stabilized kaolinitic soil using fractal geometry combined with SEM and MIP results. These fabric changes included structural changes to the soil surface and pore network during stabilization over time and were presented as fractal dimension (surface complexity) and lacunarity (texture, or pattern of voids of the fabric).
- Created ESEM micrographs for specimens of artificial and natural clays along the initial drying and secondary wetting paths of the SWRC to evaluate the evolution of surface complexity using imaging techniques and fractal geometry. Evaluated effects of magnification scale, silt content, and physicochemical parameters.
- Quantitatively evaluated structural variations occurring with hysteretic moisture changes concerning differences in silt content, initial compaction conditions, equilibration time, and montmorillonite content using fractal geometry.

6.1 Conclusions

While specific, detailed conclusions can be found at the end of each chapter, summary conclusions are as follows:

1. The use of fractal geometry was proven a viable method to quantitatively describe the evolution of surface complexity of soils with varying mineralogical and physicochemical properties. Fractal geometry quantitatively described the evolving pore structure and fabric conditions under cycles of hydrologic hysteresis as well as stabilization using a calcium-based stabilizer. Specifically, there is a relationship between fractal parameters (i.e., fractal dimension and lacunarity) mineralogy, Specific Surface Area, Cation Exchange Capacity, initial moisture conditions, strength, and particle size which shows a predictive ability of these parameters which can be used to strengthen models used in determining volumetric and strength changes for expansive soils.

This predictive ability was first shown in this study using a stabilized kaolin clay evaluated through imaging (SEM) and porosity (MIP) data as curing time increased. While SEM provided a means of viewing the soil microstructure and MIP provided map of the pore network, fractal dimension and lacunarity allowed further quantitative analysis of the soil surface and pore network evolution as the stabilization progressed. Specifically, particle surface fractal dimensions (FD_{BC}) clearly showed particle restructuring as the values of vertical and horizontal compacted samples converge after 14 days. The lacunarity also shows evidence of particle restructuring as the lacunarity values between the vertical and horizontal cross sections converge after only 1 day of curing time.

Strong positive trends between fractal dimension (FDBC) and strength (UCS) and strong negative trends between lacunarity and strength were observed. As particles flocculate, they rearrange creating more complex surface patterns, corresponding to higher compressive strength. As pore structure becomes less homogeneous, the surface exhibits higher lacunarity corresponding to a decrease in strength. Because lacunarity decreased with curing time, lower lacunarity denoted smaller, fewer, and more regular gaps between features corresponding with measured increases in compressive strength.

The fractal dimension and lacunarity obtained from analysis of SEM images provided a better understanding of structural changes with stabilization time than the fractal dimension obtained from analysis of MIP data, validating the use of the box counting procedure with images of soil fabric.

2. Structural deformations that occur at the microscale influence parameters, which affect macroscale behavior. As particles realign in reaction to changes in pore fluid, pore networks expand and contract, affecting the fluid storage, permeability, and strength at the

macroscale. In order to better understand this phenomenon at the microlevel, environmental scanning electron microscopy images of three natural soils and two single-mineral clays along the primary drying and secondary wetting cycles were created and analyzed to determine evidence of volumetric shrinking and swelling.

Effects of initial preparation conditions which influence macroscale behavior (e.g., collapse potential, desiccation cracking) can be observed at the microscale. Soil compacted wet of optimal moisture conditions are more prone to developing a dispersed clay structure and develop a thicker layer of adsorbed water. During drying, these soils experience desiccation cracking as the fluid layer recedes. The implication is significant because expansive soils are commonly compacted wet of optimum to encourage volumetric swelling with increases in pore fluid but the designs do not consider the behavior along the drying cycle in the tightly adsorbed regime.

Conventional methods to describe activity, particularly those which rely on plasticity index, are not sufficient to explain changes in the microstructure. Specifically, the Skempton activity parameter failed to differentiate between specimens with significant differences in montmorillonite content. Carnisaw (A = 0.47) and Kaolinite (A = 0.44) would be expected to have similar volumetric strains based on the Activity, but the fabric of the Carnisaw specimen evolved through hysteresis and the Kaolinite specimen remained essentially inert. This is likely due to the mineralogy of the Carnisaw, specifically the swelling mineral. While the other soils contained montmorillonite, the swelling mineral in Carnisaw is vermiculite, which is less reactive than montmorillonite. Similarly, the relative activity (A_R), also using PI in its calculation fails to assess realistic soil behavior. Using A_R, Kaolinite is most probable to react to pore fluid and Heiden is the least probable. Instead, activity

parameters obtained using physicochemical parameters (S_A, CEC) better predict the likelihood of clays to react with changing pore fluid and a parameter including mineralogy would further improve conceptual models.

3. These same ESEM images were quantitatively analyzed using fractal geometry. In order to use this methodology more broadly, a determination on the potential scale effects at magnification values was required. In this study, the interpreted box counting fractal dimension was affected by the scale at which the image was obtained, particularly between 3,500X and 800X magnification. There was a transition point, around 3,000X magnification, for the fractal dimension of Na-montmorillonite. Below 3,000X, fractal dimensions were similar and averaged 1.7, but above 3,000X the fractal dimensions were higher and averaged 1.9. At higher magnifications, more textural features of the surface were visible, resulting in a higher complexity and therefore higher fractal dimension. At lower magnifications, more interaggregate pores were visible, and the contribution of the surface texture to the image complexity diminishes, resulting in a lower fractal dimension. Fractal dimensions obtained at 3500X tended to be lower for all soils except Hollywood and Na-montmorillonite. Overall, fractal dimensions at 350X and 800X were similar for all soils. There was no statistical difference in fractal dimension obtained for Kaolinite. Lacunarity was also affected by the magnification scale. Lacunarity interpreted from micrographs of Na-montmorillonite decreased linearly with increasing magnification. For the natural soils, lacunarity increased with magnification and the smallest difference between images occurred between 350X and 800X. The trend was the opposite for the single-mineral soils. The single-mineral soils were more homogeneous at higher magnifications (lower lacunarity) while the natural soils have more complex pore networks

due to their higher gradation and therefore were more heterogeneous at higher magnifications (higher lacunarity).

Soil compacted wet of optimum showed hysteretic behavior throughout one drying/wetting cycle with respect to surface complexity while soils compacted at optimum conditions did not. As suction increased, structural features emerged which increased the interpreted surface complexity during drying. On rewetting, the bound water returned, but not to the same magnitude as observed for primary wetting. This was reflected in the fractal dimension which was higher on rewetting indicating a greater amount of surface information visible.

The fractal dimensions and lacunarity obtained can be used to improve models which attempt to describe aspects of expansive clay behavior in the unsaturated state, particularly relating to changes in pore fluid. Because fractal dimension and lacunarity are obtained from geometric measurements, models which incorporate the fractal dimension remove the unknown component associated with empirically based models.

4. Not only was the evolution of surface complexity with cycles of hydrologic hysteresis studied and a viable method determined for helping to explain what is occurring at the microscale of expansive soil particles, but a clay discrete element model incorporating physicochemical properties was calibrated and validated to accurately predict swell pressures of single-mineral and naturally occurring soils. The DEMClay program was evaluated using assemblies of Na-montmorillonite for its viability as a model to predict swell pressures of expansive clays. DEMClay-derived swell pressures were calibrated against free swell pressures from laboratory testing (ASTM D4546). Assembly geometry, loading conditions, particle spacing, number of discrete elements, and particle velocity

were evaluated for their effect on horizontal and vertical swell pressure. Once the model was calibrated using Na-montmorillonite, it was validated using montmorillonites reported in the literature with differing montmorillonite content and physicochemical parameters (CEC, S_A). The model was then used to predict swell pressures of natural soils (Heiden, Hollywood, Carnisaw) of varying mineralogy, physicochemical parameters, and silt content.

Based on the sensitivity study performed on assemblies of Na-montmorillonite, the particle velocity parameter had the greatest effect on swell pressure outside of measured parameters (e.g., CEC, S_A, void ratio, particle thickness). However, the relationship between particle velocity and swell pressure also relies on the geometry of the particle assembly, specifically the void ratio, discrete element length, and particle thickness. For dense specimens, swell pressure decreases as particle velocity increases. Conversely, for loose specimens swell pressure decreases as particle velocity increases. An exponential decay relationship was determined between void ratio and particle velocity for soils with void ratios greater than 1.1 that was used to accurately predict swell pressure of various natural clay results. For soils with void ratios less than 1.1, there was a power relation between void ratio and particle velocity.

Free swell tests performed on specimens of Na-montmorillonite showed exponentially increasing swell pressure with decreasing void ratio (increasing specimen density). The results of the one-dimensional oedometer testing showed good agreement with the swell pressures of Na-montmorillonite soils with similar physicochemical parameters and montmorillonite content.

Swell pressures of Na-montmorillonite obtained via DEMClay showed good agreement with experimental results. Because the focus of DEMClay is to model swell pressures for highly expansive soils, the model is less accurate for low swell pressures at greater densities (void ratios less than 0.6). This is particularly true in cases where soils have the same physicochemical parameters, swelling mineral, and geometry but laboratory-derived swell pressures differ.

The physicochemical parameters cation exchange capacity (CEC) and specific surface area (S_A) were effectively used to model swell pressure. The surface potential, interlayer spacing, and interparticle spacing are largely determined by these inherent soil parameters. Simulated swell pressures from the calibrated DEMClay model overall showed good agreement with the results of laboratory free swell tests on the same soils but tended to overpredict swell pressures for the Carnisaw. This is likely because the swelling mineral in Carnisaw is vermiculite rather than montmorillonite and the model was calibrated and verified using montmorillonite. It is possible that adding a mineralogical factor as well as a factor that captured the type of interlayer cation (e.g., K, Mg, Al, Fe) or layer charge could even more accurately capture the potential swell pressures of expansive clays.

6.2 Recommendations for Future Work

This study created a framework for which microscale phenomena can be viewed. To further this research, the following avenues for future research are recommended:

(1) This study analyzed the microscale pore structure and fabric of a stabilized kaolinitic soil using SEM and MIP results in tandem with fractal geometry. Investigations of stabilized clays with smaller particles (e.g., pure montmorillonites) or more complicated morphology

(e.g., naturally occurring soils) would provide valuable information on the microscale mechanism of expansive soil stabilization.

(2) The analysis of stabilized kaolinite (Chapter 2) used SEM images and MIP data of unsheared specimens. It has been shown in Tabet (2015) that shearing stabilized specimens results in a compression in void space, evidenced by changes in the pore size distribution via MIP. While this study used kaolinite data to validate the fractal techniques to be used in Chapter 4, a future study which compared differences in the MIP fractal dimension between the sheared and unsheared specimens, as well as differences in the box counting fractal dimension via analysis of SEM micrographs of sheared and unsheared specimens would be enlightening as to the effects of shearing on the pore structure.

(3) Tyler and Wheatcraft (e.g., 1990) developed a fractal dimension of the particle size distribution obtained via sieve analysis. Because a particle size distribution has been shown to be viable through analysis of an image (Chapter 2), it would be beneficial to evaluate the fractal dimension of particle size distributions of raw and stabilized soils. Furthermore, the fractal dimensions of the particle size distributions between (1) sieve analysis, (2) hydrometer analysis, and (3) image analysis should be compared to determine at what particle scales the power law relation between particle size and grain size distribution has fractal characteristics.

(4) One SEM image for each curing time and magnification was available from Tabet (2015). While the data was sufficient to generate particle size distributions and evaluate changes in the box counting fractal dimension and lacunarity with curing time, it would be beneficial to understanding structural hierarchies in the soil fabric if additional particle size distributions and fractal dimensions were obtained from a broader range of magnifications.

Changes in the slope of the particle size distribution would inform hierarchies observable at different magnifications for the soil being imaged. Changes in the fractal dimension would similarly inform ranges at which the soil structure is fractal.

(5) The ESEM micrographs were collected of kaolinitic and montmorillonite-bearing soils. While montmorillonite is a highly expansive clay mineral, other 2:1 minerals, such as vermiculite, should be studied along hysteretic moisture cycles. A potential mineralogical parameter should be determined based either on the montmorillonite content or swelling mineral type, which could be used in the DEM model to better predict swell pressures when physicochemical parameters do not sufficiently differentiate behavioral phenomena. Changes in the parameters used to model Carnisaw had an effect on the swell pressure predicted via DEMClay. In this study, the swelling mineral in Carnisaw was vermiculite rather than montmorillonite. While the physicochemical parameters and clay content of Carnisaw were similar to that of Hollywood, Carnisaw was less reactive to changes in pore fluid. Similarly, swell pressures were lower for Carnisaw than other natural soils with similar density and physicochemical parameters.

(6) The work presented in Chapter 3 and Chapter 4 provides a proof of concept that the box counting method is viable to analyze microscale changes in fabric. Future work is needed to assess repeatability of results. Specifically, multiple specimens of the same soil with repeatable parameters at the macroscale (i.e., same water content, void ratio, and sampling methodology) should be assessed for differences in fractal dimension and lacunarity from micrographs obtained at the same suction state.

(7) The kaolinitic soil was assessed for differences between the horizontal and vertical planes (Chapter 2). Similar work should be performed on the more complicated clays (e.g., the

clays assessed in Chapter 3 and Chapter 4) to measure the differences in structure between the horizontal and vertical planes as suction changes. A database of multiple samples and multiple planes would improve the repeatability of the method and quantitatively describe particle orientation with the plane of compaction beyond the qualitative edge-face and edge-edge description.

(8) Volume changes inform the deformation aspect of the micromechanics discussed in this work. Therefore, a quantitative analysis of the structural changes which occur with changes in suction is necessary. This could be achieved by obtaining a void ratio from binary images of the micrographs. That is, the ratio of pixels representing pore space to pixels representing structural features give a void ratio. Changes in void ratio provide a quantitative indication of deformation.

(9) The fractal dimensions obtained via analysis of ESEM could be used to improve hydraulic conductivity models. Specifically, current models focus on relative permittivity using a single fractal dimension for the entire range of moisture conditions. Because a database of values have been generated for fractal dimensions at varying suctions, an improved hydraulic conductivity model would use the varying fractal dimensions to generate a hydraulic conductivity – suction relationship.

(10) With the current ESEM setup, there are limiting factors to the clarity of the image obtained, specifically regarding pixel resolution. This is magnified when considering the suction range which occurs between relative humidity between 90% and 100% where a layer of tightly bound adsorbed water obscures the image. A greater pixel resolution may change the interpreted fractal dimension and lacunarity of the soil. A study which

quantifies the limiting values of pixel resolution with respect to fractal dimension and lacunarity of an image would better inform future work.

(11) A database of free swell pressures for natural soils with differing swelling minerals (i.e., montmorillonite, vermiculite, beidellite, hectorite), at varying densities (void ratios) would be beneficial for validating swell models for these problematic soil types. This database could be used to determine a possible mineralogical parameter that could be used in the model to better predict the swell pressure, particularly when the physicochemical parameters are the same but the swelling mineral (and therefore swell pressure) differs.

(12) The DEMClay program in this study was written in FORTRAN and used Intel oneAPI to compile the code. While there are benefits to using this language, with the closure of Absoft and other FORTRAN compilers, it would be beneficial to convert the code to another language.

(13) This study (Chapter 5) focused on swell pressures of expansive clays. However, the volume change is often a desirable predictor of damage resulting from clay expansion. The DEMClay program is able to produce information on simulated deformations of the clay assembly. Future studies which calibrate DEMClay to model swell strains would be valuable to understanding expansive clay behavior.

(14) While the DEMClay model using CEC and S_A to differentiate between soil types was relatively accurate, better results could be obtained by incorporating structural characteristics (e.g., surface roughness, pore morphology) into the model. The box counting fractal dimension, obtained from image analysis of ESEM micrographs quantifies surface roughness, which can be incorporated as a model parameter for the particle

assembly. Pore morphology is quantified using the fractal dimension of MIP data, which can be incorporated into the model to better tortuosity of pore networks.

References

ABDOLLAHI, M. & VAHEDIFARD, F. 2020. Prediction of Lateral Swelling Pressure in Expansive Soils. *Geocongress 2020,* 367-376.

ALBRITTON, J., JACKSON, L., & BANGERT, R. 1984. *Foundation Grouting Practices at Corps of Engineers Dams*. US Army Corps of Engineers, Technical Report GL-84-13.

ALLAIN, C. & CLOITRE, M. 1991. Characterizing the lacunarity of randon and deterministic fractal sets. *Physical Review A,* 44(6): 3552-3558.

AL-MAHBASHI, A., TAMER, E., & AL-SHAMRANI, M. 2023. The Role of Stress States on the Hysteretic Behavior of Expansive Soil under Multiple Drying-Wetting Cycles. *Buildings,* 13(7).

AL-RAWAS, A. 1999. The factors controlling the expansive nature of the soils and rocks of northern Oman. *Engineering Geology*, 53: 327-350.

AL-RAWAS, A. & MCGOWN, A. 1999. Microstructure of Omani expansive soils. *Canadian Geotechnical Journal*, 36: 272-290.

AMAKYE, S., ABBEY, S., BOOTH, C., & MAHAMADU, A. 2021. Enhancing the Engineering Properties of Subgrade Materials Using Processed Waste: A Review. *Geotechnics,* 1: 307-329.

AMARASINGHE, P. & ANANDARAJAH, A. 2013. Molecular Dynamic Study of the Swelling Behavior of Na-Montmorillonite. *Environmental and Engineering Geoscience,* 19(2): 173-183.

ANANDARAJAH, A. 1994. Discrete Element Method for Simulating Behavior of Cohesive Soils. *Journal of Geotechnical Engineering Division,* ASCE, 120(9): 1593-1615.

ANANDARAJAH, A. 2000. Numerical Simulation of One-Dimensional Behavior of Kaolinite. *Geotechnique*, 50(5): 509-519.

ANANDARAJAH, A. 2014. DEMClay User Manual: Version 37.

ANANDARAJAH, A. & AMARASINGHE, P. 2011. Influence of fabric variables on clay-water-air capillary meniscus. *Canadian Geotechnical Journal,* 48:1-8.

ANANDARAJAH, A. & AMARASINGHE, P. 2012. Behavior of Clays: A Discrete Element Study. *GeoCongress 2012, Oakland, CA, March 25-29 ASCE.*

ANANDARAJAH, A. & AMARASINGHE, P. 2013. Discrete-element Study of the Swelling Behavior of Na-Montmorillonite. *Geotechnique,* 63(8): 674-681.

ANANDARAJAH, A. & CHEN, J. 1994. Double-Layer Repulsive Force between Two Inclined Platy Particles According to the Gouy-Chapman Theory. *Journal of Colloid and Interface Science,* 168: 111-117.

ANANDARAJAH, A. & CHEN, J. 1997. Van der Waals Attractive Force Between Clay Particles in Water and Contaminants. *Soils and Foundations*, 37(2): 27-37.

ANANDARAJAH, A. & LAVOIE, D. 2002. Numerical simulation of the microstructure and compression behavior of Eckernforde Bay sediments. *Marine Geology*, 182: 3-27.

ANDERSON, A. & MCBRATNEY, A. 1995. Soil aggregates as mass fractals. Australian Journal of Soil Research, 33: 757-772.

ANDERSON, A, MCBRATNEY, A., & FITZPATRICK, E. 1996. Soil mass, surface, and spectral fractal dimensions estimated from thin section photographs. *Soil Science Society of America Journal*, 60: 962-969.

ARIFIN, Y., ARSYAD, M., & MUSLIM, H. 2021. Swelling Characteristics of Compacted Claystone-Bentonite Mixtures. *6th International Conference on Sustainable Built Envrionment (ICSBE)*, 933.

ASTM. 2011. D4404-18. Standard Test Method for Determination of Pore Volume Distribution of Soil and Rock by Mercury Intrusion Porosimetry. West Conshohocken, PA.

ASTM. 2011. D2435-04. *Standard Test Methods for One-Dimensional Consolidation Properties of Soils Using Incremental Loading*. West Conshohocken, PA.

ASTM. 2018. D4546-14. *Standard Test Methods for One-Dimensional Swell or Collapse of Soils.* West Conshohocken, PA.

ASTM. 2023. D7928. Standard Test Method for Particle-Size Distribution (Gradation) of Fine-Grained Soils Using the Sedimenation (Hydrometer) Analysis. West Conshohocken, PA.

ATHANASOPOULOU, A. 2014. Addition of lime and fly ash to improve highway subgrade soils. Journal of Materials in Civil Engineering, 26: 773-775.

BAER, J., KENT, T., & ANDERSON, S. 2009. Image analysis and fractal geometry to characterize soil desiccation cracks. *Geoderma*, 154: 153-163.

BANKOLE, S., BUCKMAN, J., STOW, D., & LEVER, H. 2019. Grain-size analysis of mudrocks: A new semi-automated method from SEM images. Journal of Petroleum Science and Engineering, 174: 244-256.

BALANKIN, A., BORY-REYES, J., & SHAPIRO, M. 2016. Towards a physics on fractals: Differential vector calculus in three-dimensional continuum with fractal metric. *Physica A: Statistical Mechanics and its Applications*, 444(15): 345-359.

BALKHANOV, V. & BASHKUEV, Y. 2004. Fractal Dimension of the Channel Network Structure of Selenga River Delta. *Water Resources*, 31(2): 165-169.

BARMAN, B., BARMAN, J., & KUMAR, B. 2022. Fractal dimensions of hydraulic parameters in sand mined alluvial channel. *Water Science & Technology,* 22(6): 6143-6156.

BARTOLI, F., PHILIPPY, R., DORISSE, M., NIQUET, S., & DUBUIT, M. 1991. Structure and self-similarity in silty and sandy soils: the fractal approach. *Journal of Soil Science*, 42: 167-185.

BAYESTEH, H. & HOSEINI, A. 2021. Effect of mechanical and electro-chemical contacts on the particle oreintation of clay minerals during swelling and sedimentaiton: A DEM simulation. *Computers and Geotechnics*, 130.

BAYESTEH, H. & MIRGHASEMI, A., 2013. Procedure to detect the contact of platy cohesive particles in discrete element analysis. *Powder Technology*, 244: 75-84.

BERODIER, E., BIZZOZERO, J., & MULLER, A. 2016. Mercury Intrusion Porosimetry. In *A Practical Guide to Microstructural Analysis of Cementitious Materials*, Karen Scrivenener, Ruben Snellings, and Barbara Lothenbach, Eds. CRC Press.

BHARADWAJ, A., HOUSTON, S., HOUSTON, W., WELFERT, B., & WALSH, K. 2013. Effect of soil replacement option on surface deflections for expansive clay profiles. In *Advances in Unsaturated Soils*, Bernardo Caicedo, Carol Murillo, Laureano Hoyos, Julio Esteban Colmenares, and Ivan Rafael Berdugo, Eds. CRC Press.

BOLT, G. 1956. Physico-chemical analysis of the compressibility of pure clays. *Geotechnique*, 6(2): 86-93.

BORCHARDT, G. 1989. Smectites. *Minerals in Soil Environments*, 1(2), Co-eds: Joe Boris Dixona nd Sterling Barg Weed. SSSA.

BROOKS, R. & COREY, A. 1964. Hydraulic Properties of Porous Media. *Hydrology Papers*, Colorado State University.

BUHLER, R. & CERATO, A. 2007. Stabilization of Oklahoma Expansive Soils using Lime and Class C Fly Ash. *GeoDenver: New Peaks in Geotechnics.* GSP 162: Problematic Soils and Rocks and In Situ Characterization. Denver, CO, Feb. 18-21. 2007.

CERATO, A. 2001. *Influence of Specific Surface Area on Geotechnical Characteristics of Fine-Grained Soils.* MS Thesis, University of Massachusetts, Amherst.

CERATO, A. & LUTENEGGER, A. 2005. Activity, relative activity and specific surface area of fine-grained soils. *Proceedings of the 16th International Conference on Soil Mechanics and Foundation Engineering*, Osaka, Japan. Sept. 12-16.

CERATO, A., HAJJAT, J., & MILLER, G. 2008. The influence of Strucutre on One-Dimensional Wetting Induced Volume Change of Compacted Soil. *Proceedings, GeoCongress 2008*: 287-294.

CERATO, A. & MILLER, G. 2013. Determination of soil stabilizer content using X-ray fluorescence. *Geotechnical Testing Journal,* 36**,** 781-785.

CHEN, J. & ANANDARAJAH, A. 1993. *Quantification of Double-Layer Repulsive Force Between Non-Parallel platy particles*. Civil Engineering Report: Johns Hopkins University.

CHEN, J. & ANANDARAJAH, A. 1996. van der Waals attractive force between spherical particles. *Journal of Colloid and Interface Science*, 180(2): 519-523.

CIMEN, O., KESKIN, S., & YILDIRIM, H. 2012. Prediction of Swelling Potential and Pressure in Compacted Clay. *Arabian Journal for Science and Engineering*, 37: 1535-1546.

COUDERT, E., DENEELE, D., RUSSO, G., VITALE, E., & TARANTINO, A. 2021. Microstructural evolution and mechanical behaviour of alkali activated fly ash binder treated clay. *Construction and Building Materials,* 285: 122917.

CRAWFORD, J. 1994. The relationship between structure and the hydraulic conductivity of soil. *European Journal of Soil Science*, 45:493-502.

CRAWFORD, J., RITZ, K., & YOUNG, I. 1993. Quantification of fungal morphology, gaseous transport and microbial dynamics in soil: An integrated framework utilising fractal geometry. Geoderma, 56: 157-172.

CUI, Y., YAHIA-AISSA, M., & DELAGE, P. 2002. A model for the volume change behavior of heavily compacted swelling clays. *Engineering Geology*, 64(2-3): 233-250.

CYGAN, R. GREATHOUSE, J., HEINZ, H., & KALINICHEV, A. 2009. Molecular models and simulations of layered materials. *Journal of Materials Chemistry*, 19(17): 2470-2481.

DANIELS, K., HARRINGTON, J., MILODOWSKI, A., KEMP, S., MOUNTENEY, I., & SELLIN, P. 2021. Gel Formation at the Front of Expanding Calcium Bentonites. *Minerals*, 11(2).

DATHE, A., EINS, S., NIEMEYER, J., & GEROLD, G. 2001. The surface fractal dimension of the soil-pore interface as measured by image analysis. *Geoderma,* 103: 203-229.

DAS, S., SAMUI, P., SABAT, A., & SITHARAM, T. 2010. Prediction of swelling pressure of soil using artificial intelligence techniques. *Environmental Earth Sciences,* 61:393-403.

DELAGE, P. & PELLERIN, F. 1984. Influence de la Lyophilisation sur la structure d'une argile sensible du Quebec. *Clay Minerals*, 19: 151-160.

DELAGE, P., TESSIER, D., & MARCEL-AUDIGUIER, M. 1982. Use of the Cryoscan Apparatus for Observation of Freeze-Fractured Planes of a Sensitive Quebec Clay in Scanning Electron Microscopy. *Canadian Geotechnical Journal*, 19(1): 111-114.

DE LAS CUEVAS, C. 1997. Pore structure characterizationin rock salt. *Engineering Geology*, 47:17-30.

DEVANEY, R., KEEN, L., & ALLIGOOD, K. 1989. *Chaos and Fractals: The Mathematics Behind the Computer Graphics*, 39. Providence, RI: American Mathematical Society.

DEVKOTA, B., KARIM, M., RAHMAN, M., & NGUYEN, H. 2022. Accounting for Expansive Soil Movement in Geotechnical Design – A State-of-the-Art Review. *Sustainability*, 14: 15662.

DIEUDONNE, A., VECCHIA, G., & CHARLIER, R. 2017. Water retention model for compacted bentonties. *Canadian Geotechnical Journal*, 54(7): 915-925.

DRNEVICH, V., SRIDHARA, A., RAO, A., & SIVAPULLAIAH, P. 1986. Swelling Pressure of Clays. *Geotechnical Testing Journal*, 9(1): 24-33.

DU, J., ZHOU, A., LIN, X., BU,Y., & KODIKARA, J. 2021. Prediction of swelling pressure of expansive soil using an improved molecular dynamics approach combining diffuse double layer theory. *Applied Clay Science*, 203: 105988.

ERZIN, Y. & GUNES, N. 2013. The unique relationship between swell percent and swell pressure of compacted clays. *Bulletin of Engineering Geology and the Environment*, 72(1): 71-80.

FADEEV, A., BORISOVA, O., & LISICHKIN, G. 1996. Fractality of Porous Silicas: A Comparison of Adsorption and Porosimetry Data. *Journal of Colloid and Interface Science*, 183: 1-5.

FARROUKH, H., MNIF, T., KAMOUN, L., & BENNOUR, F. 2018. Stabilization of clayey soils with Tunisian phosphogypsum: effect on geotechnical properties. *Arabian Journal of Geosciences*, 11:760.

FAURE, B., SALAZAR-ALVAREZ, G., & BERGSTROM, L. 2011. Hamaker Constants of Iron Oxide Nanoparticles. *Langmuir*, 27: 8659-8664.

FAZELI, M., SHORAFA, M., KHOJATESH, D., & SHAHRI, A. 2010. A Fractal Approach for Estimating Soil Water Retention Curve. *Journal of Soil Science and Environmental Management*, 1(7): 177-183.

FERBER, V., AURIOL, J., CUI, Y., & MAGNAN, J. 2009. On the Swelling Potential of Compacted High Plasticity Clays. *Engineering Geology*, 104: 200-210.

FREDLUND, D. & XING, A. 1994. Equations for the soil-water characteristic curve. *Canadian Geotechnical Journal*, 31: 521-532.

FRIESEN, W. & MIKULA, R. 1987. Fractal Dimensions of Coal Particles. *Journal of Colloid and Interface Science,* 120(1): 263-271.

GIMENEZ, D., PERFECT, E., RAWLS, W., & PACHEPSKY, Y. 1997. Fractal Models for Predicting Soil Hydraulic Properties: A Review. *Engineering Geology*, 48: 161-183.

GOODARZI, A., AKBARI, H., & SALIMI, M. 2016. Enhanced Stabilization of Highly Expansive Clays by Mixing Cement and Silica Fume. *Applied Clay Science*, 132-133: 675-684.

GOYET, J., 1996. *Physics and Fractal Structures,* Springer.

GUBER, A., PACHEPSKY, Y.,. & LEVKOVSKY, E. 2005. Fractal mass-size scaling of wetting soil aggregates. *Ecological Modelling*, 182: 317-322.

GUO, Y., HAN, C., & YU, X. 2017. Laboratory Characterization and Discrete Element Modeling of Shrinkage and Cracking in Clay Layer. *Canadian Geotechnical Journal,* 55:680-688.

HAMAKER, H. 1937. The London-van der Waals Attraction Between Spherical Particles. *Physica*, 4(10): 1058-1072.

HAN, S., WANG, B., & FENG, J. 2022. Relationship between fractal feature and compressive strenght of concrete based on MIP. *Construction and Building Materials,* 322:126504.

HATANO, R. & BOOLTINK, H. 1992. Using fractal dimensions of stained flow patterns in a clay soil to predict bypass flow. *Journal of Hydrology*, 135: 121-131.

HATANO, R., KAWAMURA, N., IKEDA, J., & SAKUMA, T. 1992. Evaluation of the effect of morphological features of flow paths on solute transport by using fractal dimensions of methylene blue staining pattern. *Geoderma*, 53: 31-44.

HEMES, S., DESBOIS, G., URAI, J., SCHROPPEL, B. & SCHWARZ, J. 2015. Mutli-scale characterization of porosity in Boom Clay (HADES-level, Mol, Belgium) using a combination of X-ray μ -CT, 2D BIB-SEM and FIB-SEM tomography. Microporous and Mesoporous Materials, 208: 1-20.

HENSEN, E. & SMIT, B. 2002. Why Clays Swell. *Journal of Physical Chemistry,* 106: 1264-1267.

HORPIBULSUK, S., RACHAN, R., CHINKULKIJNIWAT, A., RAKSACHON, Y., & SUDDEEPONG, A. 2010. Analysis of Strength Development in Cement-Stabilized Silty Clay based on Microstructural Considerations. *Construction and Building Materials*, 24: 2011-2021.

HOUSTON, S., BHARADWAJ, A., WELFERT, B., HOUSTON, W., & WALSH, K. 2015. Unsaturated Soil Mechanics Principles to Remove and Replace Mitigation for Expansive Clays. *Journal of Geotechnical and Geoenvironmental Engineering*, 142(4).

HUSSEY, N. 2010. *A Comparison of Soil Stabilization Additives to Determine Parameters Affecting Soil Strenght Values*. MS Thesis, University of Oklahoma, Norman.

INTERNATIONAL ATOMIC ENERGY AGENCY. 2013. *Characterization of Swelling Clays as Components of the Engineered Barrier System for Geological Repositories*. Results of an IAEA Coordinated Research Project 2002-2007. IAEA-TECDOC-1718.

JALAL, F., IQBAL, M., KHAN, M., SALAMI, B., ULLAH, S., HAYAT, K., & NABIL, M. 2023. Indirect Estimation of Swelling Pressure of Expansive Soil: GEP versus MEP Modelling. *Advances in Materials Science and Engineering,* 2023:1-25.

JENNINGS, H., BULLARD, J., THOMAS, J., ANDRADE, J., CHEN, J., & SCHERER, G. 2008. Characterization and Modeling of Pores and Surfaces in Cement Paste: Correlations to Processing and Properties. *Journal of Advanced Concrete Technology,* 6(1): 5-29.

JIANG, M., YU, H., & HARRIS, D. 2006. Bond rolling resitance and its effect on yielding of bonded granulates by DEM analyses. *International Journal for Numerical and Analytical Methods in Geomechanics*, 30:723-761.

JONES, L. & JEFFERSON, I. 2012. Expansive Soils. *ICE Manual of Geotechnical Engineering, Vol 1*: 413-441.

KANG, M., WATABE, Y., & TSUCHIDA, T. 2003. Effect of Drying Process on the Evaluation of Microstructure of Clays using Scanning Electron Microscope (SEM) and Mercury Intrusion Porosimetry (MIP). *Proceedings of the 13th International Offshore and Polar Engineering Conference*, Honolulu, HI, May 25-30: 385-392.

KARAKAN, E., 2022. Relationships among plasticity, clay fraction and activity of clay-sand mixtures. *Arabian Journal of Geosciences,* 15(4).

KARNLAND, O., OLSSON, S., & NILSSON, U. 2006. *Mineralogy and sealing properties of various bentonites and smectite-rich clay materials.* Technical Report: TR-06-30.

KAROL, R. 2003. *Chemical Grouting and Soil Stabilization,* 3rd ed. CRC Press, New York.

KARPERIEN, A. 2013. FracLac for ImageJ. http://rsb.info.nih.gov/ij/plugins/fraclac/FLHelp/Introduction.htm. 1999-2013.

KATTI, D., SRINIVASAMURTHY, L., & KATTI, K. 2015. Molecular modeling of initiation of interlayer swelling in Na-montmorillonite expansive clay. *Canadian Geotechnical Journal*, 52: 1385-1395.

KATTI, D., MATAR, M., KATTI, K., & AMARASHINGE, P. 2009. Multiscale Modeling of Swelling Clays: A Computational and Experimental Approach. *KSCE Journal of Civil Engineering*, 13(4): 243-255.

KAYABALI, K. & DEMIR, S. 2011. Measurement of swelling pressure: Direct method versus indirect methods. *Canadian Geotechnical Journal*, 48: 354-364.

KEIL, R. & MAYER, L. 2014. Mineral Matrices and Organic Matter. *Treatise on Geochemistry*, 2nd ed, 12: 337-359.

KESKIN, I., SALIMI, M., ATEYSEN, E., KAHRAMAN, S., & VAKILI, A. 2023. Comparative Study of Swelling Pressure in Expansive Soils considering Different Initial Water Contents and BOFS Stabilization. *Advances in Civil Engineering*: 1-11.

KHABAZIAN, M., MIRGHASEMI, A., & BAYESTEH, H. 2018. Compressibility of Montmorillonite/Kaolinite Mixtures in Consolidation Testing Using Discrete Element Method. *Computers and Geotechnics*, 104: 271-280.

KOLIJI, A., VULLIET, L., & LALOUI, L. 2010. Structural Characterization of Unsaturated Aggregated Soil. *Canadian Geotechnical Journal*, 47(3): 297-311.

LAIRD, D. 2006. Influence of layer charge on swelling of smectites. *Applied Clay Science*, 34: 74-87.

LAU, J., BISCONTIN, G., & BERTI, D. 2023. Effects of biochar on cement-stabilised peat soil. *Proceedings of the Institution of Civil Engineers – Ground Improvement*, 176(2): 76-87.

LEE, B. & LEE, S. 2013. Effects of specific surface area and porosity on cube counting fractal dimension, lacunarity, configurational entropy, and permeability of model porous networks: Random packing simulations and NMR micro-imaging study. *Journal of Hydrology*, 496: 122-141.

LEVINE, L., PEDGEN, W., & SMART, C. 2016. Apollonian structure in the Abelian sandpile. *Geometric and Functional Analysis*, 26: 306-336.

LI, X. & ZHANG, L. 2009. Characterization of dual-structure pore-size distributin of soil. *Canadian Geotechnical Journal*, 46(2): 129-141.

LIKOS, W. & LU, N. 2003. Automated Humidity System for Measuring Total Suction Characteristics of Clay. *Geotechnical Testing Journal*, 26(2): 179-190.

LIKOS, W. & LU, N. 2004. Hysteresis of Capillary Stress in Unsaturated Granual Soil. *Journal of Engineering Mechanics*, 130(6): 646-655.

LIN, B. 2012. *A Comprehensive Investigation on Microscale Properties and Macroscopic Behavior of Natural Expansive Soils*. PhD Thesis, University of Oklahoma, Norman.

LIN, B., CERATO, A., ELWOOD MADDEN, A., & ELWOOD MADDEN, M. 2013. Effect of fly ash on the behavior of expansive soils: microscopic analysis. Environmental & Engineering Geoscience, 19: 85-94.

LIN, B. & CERATO, A. 2014. Applications of SEM and ESEM in microstuctural investigation of shale-weathered expansive soils along swelling-shrinkage cycles. *Engineering Geology,* 177:66-74.

LING, E., SERVIO, P., & KIETZING, A. 2016. Fractal and Lacunarity Analyses: Quantitative Characterizaiton of Hierarchical Surface Topographies. *Microscopy and Microanalysis,* 22(1): 168-177.

LIU, K. & OSTADHASSAN, M. 2017. Quantification of the microstructures of Bakken shale reservoirs using multi-fractal and lacunarity analysis. *Journal of Natural Gas Science and Engineering*, 39: 62-71.

LIU, Z., SHI, B., INYANG, H., & CAI, Y. 2005. Magnification effects on the interpretation of SEM images of expansive soils. *Engineering Geology,* 78:89-94.

LIU, Y. & VANAPALLI, S. 2019. Influence of Lateral Swelling Pressure on the Geotechnical Infrastructure in Expansive Soils. *Journal of Geotechnical and Geoenvironmental Engineering,* 143(6).

LIUCCI, L. & MELELLI, L. 2017. The fractal properties of topography as controlled by the interactions of tectonic, lithological, and geomorphological processes. *Earth Surface Processes and Landforms*, 42(15): 2585-2598.

LLORET, A., VILLAR, M., SANCHEZ, M., GENES, A., PINTADO, X., & ALONSO, E. 2003. Mechanical behavior of heavily compacted bentonite under high suction changes. *Geotechnique*, 53(1): 27-40.

LOCAT, J., TANAKA, H., TAN, T., DESARI, G., & LEE, H. 2003. Natural soils: geotechnical behavior and geologic knowledge. In *Characterization and Engineering Properties of Natural Soils*, Tan et al., eds. Vol 1, Swets and Zeitlinger, Amsterdam, 3-28.

LU, N. & LIKOS, W. 2004. *Unsaturated Soil Mechanics.* Wiley, Hoboken, NJ.

LUDING, S. 2008. Cohesive, frictional powders: contact models for tension. *Granual Matter,* 10(4).

LUO, L. & LIN, H. 2009. Lacunarity and Fractal Analyses of Soil Macropores and Preferential Transport Using Micro-X-Ray Computed Tomography. *Vadose Zone Journal*, 8: 233-241.

MA, B., CAI, K., ZENG, X., LI, Z., HU, Z., CHEN, Q., HE, C., CHEN, B., & HUANG, X. 2021. Experimental Study on Physical-Mechanical Properties of Expansive Soil Improved by Multiple Admixtures. *Advances in Civil Engineering,* 2021: 1-15.

MA, T., YAO, C., DONG, Y., PANPAN, Y., & WEI, C. 2019. Physicochemical approach to evaluating the swelling pressure of expansie soils. *Applied Clay Science*, 172: 85-95.

MANDELBROT, B. 1967. How Long Is the Coast of Britain? Statistical Self-Similarity and Fractional Dimension. *Science* 156(3775): 636-638.

MANDELBROT, B. 1977. *The Fractal Geometry of Nature*, W. H. Freeman and Company. New York, New York.

MANDELBROT, B. 1982. *The Fractal Geometry of Nature*, Freeman, New York.

MEHTA, B. & SACHAN, A. 2017. Effect of Mineralogical Properties of Expansive Soil on Its Mechanical Behavior. *Geotechnical and Geological Engieering*, 35(6): 2923-2934.

MESHRAM, K., SINGH, N., & JAIN, P. 2021. Estimation of swelling characteristics of expansive soils with influence of clay mineralogy. *Acta Agriculture Scandinavia. Section B, Soil and Plant Science*, 71(3): 202-207.

MILLER, C., YESILLER, N., YALDO, K., & MERAYYAN, S. 2002. Impact of Soil Type and Compaction Conditions on Soil Water Characteristic, *Journal of Geotechnical and Geoenvironmental Engineering*, 128(9): 733-742.

MITCHELL, J. & SOGA, K. 2005. *Fundamentals of Soil Behavior*, 3rd ed, John Wiley & Sons.

MOJID, M., 2011. Diffuse Double Layer (DDL). In Glinski, J., Horabik, J., Lipiec, J. (eds.) *Encyclopedia of Agrophysics.* Encyclopedia of Earth Sciences Series. Springer, Dordrecht.

MONTES-H, G. 2005. Swelling-shrinkage measurements of bentonite using coupled environmetnal scanning electron microscopy and digital image analysis. *Journal of Colloid and Interface Science*, 284: 271-277.

MONTES-H, G., DUPLAY, J., MARTINEZ, L., ESCOFFIER, S., & ROUSSET, D. 2004. Structural modifications of Callovo-Oxfordian agrillite under hydration/dehydration conditions. *Applied Clay Science*, 25: 187-194.

MONTES-H, G., GERAUD, Y., DUPLAY, J., & REUSCHLE, T. 2005. ESEM observations of compacted bentonite submitted to hydration/dehydration conditions. *Colloids and Surfaces*, 262: 14-22.

MOSTEANU, N. 2019. Intelligent Tool to prevent Economic Crisis – Fractals. A Possible Solution to assess the Mangement of Financial Risk. *Calitatea*, 20(172): 13-17.

NIELSEN, B., ALBREGTSEN, F., & DANIELSEN, H. 2002. Fractal Signature Vectors and Lacunarity Class Distance Matrices to Extract New Adaptive Texture Features from Cell Nuclei. In *Fractals in Biology and Medicine*, Losa, G., Merlini, D., Nonnenmacher, T. & Weibel, E., eds. Birkhauser, Basel.

OFER, Z. 1981. Laboratory Instrument for Measuring Lateral Soil Pressure and Swelling Pressure. *Geotechnical Testing Journal*, 4(4): 177-182.

OHM, H. & HRYCIW, R. 2014. Size distribution of coarse-grained soil by sedimaging. Journal of Geotechnical and Geoenvironmental Engineering, 140(4).

OPPELT, A., KURTH, W., DZIERZON, H., JENTSCHKE, G., & GODBOLD, D. 2000. Structure and fractal dimensions of root systems of four co-occurring fruit tree species from Botswana. *Annals of Forest Science*, 57(5-6): 463-475.

ORBACH, R. 1986. Dynamics of fractal networks. *Science*, 231: 814-819.

PACHEPSKY, Y., POLUBESOVA, T., HAJNOS, M., SOKOLOWSKA, , Z., & JOZEFACIUK, G. 1995. Fractal parameters of pore surface area as influenced by simulated soil degradation. *Soil Science Society of America Journal*, 59: 68-75.

PENUMADU, D. & DEAN, J. 2000. Compressibility Effect in Evaluating the Pore-Size Distribution of Kaolin Clay Using Mercury Intrusion Porosimetry. *Canadian Geotechnical Journal*, 37(2): 393-405.

PENDELTON, D., DATHE, A., & BAVEYE, P. 2005. Influence of image resolution and evaluation algorithm on estimates of the lacunarity of porous media. *Physical Review E,* 72(4).

PERFECT, E. & KAY, B. 1995. Applications of fractals in soil and tillage research: a review. *Soil & Tillage Research*, 36:1-20.

PERFECT, E., MCLAUGHLIN, N., KAY, B., & TOPP, G. 1996. An improved fractal equation for the soil water retention curve. *Water Resources Research*, 32: 281-287.

PETERS, E. 1994. *Fractal Market Analysis: Applying Chaos Theory to Investment and Economics*. Wiley.

PLOTNICK, R., GARDNER, R., HARGROVE, W., PRESTEGAARD, K., & PERLMUTTER, M. 1996. Lacunarity analysis: A general technique for the analysis of spatial patterns. *Physical Review E*, 53(5): 5461-5468.

PLOTNICK, R., GARDNER, R., & O'NEILL, R. 1993. Lacunarity indices as measures of landscape texture. *Landscape Ecology*, 8(3): 201-211.

POLIDORI, E. 2009. Reappraisal of the Activity of Clays. Activity Chart. *Soils and* Foundations, 49(3): 431-441.

PUPPALA, A. & CERATO, A. 2009. Heave distress problems in chemically-treated sulfate-laden materials. Geo-Strata, 10(2): 28-32.

PUSCH, R. 2019. Microstructure controls physical properties of smectite clay. *Journal of Earth Sciences and Geotechnical Engineering*, 9(3): 63-98.

QI, S. & VANAPALLI, S. 2015. Hydro-mechanical coupling effect on surficial layer stability of unsaturated expansive soil slopes. *Computers and Geotechnics*, 70: 68-82.

QUIGLEY, R., SETHIS, A., BOONSINSUK, P., SHEEREN, D., & YONG, R. 1985. Geologic controls on soil composition and properties, Lake Ojibway Clay Plain, Matagami, Quebec. *Canadian Geotechnical Journal*, 22(4): 491-500.

RAK, R., KWAPIEN, J., OSWIECIMKA, P., ZIEBA, P., & DROZDZ, S. 2020. Universal features of mountain ridge networks on Earth. *Journal of Complex Networks*, 8(1).

REDDY, P. MOHANTY, B., & RAO, B. 2020. Influence of Clay Content and Montmorillonite Content on Swelling Behavior of Expansive Soils. *International Journao of Geosynthetics and Ground Engineering*, 6(1).

REES, W. 2020. Fractal biology of plague and the future of civilization. *Journal of Population and Sustainability*, 5(1).

ROJEK, J., ZUBELEWICZ, A., MADAN, N., & NOSEWICZ, S. 2018. The discrete element method with deformable particles. *International Journal for Numerical Methods in Engineering*, 114(8): 828-860.

ROLLINS, K. & KIM, J. 2010. Dynamic Compaction of Collapsible Soils Based on U.S. Case Histories. Journal of Geotechnical and Geoenvironmental Engineering, 136(9).

ROMERO, E. 1999. Thermo-hydro-mechanical behavior of unsaturated Boom clay: an experimetnal study. PhD Thesis, Universidad Politecnica de Catalunya, Barcelona, Spain.

ROMERO, E. & SIMMS, S. 2008. Microstructural Investigation in Unsaturated Soils: A Review with Special Attention to Contribution of Mercury Intrusion Porosimetry and Environmental Scanning Electron Microscopy. Geotechnical and Geological Engineering, 26: 705-727.

ROY, A., PERFECT, E., DUNNE, W., ODLING, N., & KIM, J. 2010. Lacunarity analysis of fracture networks: Evidence for scale-dependent clustering. *Journal of Structural Geology*, 32: 1444-1449.

SALA, N. 2021. Fractal Geometry in Compuer Graphics and in Virtual Reality. *Chaos and Complexity Letters*, 15(2-3): 251-265.

SALAHUDEEN, A., EBEREMU, A., & OSINUBI, K. 2014. Assessment of Cement Kiln Dust-Treated Expansive Soil for the Construction of Flexible Pavements. *Geotechnical and Geological Engineering*, 32(4): 923-931.

SCHANZ, T. & TRIPATHY, S. 2009. Swelling pressure of a divalent-rich bentonite: Diffuse double-layer theory revisited. *Water Resources Research*, 45(5).

SCHINDELIN, J., ARGANDA-CARRERAS, I., FRISE, E., KAYNIG, V., LONGAIR, M., PIETZSCH, T., PREIBISCH, S., RUEDEN, C., SAALFELD, S., SCHMID, B.,

TINEVEZ, J., WHITE, D., HARTENSTEIN, V., ELICEIRI, K., TOMANCAK, P., & CARDONA, A. 2012. Fiji: an open-source platform for biological image analysis. *Nature Methods,* 9(7): 676-682.

SEIPHOORI, A., FERRARI, A., & LALOUI, L. 2014. Water retention behavior and microstructural evolution of MX-80 bentonite during wetting and drying cycles. *Geotechnique,* 64(9): 721-734.

SIKH, T. 1993. Swell Potential Versus Overburden Pressure. *Geotechnical Testing Journal,* 16(3): 393-396.

SIMA, J., JIANG, M., & ZHOU, C. 2014. Numerical Simulation of Desiccation Cracking in a Thin Clay Layer Using 3D Discrete Element Modeling. *Computers and Geotechnics*, 56:168-180.

SHANKAR, K. 2019. *A Comparison Between Molecular Dynamics and Monte Carlo Simulations of a Lennard-Jones Fluid*. CBE 641: Nanoscale Transport Project Report.

SHE, J., LU, Z., YAO, H., FANG, R., & XIAN, S. 2019. Experimental Study on the Swelling Behavior of Expansive Soil at Different Depths under Unidirectional Seepage. *Applied Sciences*, 9: 1233.

SKEMPTON, A. 1953. The colloidal activity of clays. In *Proceedings of the third international conference on soil mechanics and foundation engineering,* Zurich, Switzerland: 57-61.

SMITH, T., LANGE, G., & MARKS, W. 1996. Fractal methods and results in cellular morphology – dimensions, lacunarity and multifractals. *Journal of Neuroscience Methods*, 69: 123-136.

SUK, J., PINER, R., AN, J., & RUOFF, R. 2013. Evaluation of elastic modulus of ultra-thin vermiculite membranes by contact mode atomic force microscopy imaging. *Thin Solid Films*, 527: 205-209.

SUN, L. HIRVI, J., SCHATZ, T., KASA, S., & PAKKANEN, T. 2015. Estimation of Montmorillonite Swelling Pressure: A Molecular Dynamics Approach. *Journal of Physical Chemistry,* 119: 19863-19868.

SUN, H., MASIN, D., NAJSER, J., NEDELA, V., & NAVRATILOVA, E. 2019. Bentonite microstructure and saturation evolution in wetting-drying cycles evaluated using ESEM, MIP and WRC measurements. *Geotechnique,* 69(8): 713-726.

SUN, H., MASIN, D., NAJSER, J., NEDELA, V., & NAVRATILOVA, E. 2020. Fractal characteristics of pore structure of compacted bentonite studied by ESEM and MIP methods. *Acta Geotechnica,* 15: 1655-1671.

TABET, W. 2015. Characterization of cement-stabilized clay using experimental and analytical techniques. Doctoral dissertation, University of Oklahoma.

TABET, W. CERATO, A., ELWOOD MADDEN, A., & JENTOFT, R. 2018. Characterization of Hydration Products' Formation and Strength Development in Cement-Stabilized Kaolinite Using TG and XRD. Journal of Materials in Civil Engineering, 30(10): 04018261.

THAKUR, V., SREEDEEP, S., & SINGH, D. 2006. Laboratory investigations on extremely high suction measurements for fine-grained soils. *Geotechnical and Geoenvironmental Engineering*, 24: 565-578.

TINJUM, J., BENSON, C., & BLOTZ, L. 1997. Soil-Water Characteristic Curves for Compacted Clays. *Journal of Geotechnical and Geoenvironmental Engineering*, 123(11): 1060-1069.

TOLEDO, P. NOVY, R., DAVIS, H., & SCRIVEN, L. 1990. Hydraulic conductivity of porous media at low water content. Soil Science Society of America Journal, 54: 673-679.

TREMBLAY, H., DUCHESNE, J., LOCAT, J., & LEROUEIL, S. 2002. Influence of the nature of organic compounds on fine soil stabilization with cement. *Canadian Geotechnical Journal*, 39: 535-546.

TSONIS, A. & ELSNER, J. 1987. Fractal Characterization and Simulation of Lightning. *Contributions to Atmospheric Physics*, 60(2): 187-192.

TURAN, C., JAVADI, A., VINAI, R., & RUSSO, G. 2022. Effects of Fly Ash Inclusion and Alkali Activation on Physical, Mechanical, and Chemical Properties of Clays. *Materials,* 15, 4628.

TURCOTTE, D. 2001. Fractals in Petrology, *Lithos,* 65:261-271.

TYLER, S., & WHEATCRAFT, S. 1989. Applications of fractal mathematics to soil water retention estimation. *Soil Science Society of America Journal*, 53: 987-996.

TYLER, S., & WHEATCRAFT, S. 1990. Fractal Processes in Soil Water Retention. Water Resources Research, 26(5): 1047-1054.

TYLER, S., & WHEATCRAFT, S. 1992. Fractal scaling of soil particle-size distribution: analysis and limitations. Soil Science Society of America Journal, 56: 362-369.

URAL, N. 2021. The significance of scanning electron microscopy (SEM) analysis on the microstructure of improved clay: An overview. *Open Geosciences,* 13(1): 197-218.

VAN GENUCHTEN, M. 1980. A Closed-form Equation for Predicting the Hydraulic Conductivity of Unsaturated Soils. *Soil Science Society of America Journal*, 44: 892-898.

VAN OLPHEN, H. 1977. *An Introduction to Clay Colloid Chemistry*. New York: Wiley.

VENKATESHAIAH, A., PADIL, V., NAGLAKSHMAIAH, M., WACLAWEK, S., CERNIK, M., & VARMA, R. 2020. Microscopic Techniques for the Analsyis of Micro and Nanostructures of Biopolymers and Their Derivatives. *Polymers*, 12(3).

VENTOLA, A., HORSTMEIER, G., HRYCIW, R., KEMPF, C., & EYKHOLT, J. 2020. Particle Size Distribution of Kalamazoo River Sediments by FieldSed. Journal of Geotechnical and Geoenvironmental Engineering, 146(12).

VILLAR, M. 2007. Water retention of two natural compacted bentonites. *Clays and Clay Materials,* 55(3): 311-322.

WANG, Y. & XU, D. 2007. Dual Porosity and Secondary Consolidation. *Journal of Geotechnical and Geoenvironmental Engineering,* 133(7): 793-801.

WATANABE, Y. & TANAKA, Y. 2023. Swelling pressure of compacted bentonite acting on constraining material with deformability. *Geotechnique,* 73(2): 95-104.

WASHBURN, E. 1921. Note on a Method of Determining the Distribution of Pore Sizes in a Porous Material. Proceedings of the National Academy of Sciences, 7(4): 115-116.

WRAY, W., & MEYER, K. 2004. Expansive Clay Soil: a Widespread and Costly GeoHazard. *GeoStrata,* ASCE, GeoInstitute, 5(4): 24-28.

XU, L., ZHA, F., LIU, C., KANG, B., LIU, J., & YU, C. 2020. Experimental Investigation on Carbonation Behavior in Lime-Stabilized Expansive Soil, *Advances in Civil Engineering,* 2020: 1-14.

YANG, L., WENDROTH, O., LIU, B., & SHI, C. 2019. Is the Laser Diffraction Method Reliable for Soil Particle Size Distribution Analysis? Soil Science Society of America Journal, 83(2): 276-287.

YANG, R., HE, S., YI, J., & HU, Q. 2016. Nano-scale pore structure and fractal dimension of organic-rich Wufeng-Longmaxi shale from Jiaoshiba area, Sichuan Basin: Investigations using FE-SEM gas adsorption and helium pycnometry. *Marine and Petroleum Geology,* 70: 27-45.

YANG, Y., QIAO, R., WANG, Y., SUN, S. 2021. Swelling pressure of montmorillonite with multiple water layers at elevated temperatures and water pressures: A molecular dynamics study. *Applied Clay Science,* 201: 105924.

YAO, M. & ANANDARAJAH, A. 2003. Three-dimensional discrete element method of analysis of clays. *Journal of Engineering Mechanics,* 129(6): 585-596.

YUAN, S., LIU, X., SLOAN, S., & BUZZI, O. 2016. Mutli-scale characterization of swelling behavior of compacted Maryland clay. *Acta Geotechnica,* 11(4):789-804.

ZAMIN, B., NASIR, H., MEHMOOD, K., IQBAL, Q., FAROOQ, A., & TUFAIL, M. 2021. An Experimental Study on the Geotechnical, Mineralogical, and Swelling Behavior of KPK Expansive Soils. *Advances in Civil Engineering*, 2021.

ZBIK, M., SMART, R., & MORRIS, G. 2008. Kaolinite flocculation structure. *Journal of Colloid and Interface Science*, 328(1): 73-80.

ZEINALI, S. & ABDELAZIZ, S. 2023. Microstructural evolution of saturated normally consolidated kaolinite clay under thermal cycles. *Engineeirng Geology*, 318:107101.

ZENG, Z., CUI, Y., ZHANG, F., CONIL, N., & TALANDIER, J. 2019. Investigation of swelling pressure of bentonite/claystone mixture in the full range of bentonite fraction. *Applied Clay Science*, 178: 105137.

ZHANG, R., LIU, Z., ZHENG, J., & ZHANG, J. 2020. Experimental Evaluation of Lateral Swelling Pressure of Expansive Soil Fill behind a Retaining Wall. *Materials in Civil Engineering*, 32(2).

ZHANG, T., CAI, G., & LIU, S. 2018. Application of Lignin-Stabilized Silty Soil in Highway Subgrade: A Macroscale Laboratory Study. *Journal of Materials in Civil Engineering*, 30(4).

ZHANG, X., GAO, J., FAN, H., LI, X., GAO, Z., XUE, L., & SUN, S. 2020. Study on the Mechanism of Nano-SiO_2 for Improving the Properties of Cement-Based Soil Stabilizer, *Nanomaterials*, 10(3).

ZHANG, Y., CHEN, M., LI, G., SHI, C., WANG, B., & LING, Z. 2020. Exfoliated vermiculite nanosheets supporting tetraethylenepentamine for CO2 capture. *Results in Materials*, 7: 100102.

ZHOU, B., WANG, J., & WANG, H. 2018. Three-dimensional sphericity, roundness and fractal dimension of sand particles. *Geotechnique*, 68(1): 18-30.

ZHOU, S., ZHOU, D., ZHANG, Y., & WANG, W. 2019. Study on Physical-Mechanical Properties and Microstructure of Expansivei Soil Stabilized with Fly Ash and Lime. *Advances in Civil Engineering*, 2019: 1-15.

ZMESKAL, O., DZIK, P., & VESELY, M. 2013. Entropy of Fractal Systems. *Computers & Mathematics with Applications*, 66(2): 135-146.

ZOU, W., YE, J., HAN, Z., VANAPALLI, S., & TU, H. 2018. Effect of montmorillonite content and sodium chloride solution on the residual swelling pressure of an expansive clay. *Environmental Earth Sciences*, 77(19).

Appendix A – ESEM Micrographs

ESEM Micrographs of Kaolinite specimens

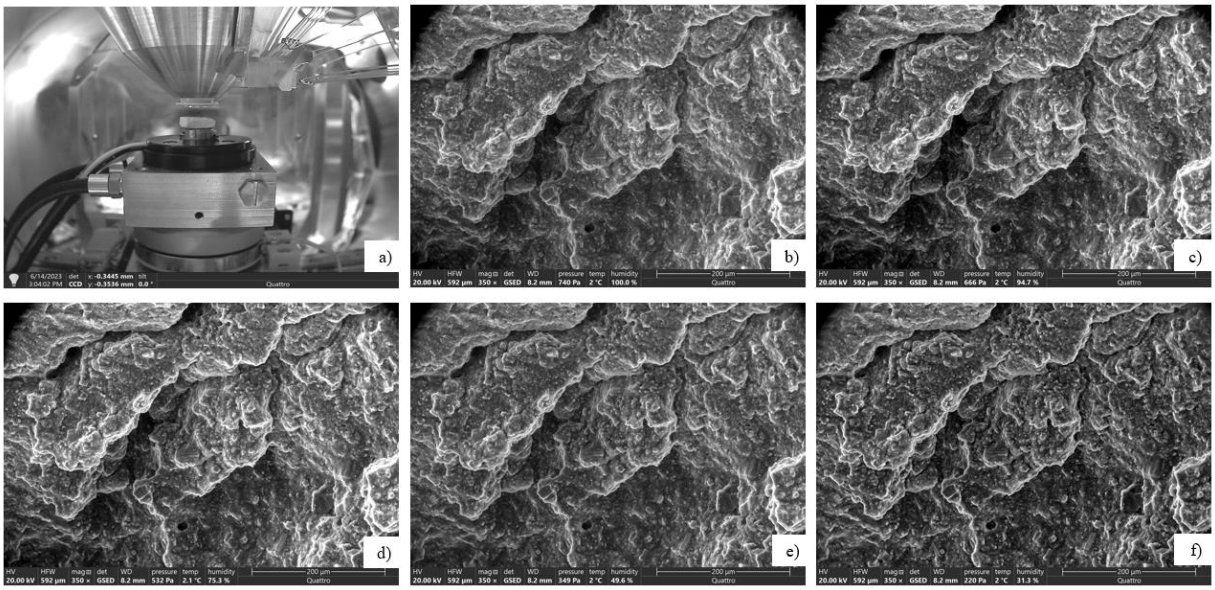

Figure A.1. Primary drying cycle of Kaolinite specimen, Magnification = 350X, T = 2C, initial dry density = 1.44 g/cm^3, compacted water content = 31%, a) Specimen seating; b) 0 MPa; c) 7 MPa; d) 36 MPa; e) 89 MPa; and f) 148 MPa

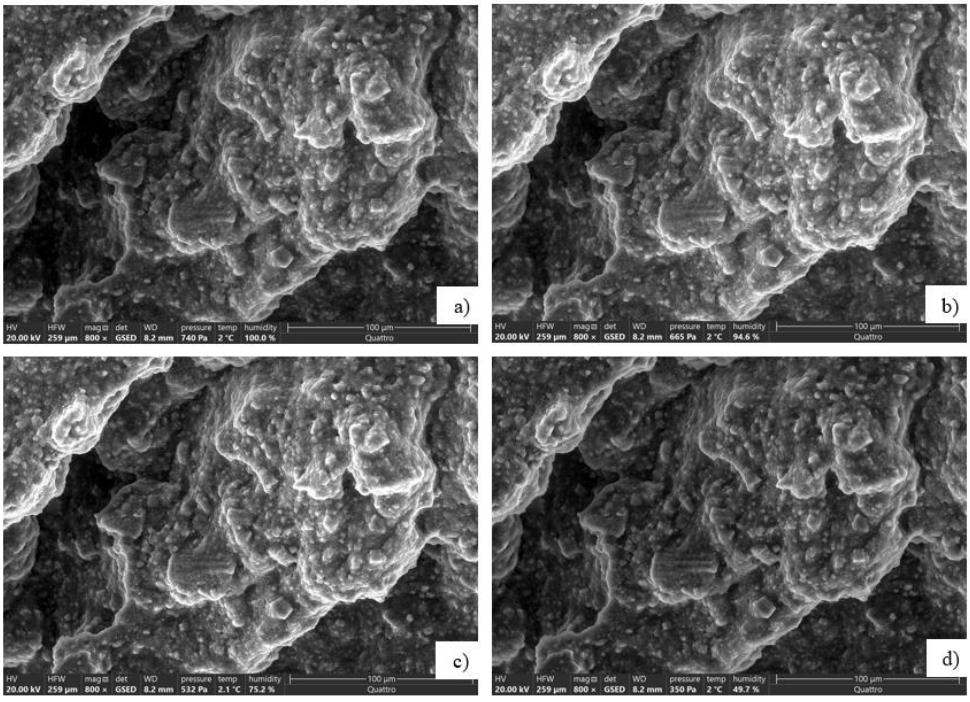

Figure A.2. Primary drying cycle of Kaolinite specimen, Magnification = 800X, T = 2C, initial dry density = 1.44 g/cm^3, compacted water content = 31%, a) 0 MPa; b) 7 MPa; c) 36 MPa; and d) 89 MPa.

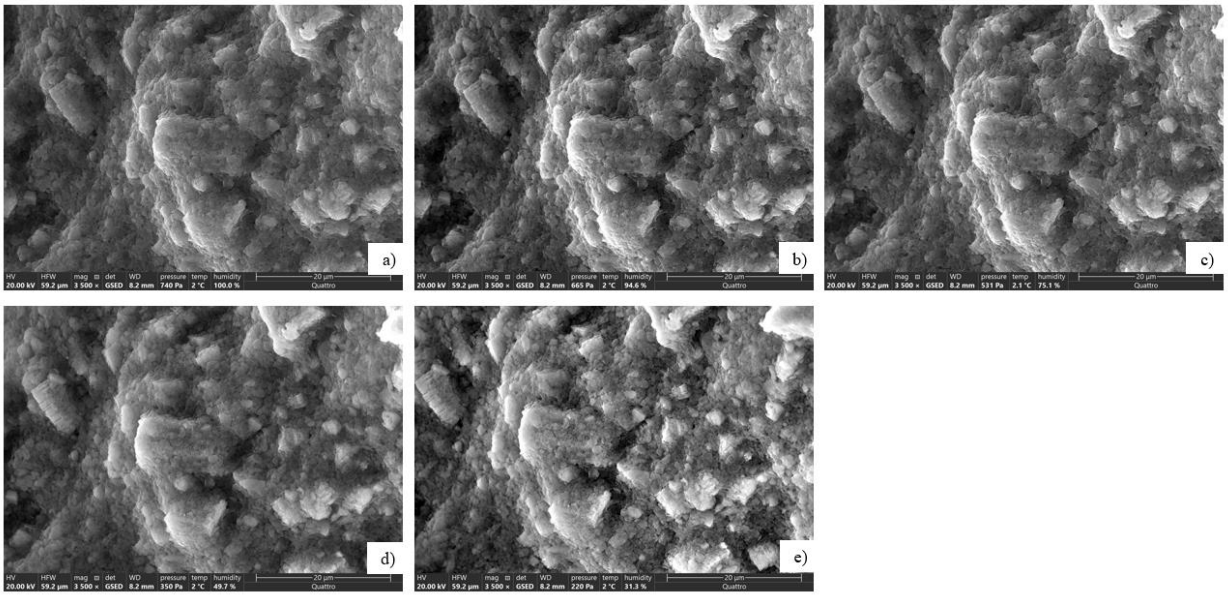

Figure A.3. Primary drying cycle of Kaolinite specimen, Magnification = 3500X, T = 2C, initial dry density = 1.44 g/cm^3, compacted water content = 31%, a) 0 MPa; b) 7 MPa; c) 36 MPa; d) 89 MPa; and e) 148 MPa

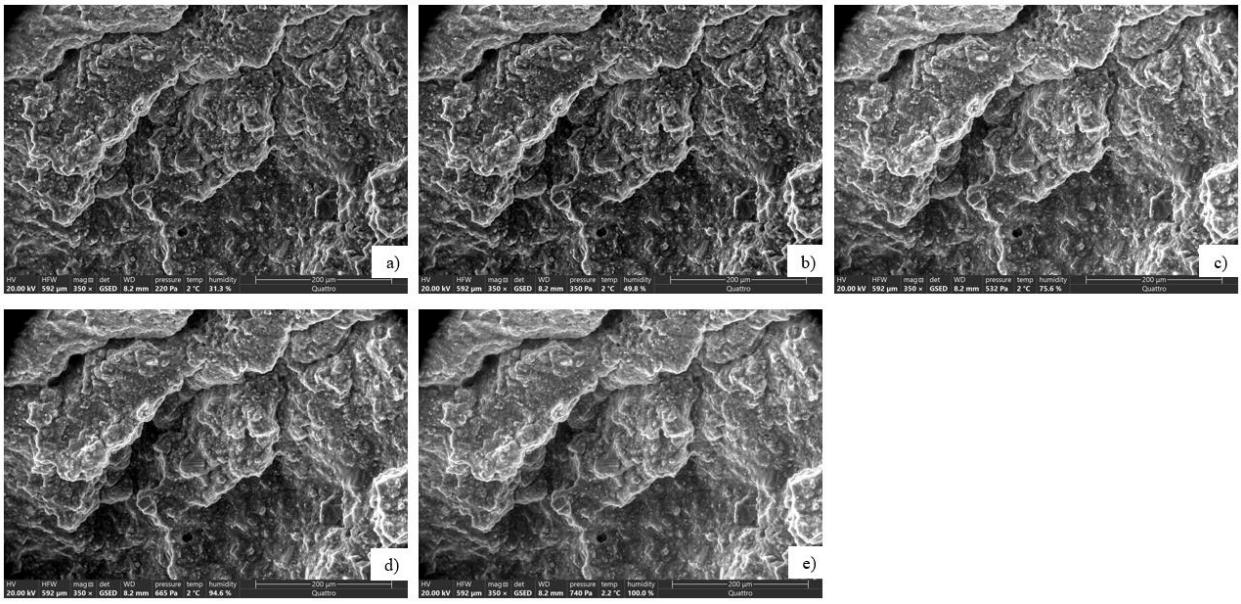

Figure A.4. Secondary wetting cycle of Kaolinite specimen, Magnification = 350X, T = 2C, initial dry density = 1.44 g/cm^3, compacted water content = 31%, a) 148 MPa; b) 89 MPa; c) 36 MPa; d) 7 MPa; and e) 0 MPa

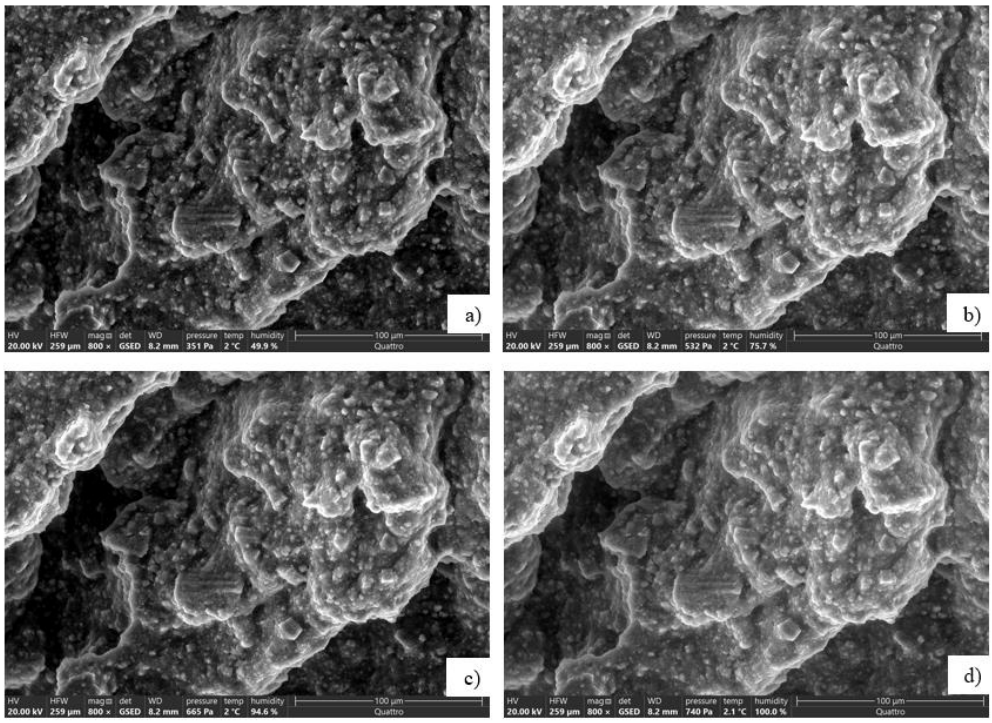

Figure A.5. Secondary wetting cycle of Kaolinite specimen, Magnification = 800X, T = 2C, initial dry density = 1.44 g/cm^3, compacted water content = 31%, a) 89 MPa; b) 36 MPa; c) 7 MPa; d) and 0 MPa

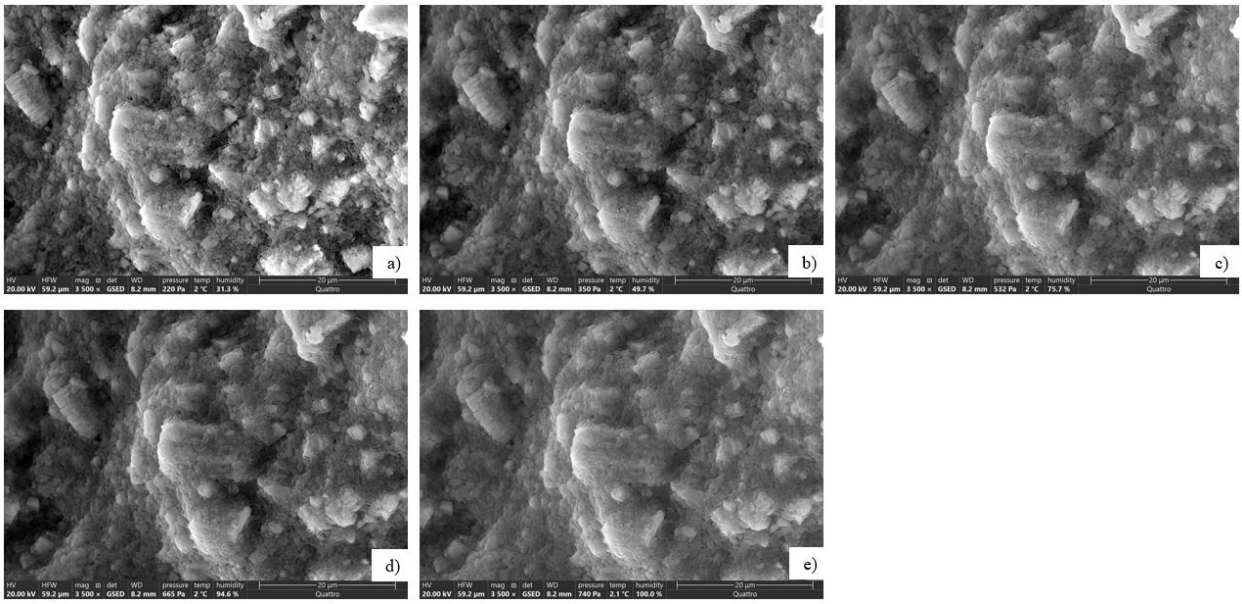

Figure A.6. Secondary wetting cycle of Kaolinite specimen, Magnification = 3500X, T = 2C, initial dry density = 1.44 g/cm^3, compacted water content = 31%, a) 148 MPa; b) 89 MPa; c) 36 MPa; d) 7 MPa; and e) 0 MPa

ESEM Micrographs of Carnisaw specimens

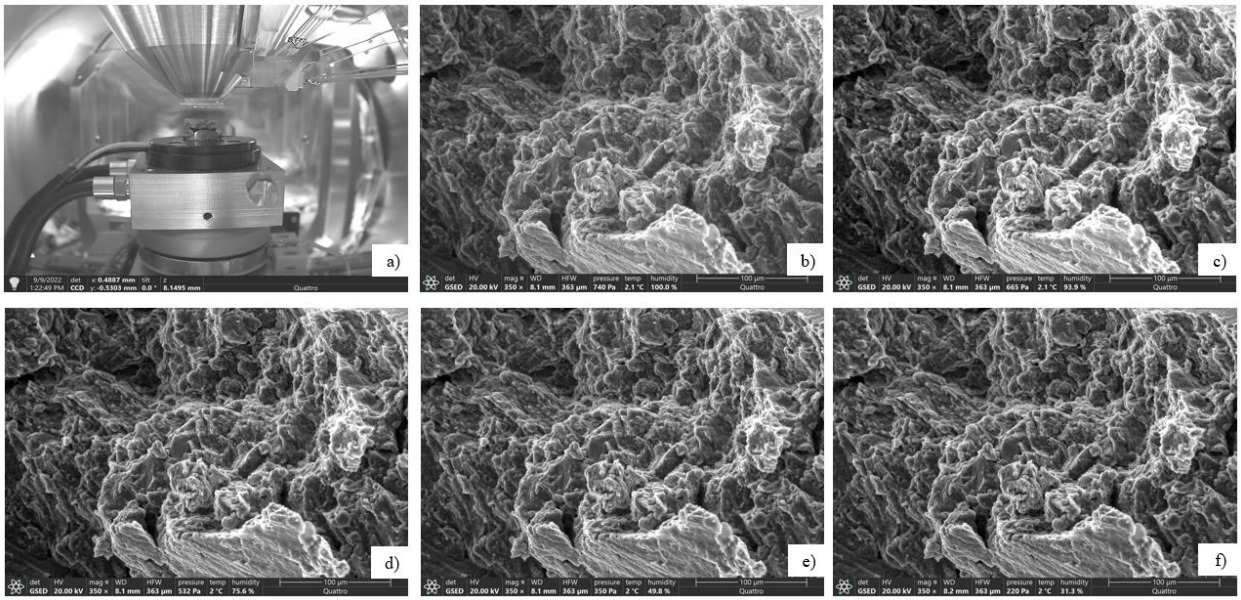

Figure A.7. Primary drying cycle of Carnisaw specimen, Magnification = 350X, T = 2C, initial dry density = 1.52 g/cm^3, compacted water content = 27%, a) Specimen seating; b) 0 MPa; c) 7 MPa; d) 36 MPa; e) 89 MPa; and f) 148 MPa

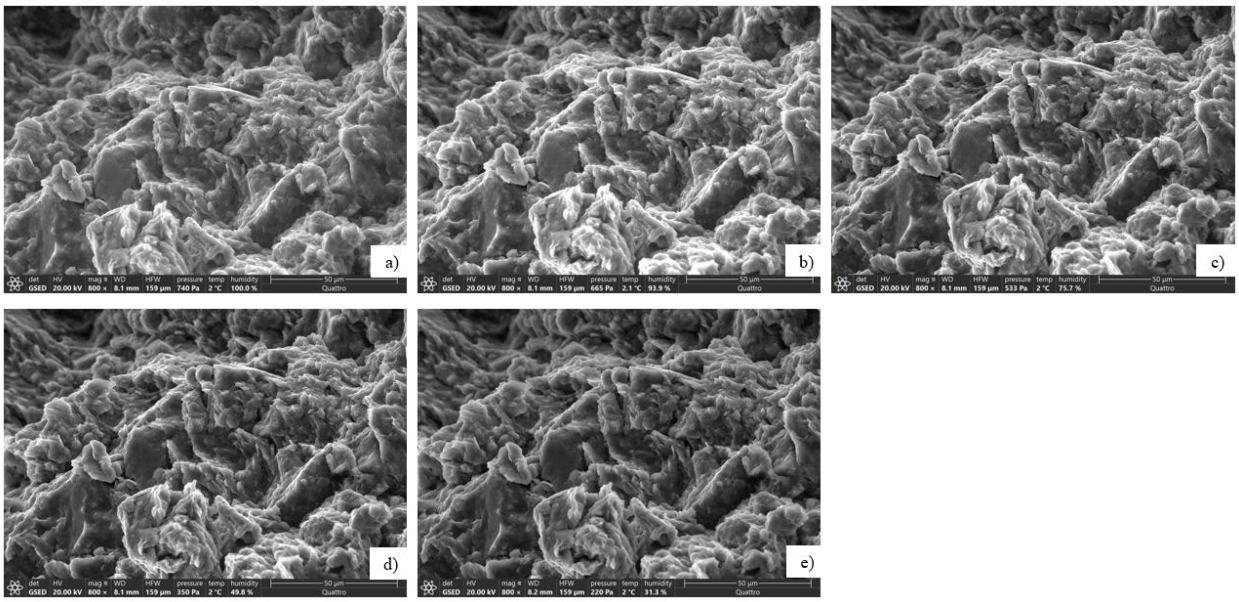

Figure A.8. Primary drying cycle of Carnisaw specimen, Magnification = 800X, T = 2C, initial dry density = 1.52 g/cm^3, compacted water content = 27%, a) 0MPa; b) 7 MPa; c) 36 MPa; d) 89 MPa; and e) 148 MPa

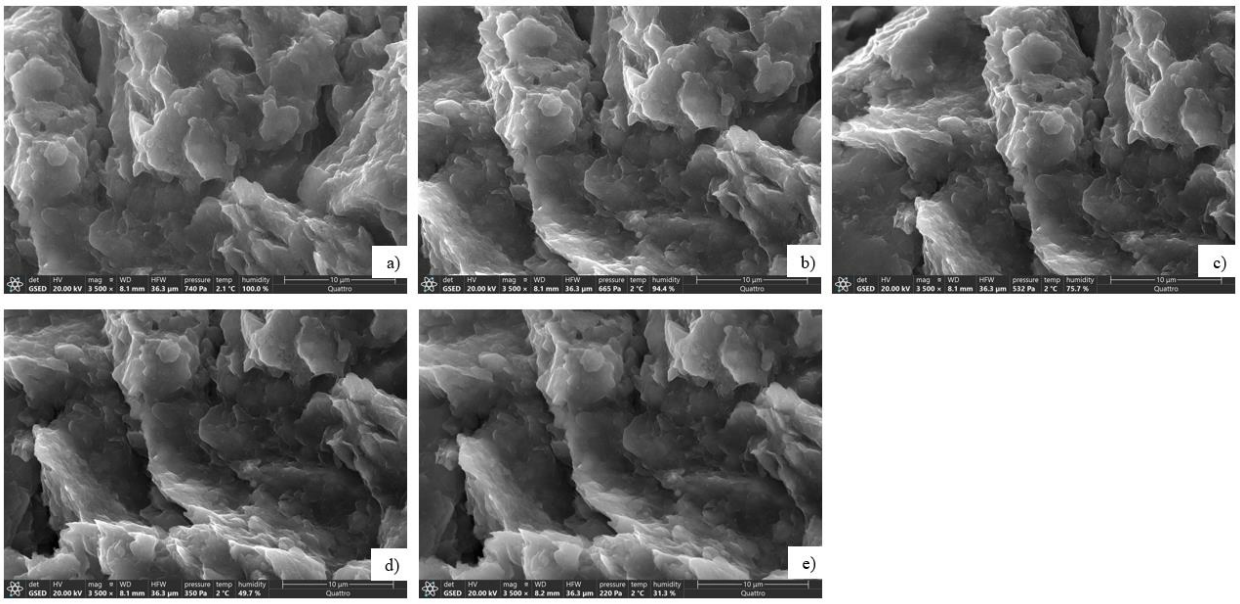

Figure A.9. Primary drying cycle of Carnisaw specimen, Magnification = 3500X, T = 2C, initial dry density = 1.52 g/cm^3, compacted water content = 27%, a) 0MPa; b) 7 MPa; c) 36 MPa; d) 89 MPa; and e) 148 MPa

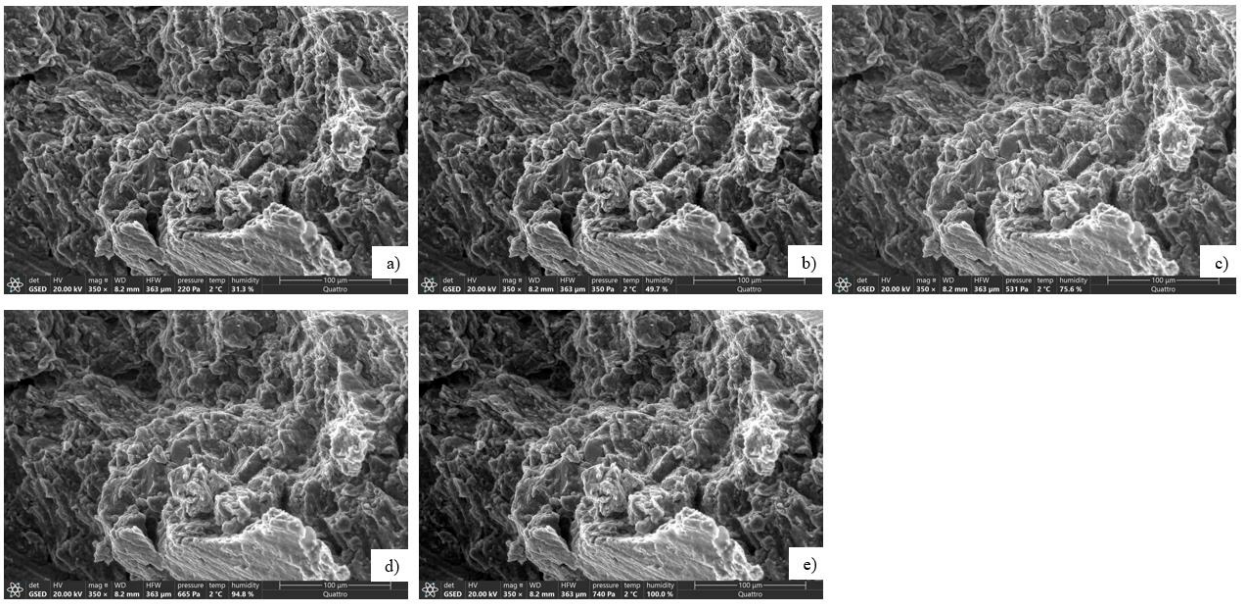

Figure A.10. Secondary wetting cycle of Carnisaw specimen, Magnification = 350X, T = 2C, initial dry density = 1.52 g/cm^3, compacted water content = 27%, a) 148 MPa; b) 89 MPa; c) 36 MPa; d) 7 MPa; and e) 0 MPa

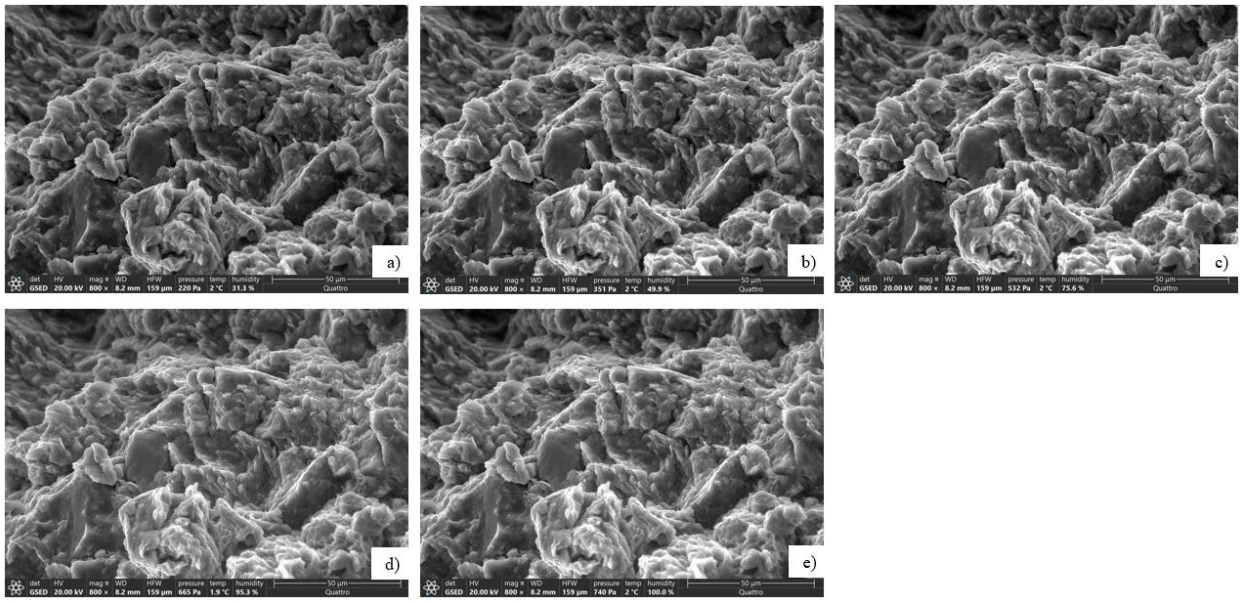

Figure A.11. Secondary wetting cycle of Carnisaw specimen, Magnification = 800X, T = 2C, initial dry density = 1.52 g/cm^3, compacted water content = 27%, a) 148 MPa; b) 89 MPa; c) 36 MPa; d) 7 MPa; and e) 0 MPa

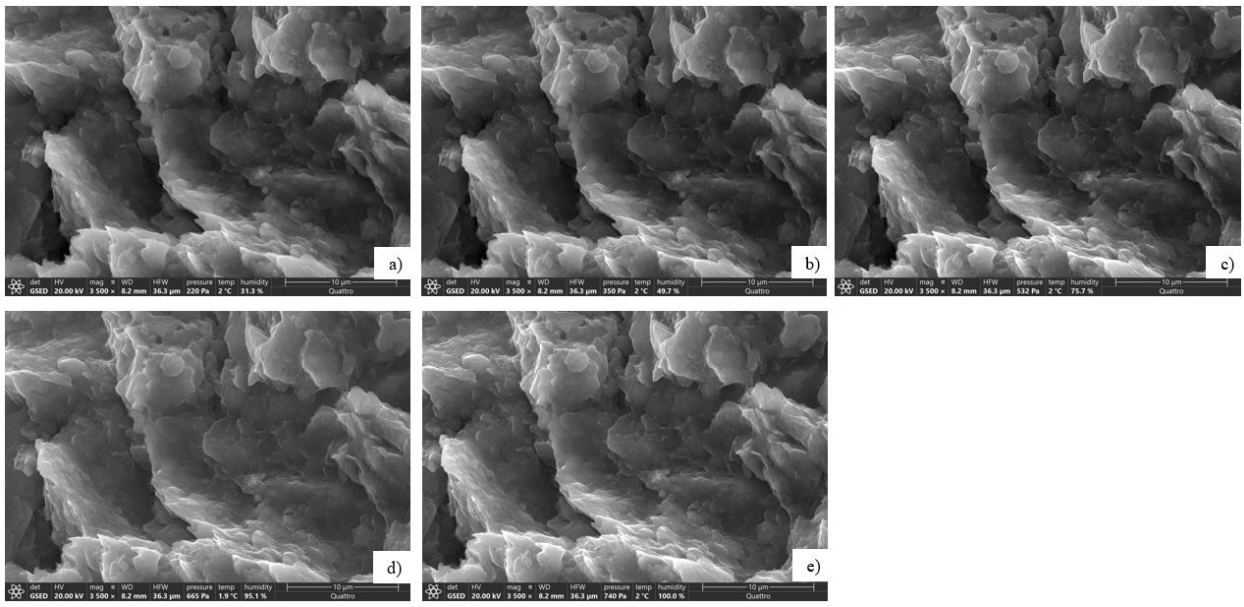

Figure A.12. Secondary wetting cycle of Carnisaw specimen, Magnification = 350X, T = 2C, initial dry density = 1.52 g/cm^3, compacted water content = 27%, a) 148 MPa; b) 89 MPa; c) 36 MPa; d) 7 MPa; and e) 0 MPa

ESEM Micrographs of Hollywood Specimens

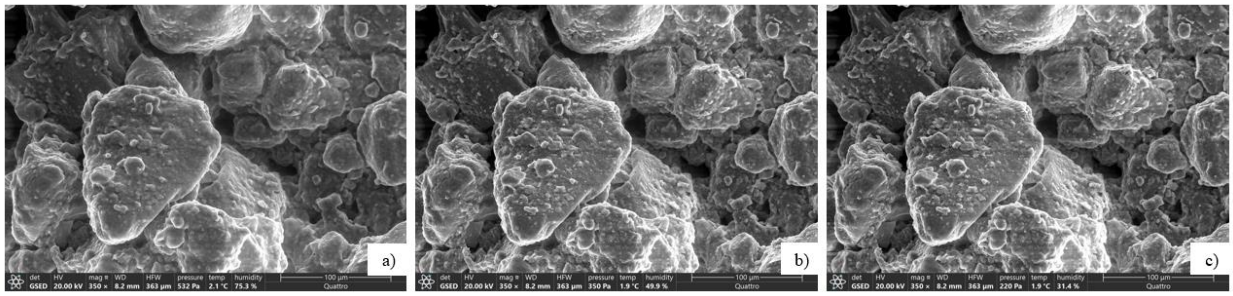

Figure A.13. Primary drying cycle of Hollywood specimen, Magnification = 350X, T = 2C, initial dry density = 1.67 g/cm^3, compacted water content = 20%, a) 36 MPa; b) 89 MPa; and c) 148 MPa

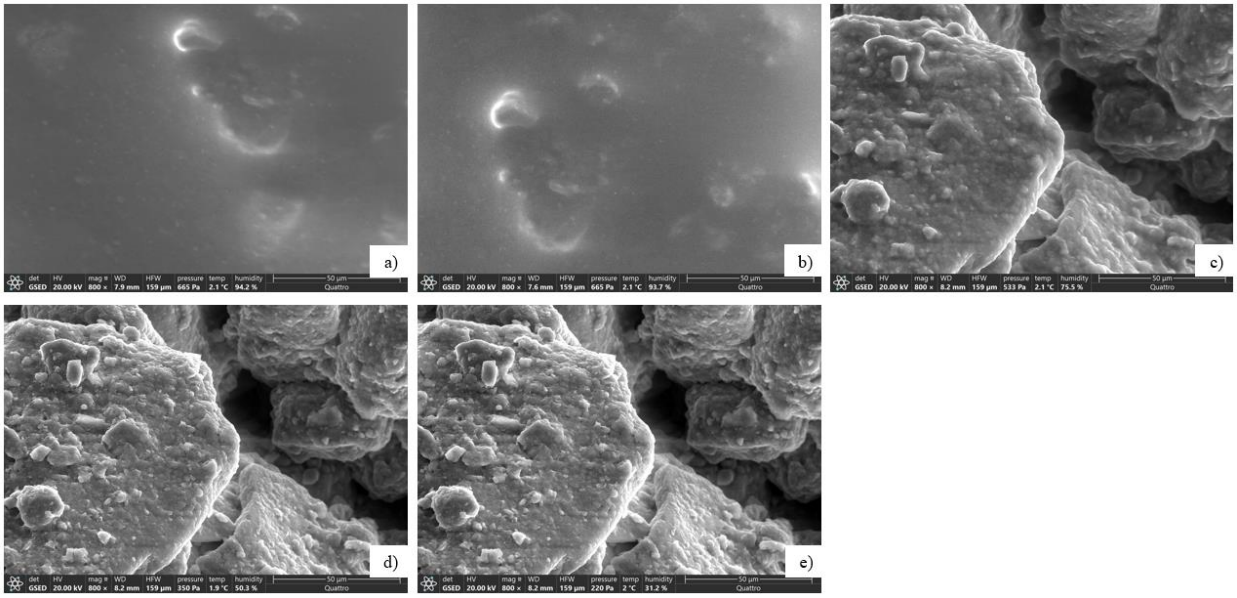

Figure A.14. Primary drying cycle of Hollywood specimen, Magnification = 800X, T = 2C, initial dry density = 1.67 g/cm^3, compacted water content = 20%, a) 7 MPa; b) 8 MPa; c) 36 MPa; d) 89 MPa; and e) 148 MPa

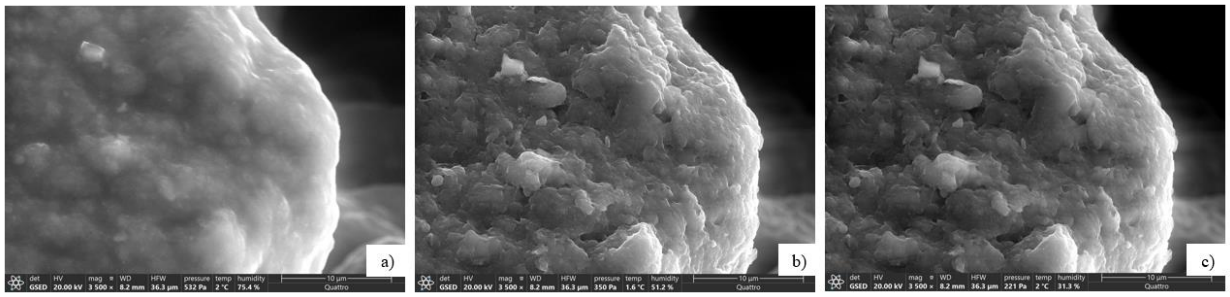

Figure A.15. Primary drying cycle of Hollywood specimen, Magnification = 3500X, T = 2C, initial dry density = 1.67 g/cm^3, compacted water content = 20%, a) 36 MPa; b) 89 MPa; and c) 148 MPa

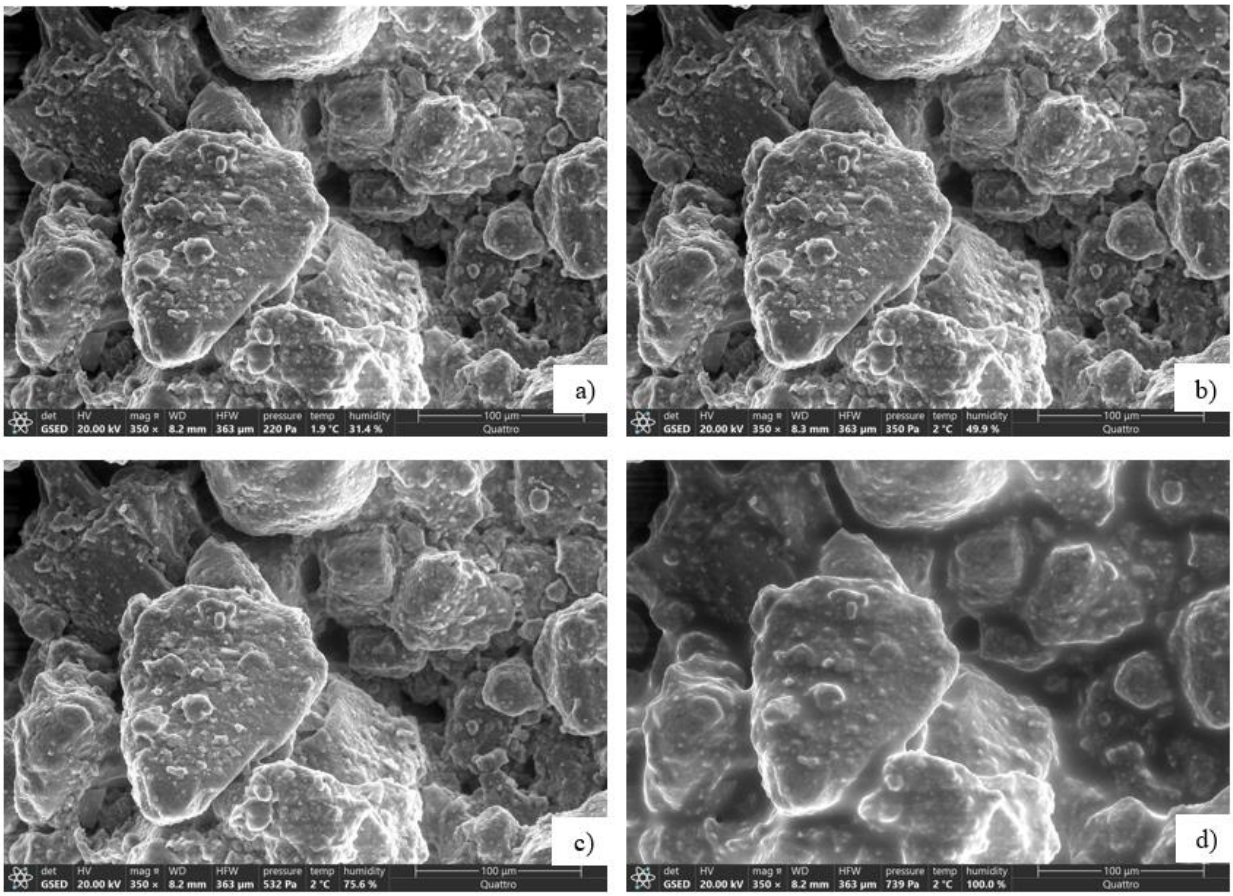

Figure A.16. Secondary wetting cycle of Hollywood specimen, Magnification = 350X, T = 2C, initial dry density = 1.67 g/cm^3, compacted water content = 20%, a) 148 MPa; b) 89 MPa; c) 36 MPa; and d) 0 MPa

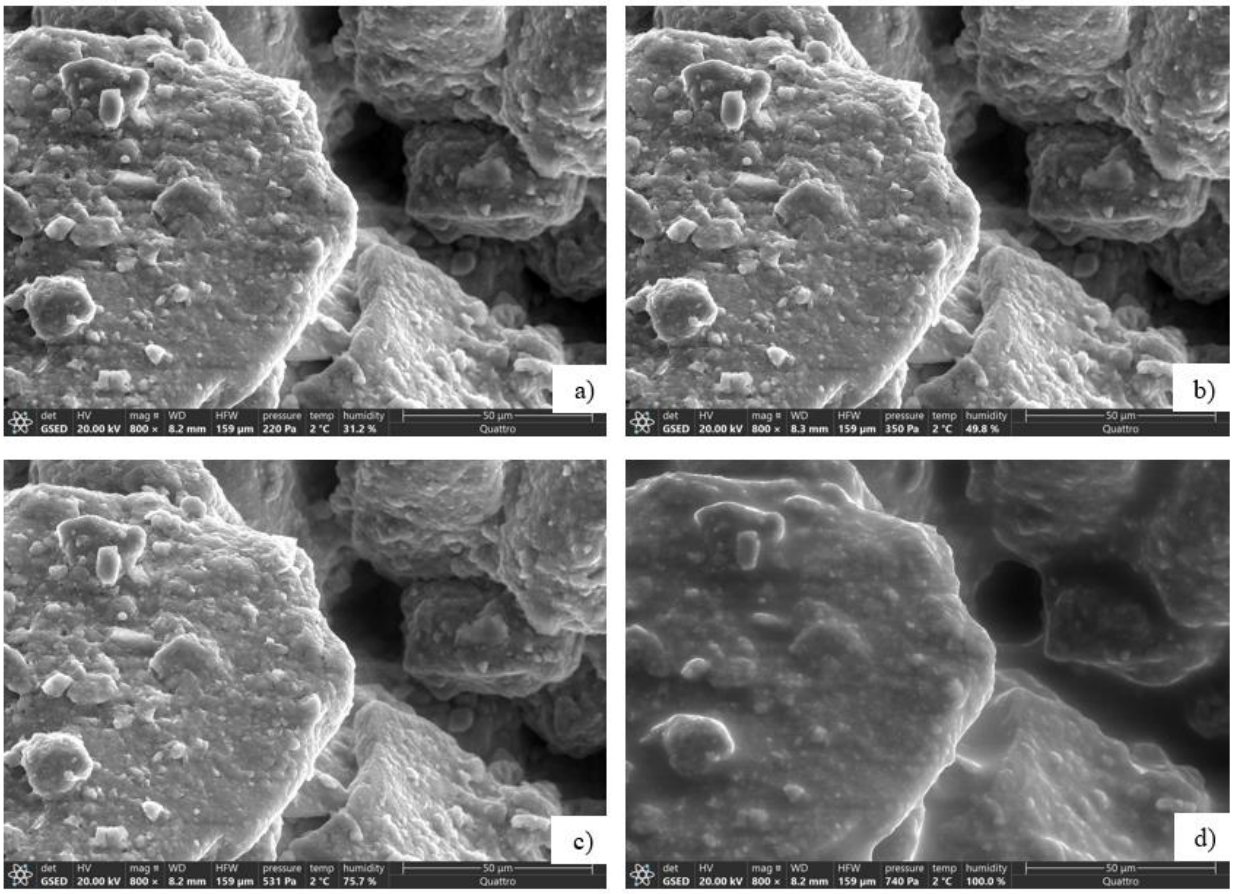

Figure A.17. Secondary wetting cycle of Hollywood specimen, Magnification = 800X, T = 2C, initial dry density = 1.67 g/cm^3, compacted water content = 20%, a) 148 MPa; b) 89 MPa; c) 36 MPa; and d) 0 MPa

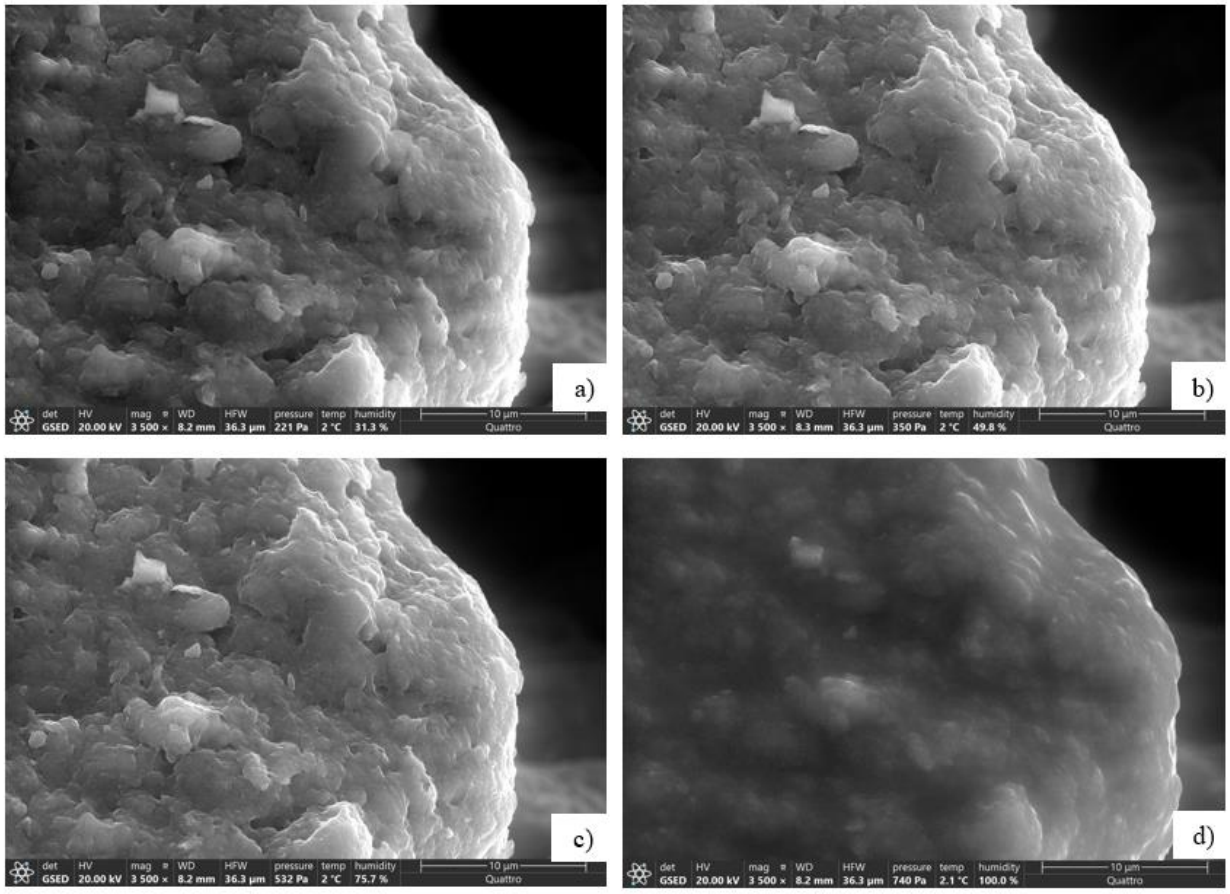

Figure A.18. Secondary wetting cycle of Hollywood specimen, Magnification = 3500X, T = 2C, initial dry density = 1.67 g/cm^3, compacted water content = 20%, a) 148 MPa; b) 89 MPa; c) 36 MPa; and d) 0 MPa

ESEM Micrographs of Heiden Specimens

Heiden opt

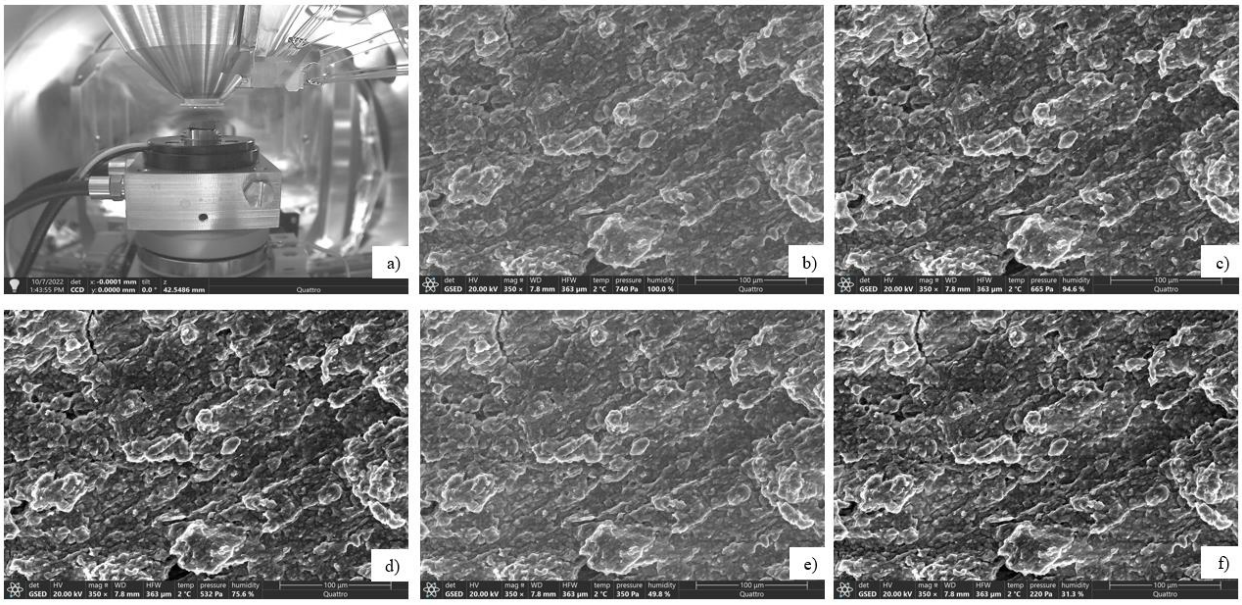

Figure A.19. Primary drying cycle of Heiden specimen, Magnification = 350X, T = 2C, initial dry density = 1.57 g/cm^3, compacted water content = 23%, a) Specimen seating; b) 0 MPa; c) 7 MPa; d) 36 MPa; e) 89 MPa; and f) 148 MPa

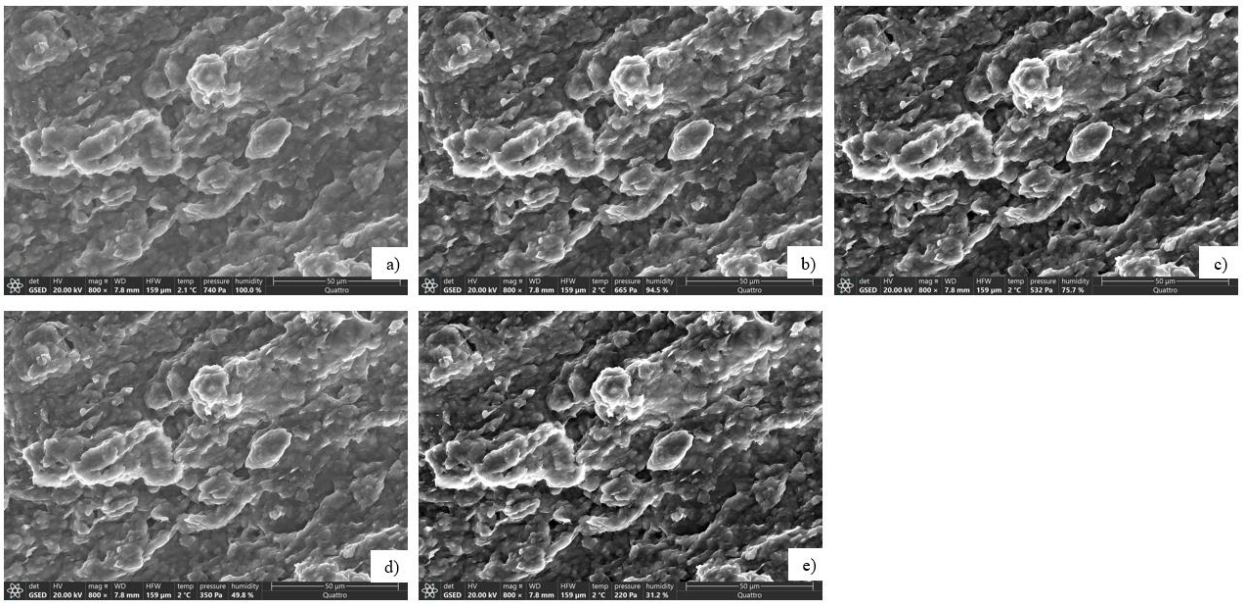

Figure A.20. Primary drying cycle of Heiden specimen, Magnification = 800X, T = 2C, initial dry density = 1.57 g/cm^3, compacted water content = 23%, a) 0 MPa; b) 7 MPa; c) 36 MPa; d) 89 MPa; and e) 148 MPa

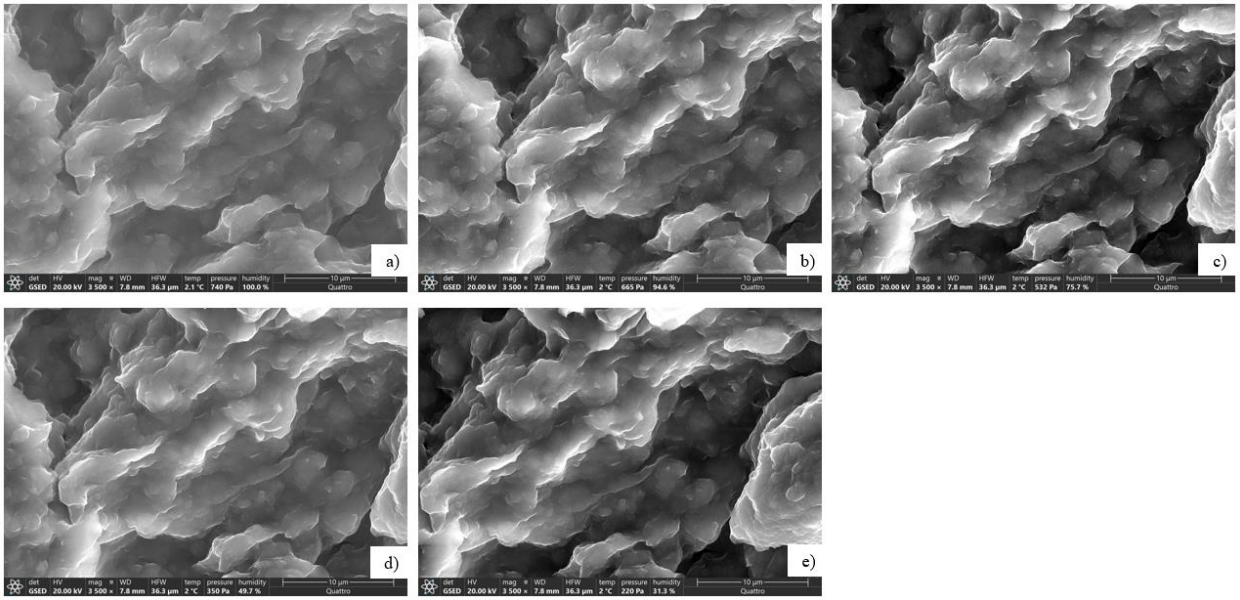

Figure A.21. Primary drying cycle of Heiden specimen, Magnification = 3500X, T = 2C, initial dry density = 1.57 g/cm^3, compacted water content = 23%, a) 0 MPa; b) 7 MPa; c) 36 MPa; d) 89 MPa; and e) 148 MPa

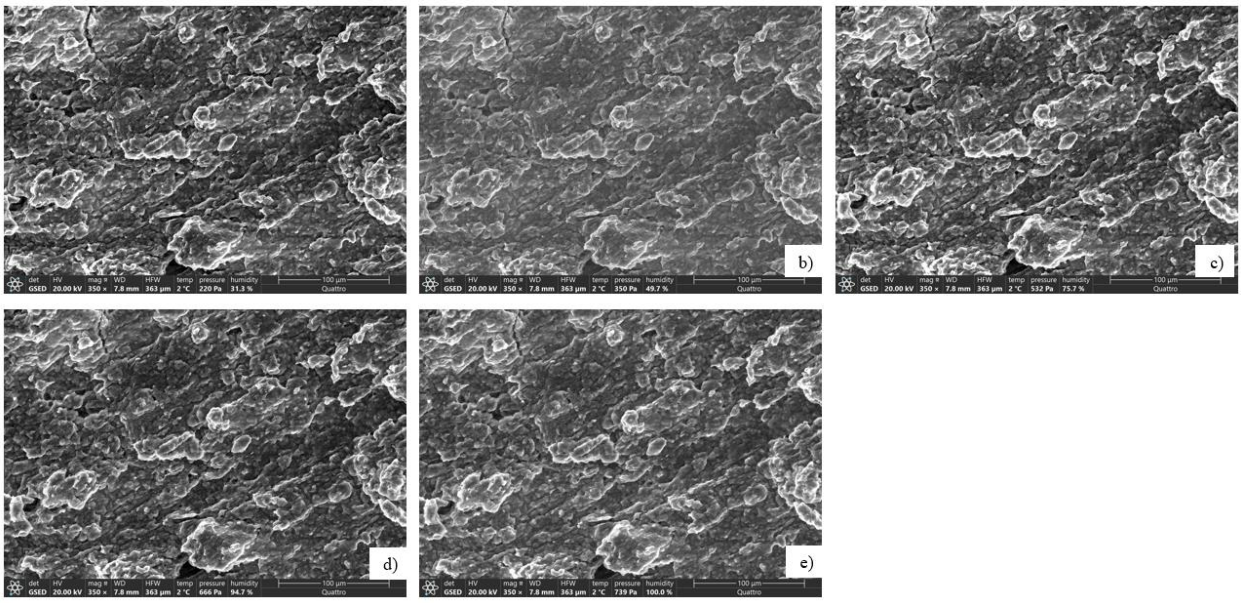

Figure A.22. Secondary wetting cycle of Heiden specimen, Magnification = 350X, T = 2C, initial dry density = 1.57 g/cm^3, compacted water content = 23%, a) 0 MPa; b) 7 MPa; c) 36 MPa; d) 89 MPa; and e) 148 MPa

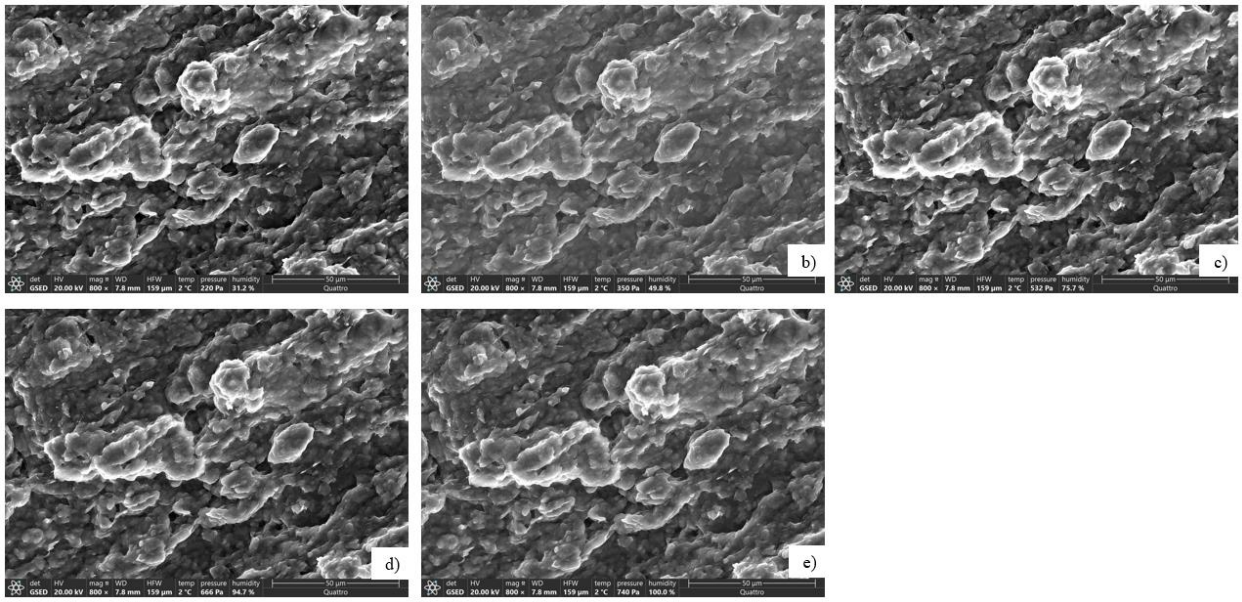

Figure A.23. Secondary wetting cycle of Heiden specimen, Magnification = 800X, T = 2C, initial dry density = 1.57 g/cm^3, compacted water content = 23%, a) 0 MPa; b) 7 MPa; c) 36 MPa; d) 89 MPa; and e) 148 MPa

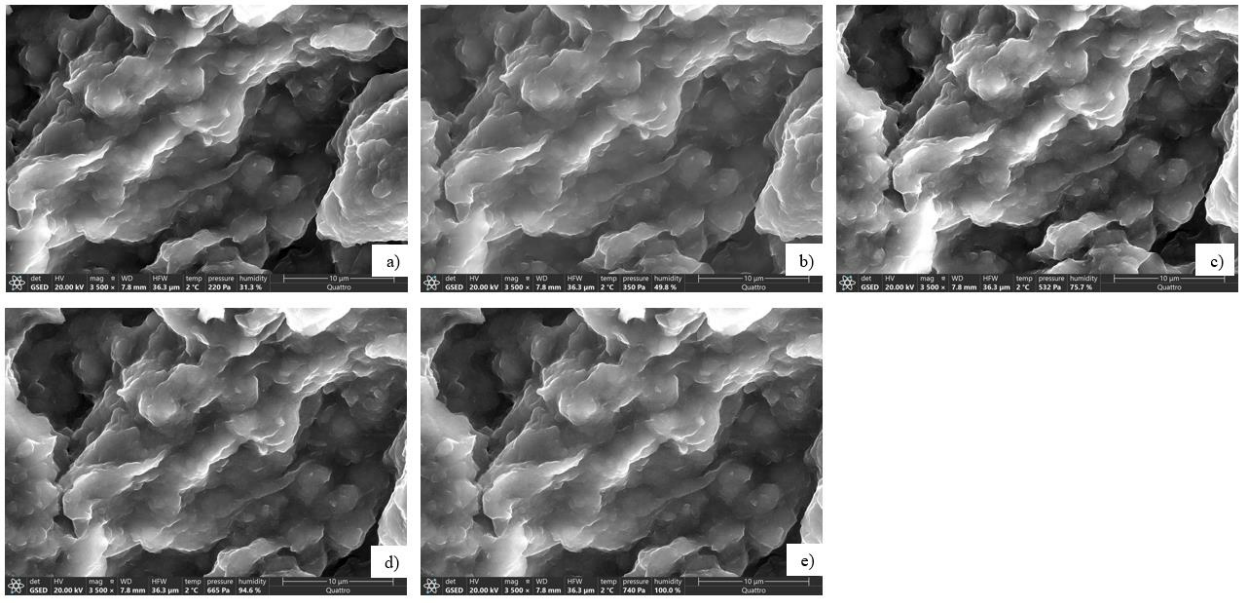

Figure A.24. Secondary wetting cycle of Heiden specimen, Magnification = 3500X, T = 2C, initial dry density = 1.57 g/cm^3, compacted water content = 23%, a) 0 MPa; b) 7 MPa; c) 36 MPa; d) 89 MPa; and e) 148 MPa

Heiden w1

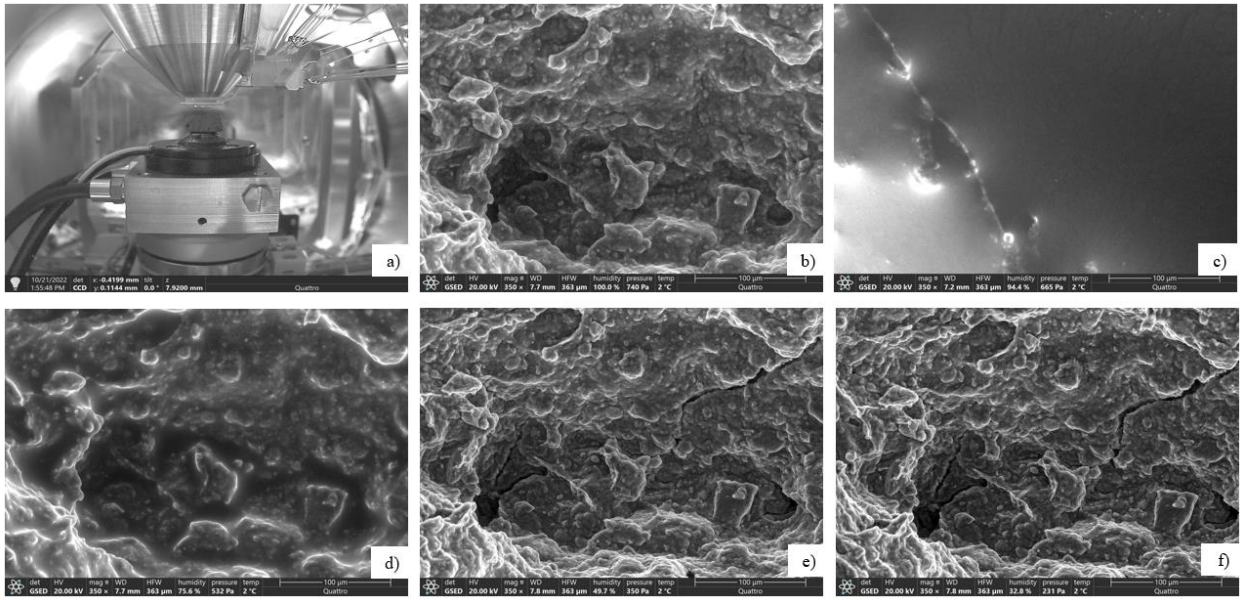

Figure A.25. Primary drying cycle of Heiden w1 specimen, Magnification = 350X, T = 2C, initial dry density = 1.22 g/cm^3, compacted water content = 41%, a) Specimen seating; b) 0 MPa; c) 7 MPa; d) 36 MPa; e) 89 MPa; and f) 148 MPa

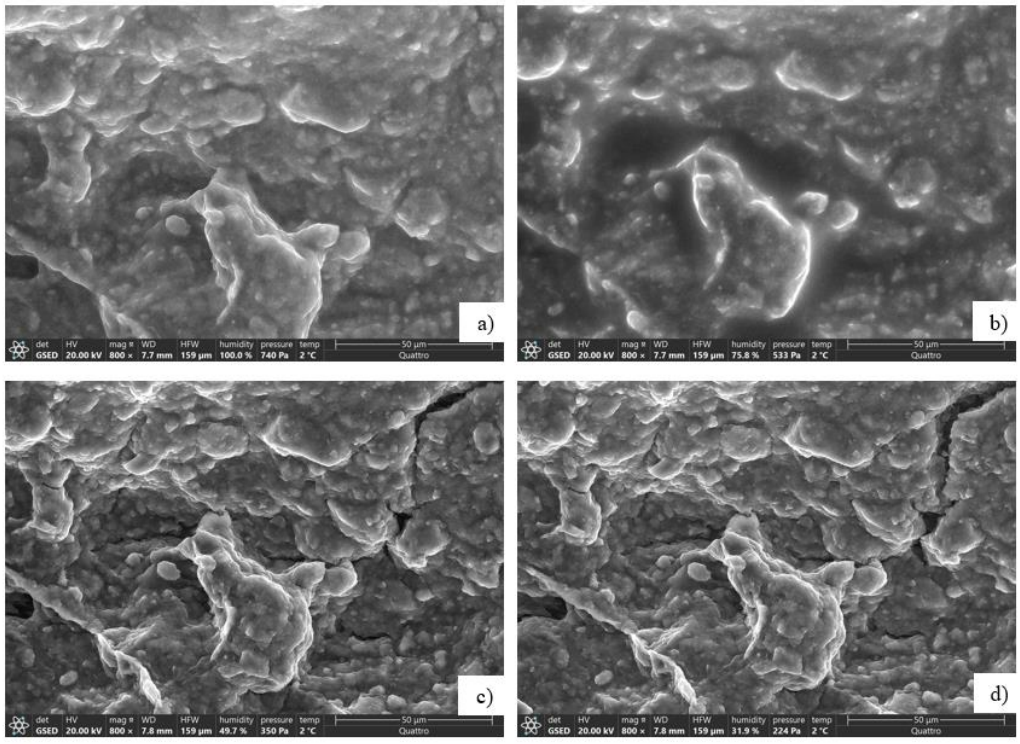

Figure A.26. Primary drying cycle of Heiden w1 specimen, Magnification = 800X, T = 2C, initial dry density = 1.22 g/cm^3, compacted water content = 41%, a) 0 MPa; b) 36 MPa; c) 89 MPa; and d) 148 MPa

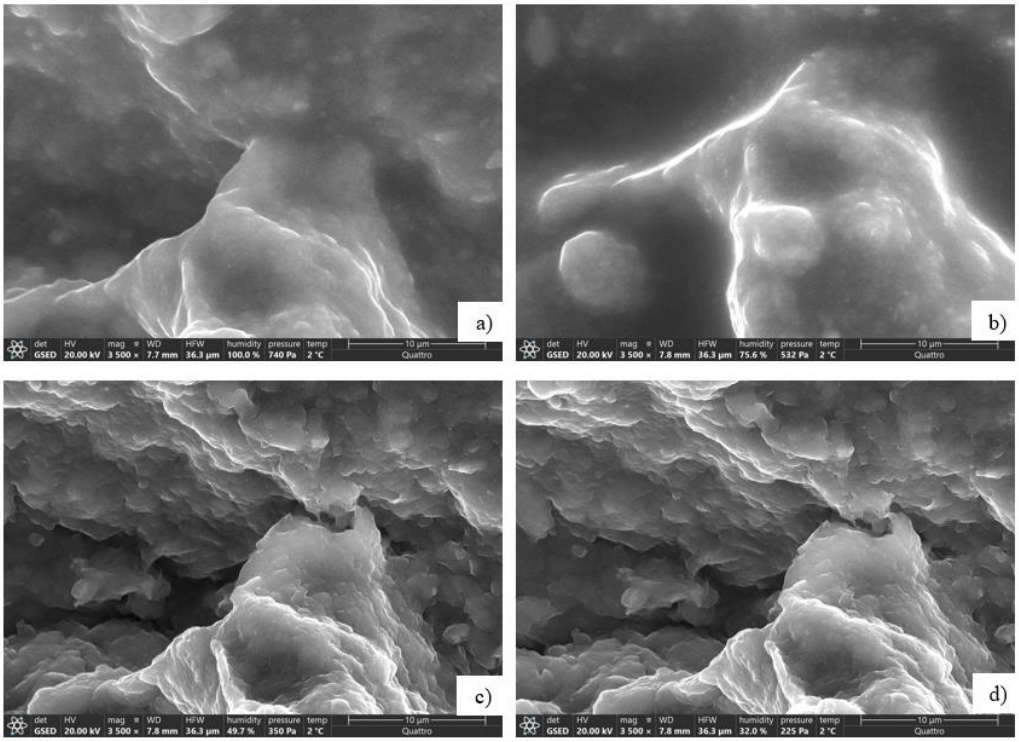

Figure A.27. Primary drying cycle of Heiden w1 specimen, Magnification = 3500X, T = 2C, initial dry density = 1.22 g/cm^3, compacted water content = 41%, a) 0 MPa; b) 36 MPa; c) 89 MPa; and d) 148 MPa

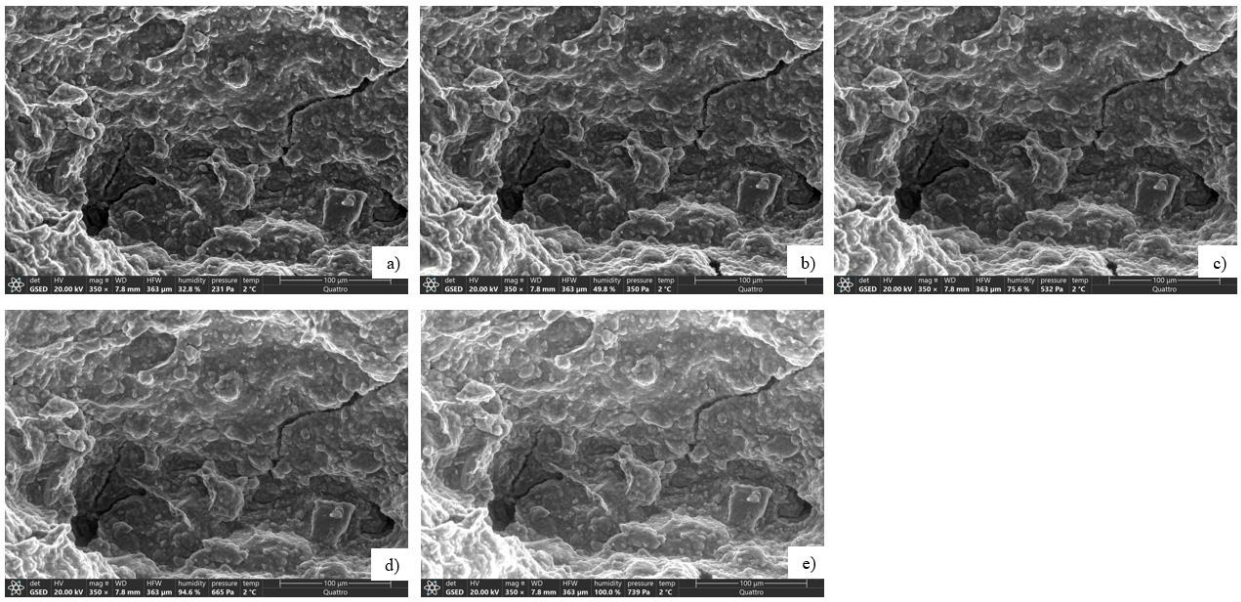

Figure A.28. Secondary wetting cycle of Heiden w1 specimen, Magnification = 350X, T = 2C, initial dry density = 1.22 g/cm^3, compacted water content = 41%, a) 0 MPa; b) 7 MPa; c) 36 MPa; d) 89 MPa; and e) 148 MPa

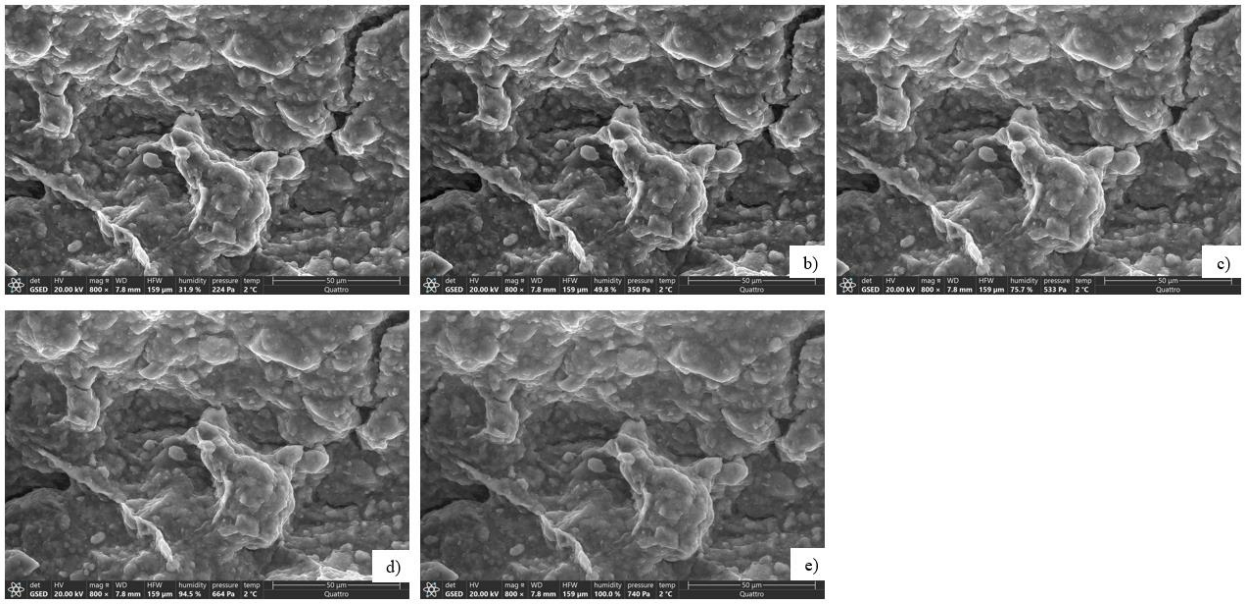

Figure A.29. Secondary wetting cycle of Heiden w1 specimen, Magnification = 800X, T = 2C, initial dry density = 1.22 g/cm^3, compacted water content = 41%, a) 0 MPa; b) 7 MPa; c) 36 MPa; d) 89 MPa; and e) 148 MPa

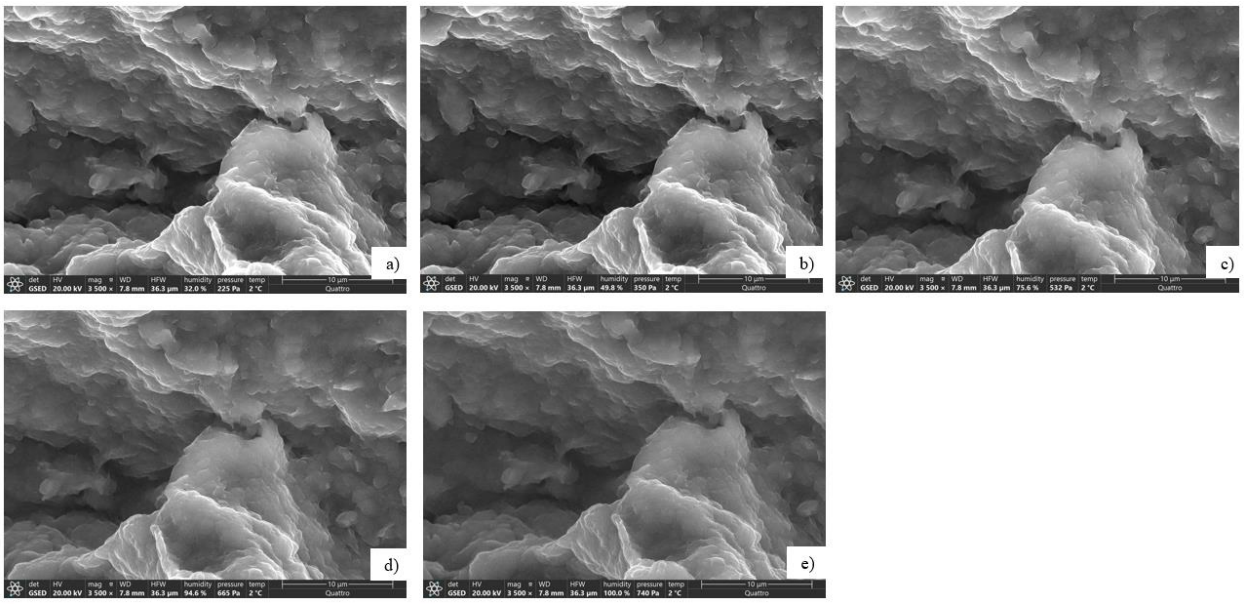

Figure A.30. Secondary wetting cycle of Heiden w1 specimen, Magnification = 3500X, T = 2C, initial dry density = 1.22 g/cm^3, compacted water content = 41%, a) 0 MPa; b) 7 MPa; c) 36 MPa; d) 89 MPa; and e) 148 MPa

Heiden w2

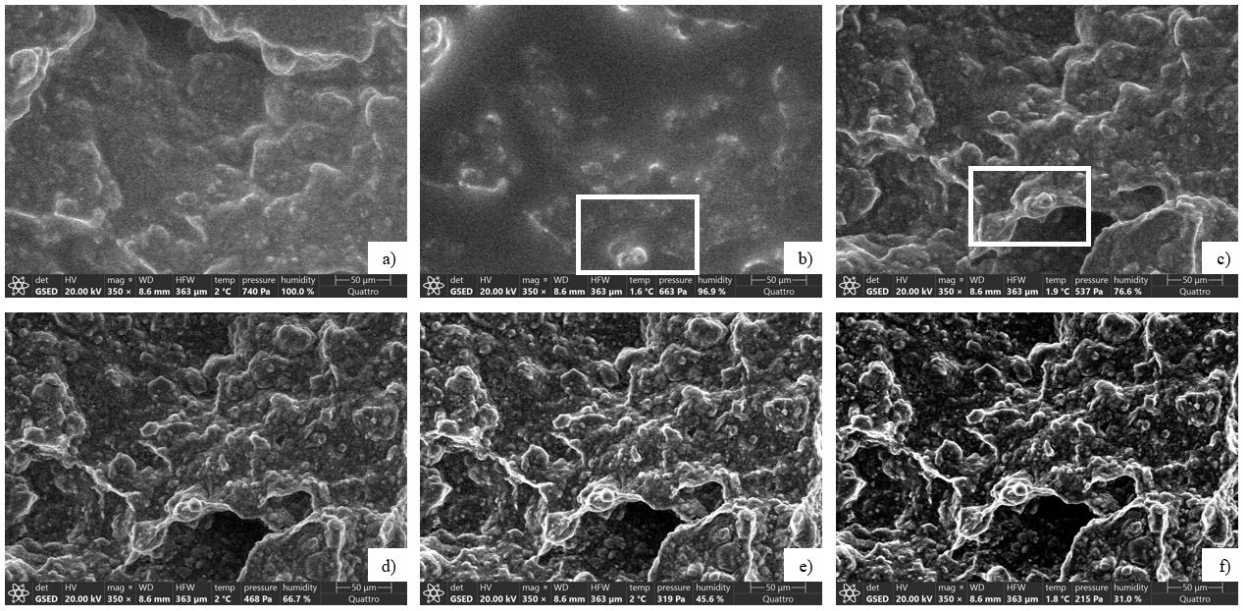

Figure A.31. Primary drying cycle of Heiden w2 specimen, Magnification = 350X, T = 2C, initial dry density = 1.25 g/cm^3, compacted water content = 37%, a) 0 MPa; b) 4 MPa; c) 34 MPa; d) 51 MPa; e) 98 MPa; and f) 148 MPa

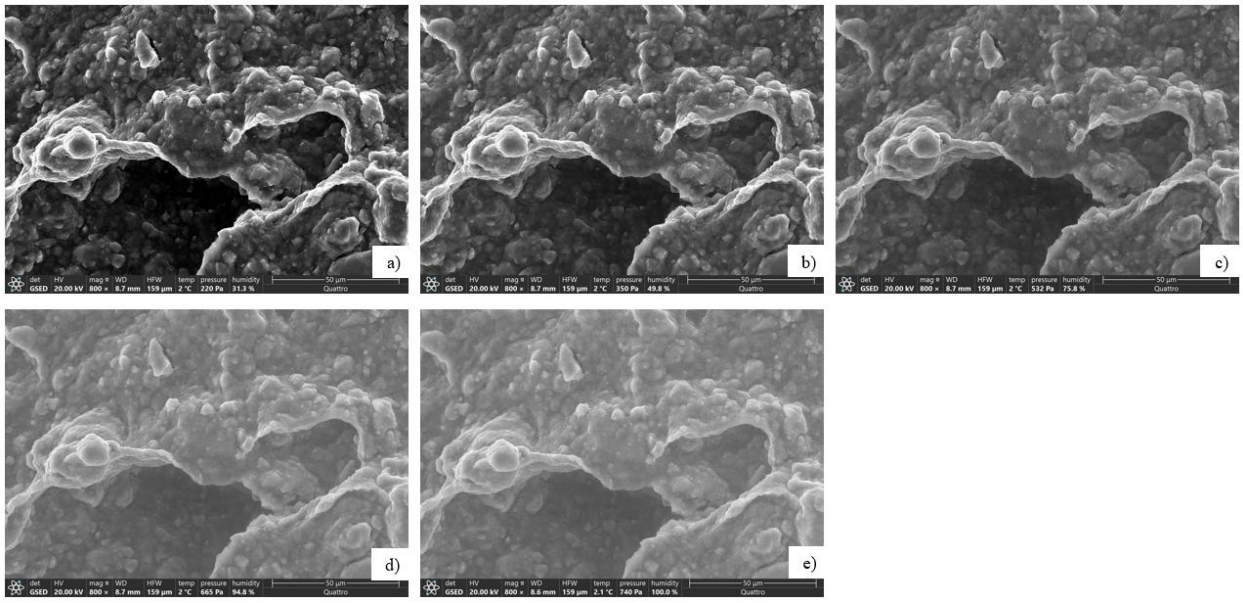

Figure A.32. Secondary wetting cycle of Heiden w2 specimen, Magnification = 800X, T = 2C, initial dry density = 1.25 g/cm^3, compacted water content = 37%, a) 148 MPa; b) 89 MPa; c) 36 MPa; d) 7 MPa; and e) 0 MPa

ESEM Micrographs of Na-montmorillonite Specimens

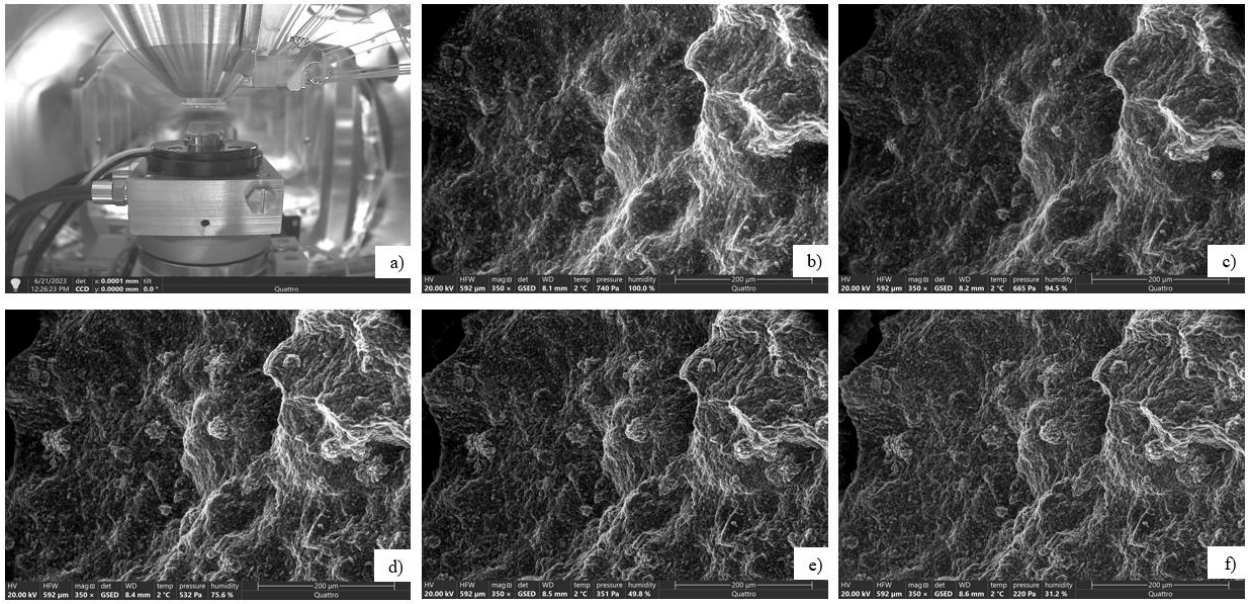

Figure A.33. Primary drying cycle of Na-Montmorillonite specimen, Magnification = 350X, T = 2C, initial dry density = 1.02 g/cm^3, compacted water content = 31%, a) Specimen seating; b) 0 MPa; c) 7 MPa; d) 36 MPa; e) 89 MPa; and f) 148 MPa

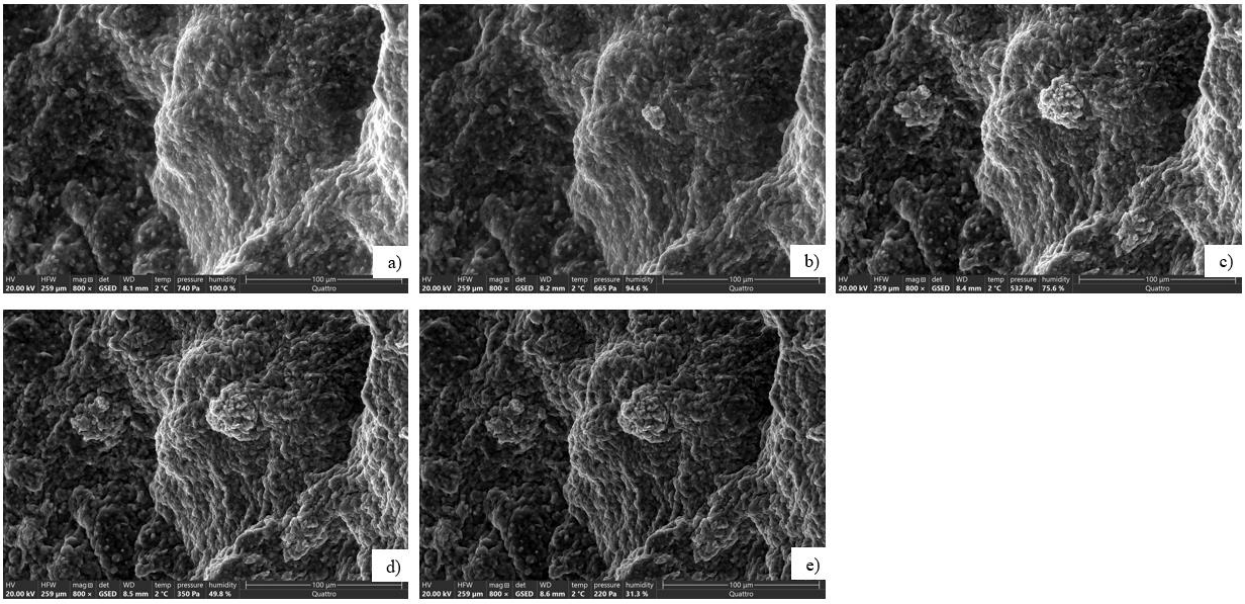

Figure A.34. Primary drying cycle of Na-Montmorillonite specimen, Magnification = 800X, T = 2C, initial dry density = 1.02 g/cm^3, compacted water content = 31%, a) 0 MPa; b) 7 MPa; c) 36 MPa; d) 89 MPa; and e) 148 MPa

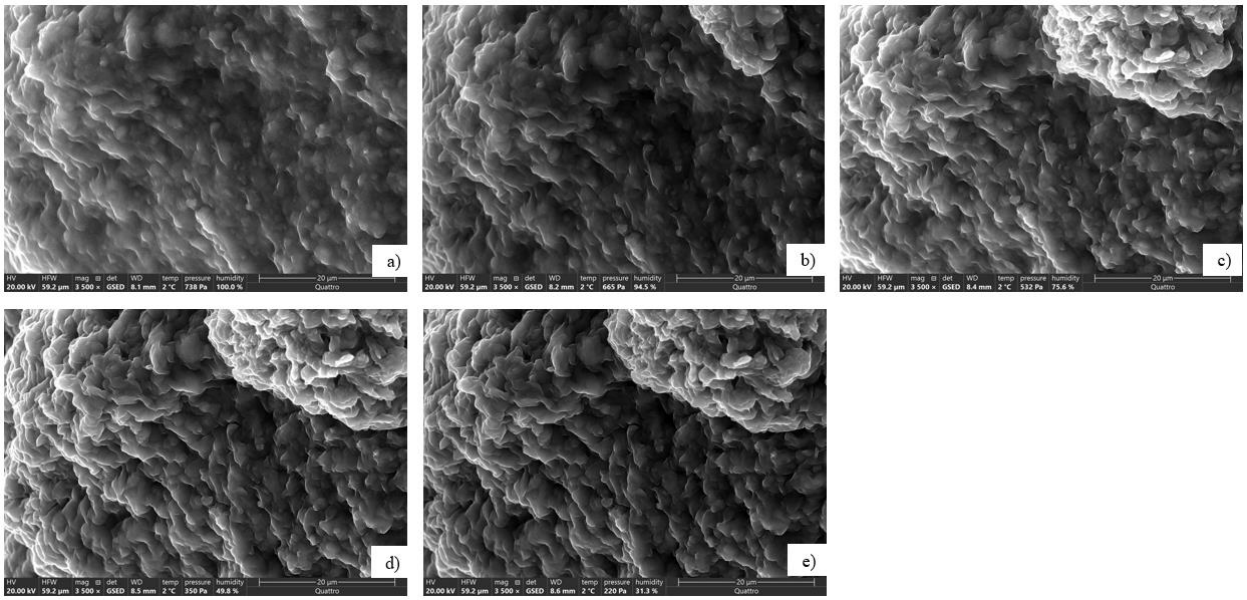

Figure A.35. Primary drying cycle of Na-Montmorillonite specimen, Magnification = 3500X, T = 2C, initial dry density = 1.02 g/cm^3, compacted water content = 31%, a) 0 MPa; b) 7 MPa; c) 36 MPa; d) 89 MPa; and e) 148 MPa

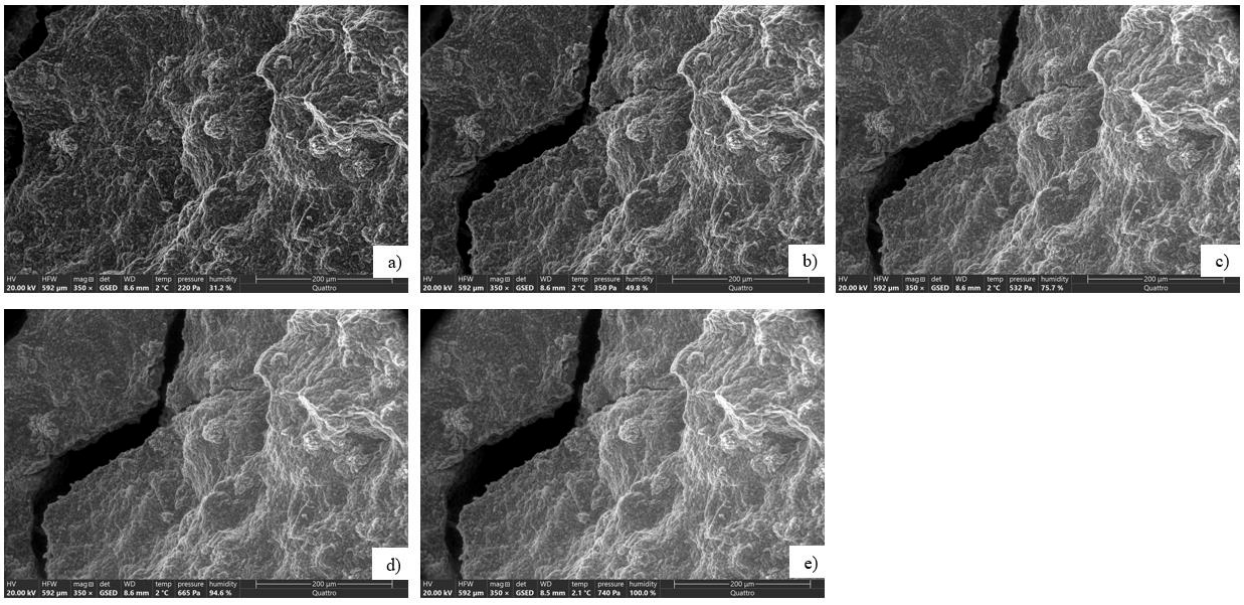

Figure A.36. Secondary wetting cycle of Na-Montmorillonite specimen, Magnification = 350X, T = 2C, initial dry density = 1.02 g/cm^3, compacted water content = 31%, a) 148 MPa; b) 89 MPa; c) 36 MPa; d) 7 MPa; and e) 0 MPa

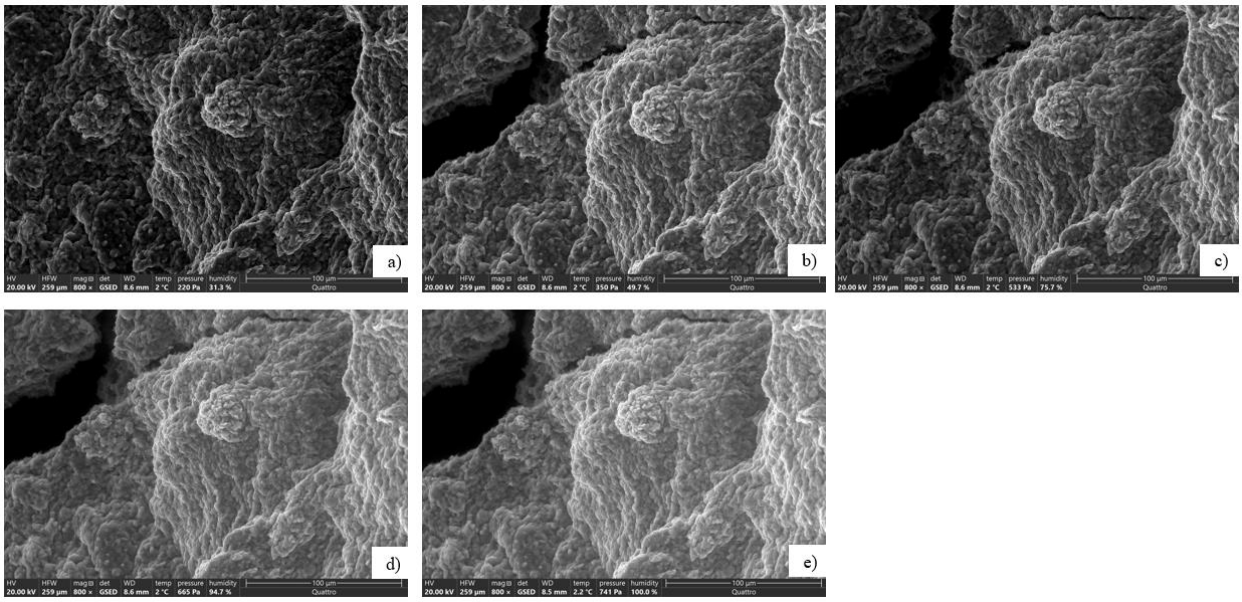

Figure A.37. Secondary wetting cycle of Na-Montmorillonite specimen, Magnification = 800X, T = 2C, initial dry density = 1.02 g/cm^3, compacted water content = 31%, a) 148 MPa; b) 89 MPa; c) 36 MPa; d) 7 MPa; and e) 0 MPa

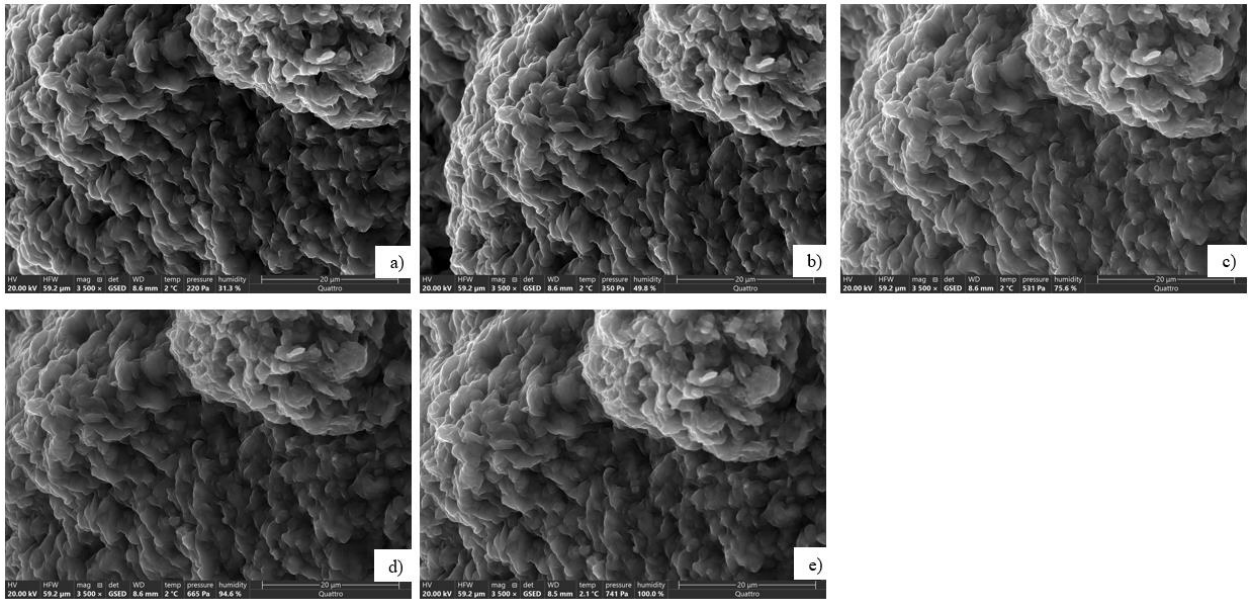

Figure A.38. Secondary wetting cycle of Na-Montmorillonite specimen, Magnification = 3500X, T = 2C, initial dry density = 1.02 g/cm^3, compacted water content = 31%, a) 148 MPa; b) 89 MPa; c) 36 MPa; d) 7 MPa; and e) 0 MPa

Appendix B – Free Swell Tests of Na-montmorillonite

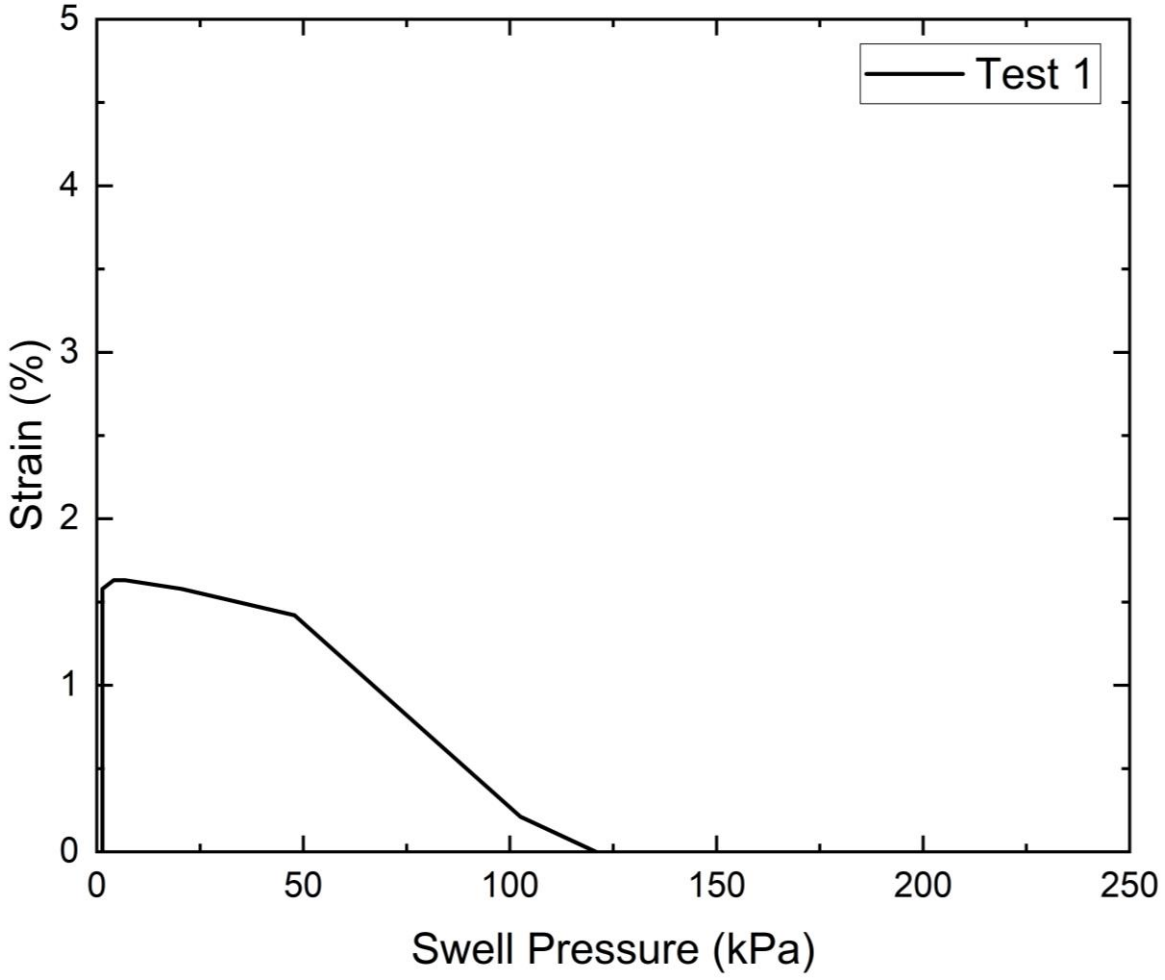

Figure B.1. Free swell results of Sample 1, e = 3.16, σ_s = 128 kPa

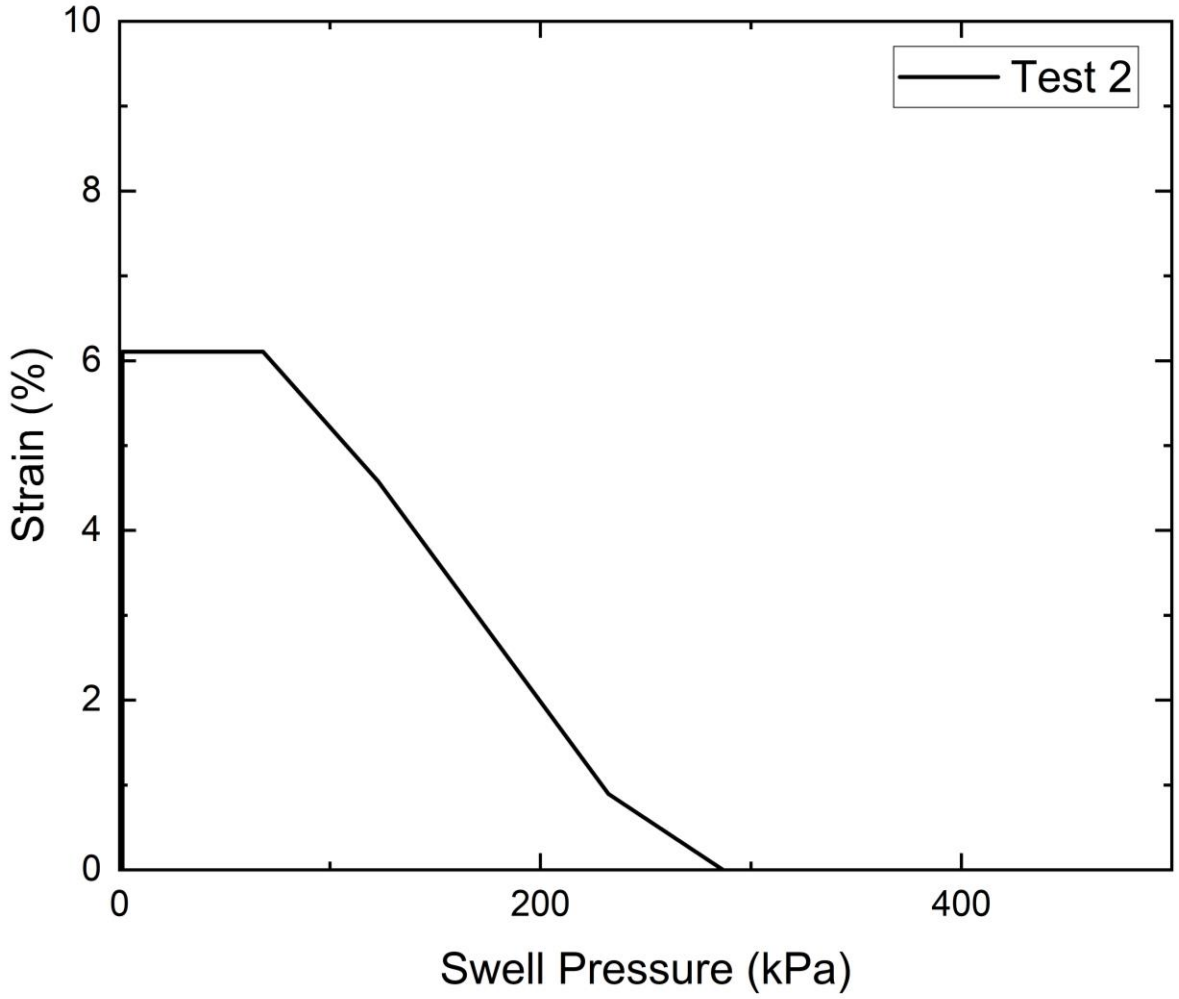

Figure B.2. Free swell results of Sample 2, e = 2.94, σ_s = 295 kPa

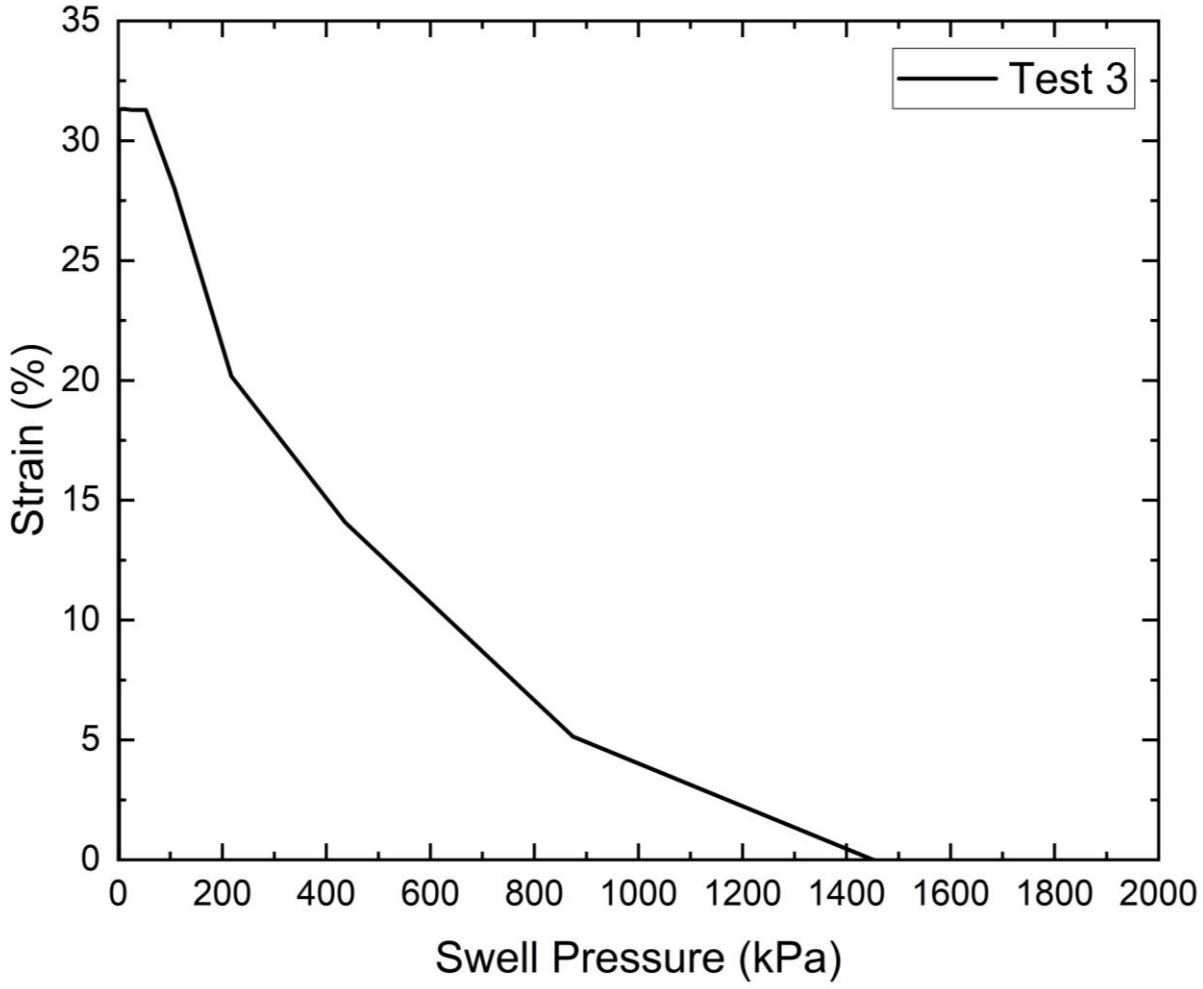

Figure B.3. Free swell results of Sample 3, e = 1.35, σ_s = 1429 kPa

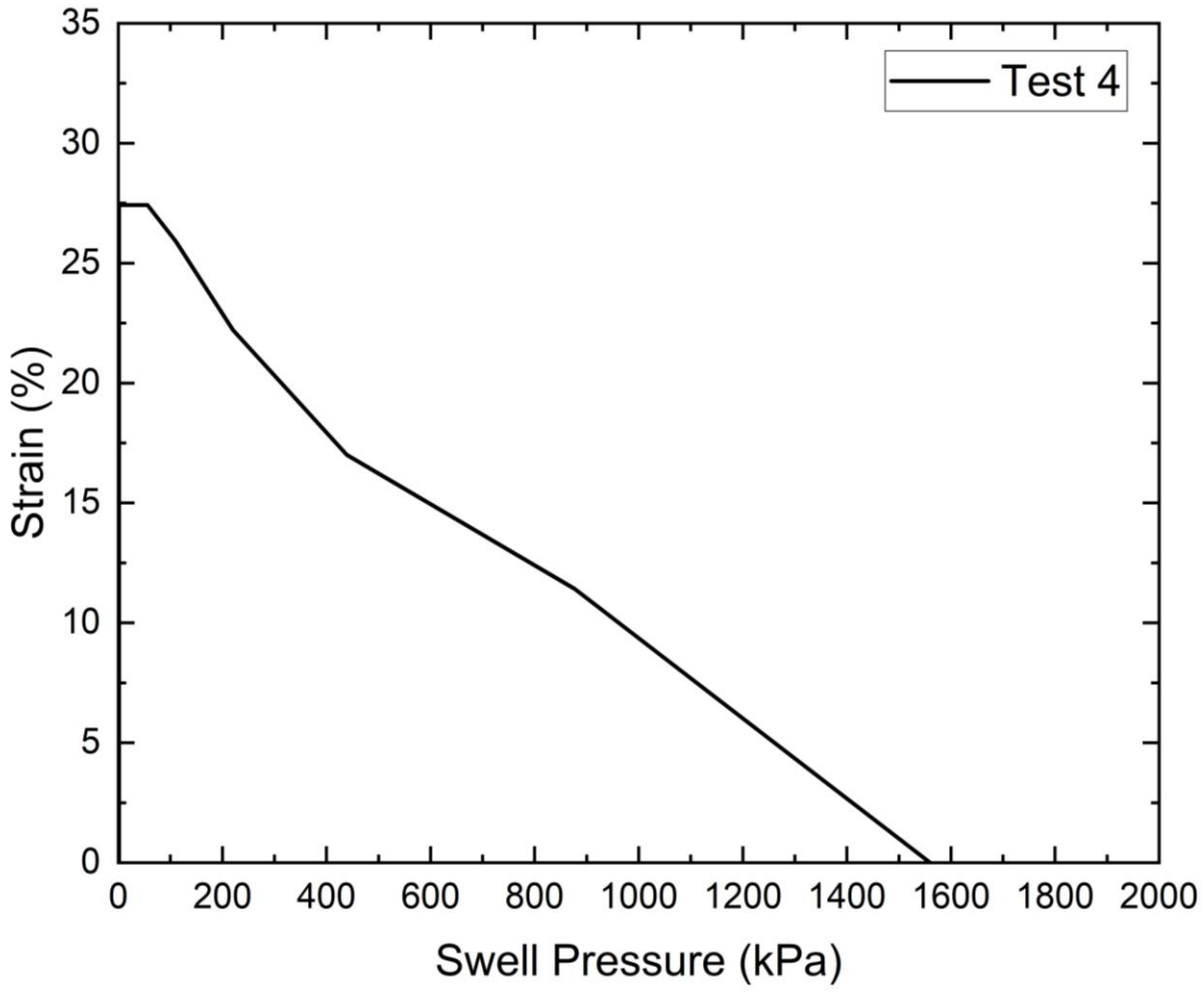

Figure B.4. Free swell results of Sample 4, e = 1.48, σ_s = 1561 kPa

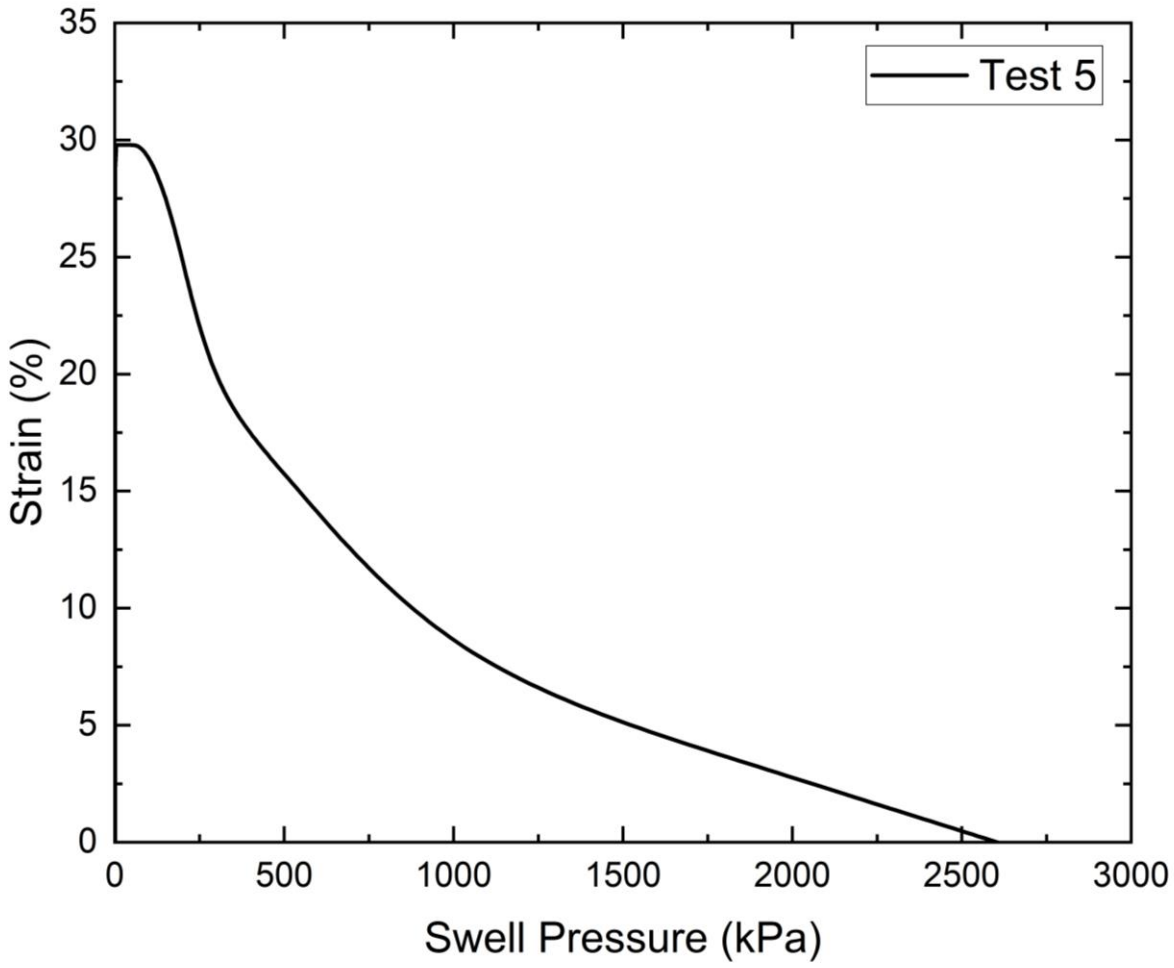

Figure B.5. Free swell results of Sample 5, e = 1.16, σ_s = 2607 kPa

Appendix C – DEMClay Manual v.37

DEMClay is a program written in FORTRAN for the analysis of clay assemblies at the microscale. Clays are modeled as an assembly of plate-like particles, made of a number of discrete elements. DEMClay version 37 is a two-dimensional analysis and clay assemblies are simulated as an assembly of straight line segments.

For this study, the DEMClay program was compiled using Intel oneAPI. Once compiled, the user can interact with the program through a system of input commands and associated variables and parameters. The input commands, parameters, and output commands are detailed in the following sections. Specific inputs and their effects on the outputs are detailed in Chapter 5 of this dissertation.

C.1 Units and Assumptions

Length: μm (microns)

Force: N (Newtons)

Time: s (seconds)

Density of clay particles: $\rho = 2.7 \times 10^{-21}$ N·sec2/μm^4

C.2 Commands

Input commands are necessary to define the assembly area, the assembly of particles, particle size and spacing, forces to consider, start/stop/save the run, and the method by which analysis will proceed. Commands are associated in the FORTRAN code with other input parameters, which are detailed in later sections.

The input commands used in DEMClay v. 37 and their definition are tabulated in Table C.1. Output commands are tabulated in Table C.2.

Table C.1 DEMClay input commands

Command	Meaning
GPAR	Generate particles
GWAL	Generate assembly walls
GCON	Generate interparticle contacts
GTOL	Add tolerance modifier
GSTE	Use time step modifier
GBOX	Generate cells (discretize assembly area into cells)
IPCF	Define internal forces (activate internal forces)
RDAM	Read and load damping parameters
REST	Restart run
RPROP	Read in particle and inter-particle properties
SAVE	Save run into output files
START	Start run
STOP	Stop execution of code
SWAM	Conduct N cycles of analysis

Table C.2. DEMClay output commands

Command	Meaning
PPAR	Generate data for plotting particles and walls (generate assembly output file)
WCON	Write out particle contact information
SWAL [*]	Command to write out stresses (STRE) or strains (STRA) over the assembly walls
HIST [*]	Create data file for histogram
CONT	Contact normal distribution for all contacts
PART	Particle orientation distribution
FABR	Calculate fabric tensors (results printed to output file *.SCR)
REPF	Repulsive force distribution for all contacts
WPRO	Write current values of properties
WSTE	Write time step
WFOR	Write data for plotting interparticle force vs displacement
WGSD	Write grain size distribution data (result printed in output file *.GSD)
CROS	Determine if particles intersected each other

Note: * denotes additional input required

C.3 Input Parameters

Each input command is one line in the input file. Input commands are associated with input parameters, which are entered on the lines following the input command. Specific input parameters are detailed in this section.

C.3.1 START

Each input file must begin with either the STAR (or START, depending on the version of FORTRAN) or REST command. The START command starts a new run of the code and the REST command restarts a priorly saved code, followed by 4 lines of code containing strings of input parameters.

Line 1: NELEM, NELEW, NCEMT, NUNCT, NINTT, IMECH

NELEM Maximum number of discrete elements used in analysis

NELEW Number of walls in the assembly. Must be less than or equal to 4

NCEMT Option for cemented contacts

NUNCT Option for uncemented contacts

NINTT Option for interelement contacts

IMECH 1 for modeling mechanical effects, 0 to ignore mechanical effects

Line 2: ULIMITS, ELLSMALL

ULIMITS Limits displacement of particles as the assembly is generated

ELLSMALL Length of a discrete element (L_{DEM})

Line 3: IPCFOR

IPCFOR Determines type of forces considered:

1 Both repulsive and attractive

2 Only repulsive force

3 Only attractive force

Line 4: RTOLE1S, RTOLE2S, ATOLE1S, ATOLE2S

RTOLE1S Defines area of influence of the repulsive force in the x direction

RTOLE2S Defines area of influence of the repulsive force in the y direction

ATOLE1S Defines area of influence of the attractive force in the x direction

ATOLE2S Defines area of influence of the attractive force in the y direction

C.3.2 GTOL

The GTOL command defines the particle thickness, or the separation distance at which interparticle mechanical contacts begin.

Line 1: TOLE1

TOLE1 Analogous to H_{DEM} (μm)

C.3.3 RPRO

The RPRO (or RPROP) command provides the parameters for the material properties used in the analysis. The type of material properties are specified under the START command and the number of lines of parameters in the input file varies depending on the number of properties selected under STAR/REST.

Cemented Contact Parameters:

N1 Index value of cemented parameters (If NCEMT =1, then N1= 1 always)

k_{nc} Interparticle compressive normal contact force stiffness (N/μm)

k_{nt} Interparticle tensile normal contact force stiffness (N/μm)

k_s Interparticle shear contact force stiffness (N/μm)

k_θ Interparticle rotational contact force stiffness (N/μm)

T_{nc} Maximum tensile normal force (N)

T_{nt} Maximum compressive normal force (N)

T_s	Maximum shear force (N) (where plastic range begins)
T_m	Maximum mechanical force (N), generally equal to T_S
n	Cementation parameter, generally 1.0

Uncemented Contact Parameters:

N1	Index value of uncemented parameters (If MUNCT = 1, then N1 = 1)
k_{nc}	Interparticle normal stiffness (N/m)
k_s	Interparticle shear stiffness (N/M)
c	Interparticle contact cohesion (N)
ϕ	Interparticle contact friction (degrees)

Inter-element Contact Parameters:

N1	Index value of interelement parameters (If NINTI = 1, then N1 = 1)
E	Young's modulus (generally accepted to use E = 0.003 N/μm)
d	Particle thickness (H_{DEM})

Physicochemical Parameters:

n	Electrolyte concentration of pore fluid (mol/L)
υ	Cation valence
T	Temperature (K)
ε	Dielectric constant of the pore fluid
$ψ_0$	Surface potential (mv)
A	Hamaker constant (J)
ICAP	Capillary force parameter (1 for applying capillary force, 0 to ignore)
INTERLF	Interlayer force parameter (1 for applying interlayer force, 0 to ignore)
S	Degree of saturation (decimal form)

θc Contact angle (degrees)

Ts Surface tension (N/μm)

σ0 Linear parameter to describe interlayer attraction

α Linear parameter to describe interlayer attraction

λ Linear parameter to describe interlayer attraction

IOPT Type of damping (1 = exponential, 2 = oscillatory, 3 = linear)

Density and Damping Parameters:

ρ Particle Density

C-MECH Local mechanical damping parameter

C-PHYCHEM Local physicochemical damping parameter

C.3.4 GWAL

The GWAL command defines the external assembly parameters, referred to here as the box dimensions. The particle assembly is defined by the walls bounding the specimen and the size of the wall assembly defines the maximum size of the specimen.

The size of the wall assembly, along with the number of discrete elements chosen, will mainly affect the void ratio. For the same number of discrete elements, a large assembly area will result in a higher void ratio (less dense specimen) and a smaller assembly area results in a lower void ratio (more dense specimen).

Walls are rigid boundaries that can be subjected to rigid body displacements but not rotations. Wall coordinates are defined in a counterclockwise manner beginning with the south-west corner. Since walls are expected to move, both with consolidation (toward the specimen) and swelling (away from the specimen), an outer buffer is maintained at least 10% larger than the inner

box dimensions. For example, a 1.5 μm x 0.5 μm sample requires a sample box 1.8 μm x 0.6 μm (Figure C.1).

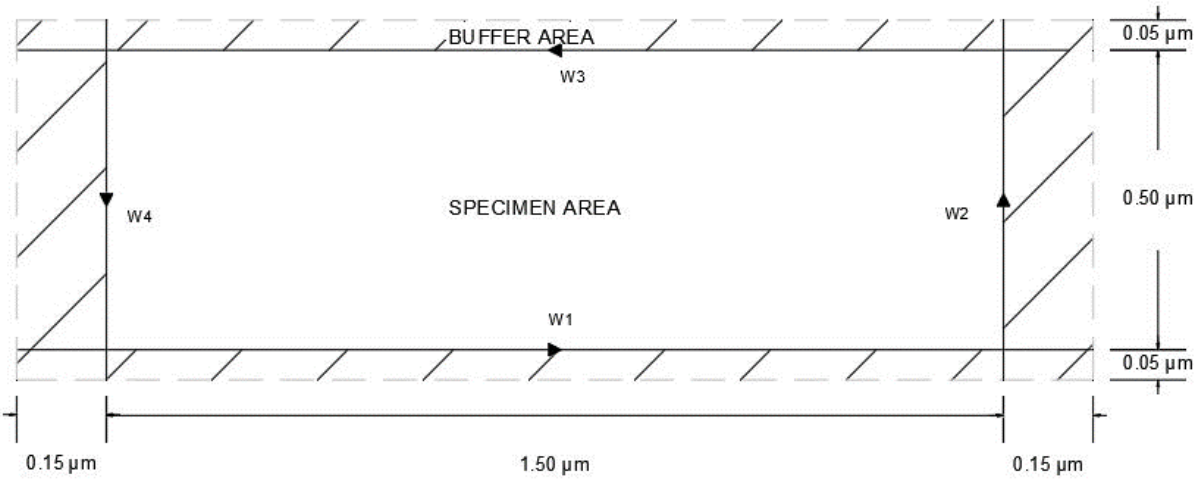

Figure C.1. Sample box dimensions

The GWAL command will generally be followed by 4 lines of inputs, unless the analysis requires fewer than 4 walls in the assembly. Each line of inputs contains x and y coordinates for the assembly wall:

X1, Y1, X2, Y2	Wall 1 (W1 = bottom horizontal wall)
X1, Y1, X2, Y2	Wall 2 (W2 = right vertical wall)
X1, Y1, X2, Y2	Wall 3 (W3 = top horizontal wall)
X1, Y1, X2, Y2	Wall 4 (W5 = left vertical wall)

C.3.5 GPAR

The GPAR command generates an assembly of discrete elements within the assembly box dimensions.

Line 1: LABEL1, LABEL2

LABEL1 Parameter to define how discrete elements are generated in the assembly

AUTO Automatically generate particles into a single layer

MANU Manually generate particles based on manual coordinates

LAYE Discretizes particle assembly into layers

LABEL2 UNIF (Generate particles with uniform thickness)

Line 2: IOPT

IOPT Parameter to define particle lengths

1 Particles generated with uniform length (L_{DEM})

2 Particles generated according to GSD (input in following lines)

Line 3: LMAX, LMIN, NTRIAL, S1 (If IOPT = 2 selected)

LMAX Maximum particle length (multiple of L_{DEM})

LMIN Minimum particle length (must be equal to L_{DEM})

NTRIAL Max number of trials allowed to randomly generate particle assembly

S1 Particle spacing parameter (S1 less than one for more dense specimens)

Line 4: M

M Number of particle size intervals used in particle size distribution

Line 5 – (5 + M): Min length, Max length, percentage

Min length Minimum particle length in particle size interval

Max length Maximum particle length in particle size interval

Percentage Percentage of GSD contained in particle size interval

Line 6 + M: S2

S2 Layer spacing parameter (S2 less than 1 for more dense layer spacing)

Line 7 + M: MM

MM Layer index parameter (generally 1)

Line 8 + M: Min, Max, Percentage

Min Minimum number of layers

Max Maximum number of layers

Percentage Percentage of layer thickness

C.3.6 GBOX

The GBOX command divides the assembly into cells before the analysis is performed. No parameters are associated with the GBOX command.

C.3.7 GCON

The GCON command establishes particle-to-particle contacts. The types of contacts between particles are defined under the STAR/REST command. No parameters are associated with the GCON command.

C.3.8 RDAM

The RDAM command reads in the damping parameters used in the analysis under the SWAM command. The parameters input under the RDAM command do not need to be the same damping parameters used with earlier commands which generated the particle assembly. The RDAM command is followed by one line of parameters.

LINE 1: C-GLOBAL, C-LOCAL

C-GLOBAL Global damping parameter

C-LOCAL Local damping parameter

C.3.9 SWAM

The SWAM command determines the method of analysis and how it will be run. SWAM is followed by 9 lines of inputs.

Line 1: LCODE-VT, LCODE-R, VMAX, XMDAMP, LCODE-T, LCDOE-F

LCODE-VT Maximum number of sub-steps for each major time step

LCODE-R Designates step number to print time histories of input data

VMAX Maximum particle velocity

XMDAMP Global damping parameter used in analysis (mass-proportional)

LCODE-T Wall velocities are applied every other LCODE-T sub-step

LCODE-F Particle coordinates are printed every LCODE-F sub-step

Line 2: RATEREP, RATEATT, RATECAP, RATEINT

RATEREP Rate used for repulsive force

RATEATT Rate used for attractive force

RATECAP Rate used for capillary force

RATEINT Rate used for interlayer force

Line 3: NCYCLE

NCYCLE Number of major time steps applied

Line 4: NWA

NWA Number of walls in the assembly (generally 4, but must not exceed 4)

Line 5: GRAVITY

GRAVITY The value of gravity being used in the assembly

Line 6-9: N1, VX, VY, VTH

N1 Designates the wall number, starting with the SE corner of the assembly

VX Linear wall velocity in the x direction

VY Linear wall velocity in the y direction

VTH Rotational velocity of the iterative wall

C.3.10 ***GSTE***

The GSTE command changes the time step modifier. The line in the input file following GSTE will be a number which will be multiplied by the time step variable. Regularly, the time step is calculated internally within the DEMClay code. This command is a method to manually change the time step and is not necessary to run the program.

C.3.11 SAVE

The SAVE command names the binary output file. This file can be used on a RESTART run of the program.

Example code:

```
SAVE
RUN1.DEM
```

C.3.12 STOP

The STOP command stops the execution of the program. No additional parameters will be read after the STOP command.

C.4 Output Files

The types of output files and their use are listed in table C.X.

Table C.X. DEMClay output files

Command	Use
*.SCR	General output file
*.PZ1	Data for plotting the particle and wall assembly
*.PLT	Raw data for plotting the particle and wall assembly
*.GSD	Grain size distribution data
*.HIS	Histogram data (type of data depends on outputs specified in input)
.*FRR	Force-displacement relations for a pair of parallel particles
*.RES	Time histories of quantities specified in input file
INTE.OUT	Histograms of particle separations when both layered particles and repulsive forces are considered

Note: * indicates file name (e.g., M001.SCR is the general output file for the M001 input)

C.5 Interpreting Output Data

The columns are not labeled in the output files. Therefore, a description of the column name, data type, and units for the *.GSD, *.PLT, *.FRR, and *.HIS files is detailed in this section.

C.5.1 GSD File (.GSD)*

The *.GSD file contains information necessary to plot a grain size distribution of the particle assembly for the final output of the code. The columns in the output file are detailed in Table C.X.

Table C.X. Column output in the *.GSD file

Column Variable	Units	Definition
L_{MAX}	μm	Particle length
Percentage	%	Percent passing

C.5.2 PLT File (.PLT)*

The *.PLT file contains information necessary to plot the particle assembly. Data is printed every LCODE-F sub intervals, detailed in the input commands. The first 4 rows contain wall data, giving

the wall number and the x and y coordinates for the endpoints of each line segment. The next rows contain particle assembly data: each row contains x and y endpoint coordinates for each discrete element in the assembly. The columns in the *.PLT output file are detailed in Table C.X.

Table C.X. Column output in the *.PLT file

Column Variable	Definition
No	Wall number or element number
x1	First x coordinate of line segment
y1	First y coordinate of line segment
x2	Second x coordinate of line segment
y2	Second y coordinate of line segment

C.5.3 FRR File (.FRR)*

The *.FRR file outputs the results of the force-separation distance relations for two parallel particles with differing separation distances. The columns in the *.FRR output file are detailed in Table C.X.

Table C.X. Column output in the *.FRR file

Column Variable	Units	Definition
D	Nm	Separation distance
F_{net}	N	Net force
F_R	N	Repulsive force
F_M	N	Mechanical force
F_A	N	Attractive force
k_{rep}	N/μm	Repulsive stiffness
k_{att}	N/μm	Attractive stiffness
k_m	N/μm	Mechanical stiffness

C.5.4 HIS File (.HIS)*

The *.HIS File contains time-history data of normal stresses on all four walls, the void ratio, linear velocity and acceleration of the particle centroid, and the number of mechanical contacts between

particles and walls along the four walls. Time-history variables are printed every LCODE-R sub step specified by the input commands. The columns in the output file are detailed in Table C.X.

Table C.X. Column output in the *.HIS file

Column Variable	Units	Definition
NSTEP	--	Step number
σ_{n1}	kPa	Stress on wall 1
σ_{n2}	kPa	Stress on wall 2
σ_{n3}	kPa	Stress on wall 3
σ_{n4}	kPa	Stress on wall 4
e	--	Void ratio
V_{max}	μm/s	Max linear velocity
a_{max}	$\mu m/s^2$	Max linear acceleration
nc_1	--	Number of contacts on wall 1
nc_2	--	Number of contacts on wall 2
nc_3	--	Number of contacts on wall 3
nc_4	--	Number of contacts on wall 4

C.6 Sample Input File

An example of an input file used for an assembly of Na-montmorillonite at the particle discretization level is presented below:

```
START
4000,4,0,1,1,1
0.0025,0.03
1
2.0,40.0,2.0,40.0
GTOL
0.005307
RPROP
1,0.64E-01,0.32E-01,0.0,20.0
1,3.0E-03,0.005307
0.04,1.0,293.0,80.0,116.0,0.000087E-20,1,1,1.0,50,0.0725,0.0077,11.0,0.0002,3
```

2.7E-21,0.02,0.02

WFOR

.004,1.0,1000,0,0.33E-03,0.1,1.2E-03

GWALL

0,0.05,1.5,0.05

1.45,0,1.45,0.5

1.5,0.45,0,0.45

0.15,0.5,0.15,0

GPAR

AUTO UNIF

2

0.1,0.025,500000,1.9

3

0.058,0.78,10

0.038,0.058,50

0.030,0.038,40

1.0

1

1,1,100

GBOX

GCON

WCON

SWAL STRE

HIST FABR

WCON

RDAM

0.01,0.01

WCON

PPAR

WGSD

CROSS

SWAM

100,20,6.0E+06,1.0E+04,10,200

0,0,0,0

20

4

0.0E+12

1,0,+5.0E+06,0

2,-5.0E+06,0,0

3,0,-5.0E+06,0

4,+5.0E+06,0,0

SWAL STRE

HIST FABR

WCON

PPAR

CROSS

SAVE

S194-8-20.DEM

STOP